construction
engineering
research
laboratory

United States Army
Corps of Engineers
...Serving the Army
...Serving the Nation

TECHNICAL REPORT M-258
April 1979

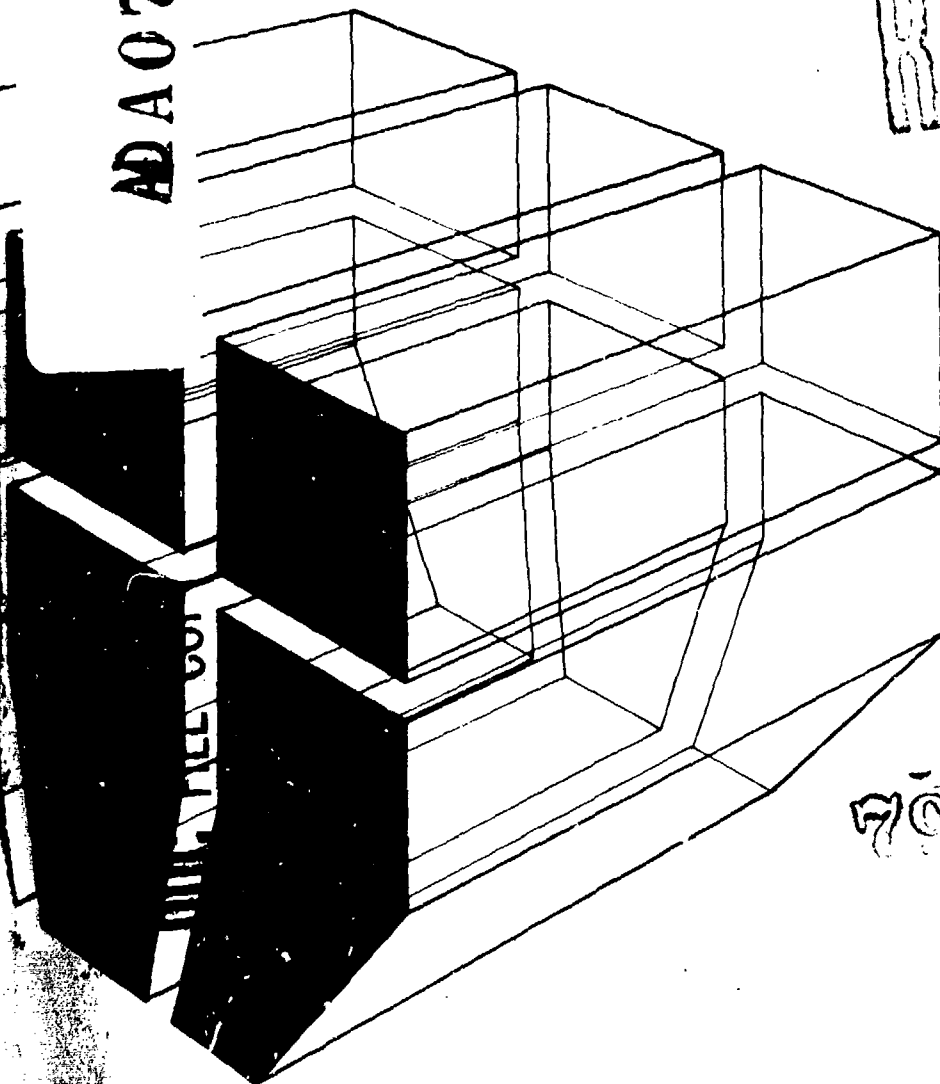# FRACTURE CHARACTERISTICS OF
STRUCTURAL STEELS: REFERENCE MANUAL

LEVEL

ADA072054

D D C
AUG 1 1979
C

by
J. Aleszka
Y. Kim
J. Scott
A. Kumar

CERL

Approved for public release; distribution unlimited.

REPORT DOCUMENTATION PAGE	READ INSTRUCTIONS BEFORE COMPLETING FORM

1. REPORT NUMBER	2. GOVT ACCESSION NO.	3. RECIPIENT'S CATALOG NUMBER
CERL-TR-M-258		

4. TITLE (and Subtitle)	5. TYPE OF REPORT & PERIOD COVERED
FRACTURE CHARACTERISTICS OF STRUCTURAL STEELS: REFERENCE MANUAL	FINAL
	6. PERFORMING ORG. REPORT NUMBER

7. AUTHOR(s)	8. CONTRACT OR GRANT NUMBER(s)
J. Aleszka Y. Kim J. Scott A. Kumar	

9. PERFORMING ORGANIZATION NAME AND ADDRESS	10. PROGRAM ELEMENT, PROJECT, TASK AREA & WORK UNIT NUMBERS
U.S. ARMY CONSTRUCTION ENGINEERING RESEARCH LABORATORY P.O. Box 4005, Champaign, IL 61820	4A761102AT23-A2-002

11. CONTROLLING OFFICE NAME AND ADDRESS	12. REPORT DATE
	April 1979
	13. NUMBER OF PAGES
	322

14. MONITORING AGENCY NAME & ADDRESS(if different from Controlling Office)	15. SECURITY CLASS. (of this report)
326p.	Unclassified
	15a. DECLASSIFICATION/DOWNGRADING SCHEDULE

16. DISTRIBUTION STATEMENT (of this Report)

Approved for public release; distribution unlimited.

17. DISTRIBUTION STATEMENT (of the abstract entered in Block 20, if different from Report)

18. SUPPLEMENTARY NOTES

Copies are obtainable from National Technical Information Service
Springfield, VA 22151

19. KEY WORDS (Continue on reverse side if necessary and identify by block number)

electron microscopes
structural steel
fracture (mechanics)

20. ABSTRACT (Continue on reverse side if necessary and identify by block number)

This report presents the findings of a scanning electron microscope
(SEM) study of tensile, fatigue, and impact fracture characteristics of
structural steels used in Army Corps of Engineers facilities and com-
ponents. Steels investigated were ASTM A-36, ASTM A-514, AX-110 weld,
HY-130, ASTM A-588, ASTM A-242, AISI 416, 17-4 PH, ASTM A-516, and
ASTM A-607. Specimens were tested in as-received, hydrogen-embrittled,
and temper-embrittled conditions. The failure mode of embrittled and

DD FORM 1473 EDITION OF 1 NOV 65 IS OBSOLETE

Block 20 continued.

unembrittled AX-110 weldments containing induced weld defects was also studied. The information contained in this reference manual will provide a basis for comparison of fracture characteristics to determine the mode of failure in analysis of components failure. Four examples of in-service failures in which the SEM provided valuable information are also presented.

FOREWORD

This investigation was conducted by the Engineering and Materials Division of the U.S. Army Construction Engineering Research Laboratory (CERL). The study was sponsored by the Directorate of Military Programs, Office of the Chief of Engineers (OCE), under Project 4A761102AT23, "Structural Systems"; Scientific Area A2; "Facility Components"; and Work Unit 002, "Characterization of Fracture of Engineering Materials." The OCE technical monitor is I. A. Schwartz.

CERL personnel connected with the investigation were J. Aleszka, Y. G. Kim, J. Scott, E. Cox, A. Kumar, R. Hannan, and R. Quattrone. Dr. G. R. Williamson is Chief of the Engineering and Materials Division.

COL J. E. Hays is Commander and Director of CERL, and Dr. L. R. Shaffer is Technical Director.

Accession For

NTIS GRA&I

DDC TAB

Unannounced

Justification

By

Distribution/

Availability Codes

Avail and/or special

Dist

A

3

CONTENTS

FIGURES

FIGURES (Con't)

6

FIGURES (Con't)

7

FIGURES (Con't)

FIGURES (Con't)

FIGURES (Con't)

11

FIGURES (Con't)

FIGURES (Con't)

13

FIGURES (Con't)

14

FIGURES (Con't)

15

FIGURES (Con't)

FIGURES (Con't)

FIGURES (Con't)

18

FIGURES (Con't)

FIGURES (Con't)

FIGURES (Con't)

22

TABLES

FRACTURE CHARACTERISTICS OF
STRUCTURAL STEELS: REFERENCE MANUAL

1 INTRODUCTION

Objective

The objective of this study is to use scanning electron microscopy
(SEM) to establish and characterize the nature of fractures in steels
and steel weldments. This characterization is to be accomplished by
laboratory simulation of those types of fracture modes and material em-
brittlements most commonly encountered in in-service failures.

Approach

The fracture characteristics of steels were analyzed. The steels
investigated were ASTM A-36, ASTM A-514, AX-110 weld, HY-130, ASTM
A-588, ASTM A-242, AISI 416, 17-4 PH, ASTM A-516, and ASTM A-607. The
materials were fractured under tensile, fatigue, and impact loading con-
ditions. The effects of hydrogen embrittlement on the steels' behavior
when fractured under tensile and fatigue conditions were investigated.
Four examples of in-service failures in which SEM provided valuable in-
formation are presented in the Appendix.

Use of Report

The fracture surface characteristics of the failed components shown
can be compared with the standard scanning electron micrographs of the
specific steel shown in Chapter 4 under tensile, fatigue, impact, and
embrittlement conditions (see Table 5 for index). The characteristic
features on the fracture surface can be identified and the mode of fail-
ure can be determined. This knowledge of the mode of failure can enable
proper material selection to avoid failures.

Background

Fracture surface features can be divided into two categories ac-
cording to the mode of fracture: transgranular (through the grains and
across grain boundaries) or intergranular (around the grain boundaries).
Transgranular fractures can occur by void coalescence, rupture, cleav-
age, or fatigue. Intergranular fractures occur by grain boundary sepa-
ration either with or without microvoid coalescence.

Many common structural metals fracture in a ductile mode under monotonic load by microvoid coalescence. Microvoids are small, discontinuous voids which nucleate at grain boundaries, second-phase particles, or other sites where strain discontinuities exist. As the applied load increases, the microvoids grow, coalesce, and eventually form a continous fracture surface which exhibits numerous cup-like depressions called "dimples"; this is referred to as "dimpled rupture," and is generally associated with ductile failure.

The shape of these dimples is strongly influenced by the orientation of the major stress axis in the individual grains and subgrains to the rolling direction of the material. Equiaxed dimples result under local conditions of uniaxial tensile stress, while elongated dimples result from failure caused by shear stress. Dimple size depends on the number of fracture nucleation sites, grain size, microstructure, and the relative ductility of the metal.

In polycrystalline body-centered cubic (bcc) metals, macroscopic cleavage fracture propagates through grains, changing directions as it crosses subgrain boundaries or passes from one grain to another. Cleavage fractures, which are usually associated with brittle failure, occur along a well-defined crystallographic plane within a grain; in ferritic steels which have a bcc crystal structure, this plane has the (100) type orientation. The change in orientation between grains and the imperfections within grains usually produce easily distinguished markings on the fracture surface. A cleavage fracture propagating across grains forms arrays of cleavage steps or "river patterns." These river patterns are rootlike networks of cleavage facets propagating on different levels.[1] The effect of variables on dimple size is discussed in "Fractography and Atlas of Fractographs," p 66 (see Footnote 1). For example, an increase in fracture nucleation sites (inclusions) will decrease the dimple size. A fine grain size will yield smaller dimple size. In face-centered cubic metals such as aluminum, separation along well-defined planes has only been observed under certain conditions.[2]

Fatigue fracture results from continuous microscopic progression of a crack caused by the application of a cyclic load. The mechanism of fatigue crack initiation is believed to involve slip plain fracture caused by repetitive reversing of the operative slip systems on the surface of the metal.[3] Crack growth caused by repetitive loading sometimes results in a fracture surface which exhibits closely spaced fatigue

---

[1] "Fractography and Atlas of Fractographs," ASM Metals Handbook, Vol 9, 8th ed. (American Society for Metals [ASM], 1974).

[2] "Fractography and Atlas of Fractographs," p 65.

[3] P. J. E. Forsyth, "Fatigue Damage and Crack Growth in Aluminum Alloys," ACTA Metallurgica, Vol 2 (1963), p 703; and C. Laird and G. C. Smith, "Crack Propagation in High Stress Fatigue," Philosophical Magazine, Vol 2 (1962), p 847.

striations or parallel markings. Each fatigue striation represents the
advance of a crack front during one loading cycle. The striations may
be absent or may differ in appearance, depending on such variables as
type of material, level and frequency of applied stress, and environ-
ment. The effect of these variables on striation spacing is discussed
in "Fractography and Atlas of Fractographs," p 118 (see Footnote 1).
The crack growth rate can be estimated by striation spacing. The stria-
tion spacing increases with the level of the applied stress. Corrosive
environments give rise to increased striation spacing. Higher frequency
leads to closer striations.

Hydrogen Embrittlement of Steel

Hydrogen embrittlement has received considerable attention,[4] since
hydrogen is easily introduced into metals by melting, casting, welding,
corrosion, and electroplating. However, most investigations of hydrogen
embrittlement have been performed under sustained-load or slow strain
rate tensile test conditions. Some research[5] has been published on the
fatigue properties of hydrogen-embrittled steels.

The degree of embrittlement generally increases with increasing hy-
drogen content and has the greatest effect on the high tensile-strength
iron-base alloys.

Hydrogen embrittlement produces a sharp loss in ductility; this
loss is most severe at room temperature and slow strain rates. The fa-
tigue lives of steels subjected to electrolytic hydrogen-charging[6] or a
high-pressure hydrogen atmosphere[7] have shown significant reductions.

---

[4] P. Cotterill, "The Hydrogen Embrittlement of Metals," Progressive Ma-
terials Science, Vol 9, No. 4 (1961); A. S. Tetelman and A. J.
McEvily, Jr., Fracture of Structural Materials (John Wiley, 1967); I.
M. Bernstein, "The Role of Hydrogen in the Embrittlement of Iron and
Steel," Materials Science and Engineering, Vol 6, No. 1 (1970), pp 1-
19; W. Beck, E. J. Jankowski, and P. Fisher, Hydrogen Stress Cracking
of High Strength Steels, NADC-MA-7140 (Naval Air Development Center,
1971); and Hydrogen Embrittlement Testing, ASTM STP543 (American Soci-
ety for Testing and Materials [ASTM], 1974).

[5] Y. G. Kim and J. Aleszka, Fatigue Failure of Hydrogen-Embrittled High-
Strength Steels, Technical Report M-143/ADA013380 (Construction
Engineering Research Laboratory [CERL], July 1975).

[6] G. Schwen, G. Sachs, and K. Tonk, ASTM Proceedings, Vol 57 (1957), pp
682-697; W. Beck, Electrochemical Technology, Vol 2 (1964), pp 74-78;
and J. D. Harrison and G. C. Smith, British Welding Journal, Vol 14
(1967), pp 493-502.

[7] W. A. Spitizig, P. M. Talda, and R. P. Wei, "Fatigue-Crack Propagation
and Fractographic Analysis of 18 Ni (250) Maraging Steel Tested in
Argon and Hydrogen Environments," Engineering Fracture Mechanics, Vol
1 (1968), pp 155-165.

The mode of failure of a hydrogen-embrittled sample depends on such variables as type of material, method of loading, and environment; martensitic steels are most susceptible.[8]

Many theories concerning the mechanism of hydrogen embrittlement have been proposed.[9] One hydrogen-embrittlement theory proposed by Zaffe was based on atomic hydrogen diffusing through the metal lattice, precipitating in internal voids as molecular hydrogen, and creating high pressures. It is assumed that high pressures in the voids, combined with externally applied stress, fracture the metal. Another theory suggested by Petch[10] is that absorption of hydrogen on the surfaces of microcracks or voids reduces the surface free energy, resulting in a decrease in the energy needed for crack propagation. A third theory proposed by Troiano[11] suggested that the critical factor is the segregation of hydrogen which, under an applied stress, diffuses to regions of triaxial stress near pre-existing voids in the steel. Thus, only hydrogen in the stressed region of the lattice or at a crack tip is responsible for hydrogen embrittlement.

Temper Embrittlement

One problem associated with heat-treating certain steels is temper embrittlement which occurs when certain commercial-purity steels are heated in or slowly cooled through the temperature range of 550°C to 350°C.[12] If the steel is subsequently reheated above 600°C for a short time and quenched to room temperature, the embrittlement disappears.

Temper embrittlement is manifested by a loss in corrosion resistance and a large, upward shift in the brittle to ductile transition temperature.[13] This reduction in toughness seriously limits the use of

[8] A. S. Tetelman and A. J. McEvily, Jr., Fracture of Structural Materials (John Wiley, 1967).

[9] C. A. Zaffee, Journal of Iron and Steel Institute, Vol 154, No. 123 (1946).

[10] N. J. Petch, "The Ductile Fracture of Polycrystalline-Iron," Philosophical Magazine, Vol 1 (1956), pp 186-191.

[11] A. Troiano, "The Role of Hydrogen and Other Interstitials in the Mechanical Behavior of Metals," Transactions of the American Society for Metals, Vol 52 (ASM, 1960), p 52.

[12] J. R. Low, Jr., Fracture of Engineering Materials (ASM, 1964), p 127; and C. J. McMahon, Jr., Temper Embrittlement in Steel, ASTM STP407 (ASTM, 1968), p 127.

[13] "Heat Treating, Cleaning, and Finishing," ASM Metals Handbook, Vol 2, 8th Edition (1964), p 245; and R. T. Ault, R. B. Holtmann, and J. R. Meyers, Heat Treatment of a Martensitic Stainless Steel for Optimum Combination of Strength, Toughness, and Stress Corrosion Resistance, Technical Report AFML-TK-68-7 (Air Force Materials Laboratory, April 1968).

alloy steels in heavy sections such as pressure vessels and steam turbine rotors, since in the heat treatment of heavy sections it is difficult to slowly cool the inner portions through the 350 to 500°C range.

It is generally believed that the equilibrium segregation of various impurities to prior austenite grain boundaries is the fundamental mechanism of temper embrittlement. Low and his associates[14] demonstrated the influence of specific impurities such as antimony, tin, phosphorus, and arsenic, and alloying elements such as nickel and chromium in promoting embrittlement. Marcus and Palmberg[15] found that when fracture occurs along prior austenite grain boundaries in low-alloy steels, significant amounts of antimony, tin, and phosphorus (100 to 500 times the bulk concentration) are present on the grain boundaries. The presence of both nickel and chromium leads to more segregation of antimony, tin, or phosphorus to the grain boundaries than when either is present alone.

Recent experiments by Ohtani[16] suggest that a central feature of temper embrittlement is the redistribution of solute during carbide precipitation. The study showed that eliminating carbide precipitation in antimony- and phosphorus-doped alloys eliminated the remaining embrittlement resulting from equilibrium segregation. Ohtani concludes that embrittlement is caused by the presence of impurities ahead of a growing carbide.

Regardless of how impurities reach the grain boundaries, it is generally accepted that they lower the maximum cohesive force along the prior austenite grain boundaries. Consequently, cracks can easily propagate along this path.

Welding of Steel

Welding is an important method of joining single members into complex structural systems required to function under diverse loading conditions in construction engineering. Arc welding has been widely used to join various constructional alloy steels. In the arc welding process, the arc supplies the heat needed to melt the filler and base metal surfaces being joined. Even when the proper electrodes, heat input, and

---

[14] J. R. Low, Jr., D. F. Stein, A. M. Turkalo, and R. P. Lafarci, Transactions of AIME, MT6TB, Vol 242 (1968), pp 14-24.

[15] H. L. Marcus, Jr. and P. W. Palmberg, "Effect of Solute Elements on Temper Embrittlement of Low Alloy Steels," Temper Embrittlement of Steels, ASTM STP499 (ASTM, 1971), pp 90-103.

[16] H. Ohtani, H. C. Feng, and C. J. McMahon, Jr., "New Information on the Mechanism of Temper Embrittlement of Alloy Steels," Metallurgical Transactions, Vol 5 (1974), pp 516-518.

weld techniques are used,[17] weld deposits are rarely free of discontinuities; many types of defects may occur, including porosity, lack of fusion (LOF), lack of penetration (LOP), cracks, undercuts, inclusions, and burn-through. The effects of these defects on the mechanical properties of the joint differ and depend on such factors as size, shape, orientation, distribution, and service environment, all of which play important roles in determining the performance of a weldment.

Porosity, one of the most frequent weld defects, is formed by entrapment of evolved gases in the solidifying metal. Because of their reduced solubility, the gases are driven from solution in the wid metal as the temperature drops. Gas bubbles are formed at the solid-liquid interface and remain there until they are large enough to float through the molten metal and escape to the atmosphere.[18] If the rate of flotation is less than the rate of the solidifying front's advance, the bubbles are trapped, creating porosity.

LOP defects result when the weld and base metals (or the base metal alone if no filler metal is used) do not integrally fuse at the root of the weld. This occurs when the weld metal fails to reach the root of a fillet weld or the root face of a groove weld fails to reach fusion temperature along its entire length.

LOF occurs when adjacent layers of weld metal, or weld metal and base metal, fail to fuse because the temperature of one of the metals does not reach its melting point during a weld pass.

---

[17] A. Phillips, ed., The Welding Handbook, Vol 1 (American Welding Society, 1968).

[18] D. Warren and R. D. Stout, Welding Journal, Vol 3, No. 8, Research Support 381-5 (1952).

2. EXPERIMENTAL PROCEDURES

Materials

The steels investigated in this study were ASTM A-36, ASTM A-514, HY 130, AX-110 weld deposit, ASTM A-588, ASTM A-242, ASTM A-516, ASTM A-607, AISI 416, and 17-4PH. The chemical composition of these steels is shown in Table 1.

Type A-36 is the most common grade of structural steel used in bridges and buildings and for other general structural purposes. Its microstructure consists of regions of ferrite and pearlite. Type A-514 Grade F structural steel is a high-strength, low-alloy, quenched and tempered steel used in such applications as welded bridges, buildings, and pressure vessels.

HY-130 is also a low-carbon, quenched, and tempered alloy steel with a high yield strength. This steel has high toughness and adequate hardenability even for thick plate applications. The ASTM A-514 and HY-130 have tempered martensitic microstructures.

The ASTM types A-588 and A-242 are high-strength, low-alloy structural steels generally used where weight savings or added corrosion resistance are important. Their microstructures consist of regions of ferrite and pearlite. ASTM type A-516 is a carbon steel intended primarily for use in welded pressure vessels where improved notch toughness is important. Its microstructure consists of fine-grained ferrite. Type A-607 is a high-strength, low-alloy columbium and/or vanadium steel intended for use in structures where strength and savings in weight are important. Its as-received microstructure is fine-grained ferritic. Type 416 is designed for use in free-machining stainless and heat-resisting steel wire and bars where optimum machinability, general corrosion resistance, and high temperature service are required. The microstructure is martensitic.

Type 17-4PH is used for hot-rolled and cold-finished age-hardening stainless and heat-resisting steel bars and shapes where corrosion resistance and high strength at room and elevated temperatures are required. It is precipitation-hardenable and has a martensitic microstructure.

The gas-metal arc (GMA) welding process was used to prepare the ASTM A-514 steel weldments. The weld passes were deposited in either a 60-degree double-V groove or a single-V groove. Table 2 gives the welding parameters.

31

Table 1

Chemical Composition of Steels and Weld Metal

Steel Compositions %	ASTM A-36	ASTM A-514 Grade F	AX110 Weld Deposit	HY130**
C	0.26 max	0.10-0.20	0.085 max	0.12 max
Mn	0.85-1.35*	0.60-1.00	1.43 max	0.60-0.90
P	0.04 max	0.035 max	0.011 max	0.010 max
S	0.05 max	0.04 max	0.010 max	0.015 max
Si	0.15-0.030*	0.15-0.35	0.42 max	0.20-0.35
Cu	0.20	0.15-0.50	–	–
Ni	–	0.70-1.00	2.29 max	4.75-5.25
Ti	–	–	0.009 max	–
Cr	–	0.40-0.65	0.16 max	0.40-0.70
Mo	–	0.40-0.60	0.52 max	0.30-0.65
V	–	0.03-0.08	0.0094 max	0.05-0.10
B	–	0.002-0.006	–	–
Al	–	–	0.005 max	–

*For shapes over 426 lb/ft (633.96 kg/m).
**Data provided by U.S. Steel.

Element	ASTM A-588,%	ASTM A-242,%	AISI 416,%	17-4PH,%	ASTM A-516 grade 70,%	ASTM A-607 grade 65,%
C	0.10-0.19	0.15 max.	0.15 min.	0.07	0.28 (maxa)	0.30 (max)
Mn	0.90-1.25	1.00 max.	1.25	1.0	0.80-1.25	1.55 (max)
P	0.04 max.	0.15 max.	0.06	0.04	0.035 (max)	0.05 (max)
S	0.05 max.	0.05 max.	0.15 min.	0.03	0.04 (max)	0.06 (max)
Si	0.15-0.30	---	1.0	1.0	0.13-0.33	–
Cr	0.40-0.65	---	12-14	15.5-17.5	–	0.004 (min)
Cu	0.25-0.40	0.20 Min.	---	3.0-5.0	–	0.015 (max)
Mo	---	---	0.60 (Opt.)	---	–	–
Ni	---	---	---	3.0-5.0	–	–
Cb+Ta	---	---	---	0.15-0.45		
V	0.02-0.10	---	---	---		

Table 2

Welding Parameters

Voltage	Amperage	Travel Speed (in./min)	Preheat & Interpass Temp
220V	350 amp	12 (30.48 cm/min)	93°C

Shielding Gas	Heat Input (kJ/in.)	No. of Weld Passes
62% Oxygen-Argon	60-65	4

Normal welding procedures were intentionally disturbed to obtain the desired weld discontinuities. Clustered porosity was produced by shutting off the shielding gas, thereby contaminating the molten weld metal in the root of the joint with oxygen. Isolated porosity was introduced by shutting off the oxygen in the shielding gas, thus decreasing arc stability.

Lack of penetration defect (LOP) was created in a double-V groove plate by butting the lands tightly together to prevent complete penetration of the weld metal. Using a single pass on each side resulted in excessive distortions; to correct this, the specimens were welded using two alternate passes on each side. The LOP was a planar, centrally located defect extending the full length of the weld.

Lack of fusion defects (LOF) were produced by lowering the heat input 90 percent on the first pass.

Each weldment was radiographed to verify the existence of the desired defects.

Specimen Fabrication and Testing

Figures 1 and 2 show the specimen geometries for the tensile, impact, and fatigue tests. The tensile and fatigue plate specimens were machined with their longitudinal axes parallel to the rolling direction, while the longitudinal axes of the impact specimens were perpendicular to the rolling direction. The weldment specimens were machined with their longitudinal axes perpendicular to the weld axis.

The mechanical tensile tests were conducted at 23°C at a constant strain rate of 0.001 in./in./min (0.001 cm/cm/min). The mechanical properties are shown in Table 3. To determine the effect of temperature
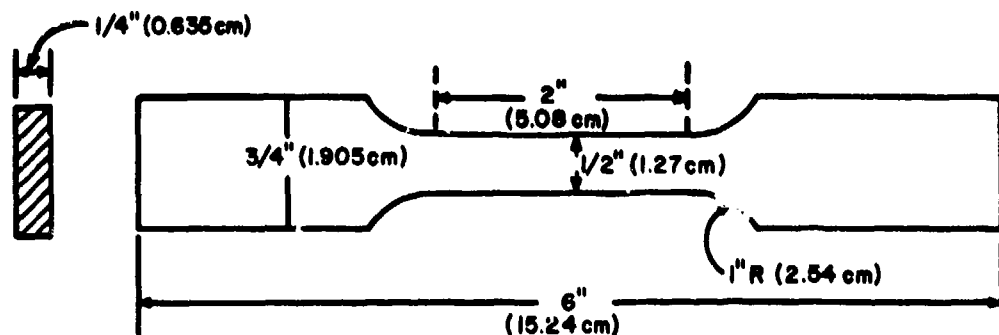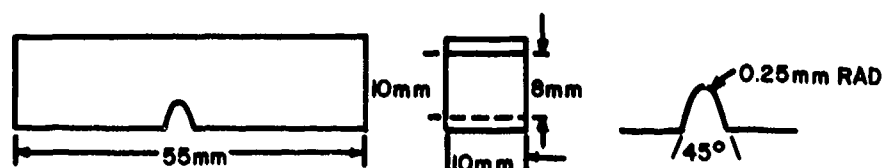
33
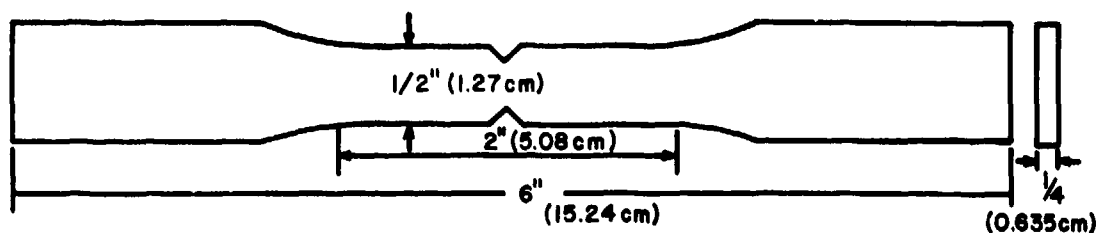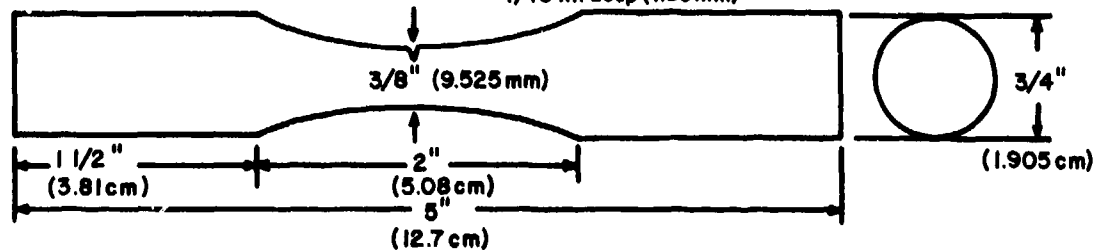
Figure 1.   Specimen geometry for tensile, Charpy, and fatigue
            tests of A-36, A-514 and HY-130 steels. (The term
            longitudinal [with grain] is used to mean parallel
            to rolling direction.)

34
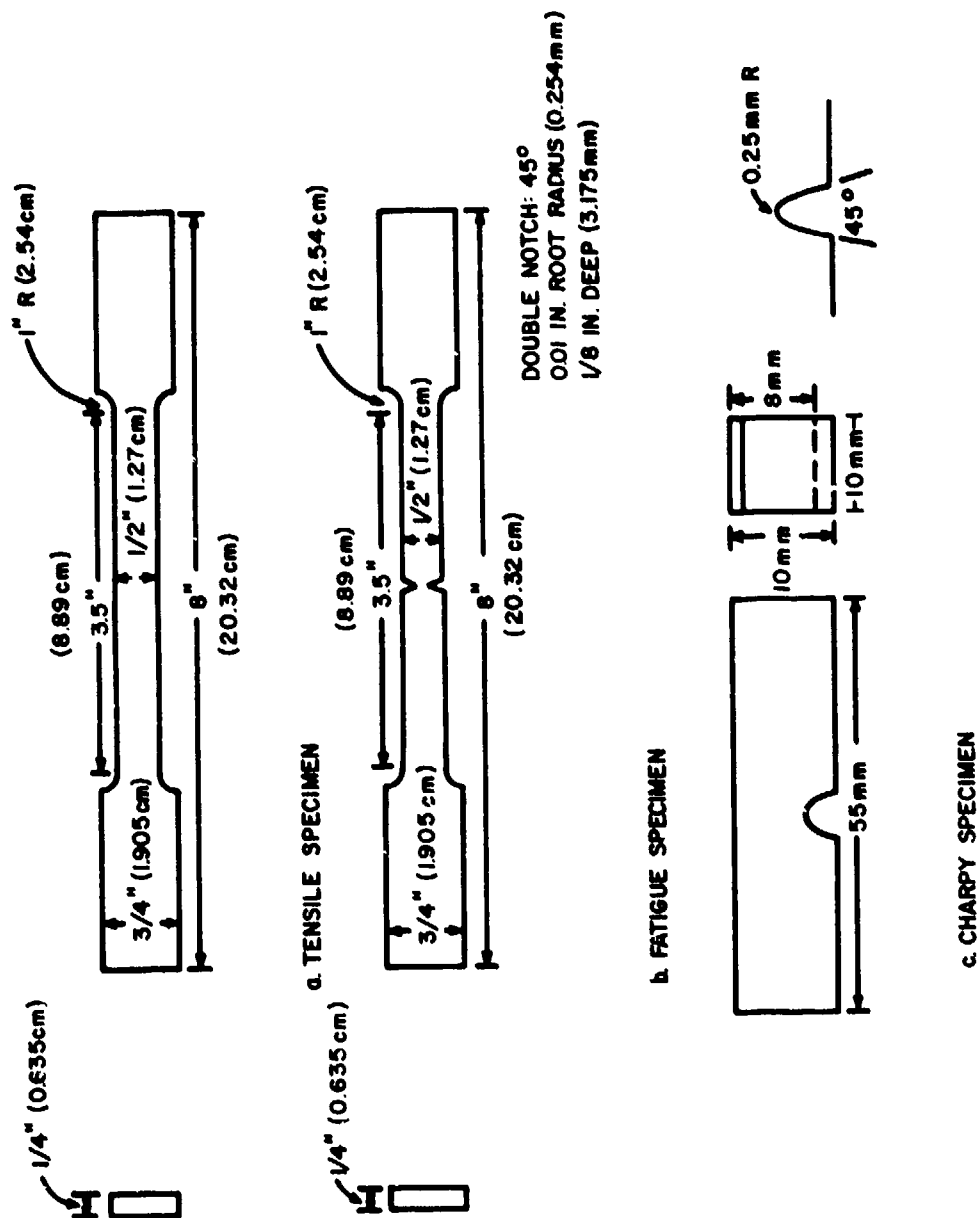
Figure 2. Specimen geometry for tensile, fatigue, and Charpy impact tests of A-588, A-242, AISI 416, 17-4PH, A-516, and A-607 steels.

35

Table 3

Mechanical Properties of Steels and Weld Metal

Steel	Yield Strength ksi (MPa) (0.2% offset)	Tensile Strength ksi (MPa)
A-36	32-36 min (225-253)	58-80 (408-562)
A-514	100 min (703)	115-135 (808-949)
AX-110 weld deposit	100 min (703)	115-135 (808-949)
HY-130	130 min (913)	150-180 (1054-1266)

Steel	Yield Strength, ksi (MPa)	Tensile Strength ksi (MPa)
A-588, as rolled	58.4 (403.0)	90.0 (621.0)
A-588, hydrogen-embrittled	59.2 (408.5)	88.8 (612.7)
A-588, reheat-treated	57.6 (397.4)	83.2 (574.1)
A-242, as-rolled, longitudinal	48.0 (331.2)	76.0 (524.4)
A-242, as-rolled, transverse	48.0 (331.2)	75.2 (518.9)
A-242, hydrogen-embrittled, longitudinal	49.6 (342.2)	76.0 (524.4)
A-242, hydrogen-embrittled, transverse	47.2 (325.7)	72.8 (502.3)
A-242, reheat-treated, longitudinal	48.8 (336.7)	73.6 (507.8)
A-242, reheat-treated, transverse	42.4 (292.6)	68.0 (469.2)
A-516	77.0 (531.3)	40.8 (281.5)
A-516, hydrogen-embrittled	78.0 (538.2)	42.0 (289.8)
A-607	89.0 (614.1)	81.2 (560.3)
A-607, hydrogen-embrittled	85.6 (590.6)	71.2 (491.3)
416, quenched	168.0 (1159.2)	212.0 (146?.8)
416, tempered at 593°C	92.0 (634.8)	110.4 (761.8)
416, tempered at 316°C	147.0 (1915.7)	193.6 (1335.8)
416, tempered at 954°C	120.0 (828.0)	192.8 (1339.3)
416, tempered at 483°C	144.0 (993.6)	186.4 (1286.2)
416, hydrogen-embrittled	134.4 (927.4)	214.0 (1479.4)
17-4PH, solution heat-treated	97.6 (673.5)	152.0 (1048.8)
17-4PH, hydrogen-embrittled	104.0 (717.6)	152.8 (1054.3)
17-4PH, aged at 482°C	150.4 (1037.8)	164.8 (1137.1)
17-4PH, aged at 538°C	153.6 (1059.8)	164.0 (1131.6)
17-4PH, aged at 454°C	156.0 (1076.4)	184.8 (1275.1)

on the fracture mode of the Charpy specimens, tests were conducted at a wide range of temperatures (Table 4) using a temperature control bath. The fatigue tests were conducted at 10 cycles/sec in a tension-tension sinusoidal mode at room temperature, using a 50-kip MTS unit. All fatigue and tensile tests of the defective weldments were conducted perpendicular to the weld axis.

Table 4

Temperatures and Environments of Charpy Tests

Temp ^{o}C	Environment
-196	Liquid Nitrogen
-83	Dry Ice/Ethyl Alcohol
-18	Ice/Salt Water
23	Ambient

Hydrogen Embrittlement

To induce hydrogen embrittlement, the machine samples were cathodically charged in a solution of 10 weight percent (wt%) H_2SO_4 and 0.3 wt% As_2C_3. The As_2O_3 was used to promote penetration of hydrogen during cathodic polarization. The cathodic charging was conducted at a current density of 6 mA/sq in. (.93 mA/cm^2) for 12 hours prior to testing.

Temper Embrittlement

ASTM A-514 specimens were temper-embrittled using the following step-cooling procedure:[19]

1. Temper 1 hour at 593°C.
2. Furnace-cool to 528°C and temper for 15 hours.
3. Furnace-cool to 524°C and temper for 24 hours.
4. Furnace-cool to 496° and temper for 48 hours.
5. Furnace-cool to 468°C and temper for 72 hours.
6. Furnace-cool to 315°C.
7. Air-cool to room temperature.

---

[19] A. Joshi and D. F. Stein, "Temper Embrittlement of Alloy Steels," ASTM STP499 (ASTM, 1972) pp 59-89.

The ASTM A-36 and HY-130 specimens were temper-embrittled using the following procedure:[20]

1. Temper 1 hour at 593°C.
2. Furnace-cool to 515°C and temper for 16 hours.
3. Furnace-cool to 502°C and temper for 24 hours.
4. Furnace-cool to 468°C and temper for 96 hours.
5. Furnace-cool to 452° and temper for 144 hours.
6. Furnace-cool to 441°C and temper for 168 hours.
7. Furnace-cool to 344°C.
8. Air-cool to room temperature.

Since A-588 and A-242 are normally used in the hot-rolled condition, temper embrittlement is not a serious problem. However, several specimens were slowly cooled from the austenitizing range in an attempt to embrittle them. No temper embrittlement was found.

The 416 stainless steel specimens were placed in a preheated 538°C furnace, heated to 954°C, held for 30 minutes, then oil-quenched. This is a solution heat treatment during which all precipitating elements are taken into solid solution. Four groups of specimens were then tempered according to the following schedules.

1. Place in preheated 593°C furnace, temper for 1 hour, oil quench.

2. Place in preheated 316°C furnace, temper for 1 hour, oil quench.

3. Place in preheated 954°C furnace, temper for 1 hour, slow cool.

4. Place in preheated 483°C furnace, temper for 1 hour, slow cool.

Schedules 1 and 2 are normal tempering conditions; schedules 3 and 4 simulate possible embrittling conditions.

The 17-4PH specimens were solution heat-treated by a 538°C preheat followed by being heated to 1038°C, held for 30 minutes, then oil-quenched. Three groups of specimens were age-hardened using the following heat treatments:

---

[20] J. Aleszka and Y. Kim, Fracture Characteristics of Structural Steels and Weldments, Technical Report M-170/ADA019930 (CERL, November 1975).

38

1. Place in 482°C preheated furnace for 1 hour, air cool.

2. Place in 538°C preheated furnace for 1 hour, slow cool.

3. Place in 454°C preheated furnace for 1 hour, slow cool.

Schedule 1 is a normal age hardening treatment; schedules 2 and 3 are embrittling treatments.

3 MECHANICAL TEST RESULTS

ASTM A-36

1. A-36 steel was found to be susceptible to hydrogen embrittlement, which caused reduction in fatigue life. The effect of hydrogen embrittlement on the tensile strength of ferritic steels is minimal. Tensile failure in the hydrogen-embrittled specimens occurred mainly by dimple rupture and microvoid coalescence, resulting in the formation of elongated or equiaxed dimples. The fracture surface of the hydrogen-embrittled specimen also contained regions of quasi-cleavage.

2. The effect of testing temperature on the Charpy specimens of A-36 steel was seen in a change from cleavage failure at low temperatures to dimple rupture at room temperature.

3. A-36 steel was found not to be susceptible to temper embrittlement.

ASTM A-514 and Weld Metal

1. The fracture surfaces of the as-received and temper-embrittled ASTM A-514 and weld metal (plate and weld) tensile samples were identical. Failure in each case occurred by dimple rupture and void coalescence; therefore, the fracture appearance of tensile specimens is not a dependable method for determining temper embrittlement.

2. The effect of hydrogen embrittlement was quite severe in quenched and tempered ASTM A-514 martensitic steel tested in fatigue. A significant reduction in fatigue life was observed, and the fatigue regions were found to contain a dispersion of craters. Again, the effect of hydrogen embrittlement on the tensile strength was minimal. In the hydrogen-embrittled weld samples, small fisheyes which were believed to result from pockets of entrapped hydrogen were evident in fatigue specimens.

3. Subsurface crack nucleation in ASTM A-514 steel appears to occur in regions where a critical combination of triaxial stress and hydrogen concentration exists. Transverse cracks, which propagate on a plane perpendicular to the major stress axis, intersect longitudinal cracks formed at matrix-stringer interfaces. Subsequent cycling produces the craters on the fracture surface.

4. Nucleation and propagation of subsurface fatigue cracks in the hydrogen-embrittled samples of ASTM A-514 appear responsible for the severe reduction in fatigue life.

5. When fractured in fatigue, the temper-embrittled plate and, to a lesser extent, ASTM A-514 weld were susceptible to lamellar tearing.

6. Fractures of defective welds of ASTM A-514 originated at the internal defect. However, when these specimens were hydrogen-embrittled prior to fatigue testing, failure also originated at an outside free surface.

HY-130

1. The effect of hydrogen embrittlement was quite severe in HY-130 tested in fatigue. A significant reduction in fatigue life was observed. In fatigue samples, small fisheyes which were believed to result from pockets of entrapped hydrogen were evident.

2. HY-130 exhibited a markedly increased susceptibility to lamellar tearing when temper-embrittled and tested in tension and fatigue.

ASTM A-588 and A-242

1. ASTM A-588 was found to be susceptible to hydrogen-embrittlement. Cleavage fracture in the tensile and intergranular fracture in the fatigue specimen indicate a loss in material ductility as a result of the hydrogen-charging procedure.

2. ASTM A-242 was found to be unsusceptible to hydrogen embrittlement in this study. Since the as-received A-242 material was in an abnormally low toughness condition, however, the effect of hydrogen charging on the material would be masked by this condition. A high-strength, low-alloy structural steel such as A-242 in a quenched and tempered condition would ordinarily be susceptible to hydrogen embrittlement, as the similar A-588 steel was shown to be.

3. The orientation of the specimens with respect to the rolling direction was shown to slightly affect the tensile strength of A-242 steel. The fracture surfaces of transverse specimens contained elongated inclusions, but no change in fracture mechanism from that of the longitudinal specimens was observed.

41

ASTM A-516

1. The presence of fatigue striae on the ASTM A-516 steel hydrogen-embrittled fatigue specimen that were not noted on the embrittled fatigue specimen indicated that hydrogen embrittlement has some effect on the microstructure of the ASTM A-516 steel. The effect is assumed to be small, however, since the mechanical strength of the steel was not significantly altered.

2. The ASTM A-516 Charpy specimens were extremely tough in the orientation in which they were machined due to the presence of elongated inclusions perpendicular to the crack plane created by rolling.

ASTM A-607

1. The ASTM A-607 hydrogen-embrittled fatigue specimen showed more areas of fatigue striae than the unembrittled specimen, again indicating the effect of hydrogen embrittlement on the microstructure of the steel. The data demonstrate that the A-607 steel tested had superior tensile properties to those of the A-516 steel tested.

2. The effect of testing temperature on the ASTM A-607 Charpy specimens was seen in a change from low-energy, brittle fracture (primarily cleavage) at low temperatures to higher energy, ductile fracture (primarily dimple rupture) at elevated temperatures. Data also indicate that A-516 has superior Charpy V-notch properties compared to those of A-607 steel.

AISI 416 and 17-4PH

The stainless steels, AISI 416 and 17-4PH were found to be unsusceptible to the hydrogen-charging procedure performed in this study.

42

4   SCANNING ELECTRON MICROGRAPHS

This chapter reports the results cf SEM observation of ASTM A-36, ASTM A-514, AX-110 weld, HY-130, ASTM A-588, ASTM A-242, ASTM A-516, ASTM A-607, ASI 416, and 17-4PH plate specimens broken in tension, fatigue, and impact modes. The effects of hydrogen and temper embrittlements on the fracture surfaces of these materials are also reported. Table 5 summarizes tests conducted in this study.

The following information is shown for each steel studied: (1) the tensile loading mode, (2) the effects of hydrogen and/or temper embrittlement on the tensile fracture surface, (3) the fatigue fracture surface and the effects of hydrogen and/or temper embrittlement on the fatigue fracture, and (4) the effect of temperature on the impact loading.

The mechanical properties and SEM micrographs are presented for each loading condition. Table 5 shows the general index of SEM fractographs (Figures 3 through 243). In designating the areas scanned on the fracture surface, location "A" was chosen, to correspond to origin of fracture. In certain cases of overload, the origin was not apparent, and area "A" designates the general fracture surface. Typica fatigue areas are designated "B," while "C" designates a change in texture on the fracture surface. "D" designates the fracture surface near the weld defect.

43

Table 5

Summary of Tests Conducted in This Study
(Figure numbers which correspond to the test are shown.)

Material	Tensile			Fatigue			Impact
Material	As Rec.	H$_2$-Embr.	Temper-Embr.	As Rec.	H$_2$-Embr.	Temper-Embr.	23°C to -196°C
ASTM A-36	3 - 5	6 - 8		9 - 13	14 - 16		17 - 26
ASTM A-514	27 - 29	30 - 32	33 - 35	36 - 39	40 - 44	45 - 50	51 - 60
HY-130	61 - 63	64 - 68	69 - 71	72 - 75	77 - 79	80 - 85	86 - 94
ASTM A-514 weld (AX-110)	95 - 96	97 - 100	101 - 102	103 - 105	106 - 107	110 - 113	114 - 122
ASTM 514 weld defects (AX-110)	124 - 130	142 - 143	131 - 141	144 - 148	149 - 155		
ASTM A-588	156 - 157	158 - 159		160 - 162	163 - 165		166 - 170
ASTM A-242	171 - 173	174 - 178		179 - 180	181 - 182		183 - 190
ASTM A-516	191	195		192 - 194	196 - 198		199 - 203
ASTM A-607 Pipe	204 - 205	208		206 - 207	209 - 210		211 - 218
AISI 416	219 - 221			222 - 224			225 - 229
17-4 H	230 - 234	235 - 238		239 - 241			242 - 243

44

ASTM A-36 PLATE

Material: ASTM A-36 Plate

Heat Treatment: As received
Test Direction: Longitudinal parallel to the rolling direction
Mode or Condition of Test: Tensile
Test Temperature: Ambient
Test Environment: Air
Test Results:

Mechanical Properties:

Yield Stress
34,400 psi (237.4 MPa)

Ultimate Fracture Stress
66,600 psi (459.6 MPa)

Fractographic Analysis:

Failure occurred entirely by inclusion generated dimple rupture (Figures 3 through 5). The fracture surface was slanted, being somewhat flat in the central portion of the specimen, and sloping up to a shear lip on an outside edge.
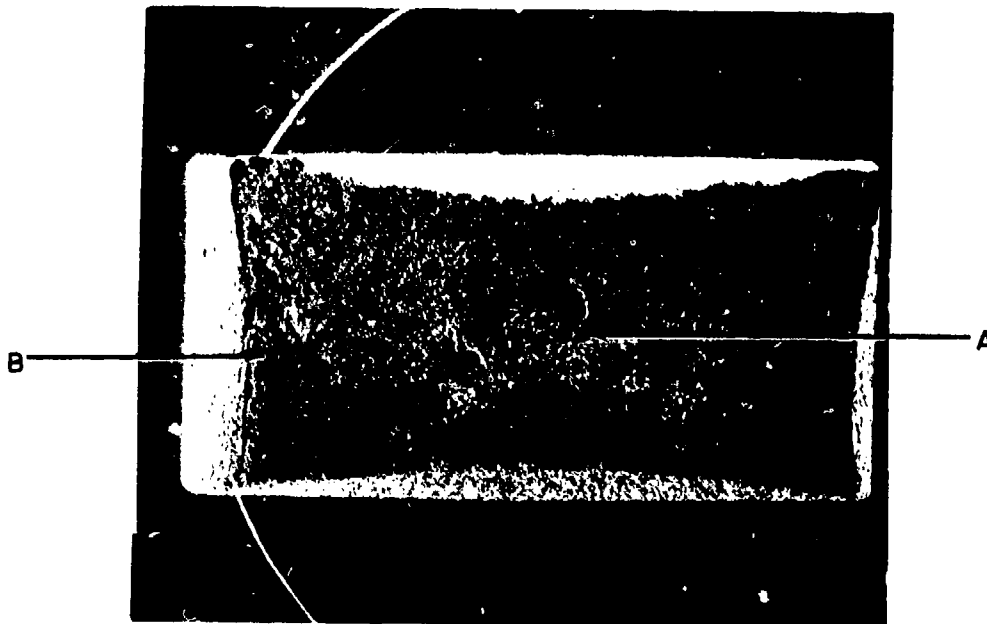
Figure 3. Tensile fracture surface of A-36 steel, 12x.
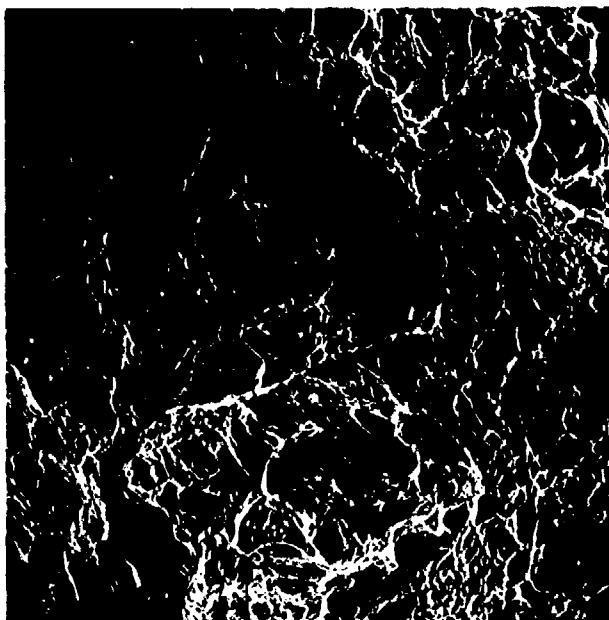
Figure 4.   Dimple rupture in A-36 steel, 1000x.

Figure 5.   Dimple rupture in A-36 steel, 3000x.

Material: ASTM A-36 Plate

Heat Treatment: As Received
Test Direction: Longitudinal (parallel to the rolling direction)
Mode or Condition of Test: Hydrogen-embrittled tensile
Test Temperature: Ambient
Test Environment: Air
Hydrogen Charging Conditions:

Current Density: 6 mA/in.^{2} (0.93 mA/cm^2)

Charge Time: 12 hours

Electrolyte: 0.3 wt% As_2O_3

10.0 wt% H_2SO_4

Test Results:

Mechanical Properties:

Yield Stress
36,000 psi (248.4 MPa)

Ultimate Fracture Stress
68,700 psi (447 MPa)

Fractographic Analysis:

Failure occured by quasi-cleavage and dimple rupture. The wavy
bands are indicative of serpentine glide (Figures 6 through 8). The
fracture surface was rough and jagged. Failure occurred without neck-
ing.

Material: ASTM A-36 Plate

Heat Treatment: As received
Test Direction: Longitudinal (parallel to the rolling direction)
Mode or Condition of Test: Hydrogen-embrittled fatigue
Test Temperature: Ambient
Test Environment: Air
Hydrogen Charging Conditions:

   Current Density: 6 mA/in.^{2} (0.93 mA/cm^2)

   Charge Time: 12 hours

   Electrolyte: 0.3 wt% As_2O_3

              10.0 wt% H_2SO_4

Test Results:

   Mechnical Properties:

          Maximum Stress
          61,000 psi (420.9 MPa)

          Minimum Stress
          5,000 psi (34.5 MPa)

          Test Frequency
          10 cycles/sec.

          Cycles to Failure
                4576

   Fractographic Analysis:

   The fatigue region contained numerous secondary cracks on many dif-
ferent levels. Most of the fatigue striations were found to be parallel
to the machined notch. The central portion of the fracture surface con-
sisted of dimple rupture. The overall appearance was not noticeably
different from the unembrittled condition (Figures 13 through 16). The
fracture surface was fairly flat and contained small shear lips on the
outside edges of the specimen.

Figure 6. Tensile fracture surface of hydrogen-embrittled A-36 steel, 10x.
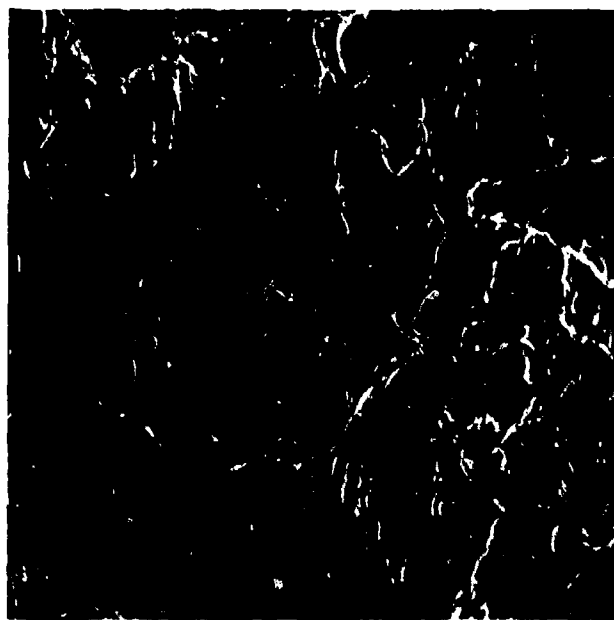
Figure 7. Quasi-cleavage facets in hydrogen-embrittled A-36 steel, 1100x.
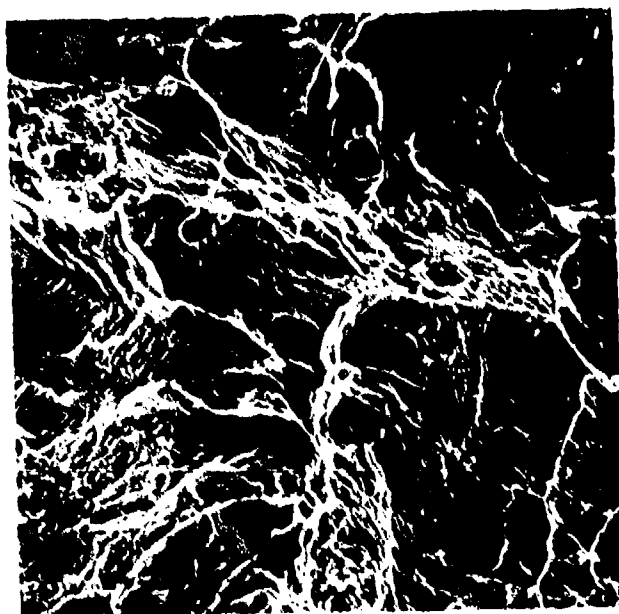
Figure 8. Inclusion-nucleated dimples in hydrogen-embrittled A-36 steel, 2000x.

Material: ASTM A-36 Plate

Heat Treatment: As received
Test Direction: Longitudinal (parallel to the rolling direction)
Mode or Condition of Test: Fatigue
Test Temperature: Ambient
Test Environment: Air
Test Results:

Mechanical Properties:

Maximum Stress
61,000 psi (420.9 MPa)

Minimum Stress
5,000 psi (34.5 MPa)

Test Frequency
10 cycles/sec.

Cycles to Failure
6600

Fractographic Analysis:

The crack front propagated on many different levels within the fatigue zone. The fatigue striations were found to be parallel to the machined notch. The central portion of the fracture surface, where tensile overload occurred, consisted of dimple rupture (Figures 9 through 16). The fracture surface was fairly flat and contained small shear lips on the outside edges of the specimen.
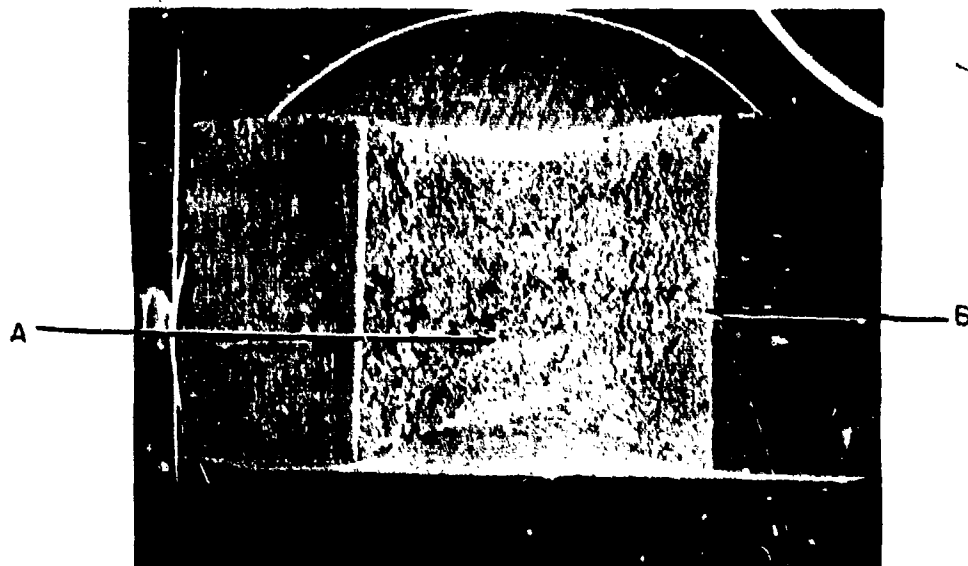
Figure 9.   Fatigue fracture surface of A-36 steel, 8x.
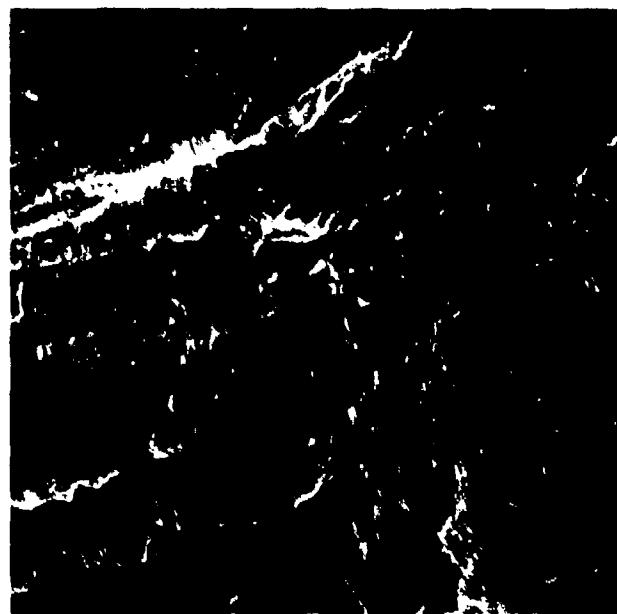
Figure 10. Fatigue striations on surface of A-36 steel, 4000x.

Figure 11.   A stereomicrograph of the fatigue zone in A-36 steel, 500x.
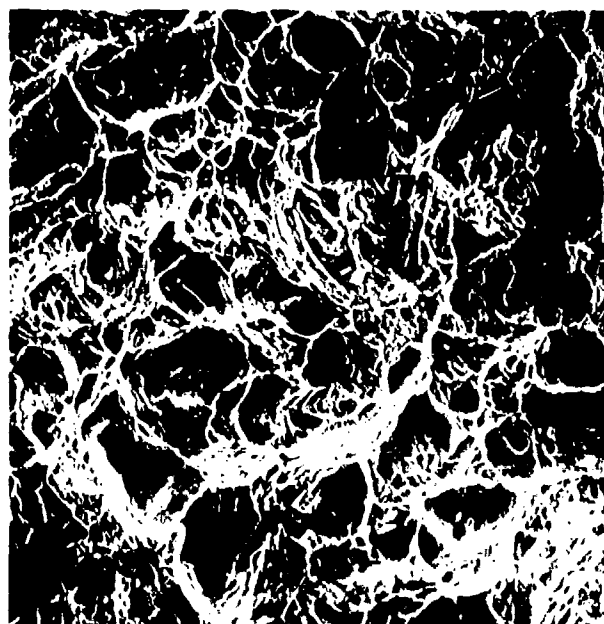
Figure 12.   Tensile overload region in the A-36 fatigue specimen, 700x.

Figure 13. Fracture surface of a hydrogen-embrittled A-36 fatigue specimen, 8x.

Figure 14. Fatigue striations on surface of a hydrogen-embrittled A-36 fatigue specimen, 4250x.

Figure 15. A stereomicrograph of the fatigue zone in hydrogen-embrittled A-36 steel, 500x.
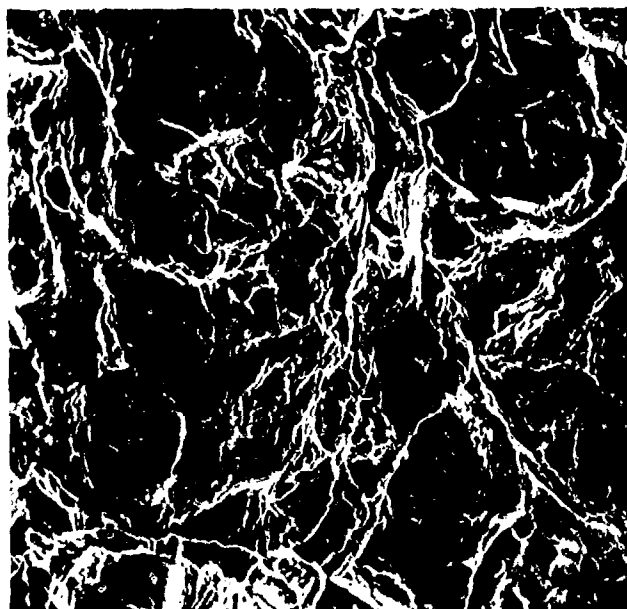
Figure 16. Tensile overload region in the hydrogen-embrittled A-36 fatigue specimen, 700x.

Material: ASTM A-36 Plate

Heat Treatment: As received
Test Direction: Longitudinal (parallel to the rolling direction)
Mode or Condition of Test: Charpy impact
Test Temperature: -196^{0}
Test Environment: Air
Test Results:

Mechanical Properties:

Fracture Energy
13 ft-lb (17.7 joule)

Fractographic Analysis:

Failure occurred entirely by cleavage. The direction of crack propagation within each cleavage facet is shown by river patterns (Figures 17 and 18). The fracture surface was entirely flat and very shiny.
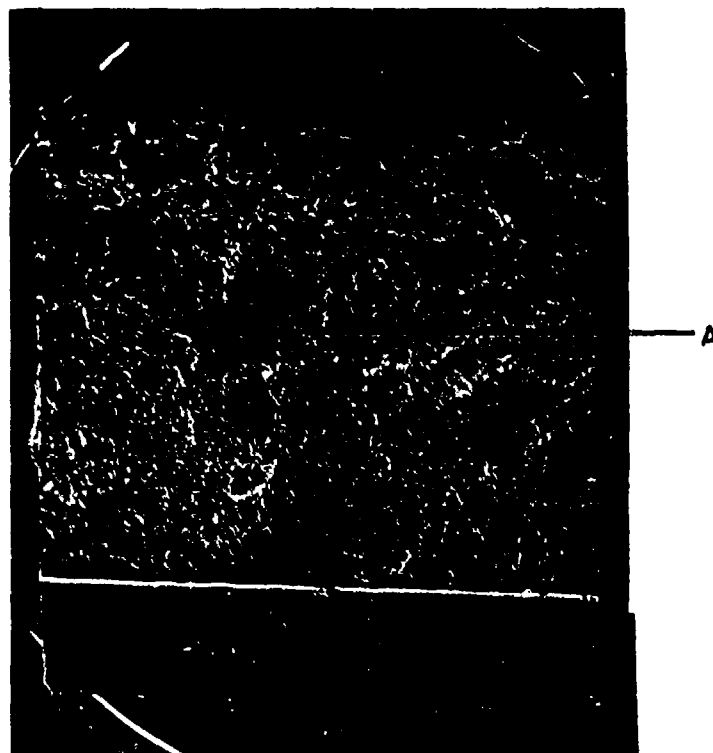
Figure 17.   Fracture surface of an A-36 Charpy specimen tested at -196°C, 7x

Figure 18.   River patterns in cleavage facets, 500x.

59

Material: ASTM A-36 Plate

Heat Treatment: As received
Test Direction: Longitudinal (with grain)
Mode or Condition of Test: Charpy impact
Test Temperature: -83°C
Test Environment: Air
Test Results:

Mechnical Properties:

Fracture Energy
15 ft-lbs (20.4 joule)

Fractographic Analysis:

Failure occurred by a mixed mode of cleavage and microvoid coalescence (Figures 19 and 20). The fracture surface was entirely flat and very shiny.
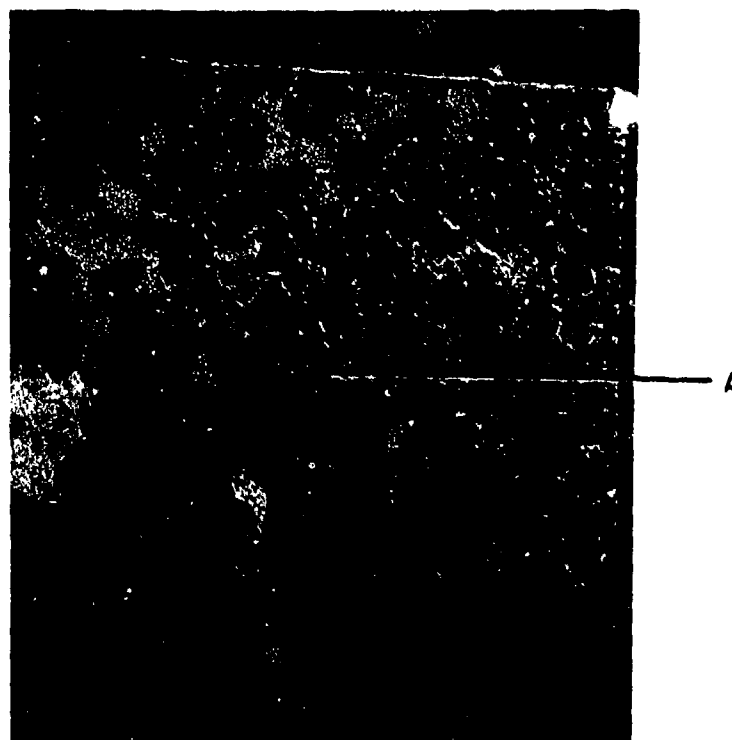
Figure 19. Fracture surface of an A-36 Charpy specimen tested at -83°C, 7x.

Figure 20. Mixed mode failure in an A-36 Charpy specimen tested at -83°C, 100x.

Material: ASTM A-36 Plate

Heat Treatment: As received
Test Direction: Longitudinal (with grain)
Mode or Condition of Test: Charpy impact
Test Temperature: -18°C
Test Environment: Air
Test Results:

Mechanical Properties:

Fracture Energy
26 ft-lb (35.4 joule)

Fractographic Analysis:

Failure occurred by cleavage in the center of the specimen and dimple rupture in the outside edges (Figures 21 through 23). The fracture surface was flat and shiny in the central portion of the specimen, but was rough and fibrous along the outside edges. The sides of the specimen exhibited a small shear lip.
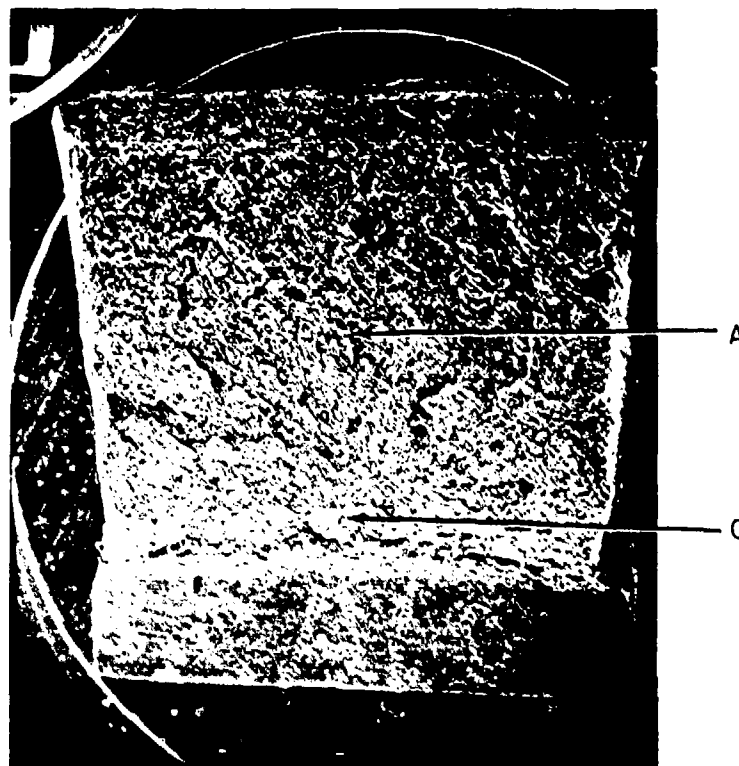
Figure 21. Fracture surface of an A-36 Charpy specimen tested at -18°C, 7x.

Figure 22.   Dimple rupture in notch region of an A-36 Charpy
specimen tested at -18°C, 100x.

Figure 23.   Mixed mode failure in central region of an A-36
Charpy specimen tested at -18°C, 100x.

Material: ASTM A-36 Plate

Heat Treatment: As received
Test Direction: Longitudinal (with grain)
Mode or Condition of Test: Charpy impact
Test Temperature: Ambient
Test Environment: Air
Test Results:

Mechanical Properties:

$$\frac{\text{Fracture Energy}}{55 \text{ ft-lb } (74.8 \text{ joule})}$$

Fractographic Analysis

Failure in the central portion of the specimen occurred by cleavage and microvoid coalescence. Near the outside of the specimen the failure mode was entirely one of dimple rupture (Figures 24 through 26). The center of the specimen was flat and shiny, while the outside edges were rough and woody. A considerable amount of plastic deformation and tearing was evident in the specimen, with large shear lips being present on the outside edges.
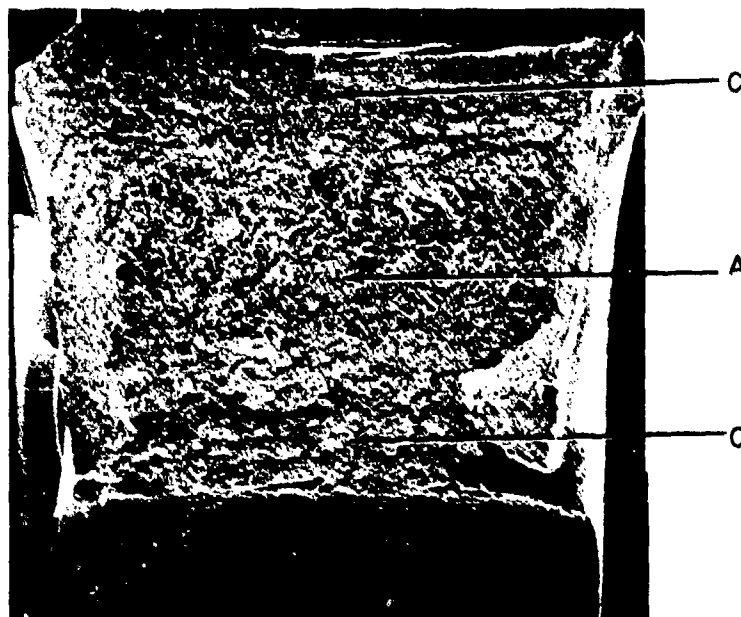
Figure 24. Fracture surface of an A-36 Charpy specimen tested at room temperature, 7x.

64
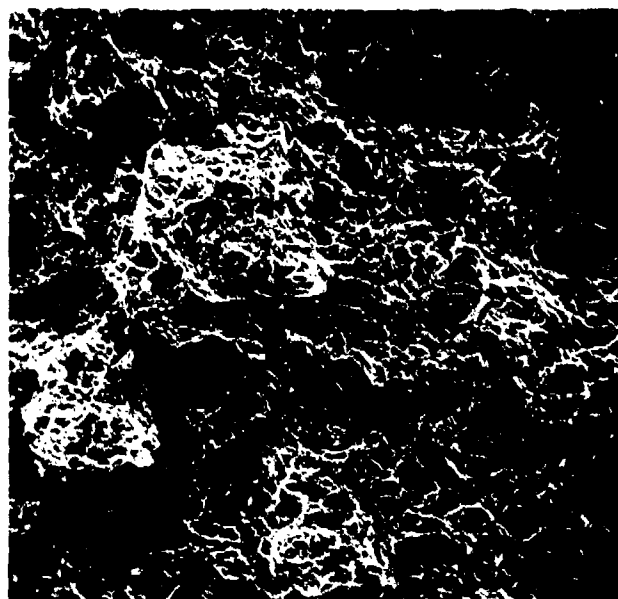
Figure 25.   Dimple rupture in notch region of an A-36 Charpy specimen tested at room temperature, 100x.
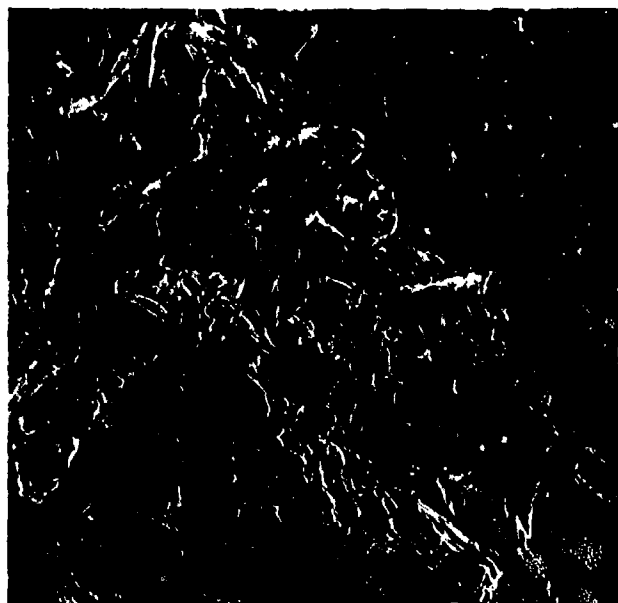
Figure 26.   Cleavage fracture in central region of an A-36 Charpy specimen tested at room temperature, 100x.

ASTM A-514 PLATE

Material: ASTM A-514 Grade F Plate

Heat Treatment: Quenched and tempered
Test Direction: Longitudinal (parallel to the rolling)
Mode or Condition of Test: Tensile
Test Temperature: Ambient
Test Environment: Air
Test Results:

Mechanical Properties:

Yield Stress
121,000 psi (834.9 MPa)

Ultimate Fracture Stress
127,000 psi (876.3 MPa)

Fractographic Analysis:

Failure occurred by normal rupture in the central portion of the
specimen and shear rupture along the outside edges (Figures 27 through
29.) The tensile test produced a slant-type fracture surface such that a
shear lip was completely absent from one side of the surface. The cen-
tral region was somewhat flat and displayed a fibrous texture.
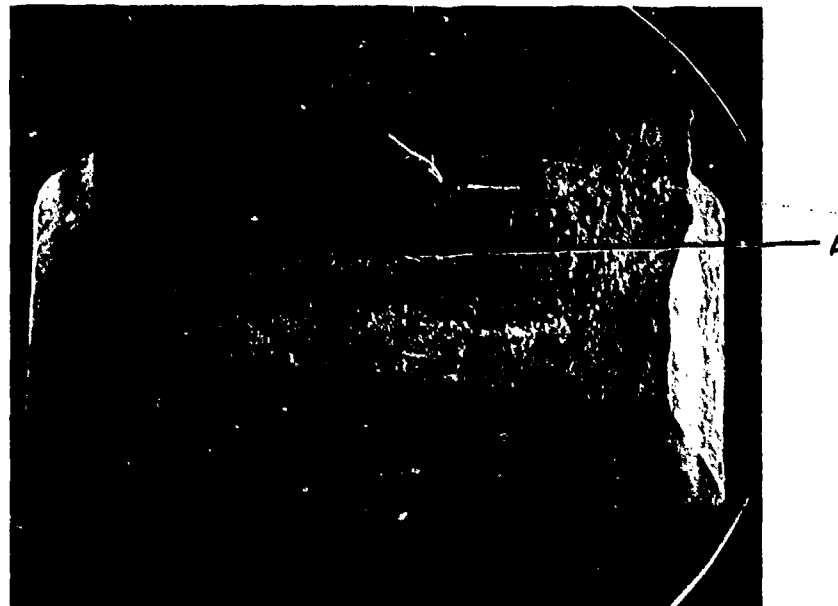
Figure 27.   Tensile fracture surface of an A-514 steel
plate specimen, 8x.

66
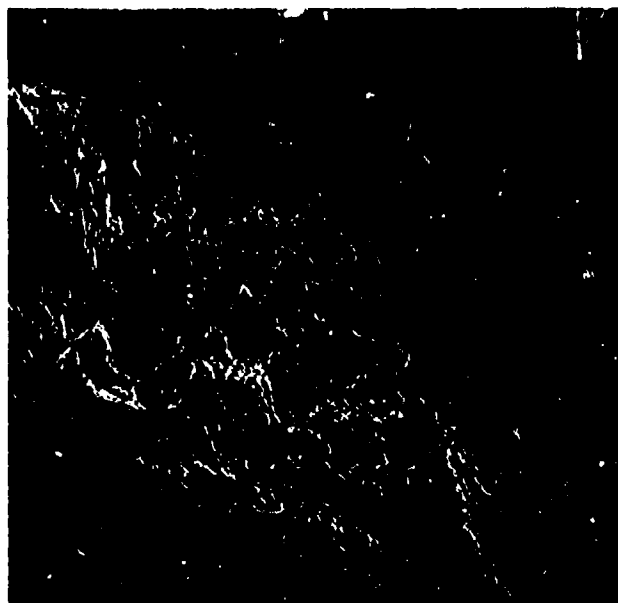
Figure 28. Tensile failure of A-514 steel by dimple rupture, 375x.
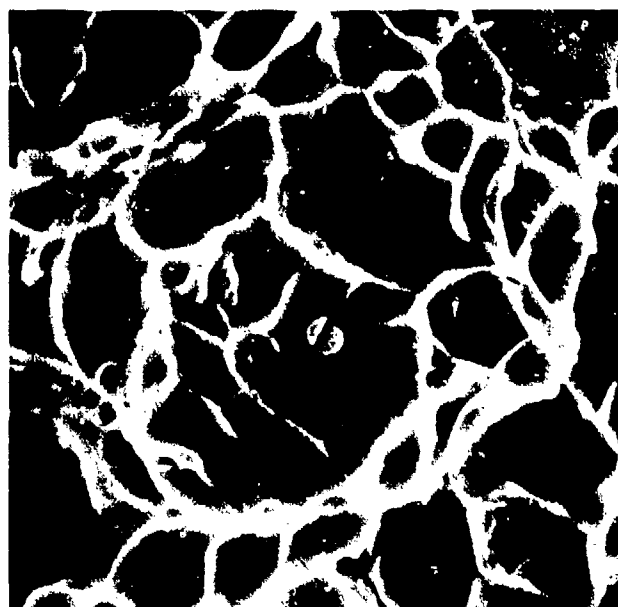
Figure 29. Equiaxed dimples containing inclusions, 7500x.

Material: ASTM A-514 Grade F Plate

Heat Treatment: Quenched and tempered
Test Direction: Longitudinal (parallel to the rolling)
Mode or Condition of Test: Hydrogen-embrittled tensile
Test Temperature: Ambient
Test Environment: Air
Hydrogen Charging Conditions:

Current Density: 6 mA/in.^{2} (0.93 mA/cm^2)

Charge Time: 12 hours

Electrolyte: 0.3 wt% As_2O_3

10.0 wt% H_2SO_4

Test Results:

Mechanical Properties:

Yield Stress
120,000 (828 MPa)

Ultimate Fracture Stress
127,000 (876.3 MPa)

Fractographic Analysis:

Failure occurred by dimple rupture and microvoid coalescence. The dimples and microvoids were very shallow (Figures 30 through 32). The fracture surface was fairly flat except for two large shear lips which were present at opposite corners of the surface. The central portion of the surface contained small cracks.
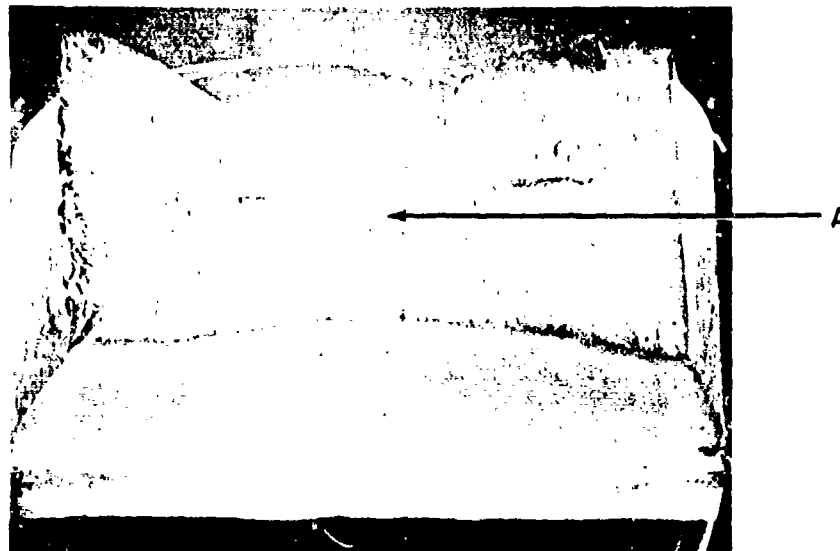
Figure 30. Tensile fracture surface of hydrogen-embrittled A-514 steel, 8x.
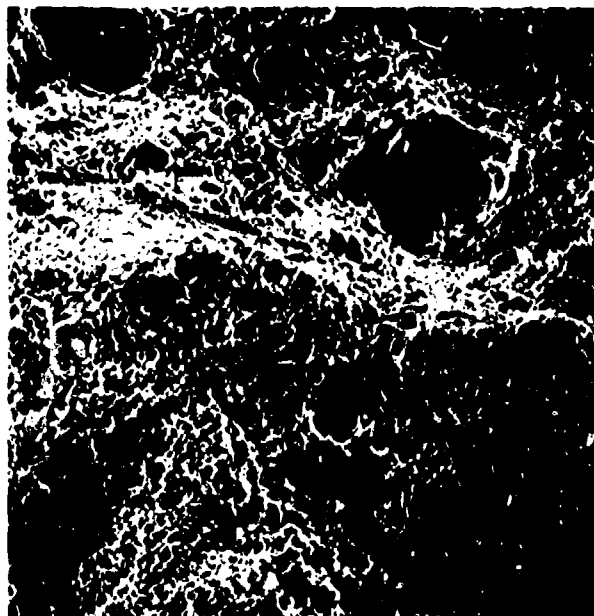
Figure 31. Tensile failure of hydrogen-embrittled A-514 steel by dimple rupture, 650x.
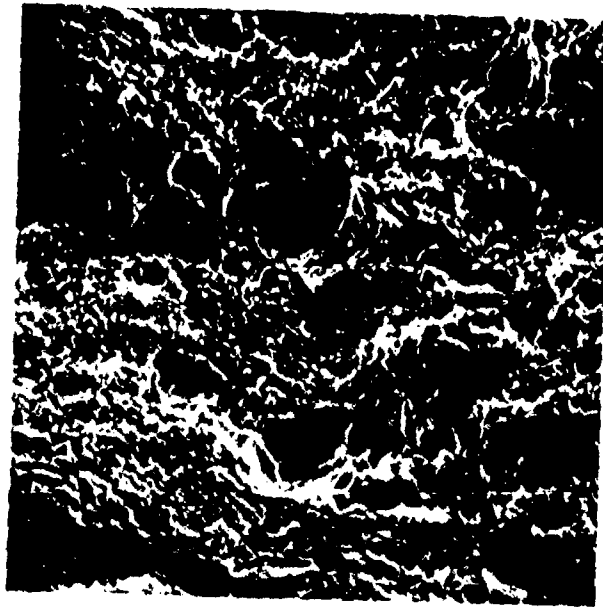
Figure 32. Tensile failure of hydrogen-embrittled A-514
steel by dimple rupture, 1500x.

Material: ASTM A-514 Gra   `e

Heat Treatment: Temper
Test Direction: Longitu   grain)
Mode or Condition of Tes   ϶
Test Temperature: Ambie
Test Environment: Air
Temper Embrittlement He   t:
   Temper 1 hour at 593
   Furnace cool to 538^{0} for 15 hours
   Furnace cool to 524^{0} er for 24 hours
   Furnace cool to 496^{0} ρper for 48 hours
   Furnace cool to 468^{0} mper for 72 hours
   Furnace cool to 315^{C}
   Air cool to room ter.   ϶

Test Results:

    Mechanical Properties:

        Yield Stress
        120,000 psi (828 MPa)

        Ultimate Fracture Stress
        128,000 psi (883.2 MPa)

    Fractographic Analysis:

    Failure occurred by normal rupture in the center of the specimen
and shear rupture along the edges (Figures 33 through 35). The fracture
surface was characteristic of a slant-type failure with shear lips
present on three sides of the specimen. The central region was somewhat
flat and fibrous in appearance.

71
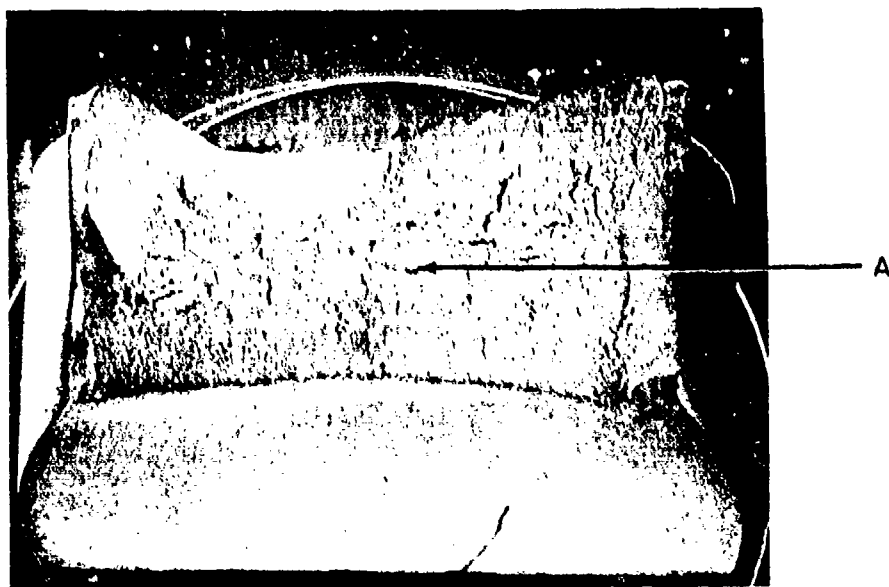
Figure 33. Tensile fracture surface of temper-embrittled A-514 steel, 8x.
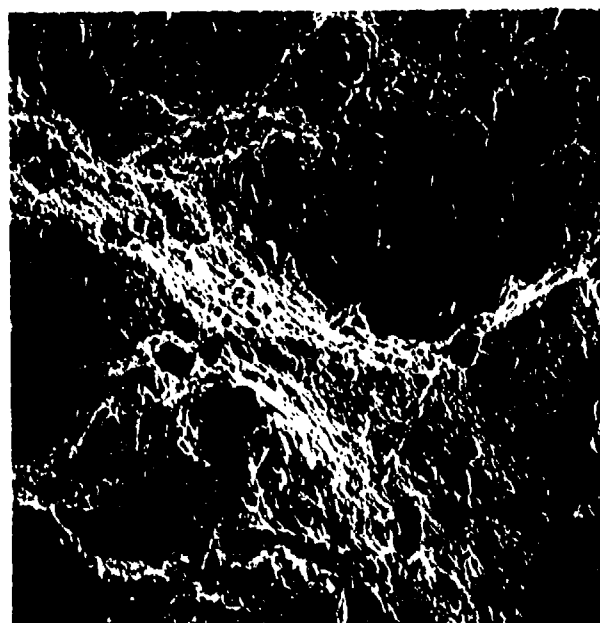
Figure 34. Tensile failure of temper-embrittled A-514 steel by dimple rupture, 375x.

72
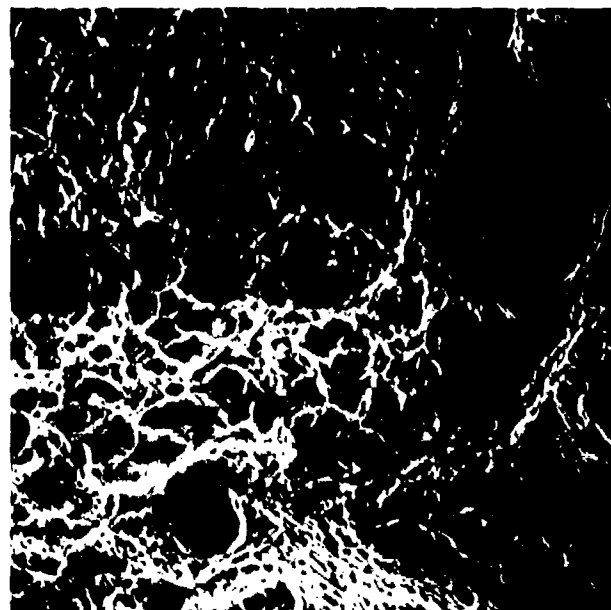
Figure 35. Equiaxed dimples and microvoid coalescence
in temper-embrittled A-514 steel, 1500x.

Material: ASTM A-514 Grade F Plate

Heat Treatment: Quenched and tempered
Test Direction: Longitudinal (with grain)
Mode or Condition of Test: Fatigue
Test Temperature: Ambient
Test Environment: Air
Test Results:

Mechanical Properties:

Maximum Stress
100,000 psi (690 MPa)

Minimum Stress
15,000 psi (103.5 MPa)

Test Frequency
10 cycles/sec

Cycles to Failure
6,035

Fractographic Analysis:

The fatigue zone was not as flat as it appeared macroscopically, but instead consisted of numerous ridges of varying heights. The fatigue striations remained nearly parallel to the machined notch although occasionally secondary cracking was evident. The central portion of the specimen failed by normal rupture producing equiaxed dimples (Figures 36 through 39). The fatigue zones were flat while the central portion of the specimen was rough with shear lips present on the sides.
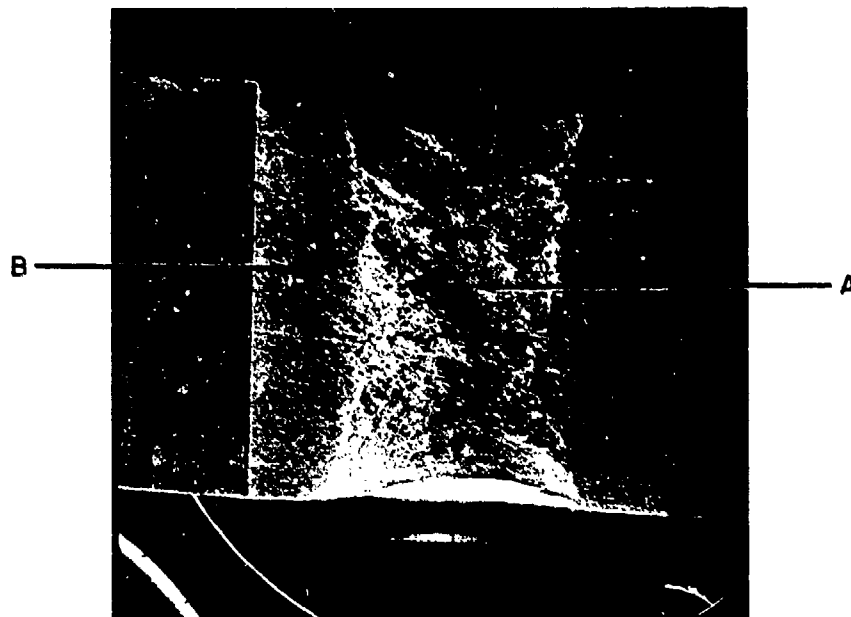
Figure 36. Fatigue fracture surface of an A-514 steel plate specimen, 10x.

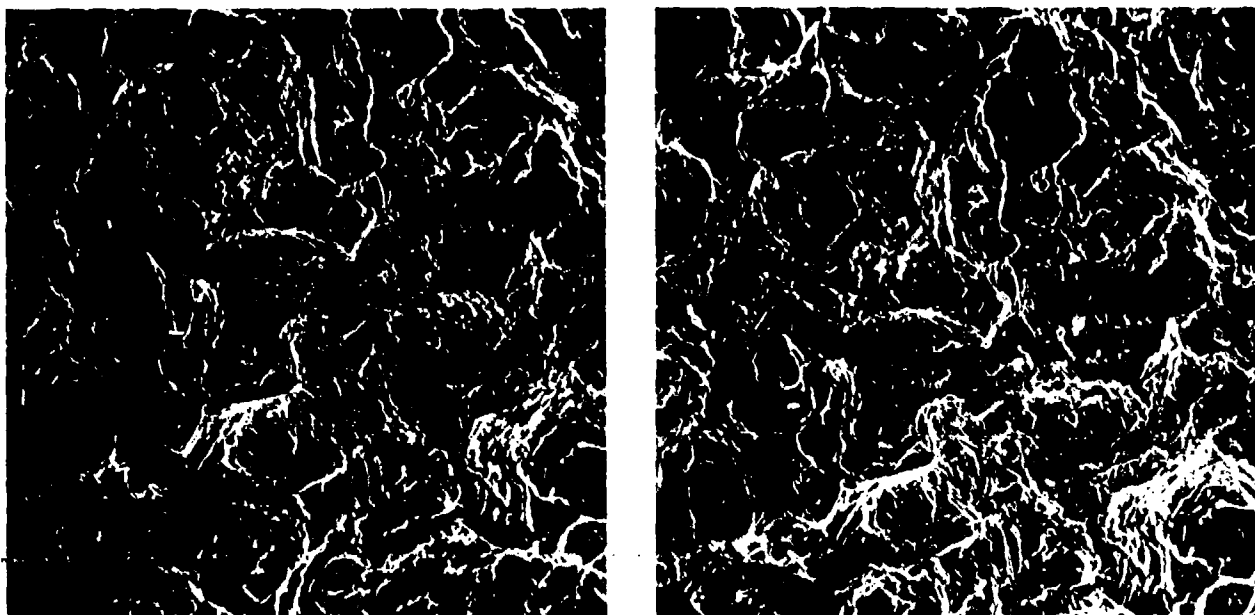Figure 37. Fatigue striations on surface of an A-514 fatigue specimen, 1000x.
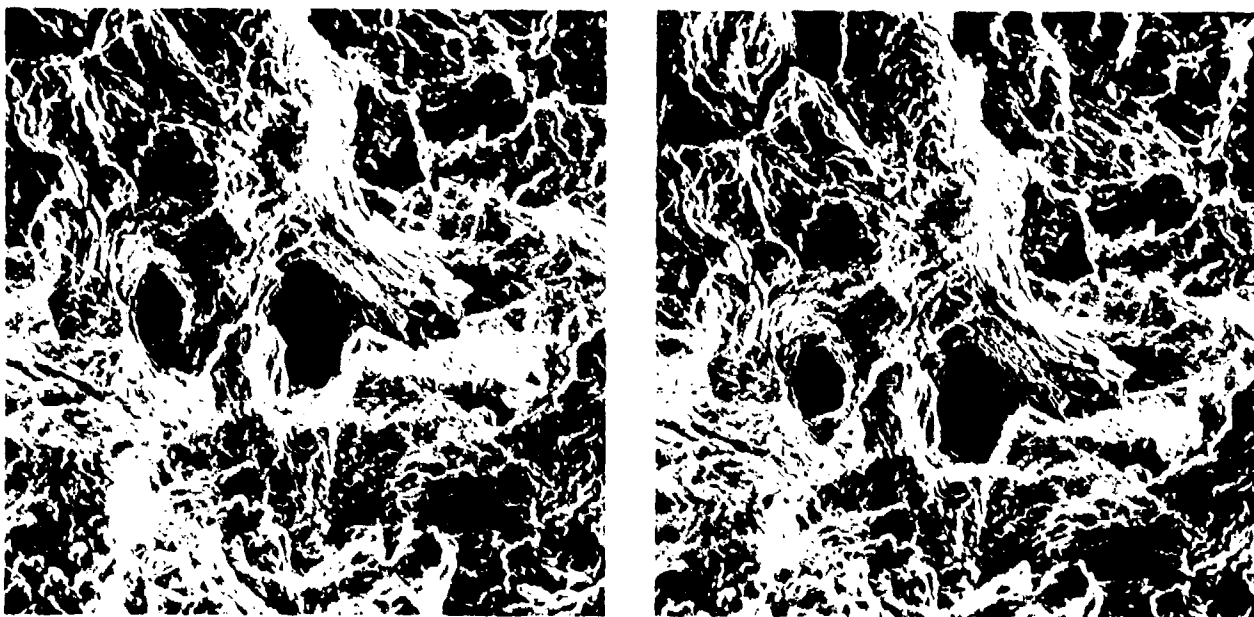
Figure 38.   A stereomicrograph of the fatigue zone in A-514 steel, 1600x.
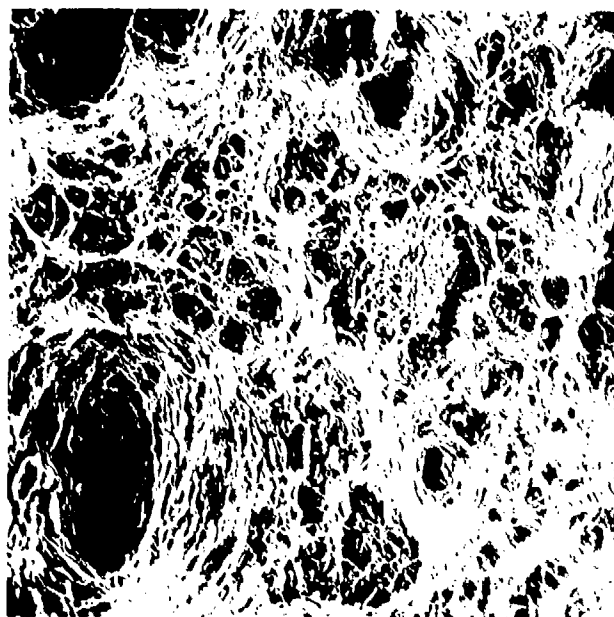
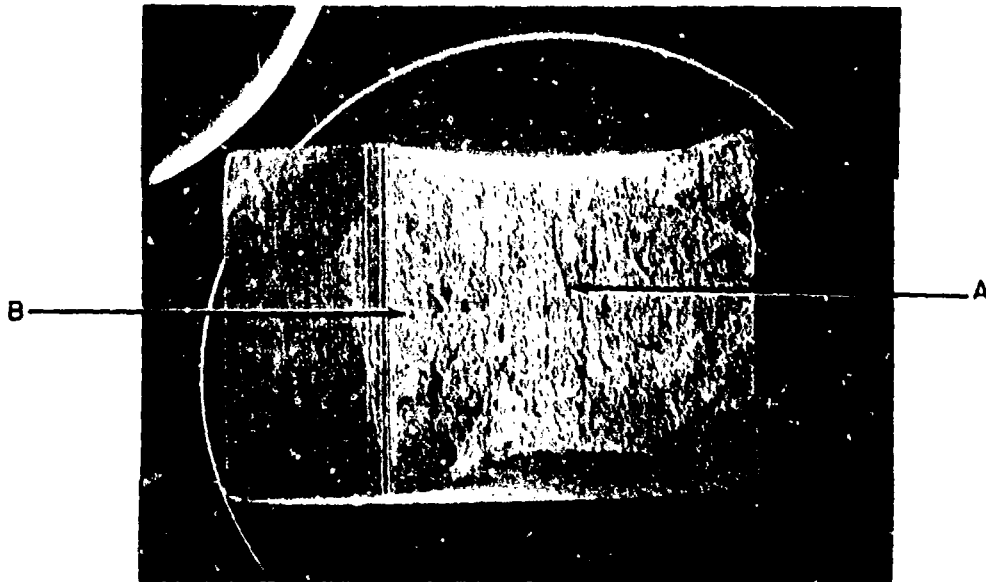Figure 39. Tensile overload region of an A-514 fatigue specimen, 700x.

Material: ASTM A-514 Grade F Plate

Heat Treatment: Quenched and tempered
Test Direction: Longitudinal (with grain)
Mode or Condition of Test: Hydrogen-embrittled fatigue
Test Temperature: Ambient
Test Environment: Air

Hydrogen Charging Conditions:

  Current Density: 6 mA/in^2 (0.93 mA/cm^2)

  Charge Time: 12 hours

  Electrolyte: 0.3 wt% As_2O_3

              10.0 wt% H_2SO_4

Test Results:

    Mechanical Properties:

            Maximum Stress
            100,000 psi (690 MPa)

            Minimum Stress
            15,000 psi (103.5 MPa)

            Test Frequency
            10 cycles/sec.

            Cycles to Failure
                3470

    Fractographic Analysis:

    The fatigue region contained parabolic contours or "craters." Many
of these craters contained cracks oriented perpendicular to the machined
notch. Failure occurred by quasi-cleavage inside the craters, while
outside, considerable secondary cracking resulted in multidirectional
fatigue striations. There were no fatigue striations evident near the
notch indicating subsurface nucleation. Failure occurred by dimple
rupture in the central portion of the specimen (Figures 40 through 46).
The fatigue regions were flat, while the tensile overload region in
the center of the specimen was rough and jagged with shear lips present
on the outside edges.
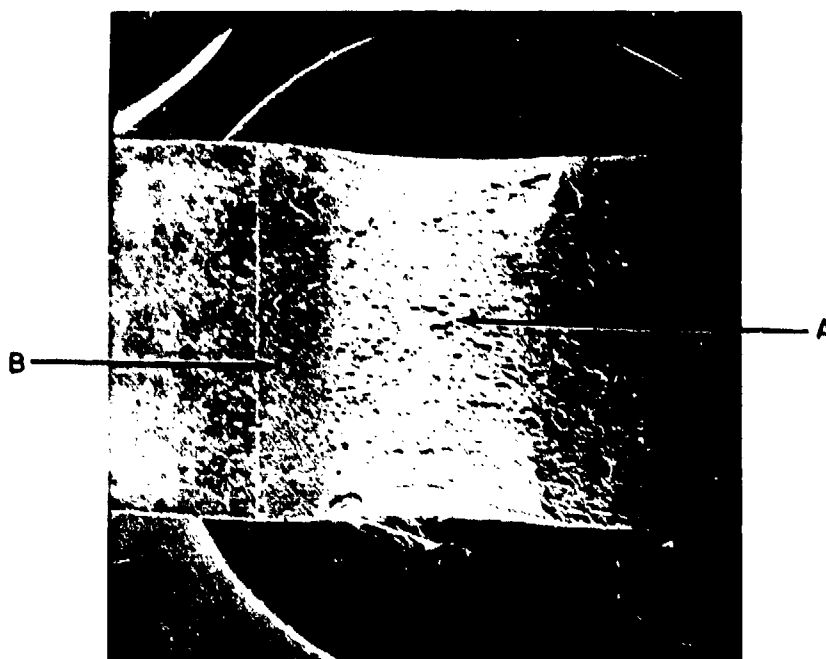
Figure 40. Fracture surface of a hydrogen-embrittled A-514 plate fatigue specimen, 8x.
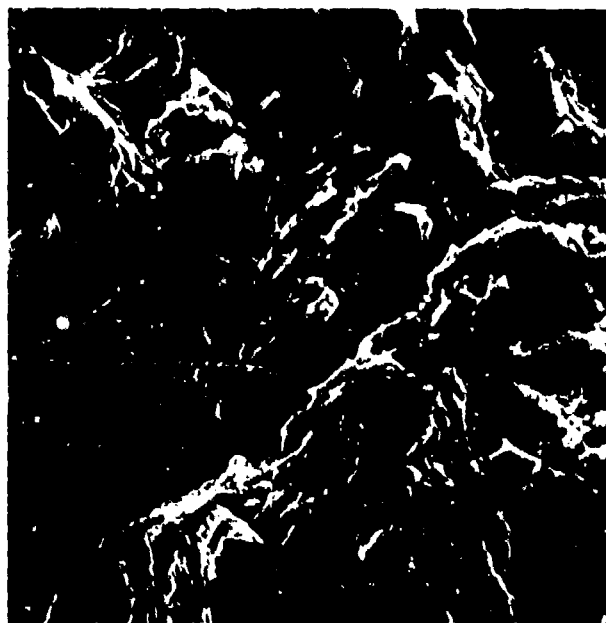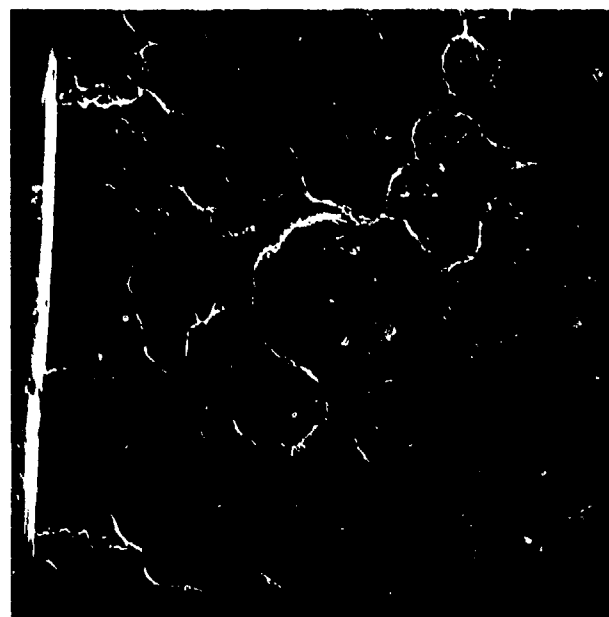

Figure 41. Fatigue zone of hydrogen-embrittled A-514 plate fatigue specimen, 60x.
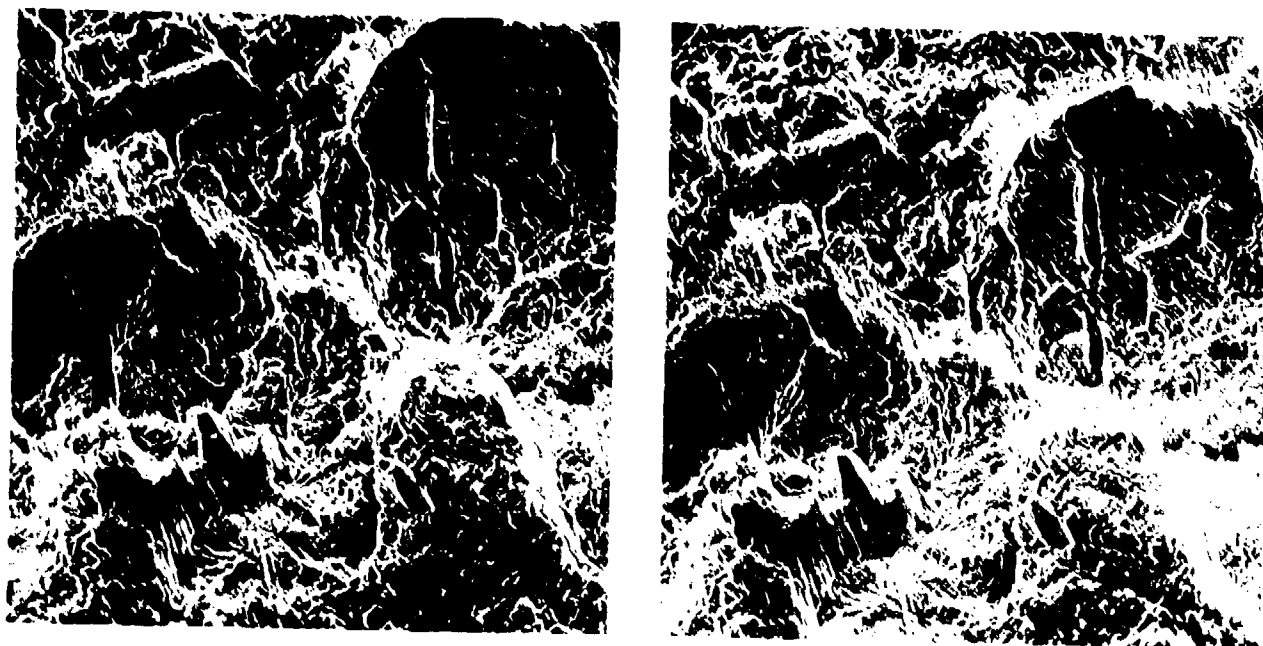
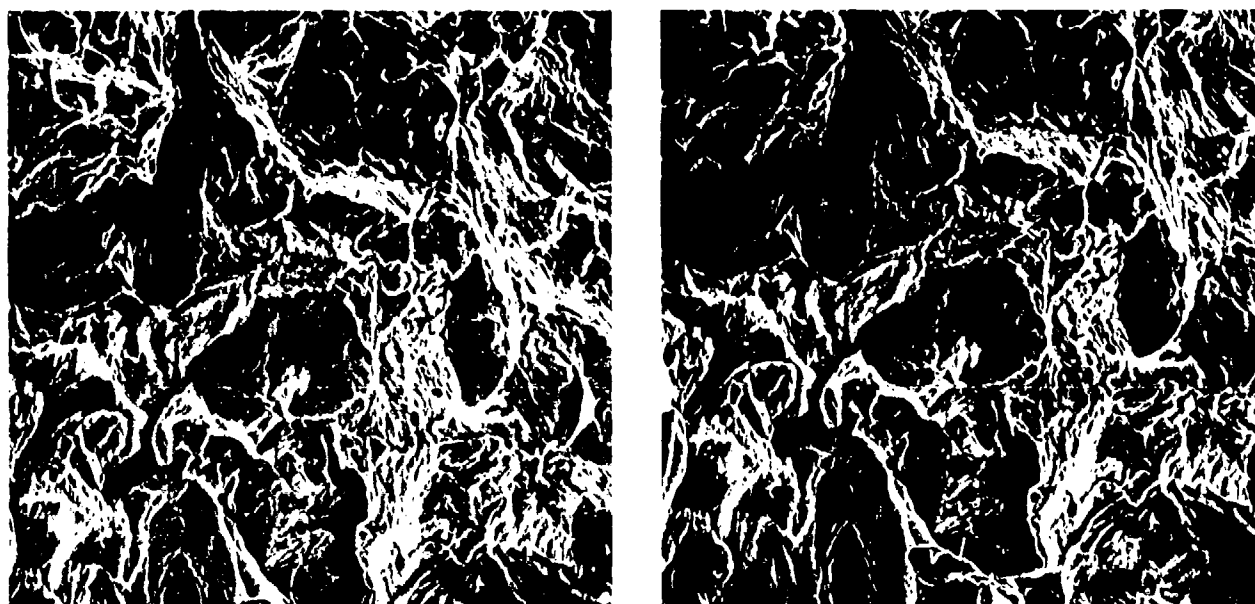Figure 42. A stereomicrograph of the fatigue zone in hydrogen-embrittled A-514 steel, 400x.

80
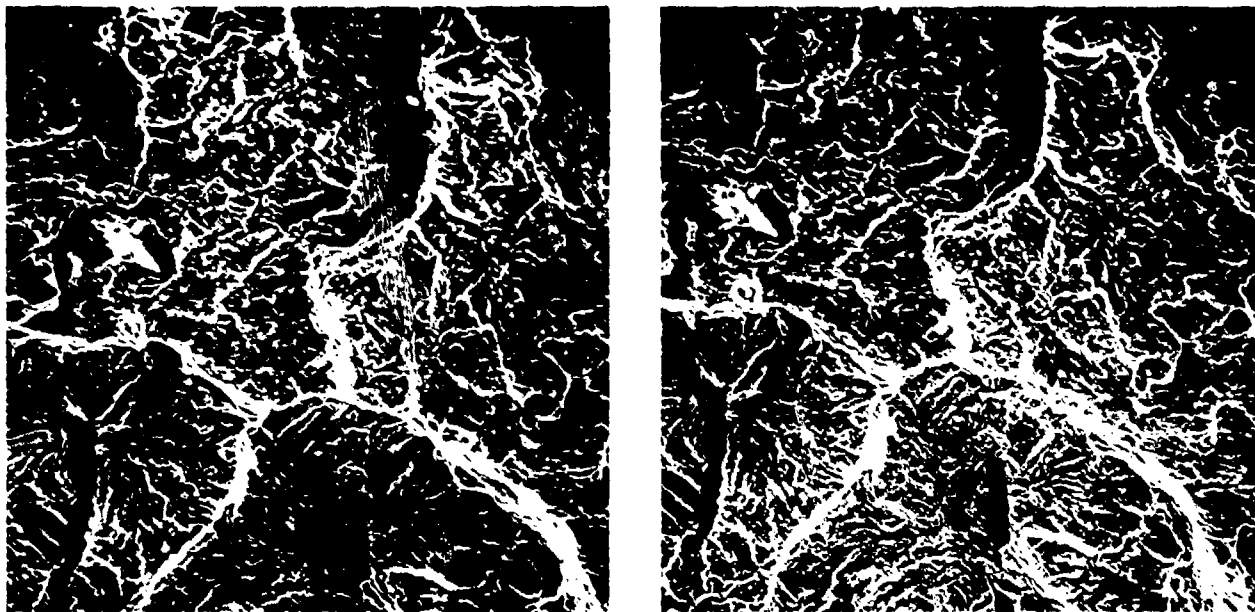
Figure 43. A stereomicrograph of the fatigue zone in hydrogen-embrittled A-514 steel, 500x.
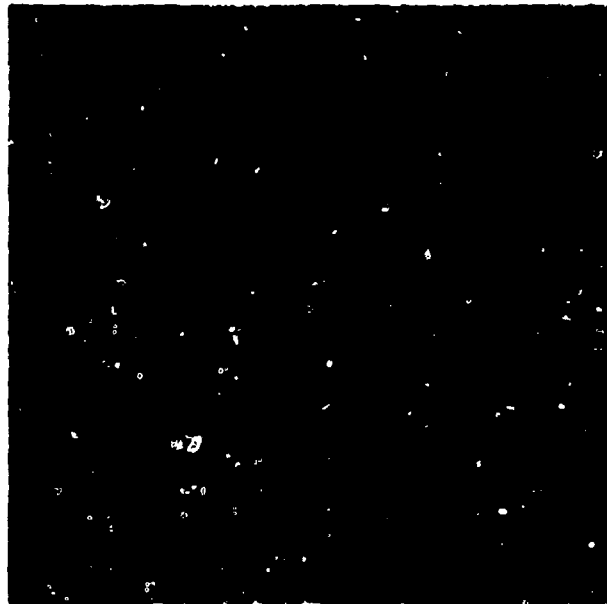
Figure 44. Tensile overload region of a hydrogen-embrittled A-514 plate
fatigue specimen, 140x.
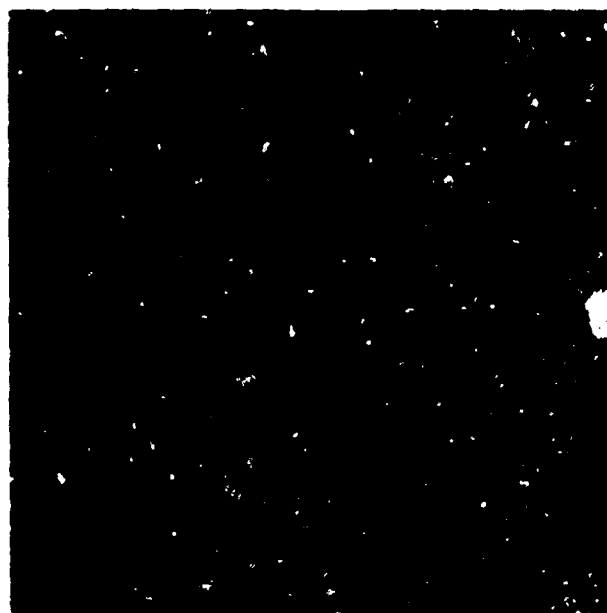
Figure 45. Optical micrograph showing the beginning and intermediate
stages of crater, 550x.
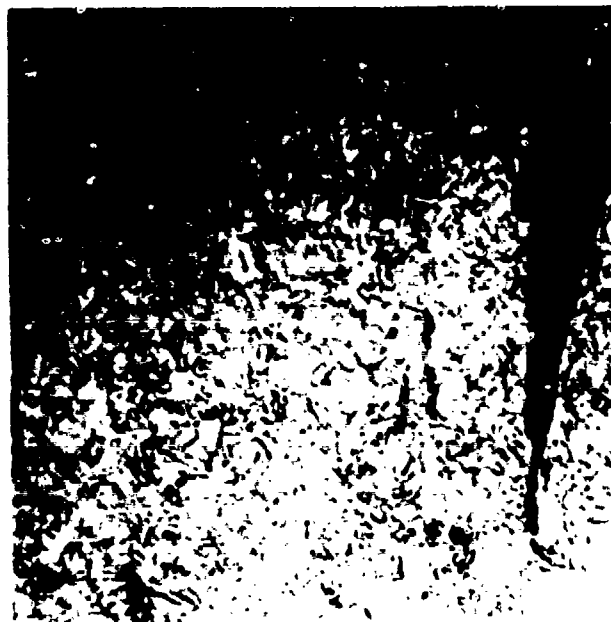
Figure 46. Optical micrograph of a longitudinal section of the fatigue zone in hydrogen-embrittled A-514 steel showing fully completed crater, 550x.

Material: ASTM A-514 Grade F Plate

Heat Treatment: Temper embrittled
Test Direction: Longitudinal (with grain)
Mode or Condition of Test: Fatigue
Test Temperature: Ambient
Test Environment: Air
Temper Embrittlement Heat Treatment:
   Temper 1 hour at 593°C
   Furnace cool to 538°C and temper for 15 hours
   Furnace cool to 524°C and temper for 24 hours
   Furnace cool to 496°C and temper for 48 hours
   Furnace cool to 468°C and temper for 72 hours
   Air cool to room temperature

Test Results:

   <u>Mechanical Properties</u>:

       <u>Maximum Stress</u>
       100,000 psi (690 MPa)

       <u>Minimum Stress</u>
       15,000 psi (103.5 MPa)

       <u>Test Frequency</u>
       10 cycles/sec

       <u>Cycles to Failure</u>
       5417

   <u>Fractographic Analysis</u>:

   The fatigue striations were parallel to the machined notch. The central portion of the specimen failed by dimple rupture (Figures 47 through 50). The fatigue and tensile overload regions contained a number of large lamellar tears oriented parallel to the machined notch and the rolling direction. The central portion of the specimen was rough and contained shear lips on the outside edges.
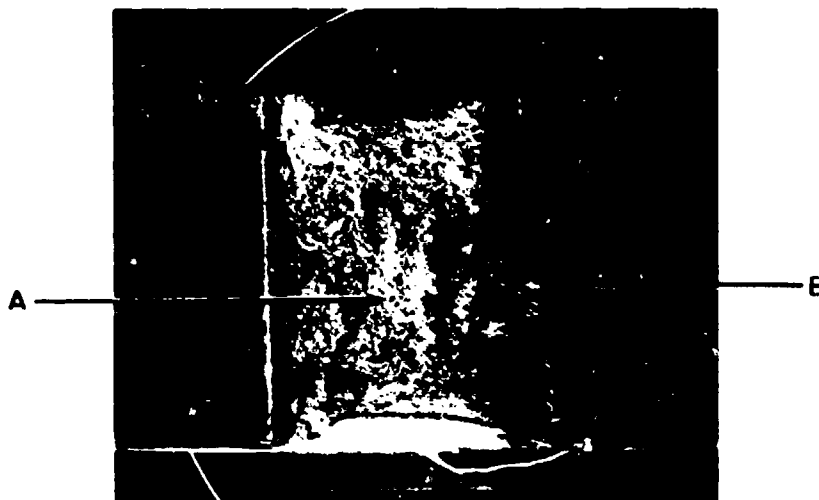
Figure 47. Fracture surface of a temper-embrittled A-514 plate fatigue specimen, 10x.

Figure 48. Transition region from fatigue to tensile overload in a temper-embrittled A-514 fatigue specimen 35x.

85
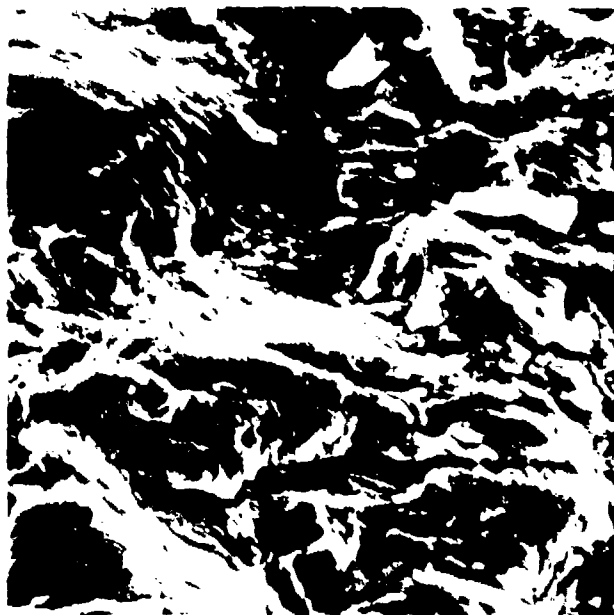
Figure 49. Fatigue striations on fracture surface of temper-embrittled A-514 steel. 5000x.
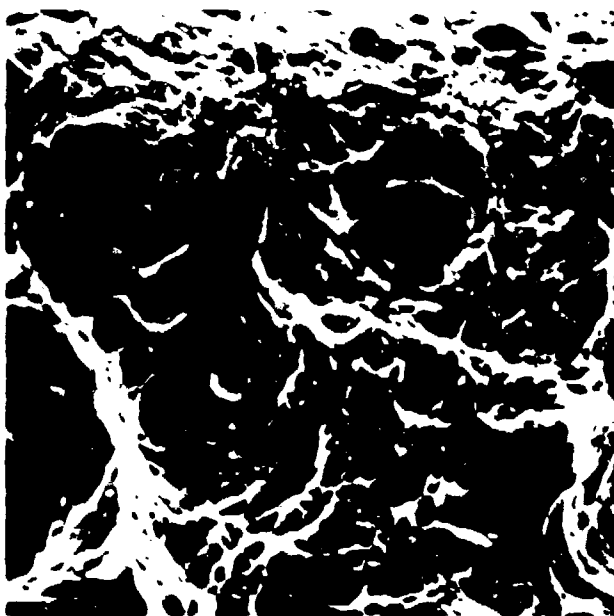
Figure 50. Dimple rupture in tensile overload region of a temper-embrittled A-514 steel fatigue specimen, 3500x.

Material: ASTM A-514 Grade F Plate

Heat Treatment: Quenched and tempered
Test Direction: Longitudinal (with grain)
Mode or Condition of Test: Charpy impact
Test Temperature: -196°C
Test Environment: Air
Test Results:

Mechanical Properties:

Fracture Energy
18 ft-lb (24.5 joule)

Fractographic Analysis:

Failure was entirely by cleavage. The tear lines or "river patterns" which show the direction of crack propagation across each cleavage facet are clearly evident (Figures 51 through 53). The fracture surface was extremely flat and shiny.
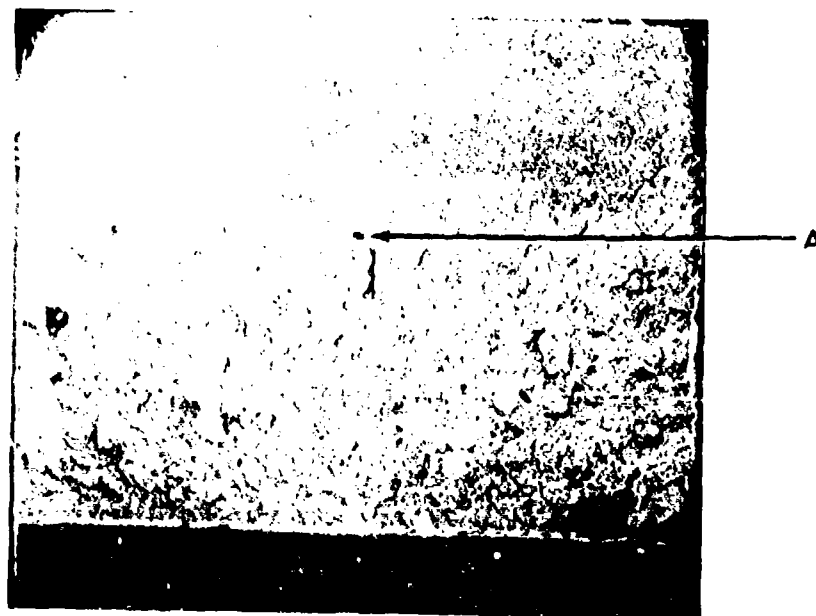
Figure 51. Fracture surface of an A-514 Charpy specimen tested at -196°C.
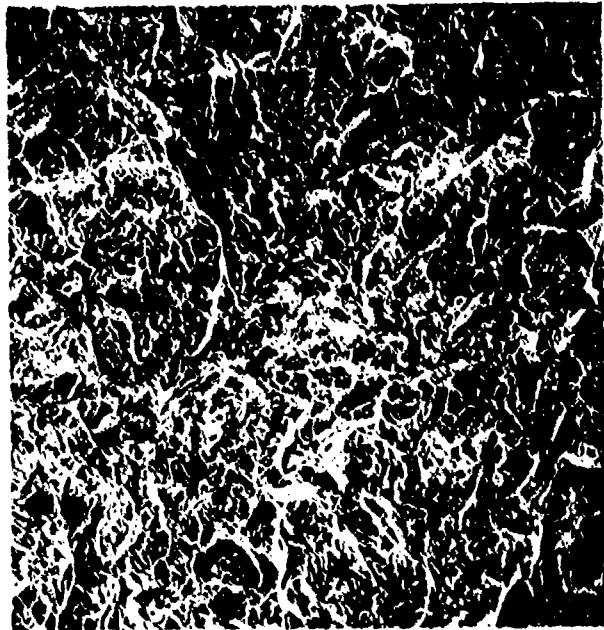
Figure 52. Cleavage fracture in an A-514 Charpy specimen tested at -196°C, 250x.
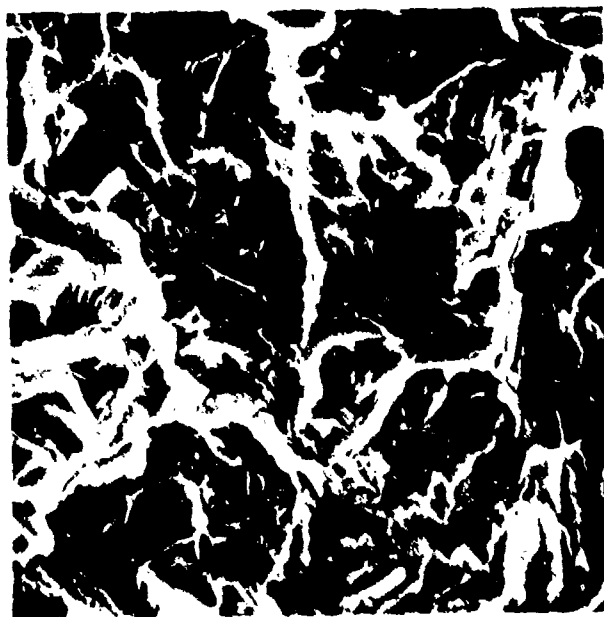
Figure 53. Cleavage facets containing tear lines, 5000x.

Material: ASTM A-514 Grade F Plate

Heat Treatment: Quenched and tempered
Test Direction: Longitudinal (with grain)
Mode or Condition of Test: Charpy impact
Test Temperature: -83°C
Test Environment: Air
Test Results:

Mechanical Properties:

Fracture Energy
50 ft-lb (68 joule)

Fractographic Analysis:

Failure occurred in a mixed mode fashion. Near the outer surface, failure was by dimple rupture, while in the center of the specimen failure occurred by cleavage (Figures 54 through 56). The fracture surface was fairly flat and displayed a slightly textured appearance. A shear lip was present on one side of the surface.
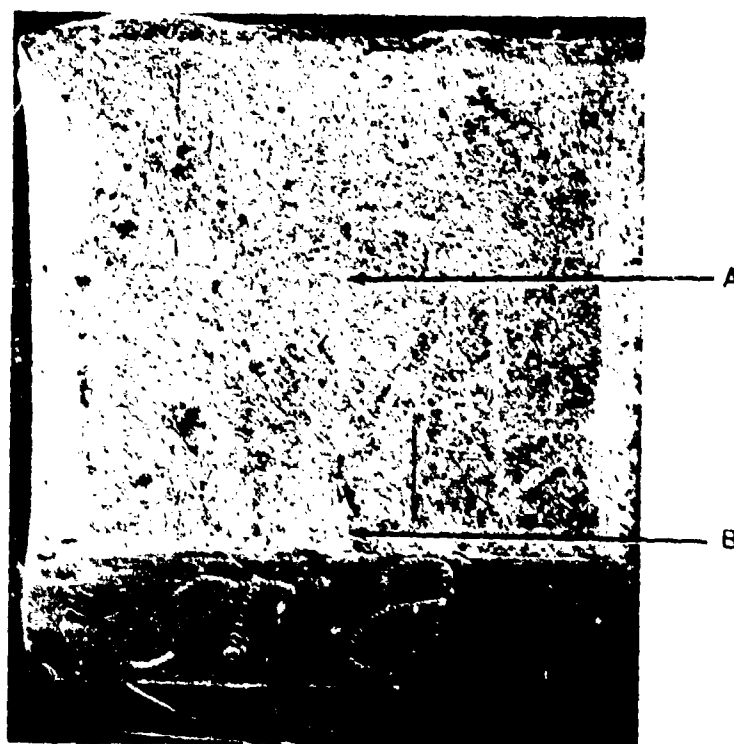
Figure 54. Fracture surface of an A-514 Charpy specimen
tested at -83°C, 8x.
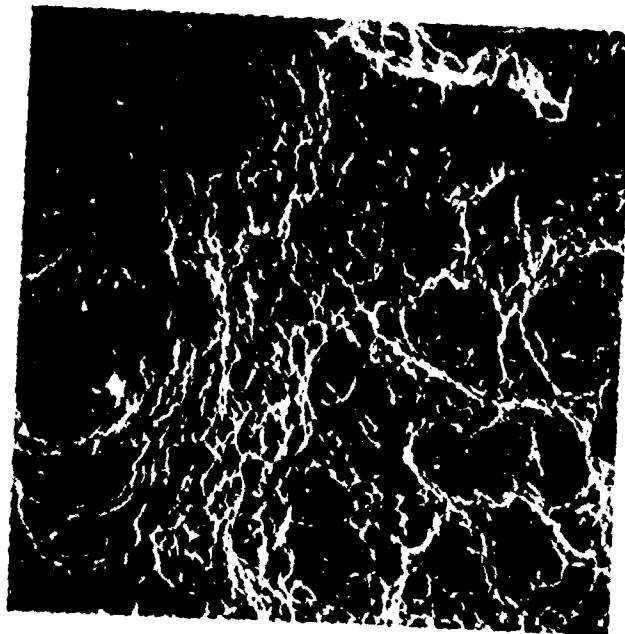
Figure 55. Edge region of an A-514 Charpy specimen tested at -83°C, 1000x.
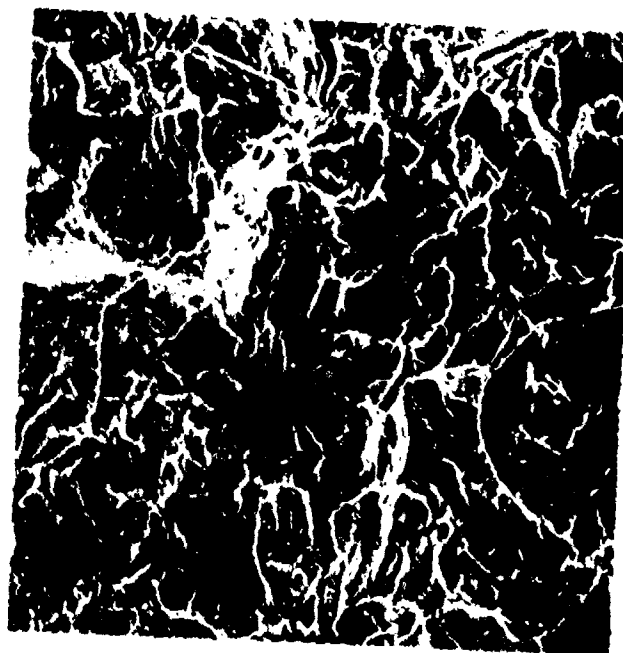
Figure 56. Central region of an A-514 Charpy specimen tested at -83°C, 1000x.

Material: ASTM A-514 Grade F Plate

Heat Treatment: Quenched and tempered
Test Direction: Longitudinal (with grain)
Mode or Condition of Test: Charpy impact
Test Temperature: -18°C
Test Environment: Air
Test Results:

Mechanical Properties:

Fracture Energy
73 ft-lb (99.3 joule)

Fractographic Analysis:

Failure occurred by dimple rupture and microvoid coalescence (Figures 57 and 58). The fracture surface was fairly coarse and woody in appearance. It also contained a shear lip on one edge.
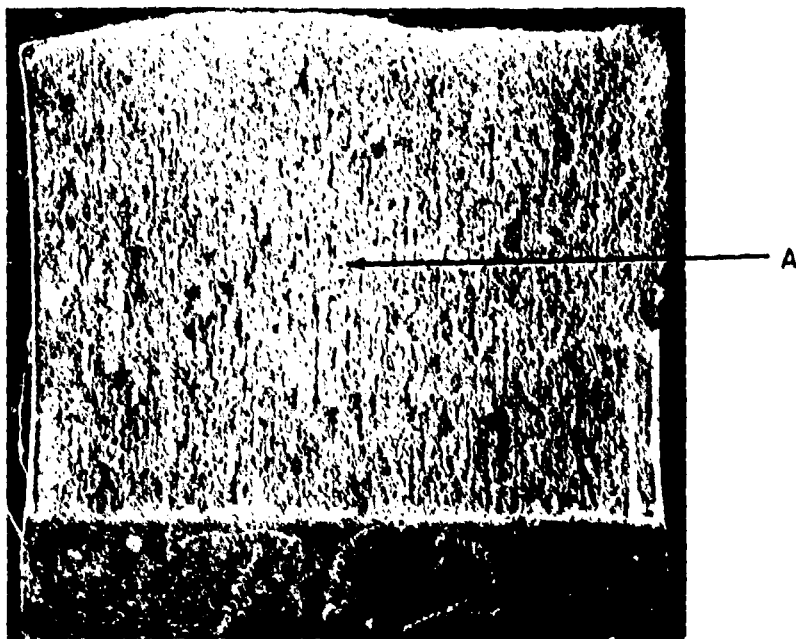
Figure 57. Fracture surface of an A-514 Charpy specimen tested at -18°C, 8x.
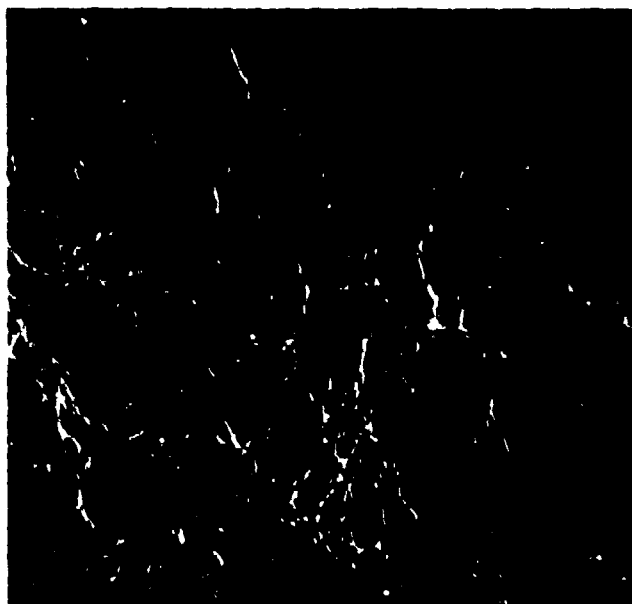
Figure 58. Failure of an A-514 Charpy specimen tested at -18°C by dimple rupture, 1000x.

Material: ASTM A-514 Grade F Plate

Heat Treatment: Quenched and tempered
Test Direction: Longitudinal (with grain)
Mode or Condition of Test: Charpy impact
Test Temperature: Ambient
Test Environment: Air
Test Results:

Mechanical Properties:

Fracture Energy
83 ft-lbs (113 joule)

Fractographic Analysis:

Failure was by dimple rupture and microvoid coalescence (Figures 59 and 60). The fracture surface was somewhat coarse and clearly indicated the texture of the steel. A shear lip was present on one edge.

Figure 59. Fracture surface of an A-514 Charpy specimen tested at room temperature, 10x.
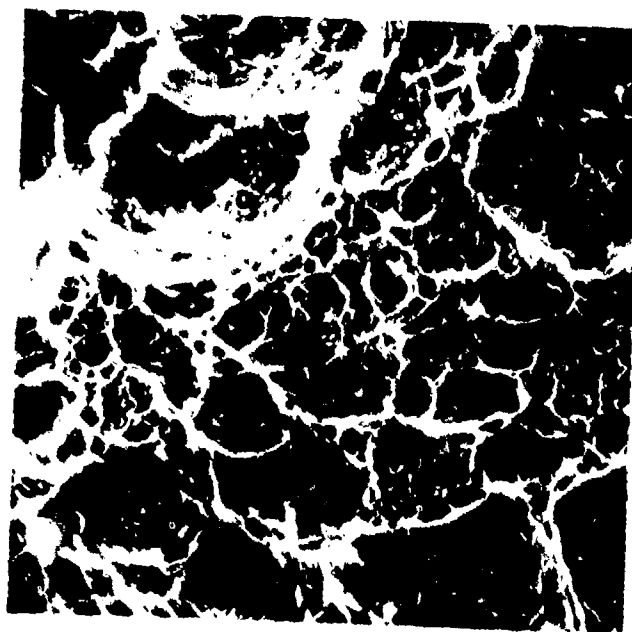
Figure 60. Failure of an A-514 Charpy specimen tested at room temperature by dimple rupture, 1700x.

Material: HY-130 Plate

ᵣeat Treatment: Quenched and tempered
Test Direction: Longitudinal (with grain)
Mode or Condition of Test: Tensile
Test Temperature: Ambient
Test Environment: Air
Test Results:

Mechanical Properties:

Yield Stress
142,500 psi (983.2 MPa)

Ultimate Fracture Stress
150,500 psi (1038.4 MPa)

Fractographic Analysis:

Failure occurred by normal rupture in the center of the specimen
and shear rupture on the edges (Figures 61 through 63). Plastic defor-
mation of the material during testing resulted in the formation of prom-
inent shear lips on all sides of the specimen. A few small tears were
observed in the central portion of the specimen.

Figure 61. Tensile fracture surface of an HY-130 steel
specimen, 8x.
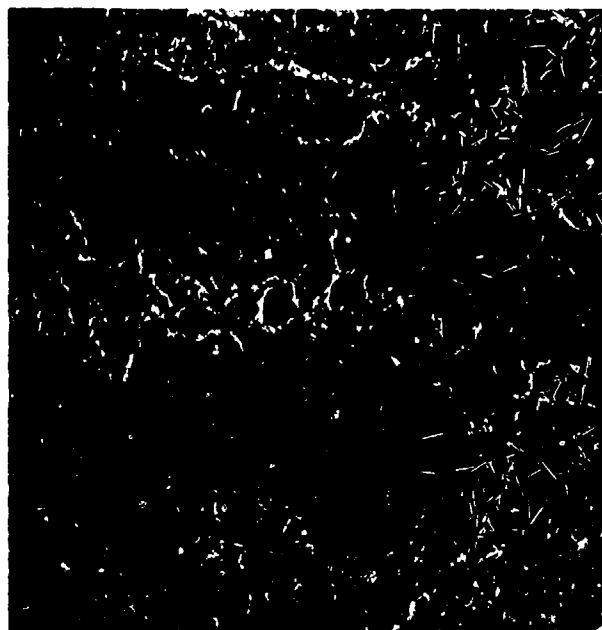
Figure 62. Central region of HY-130 tensile specimen, 1500x.
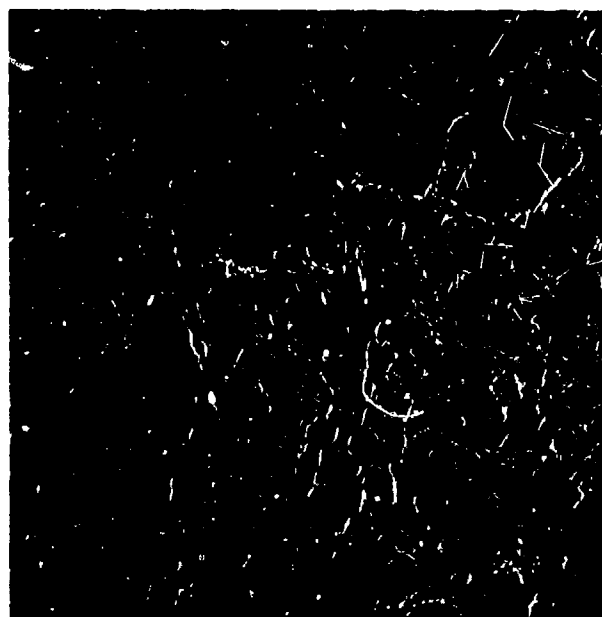
Figure 63. Edge region of HY-130 tensile specimen, 1600x.

Material: HY-130 Plate

Heat Treatment: Quenched and tempered
Test Direction: Longitudinal (with grain)
Mode or Condition of Test: Hydrogen-embrittled tensile
Test Temperature: Ambient
Test Environment: Air
Hydrogen Charging Conditions:

  Current Density: 6 mA/in.^{2} (0.93 mA/cm^2)

  Charge Time: 12 hours

  Electrolyte: 0.3 wt% As_2O_3

              10.0 wt% H_2SO_4

Test Results:

    Mechanical Properties:

        Yield Stress
        142,500 psi

        Ultimate Fracture Stress
              149,000 psi

    Fractographic Analysis:

    Failure generally occurred by a combination of grain boundary separa-
tion with microvoid coalescence. The small, circular areas were iden-
tified as "fisheyes," which were believed to have resulted from pockets
of entrapped molecular hydrogen. The center of the fisheyes contained
a hollow pocket. Failure was by quasi-cleavage in these areas (Figures
64 through 68). The fracture surface was very jagged with little indi-
cation of plastic deformation having occurred. Small, circular, flat
areas were extensively present on the surface.
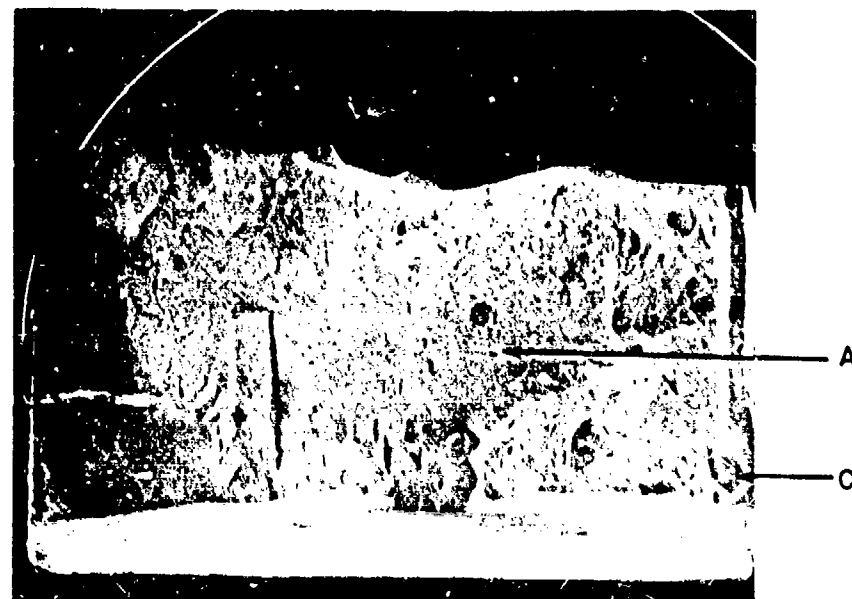
Figure 64.   Tensile fracture surface of a hydrogen-embrittled HY-130 specimen, 9x.
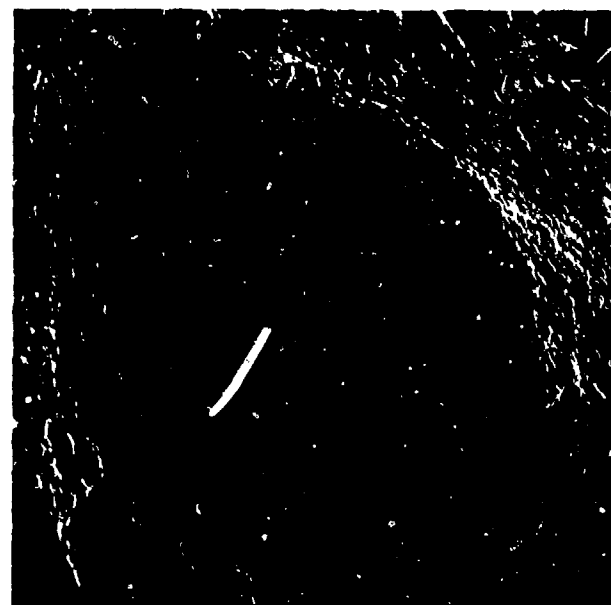
Figure 65.   "Fisheyes" on surface of a hydrogen-embrittled HY-130 tensile specimen, 120x.
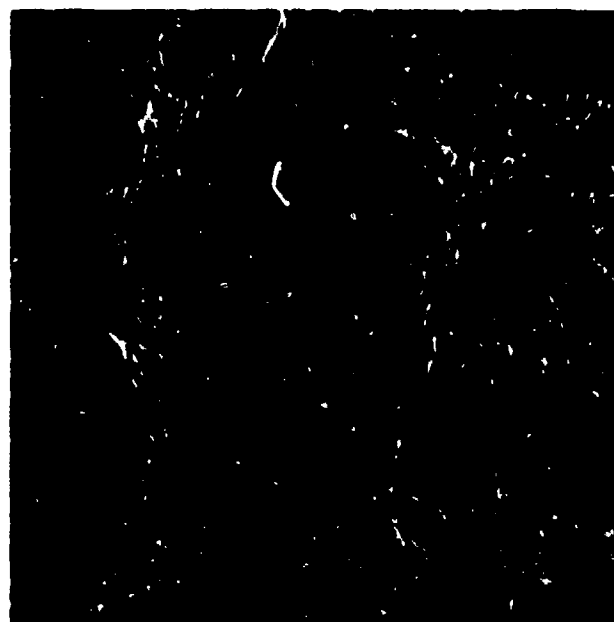
Figure 66. A stereomicrograph of a "fisheye" on the fracture surface of a
hydrogen-embrittled HY-130 tensile specimen, 1400x.
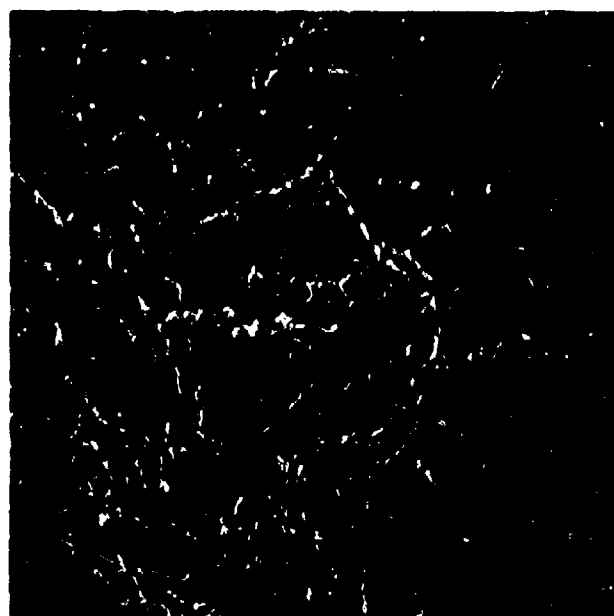
Figure 67. Quasi-cleavage fracture in "fisheye," 1600x.
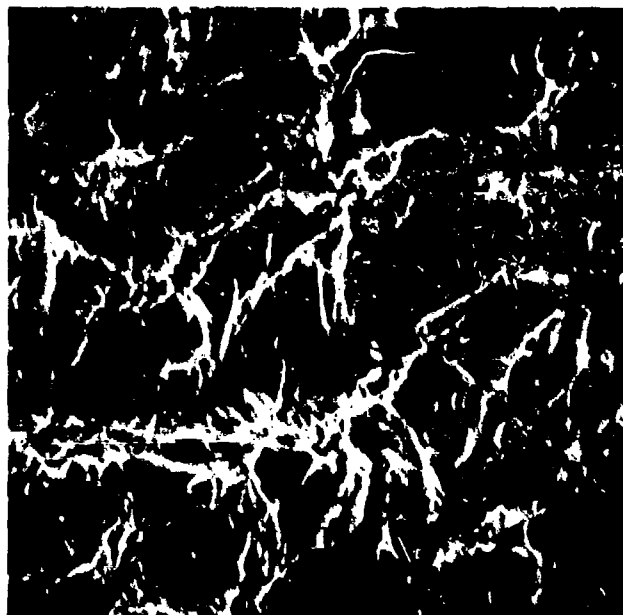
Figure 68. Intergranular slip and microvoid coalescence in a hydrogen-embrittled HY-130 tensile specimen, 3000x.

Material: HY-130 Plate

Heat Treatment: Temper embrittled
Test Direction: Longitudinal (with grain)
Mode or Condition of Test: Tensile
Test Temperature: Ambient
Test Environment: Air
Temper Embrittlement Heat Treatment:
Temper 1 hour at 593°C
Furnace cool to 515°C and temper for 16 hours
Furnace cool to 502°C and temper for 24 hours
Furnace cool to 468°C and temper for 96 hours
Furnace cool to 452°C and temper for 144 hours
Furnace cool to 441°C and temper for 168 hours
Furnace cool to 344°C
Air cool to room temperature

Test Results:

Mechanical Properties:

Yield Stress
151,000 psi (1041.9 MPa)

Ultimate Fracture Stress
160,000 psi (1104 MPa)

Fractographic Analysis:

Failure occurred by slip, tearing, and microvoid coalescence. Note
the serpentine glide patterns (similar to fatigue striations) on the
fracture surface (Figures 69 through 71). The fracture surface ex-
hibited extensive lamellar tearing which occurred parallel to the major
stress exit. In one instance the tear propagated about 1/4 in. (6.4 mm)
below the fracture surface.
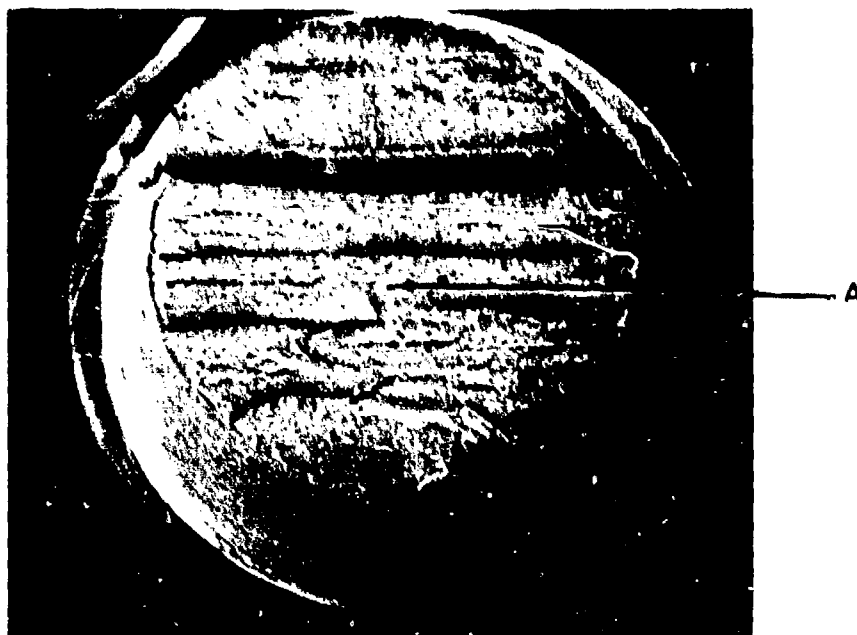
Figure 69. Tensile fracture surface of a temper-embrittled HY-130 specimen, 8x.
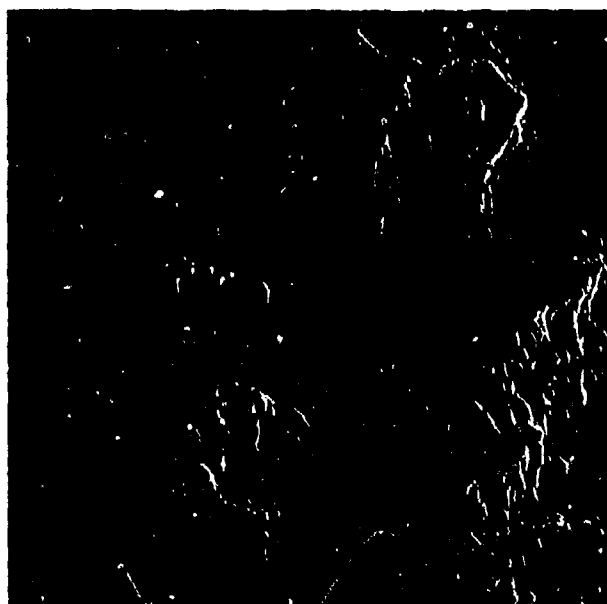
Figure 70. Fracture surface of a temper-embrittled HY-130 tensile specimen, 375x.
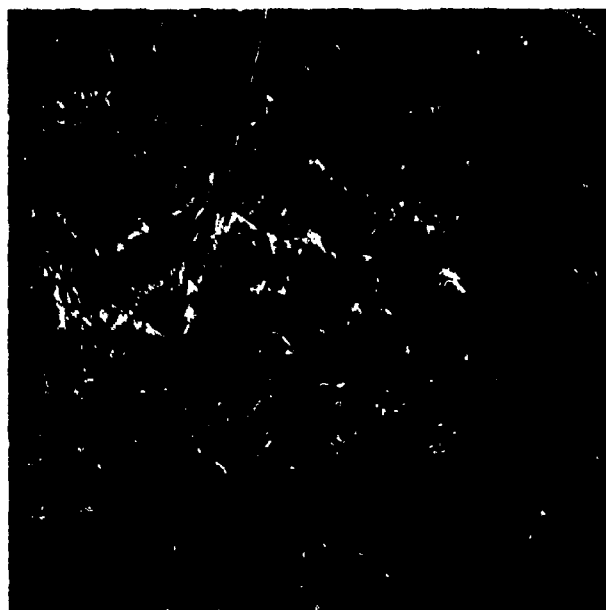
Figure 71. Fracture of a temper-embrittled HY-130 tensile specimen by tear, stretching, and microvoid coalescence, 1500x.

Material: HY-130 Plate

Heat Treatment: Quenched and tempered
Test Direction: Longitudinal (with grain)
Mode or Condition of Test: Fatigue
Test Temperature: Ambient
Test Environment: Air
Test Results:

Mechanical Properties:

Minimum Stress
134,000 psi (924.6 MPa)

Minimum Stress
18,000 psi (124.2 MPa)

Test Frequency
10 cycles/sec

Cycles to Failure
11,560

Fractographic Analysis:

The fatigue striations were parallel to the machined notch across
the entire fatigue region. The central region failed by rupture which
resulted in the formation of equiaxed and elongated dimples (Figures 72
through 74). The fatigue region was extremely flat while the central
region was somewhat rough and contained shear lips on each side.
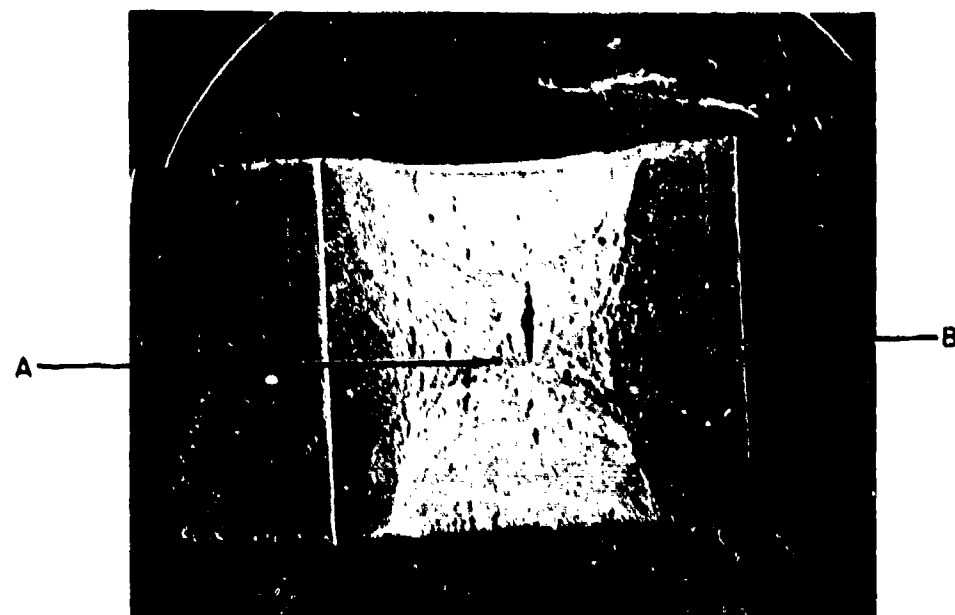
Figure 72.   Fracture surface of an HY-130 fatigue specimen, 10x.
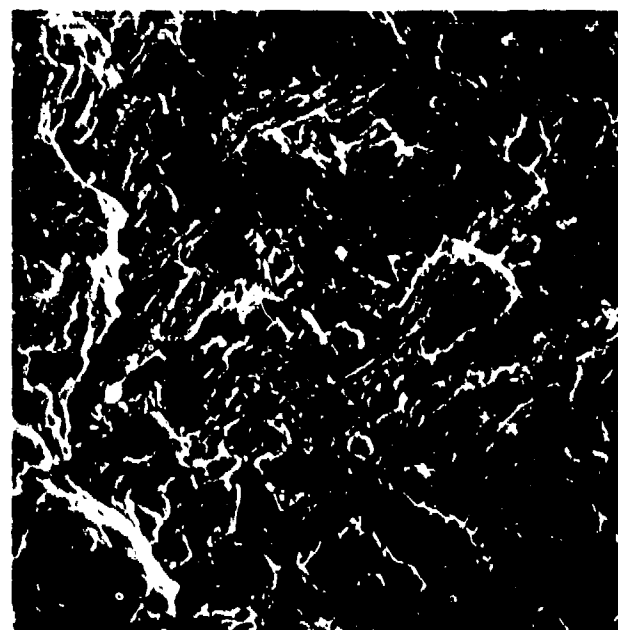
Figure 73.   Fatigue striations on fracture surface of HY-130
steel, 1450x.
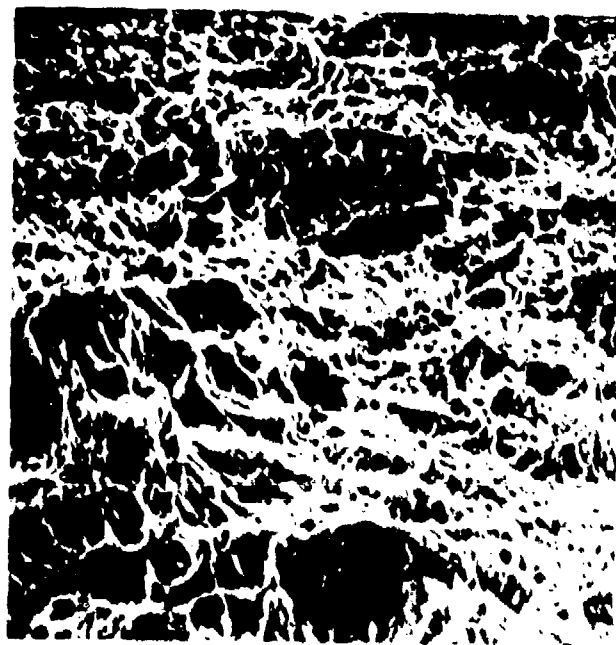
Figure 74.   Tensile overload zone in an HY-130 fatigue
specimen, 1500x.

Material: HY-130 Plate

Heat Treatment: Quenched and tempered
Test Direction: Longitudinal (with grain)
Mode or Condition of Test: Hydrogen-embrittled fatigue
Test Temperature: Ambient
Test Environment: Air
Hydrogen Charging Conditions:

  Current Density: 6 mA/in.^{2} (0.93 mA/cm^2)

  Charge Time: 12 hours

  Electrolyte: 0.3 wt% As_2O_3

                10.0 wt% H_2SO_4

Test Results:

  Mechanical Properties:

            Maximum Stress
            134,000 psi (924.6 MPa)

            Minimum Stress
            18,000 psi (124.2 MPa)

            Test Frequency
            10 cycles/sec

            Cycles to Failure
                4410

  Fractographic Analysis:

    The fatigue region contained parabolic contours similar to those
present on the hydrogen-embrittled ASTM A-514 sample. The fatigue stri-
ations had multiple orientations and were usually associated with sec-
ondary cracking. The central region consisted of dimple rupture and mi-
crovoid coalescence (Figures 75 through 79). The fatigue region was
fairly rough and not well delineated from the tensile overload region.
The central region was fibrous in appearance and the outer edges con-
tained shear lips.

107
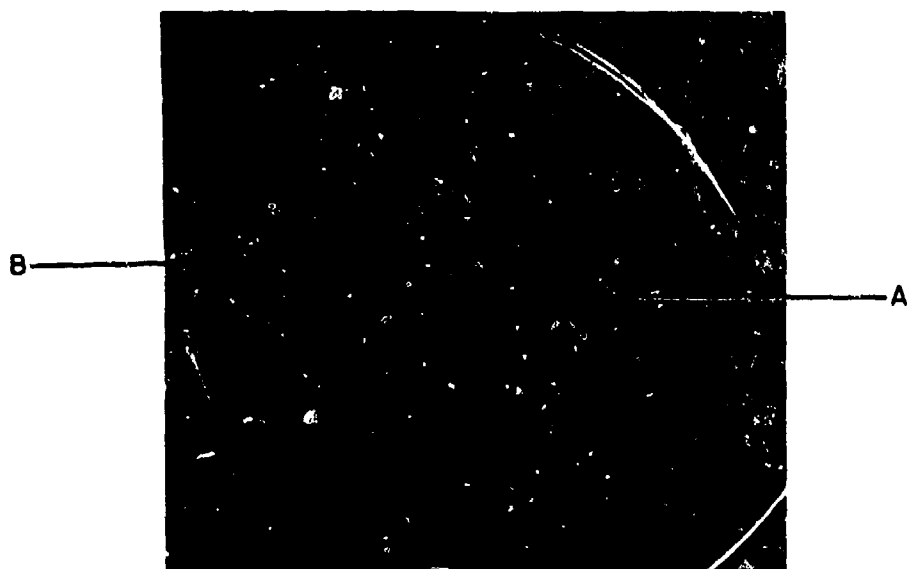
Figure 75. Fracture surface of a hydrogen-embrittled HY-130 fatigue specimen, 10x.
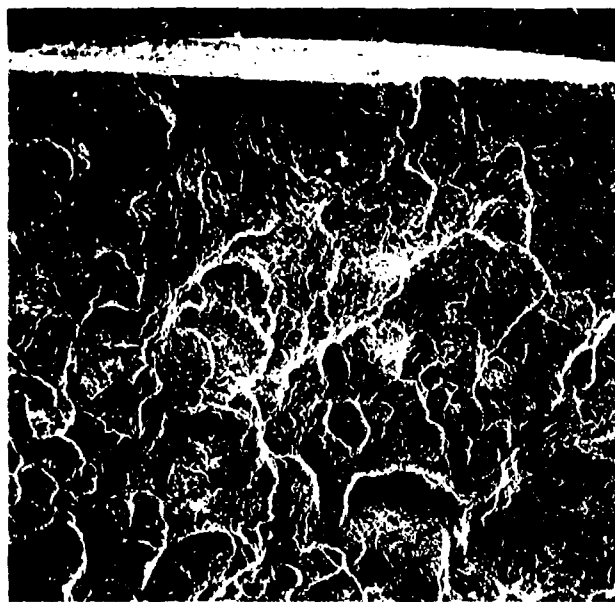
Figure 76. Fatigue region of a hydrogen-embrittled HY-130 fatigue specimen, 40x.
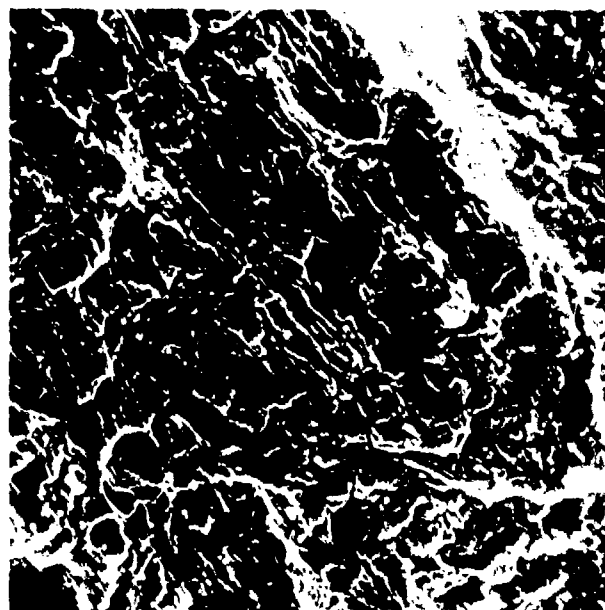
Figure 77. Fatigue striations on fracture surface of hydrogen-embrittled HY-130 steel, 1600x.
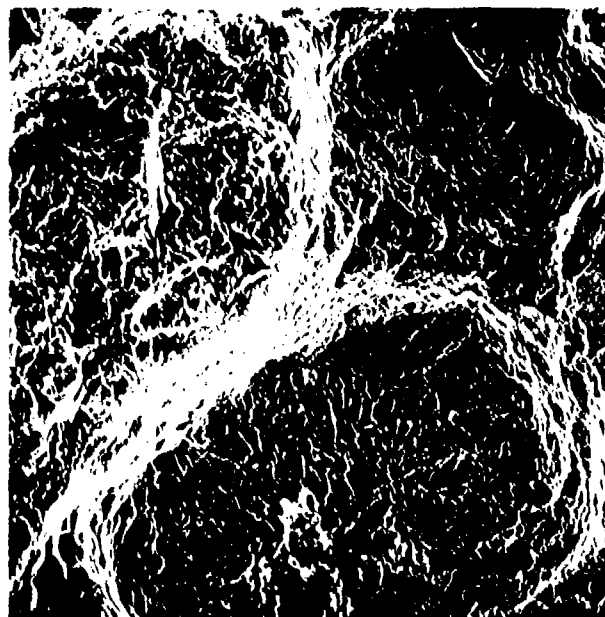
Figure 78. A stereomicrograph of the fatigue zone in hydrogen-embrittled HY-130 steel, 400x.

109
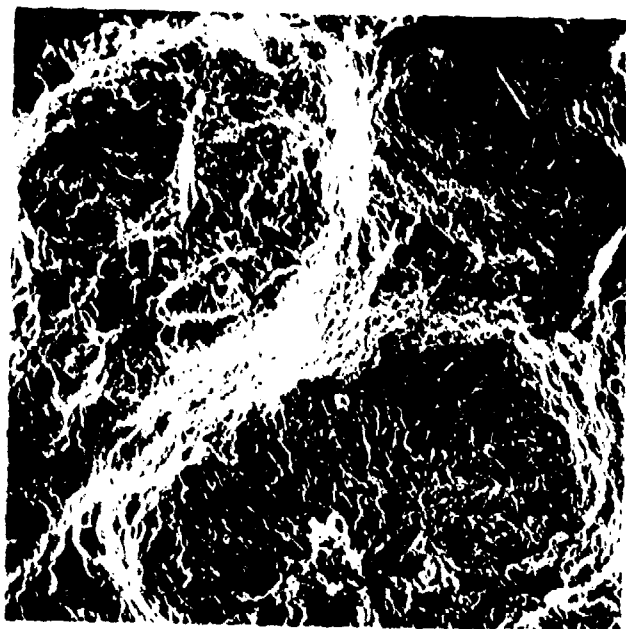
Figure 78. (con't).
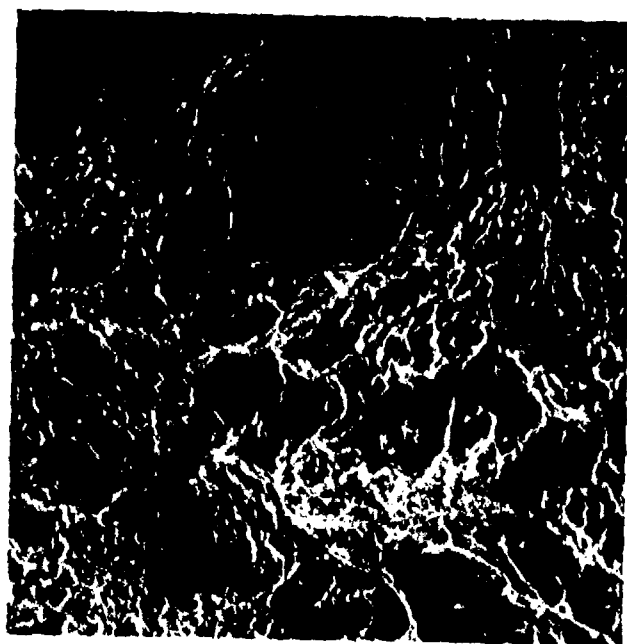
Figure 79. Tensile overload region in hydrogen-embrittled
HY-130 steel, 1500x.

Material: HY-130 Plate

Heat Treatment: Temper embrittled
Test Direction: Longitudinal (with grain)
Mode or Condition of Test: Fatigue
Test Temperature: Ambient
Test Environment: Air
Temper Embrittlement Heat Treatment:
    Temper 1 hour at 593°
    Furnace cool to 515°C and temper for 16 hours
    Furnace cool to 502°C and temper for 24 hours
    Furnace cool to 468°C and temper for 96 hours
    Furnace cool to 452°C and temper for 144 hours
    Furnace cool to 441°C and temper for 168 hours
    Furnace cool to 344°C
    Air cool to room temperature

Test Results:

   Mechanical Properties:

           Maximum Stress
           134,000 psi (924.6 MPa)

           Minimum Stress
           18,000 psi (124.2 MPa)

           Test Frequency
           10 cycles/sec

           Cycles to Failure
                 9745

   Fractographic Analysis:

       Crack propagation in the fatigue region occurred or relatively few
   levels, with the fatigue striations remaining parallel to the notch. In
   the central region, failure occurred by slip, tearing, and void
   coalescence. A region of intergranular fracture was observed between
   the fatigue zone and tensile overload region (Figures 80 through 85).
   The fatigue regions were extremely flat while the tensile overload
   region exhibited extensive lamellar tearing. The large tear in the
   sample extended over 1/4 in. (6.3 mm) below the fracture surface.

111
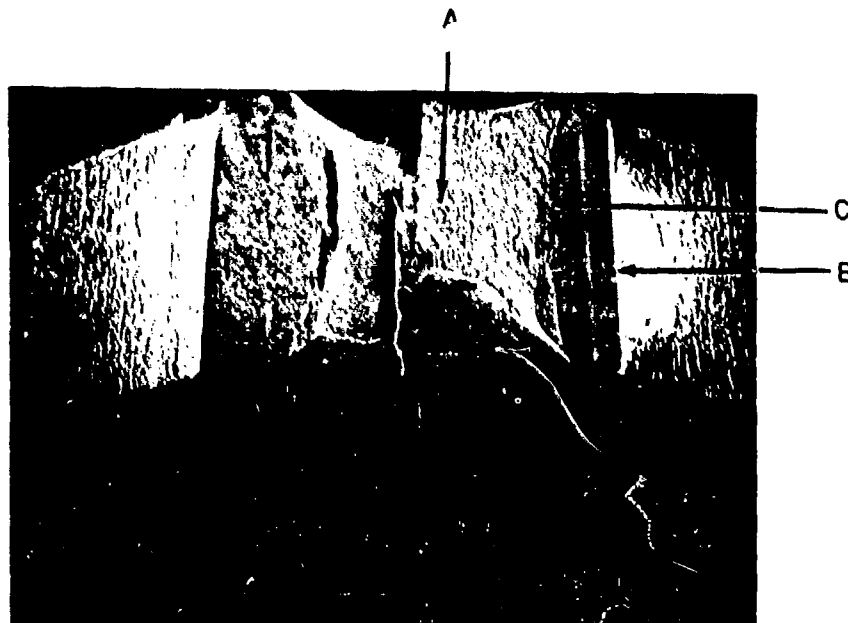
Figure 80.   Fracture surface of a temper-embrittled HY-130 fatigue
specimen, 8x.

Figure 81.   Fatigue region of a temper-embrittled HY-130 fatigue
specimen, 60x.

112

Figure 82. Fatigue striations on fracture surface of temper-
embrittled HY-130 steel, 1600x.
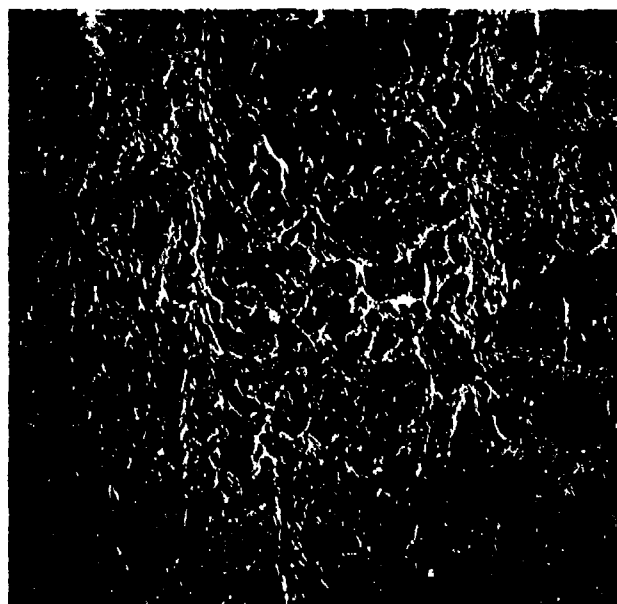
Figure 83. Bond of intergranular fracture between the fatigue
and tensile overload zones, 160x.

113

Figure 84.   Intergranular fracture in temper-embrittled HY-130 steel, 1600x.
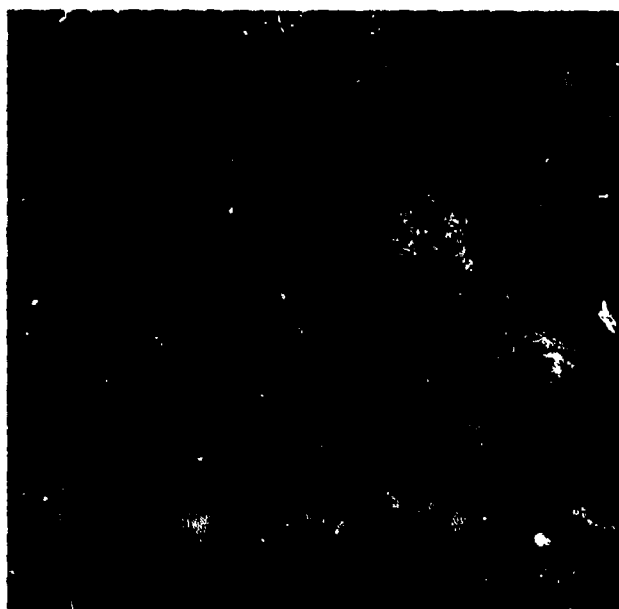
Figure 85.   Intergranular fracture and microvoid coalescence in temper-
embrittled HY-130 steel, 800x.

114

Material: HY-130 Plate

Heat Treatment: Quenched and tempered
Test Direction: Longitudinal (with grain)
Mode or Condition of Test: Charpy Impact
Test Temperature: -196^{0}
Test Environment: Air
Test Results:

Mechanical Properties:

Fracture Energy
27 ft-lb (36.7 joule)

Fractographic Analysis:

Failure occurred entirely by cleavage (Figures 86 and 87). The surface was relatively flat and contained ridges emanating from the initiation point of failure (i.e., the notch).
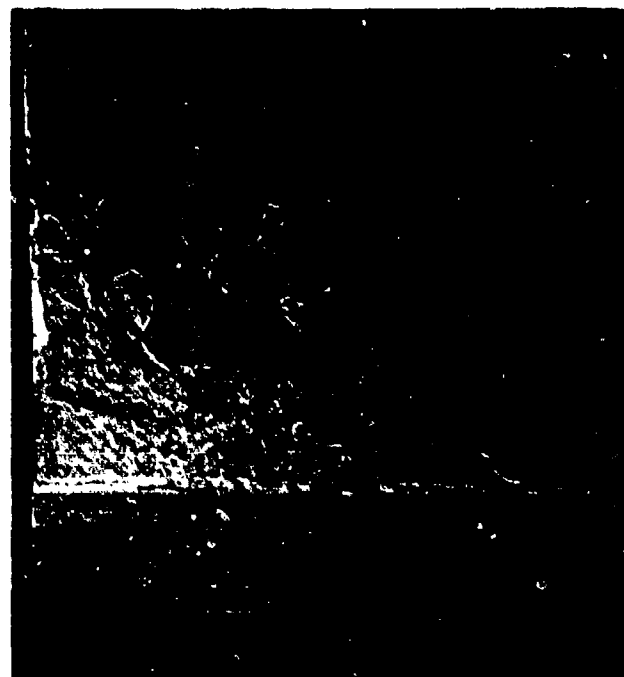
Figure 86.   Fracture surface of an HY-130 Charpy specimen tested at -196°C, 8x.
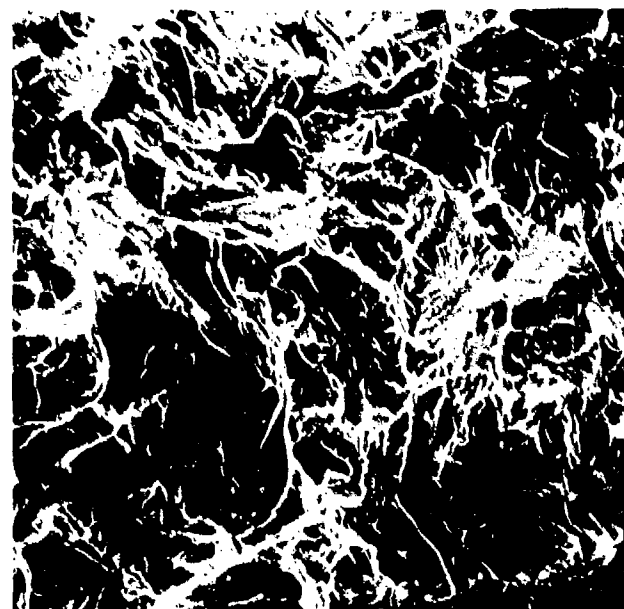
Figure 87.   Cleavage fracture in an HY-130 Charpy specimen tested at -196°C, 1600x.

Material: HY-130 Plate

Heat Treatment: Quenched and tempered
Test Direction: Longitudinal (with grain)
Mode or Condition of Test: Charpy impact
Test Temperature: -83°C
Test Environment: Air
Test Results:

Mechanical Properties:

Fracture Energy
75 ft-lb (102 joule)

Fractographic Analysis:

Failure occurred by cleavage in the central region and dimple rupture on the outside edges (Figures 88 through 90). The surface was relatively flat and contained shear lips on the outside edges.
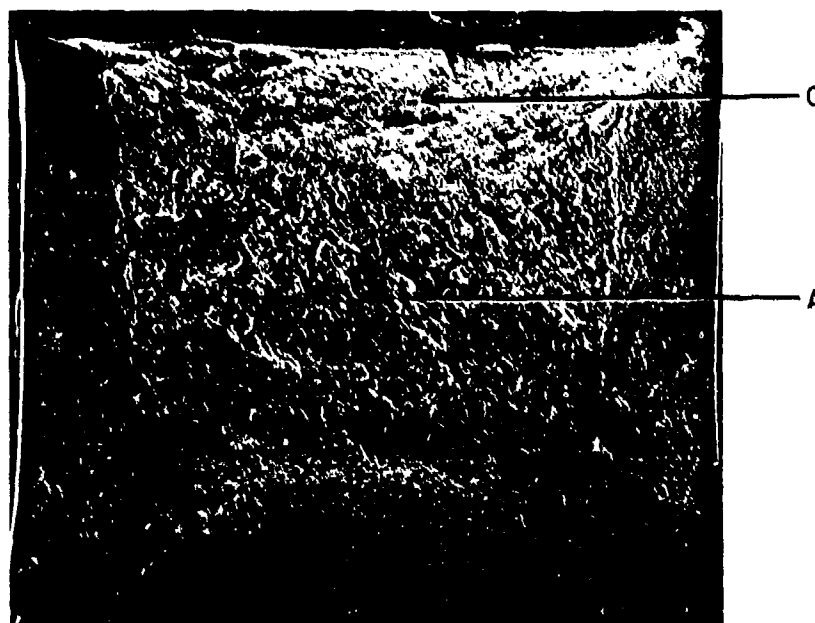
Figure 88. Fracture surface of an HY-130 Charpy specimen tested at -83ºC, 10x.

117
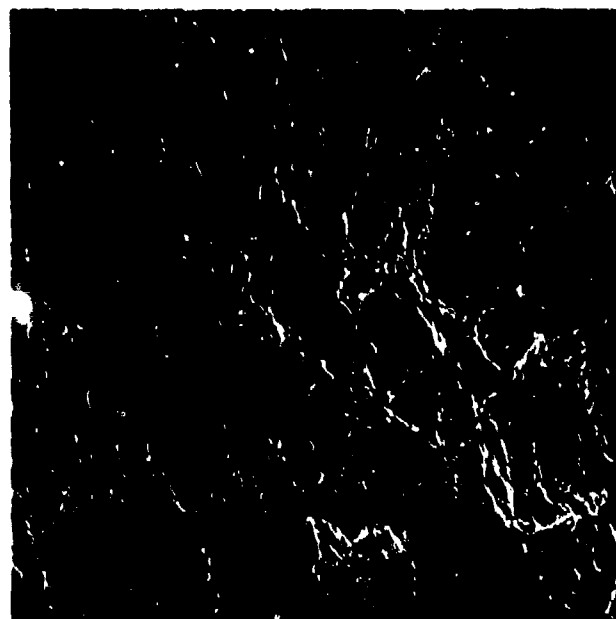
Figure 89. Edge region of an HY-130 Charpy specimen tested at -83°C, 650x.
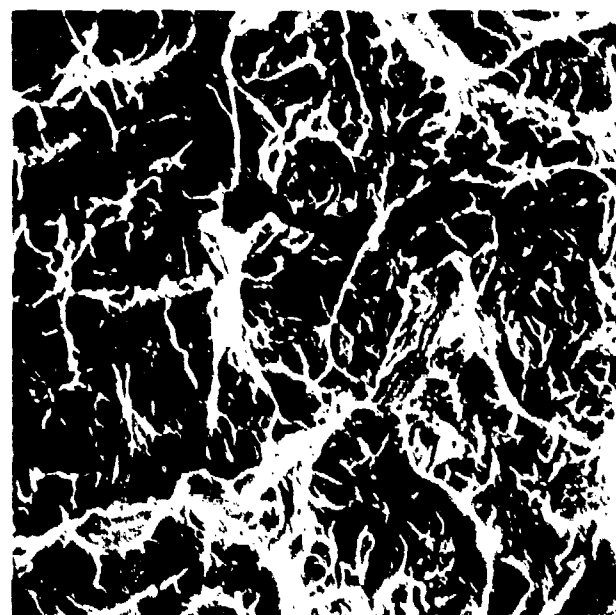
Figure 90. Central region of an HY-130 Charpy specimen tested at -83°C, 1600x.

118

Material: HY-130 Plate

Heat Treatment: Quenched and tempered
Test Direction: Longitudinal (with grain)
Mode or Condition of Test: Charpy impact
Test Temperature: -18^0
Test Environment: Air
Test Results:

Mechanical Properties:

Fracture Energy
100 ft-lb (136 joule)

Fractographic Analysis:

Failure occurred entirely by dimple rupture and microvoid
coalescence (Figures 91 and 92). The surface was relatively flat and
contained shear lips on the outside edges.
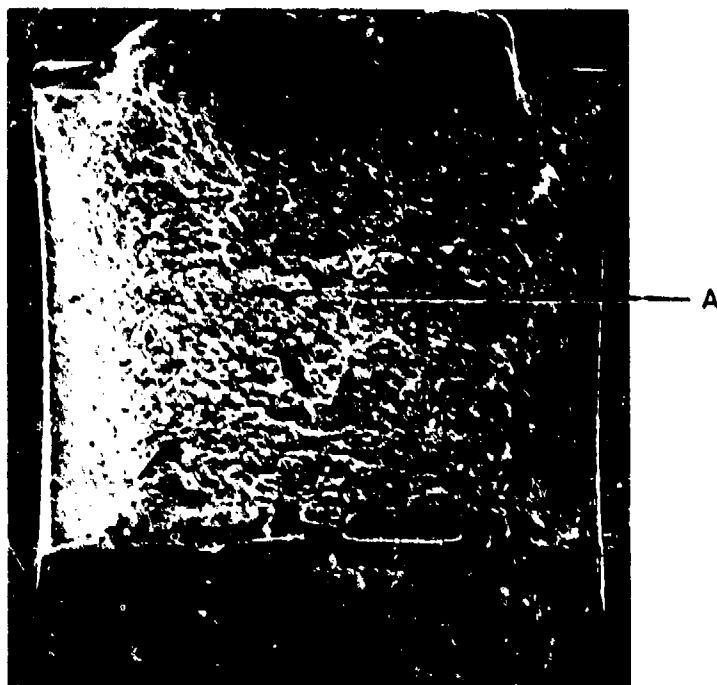
Figure 91. Fracture surface of an HY-130 Charpy specimen tested at -18°C, 8x.
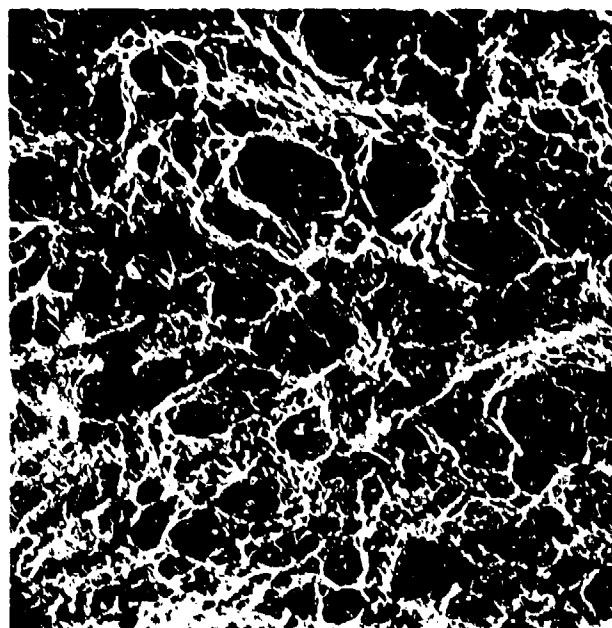
Figure 92. Failure of an HY-130 Charpy specimen tested at -18°C by dimple rupture, 1600x.

Material: HY-130 Plate

Heat Treatment: Quenched and tempered
Test Direction: Longitudinal (with grain)
Mode or Condition of Test: Charpy impact
Test Temperature: Ambient
Test Environment: Air
Test Results:

Mechanical Properties:

Fracture Energy
114 ft-lb (155 joule)

Fractographic Analysis:

Failure occurred entirely by dimple rupture and microvoid
coalescence (Figures 93 and 94). The surface was relatively flat and
contained shear lips on the outside edges.

121
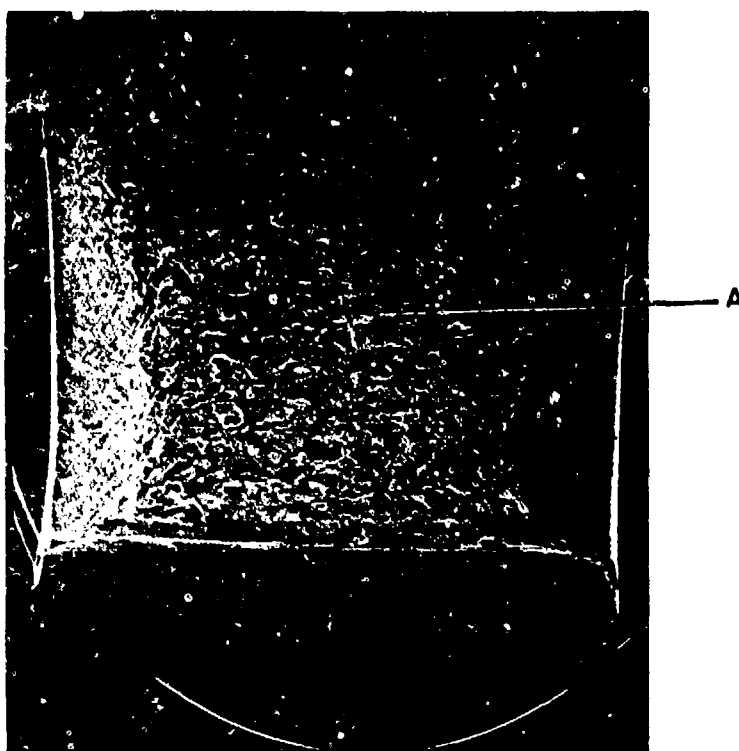
Figure 93. Fracture surface of an HY-130 Charpy specimen tested at room temperature, 8x.
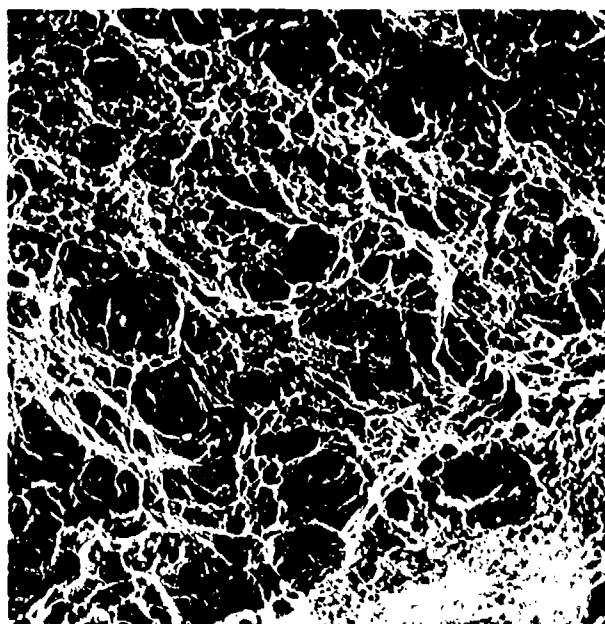
Figure 94. Failure of an HY-130 Charpy specimen tested at room temperature by dimple rupture, 1600x.

AX-110 WELD METAL

Material: AIRCO AX 110 Weld Metal

Process: GMA
Heat Treatment: As welded
Mode or Condition of Test: Tensile
Test Temperature: Ambient
Test Environment: Air
Test Results:

Mechanical Properties:

Ultimate Fracture Stress
136,000 psi (938.4 MPa)

Fractographic Analysis:

Failure was entirely by dimple rupture and microvoid coalescence (Figures 95 and 96). Considerable necking of the specimen was evident and resulted in shear lips present on the outside edges. The central region was somewhat flat and had a fibrous appearance.
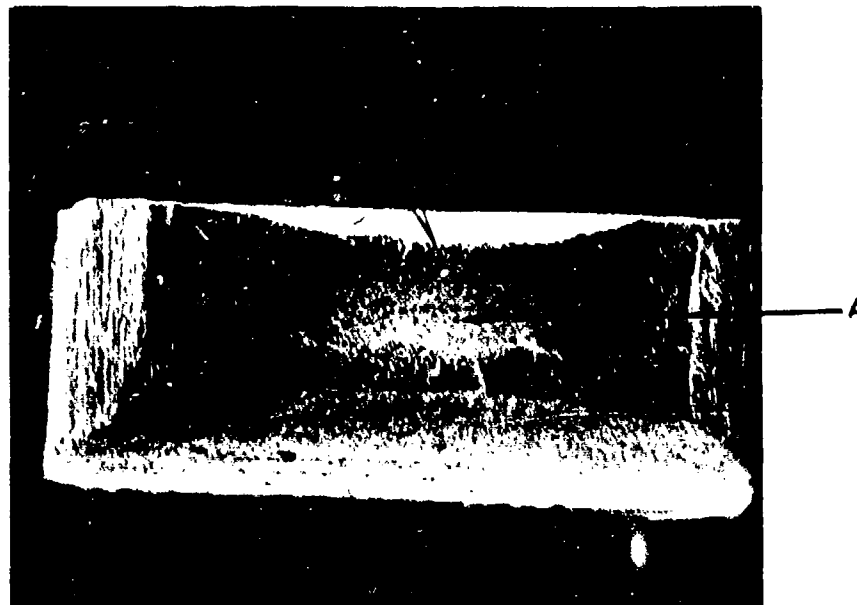
Figure 95.   Tensile fracture surface of an A-514 weld specimen, 25x.
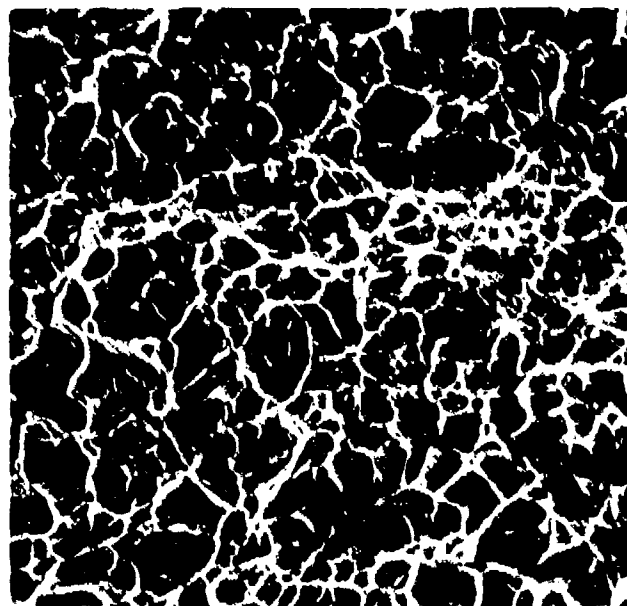
Figure 96.   Tensile failure of an A-514 weld material by dimple rupture, 4000x.

Material: AIRCO AX 110 Weld Metal

Process: GMA
Heat Treatment: As welded
Mode or Condition of Test: Hydrogen-embrittled tensile
Test Temperature: Ambient
Test Environment: Air
Hydrogen Charging Conditions:

  Current Density: 6 mA/in.^{2} (0.93 mA/cm^2)

  Charge Time: 12 hours

  Electrolyte: 0.3 wt% As_2O_3

              10.0 wt% H_2SO_4

Test Results:

    Mechanical Properties:

        Ultimate Fracture Stress
        108,000 psi (745 MPa)

    Fractographic Analysis:

    In one area of the surface, small "fisheyes" were present, which
consisted of small cleavage facets. The remainder of the surface dis-
played microvoids and dimples (Figures 97 through 100). The fracture
surface was angled about 45 degrees characteristic of a slant fracture.
Very little necking was evident.
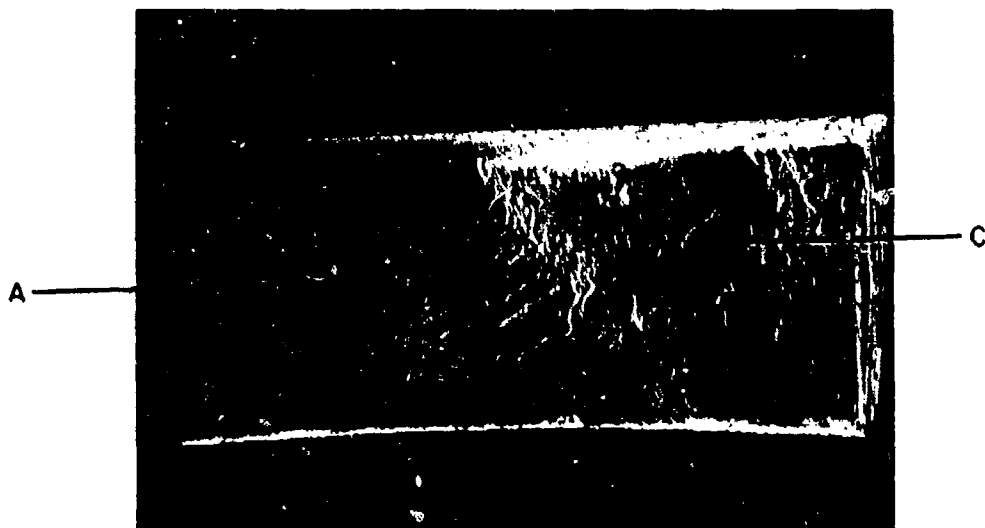
Figure 97. Tensile fracture surface of a hydrogen-embrittled A-514 weld specimen, 25x.
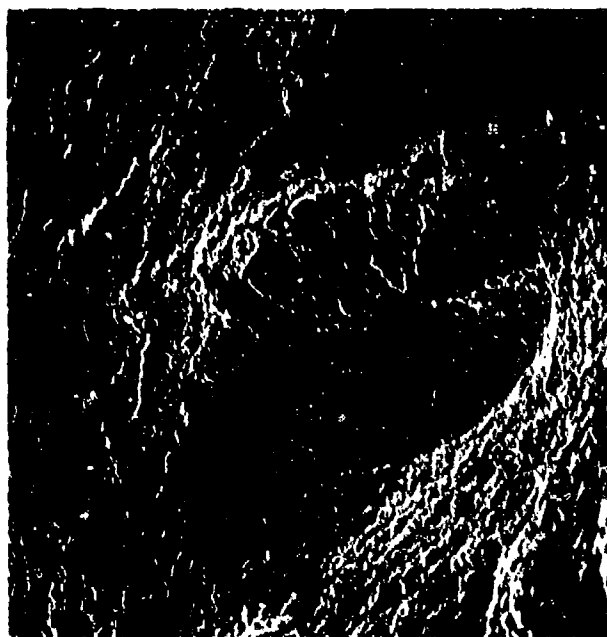
Figure 98. "Fisheye" on the fracture surface of a hydrogen-embrittled A-514 weld specimen, 25x.
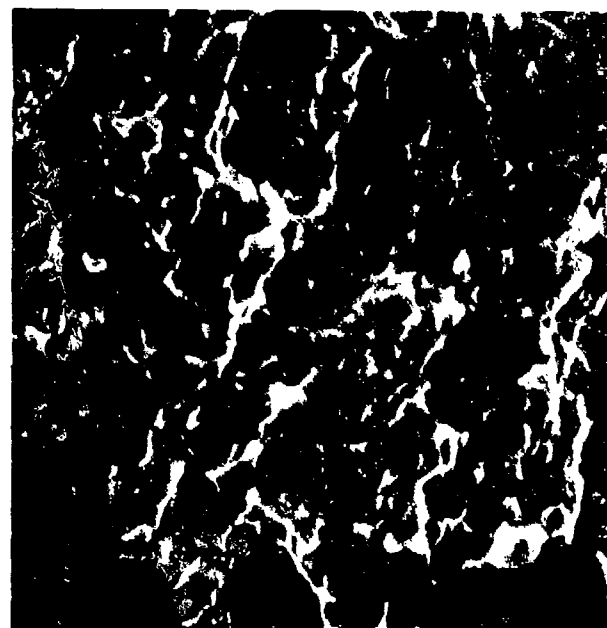
Figure 99. Small cleavage facets located in a "fisheye," 4000x.
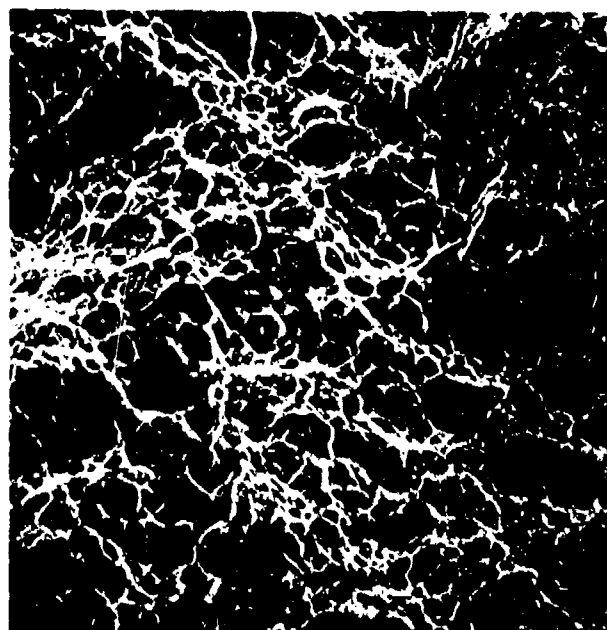
Figure 100. Fracture surface of hydrogen-embrittled Λ-514 weld specimen away from "fisheye," 1500x.

Material: AIRCO AX 110 Weld Metal

Process: GMA
Heat Treatment: Temper embrittled
Mode or Condition of Test: Tensile
Test Temperature: Ambient
Test Environment: Air
Temper Embrittlement Heat Treatment:
   Temper 1 hour at 593°C
   Furnace cool to 538°C and temper for 15 hours
   Furnace cool to 524°C and temper for 24 hours
   Furnace cool to 496°C and temper for 48 hours
   Furnace cool to 468°C and temper for 72 hours
   Furnace cool to 315°C
   Air cool to room temperature

Test Results:

   Mechanical Properties:

      Ultimate Fracture Stress
      117,000 psi (807.3 MPa)

   Fractographic Analysis:

   Failure occurred entirely by dimple rupture and microvoid
coalescence (Figures 101 and 102). The sample displayed considerable
necking with shear lips evident on all sides. The central region was
somewhat flat and had a fibrous appearance.
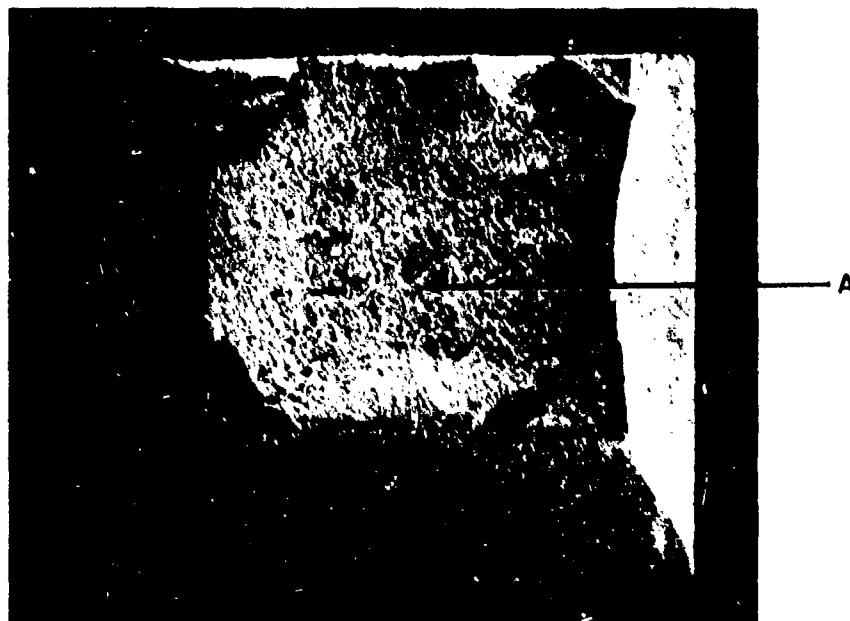
Figure 101.   Tensile fracture surface of a temper-embrittled A-514 weld specimen, 15x.
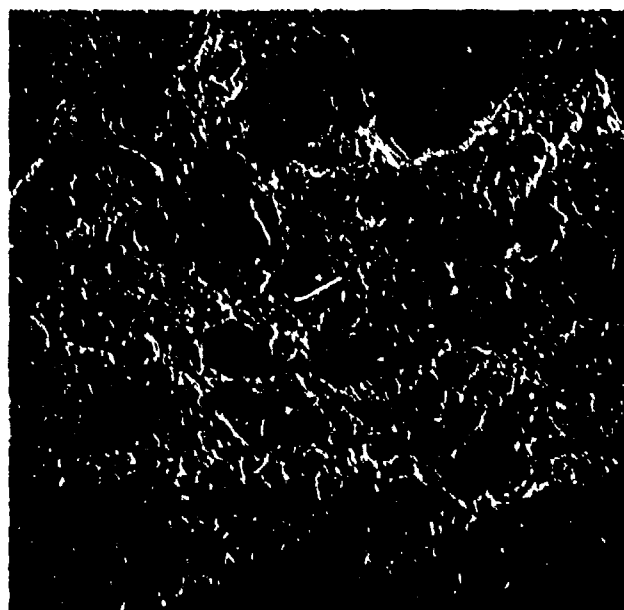
Figure 102.   Tensile failure of a temper-embrittled A-514 weld specimen by dimple rupture, 750x.

Material: AIRCO AX 110 Weld Metal

Process: GMA
Heat Treatment: As welded
Mode or Condition of Test: Fatigue
Test Temperature: Ambient
Test Environment: Air
Test Results:

Mechanical Properties:

Maximum Stress
100,000 psi (690 MPa)

Minimum Stress
15,000 psi (103.5 MPa)

Test Frequency
10 cycles/second

Cycles to Failure
5510

Fractographic Analysis:

The fatigue region consisted of parallel microcracks rather than
striations. Failure in the central region was by dimple rupture and mi-
crovoid coalescence (Figures 103 through 105). The fatigue regions were
very flat while the tensile overload region in the center of the speci-
men was rougher and contained shear lips on the outside edges.
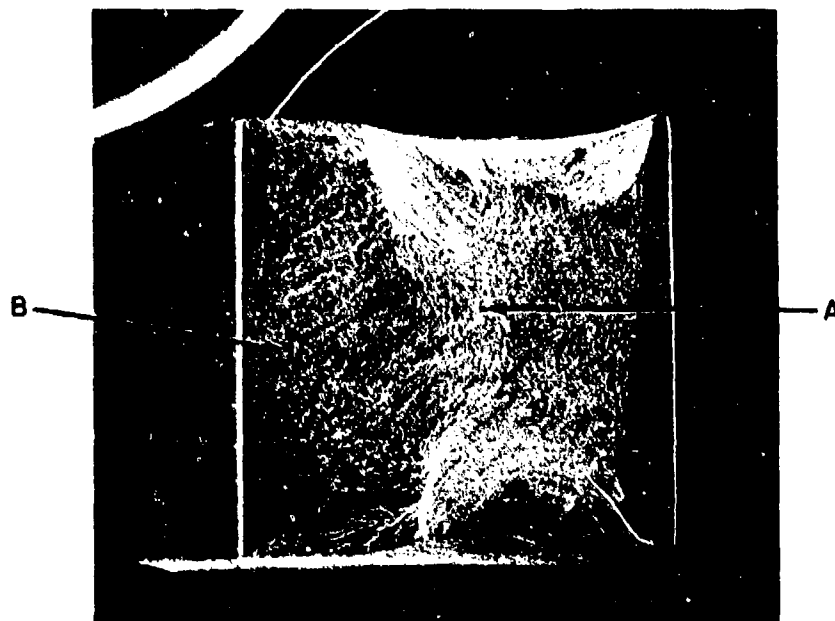
Figure 103. Fatigue fracture surface of an A-514 weld specimen, 11x.
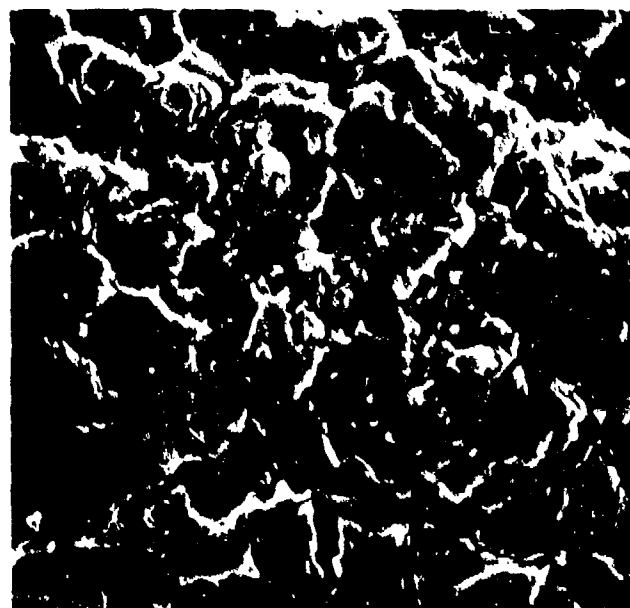
Figure 104. Fatigue striations on fracture surface of A-514 weld material, 4000x.
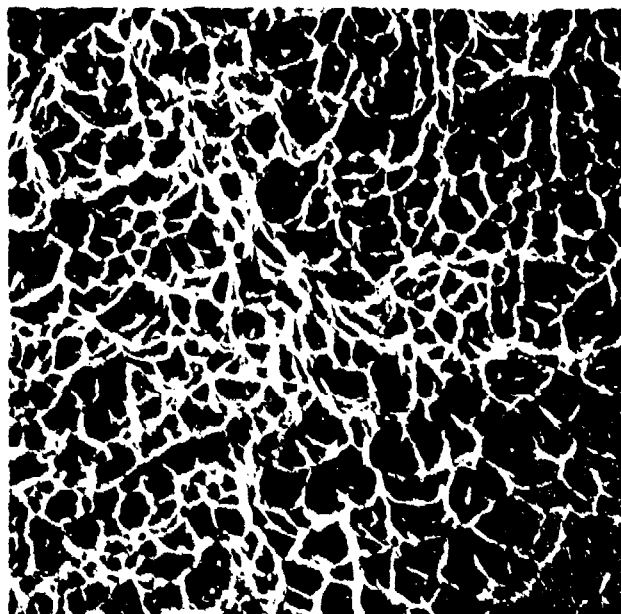
Figure 105. Tensile overload region of an A-514 weld fracture
surface, 1500x.

Material: AIRCO AX 110 Weld Metal

Process: GMA
Heat Treatment: As welded
Mode or Condition of Test: Hydrogen-embrittled fatigue
Test Temperature: Ambient
Test Environment: Air
Hydrogen Charging Conditions:

Current Density: 6 mA/in.^{2} (0.93 mA/cm^2)

Charge Time: 12 hours

Electrolyte: 0.3 wt% As_2O_3

10.0 wt% H_2SO_4

Test Results:

Mechanical Properties:

Maximum Stress
100,000 psi

Minimum Stress
15,000 psi

Test Frequency
10 cycles/sec

Cycles to Failure
4135

Fractographic Analysis:

The fatigue regions consisted of numerous craters, many of which contained microcracks. Fatigue striations were presnt on the fracture surface around the craters. Even in the central region where failure occurred by dimple rupture and microvoid coalescence, crater formation was evident (Figures 106 through 109). The fatigue region was very rough and coarse. The central region was fibrous in appearance and contained shear lips on the outside edges.
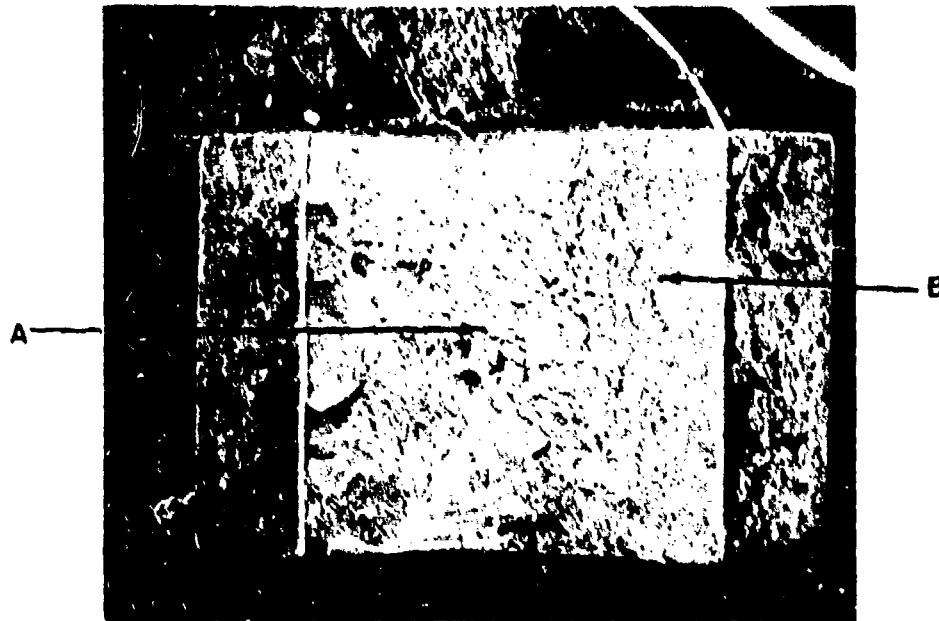
Figure 106.   Fatigue fracture surface of a hydrogen-embrittled A-514 weld specimen, 10x.
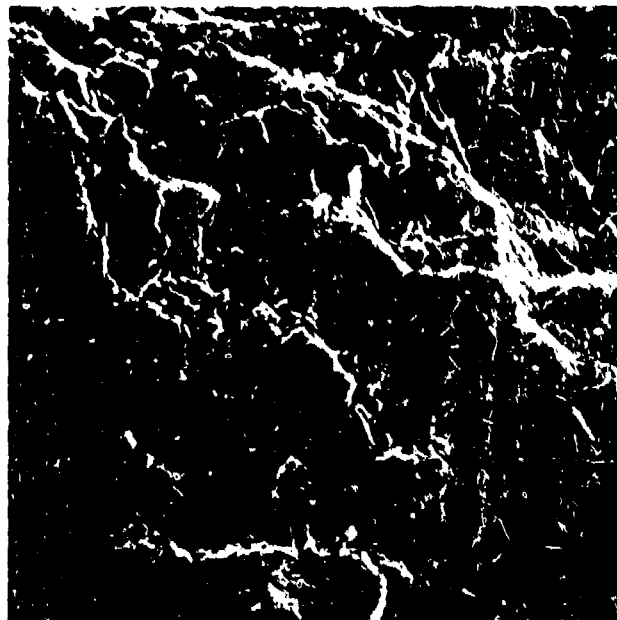
Figure 107.   Fatigue striations on surface of a hydrogen-embrittled A-514 weld fatigue specimen, 2000x.
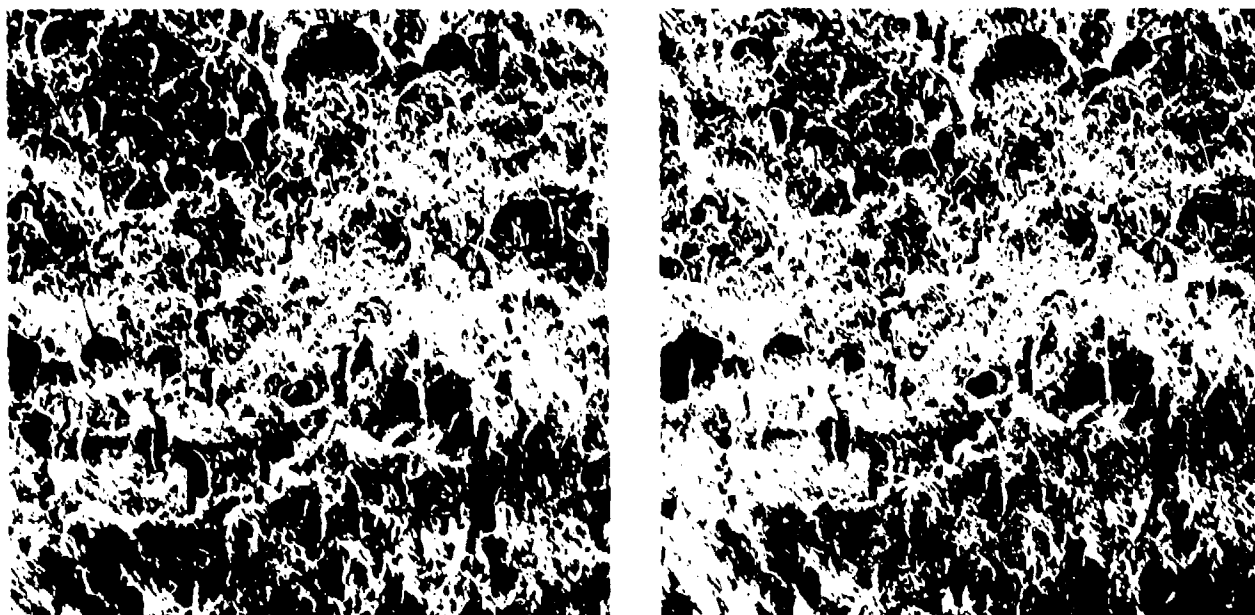
Figure 108.   A stereomicrograph of the fatigue region in a hydrogen-
embrittled A-514 weld specimen, 40x.

135
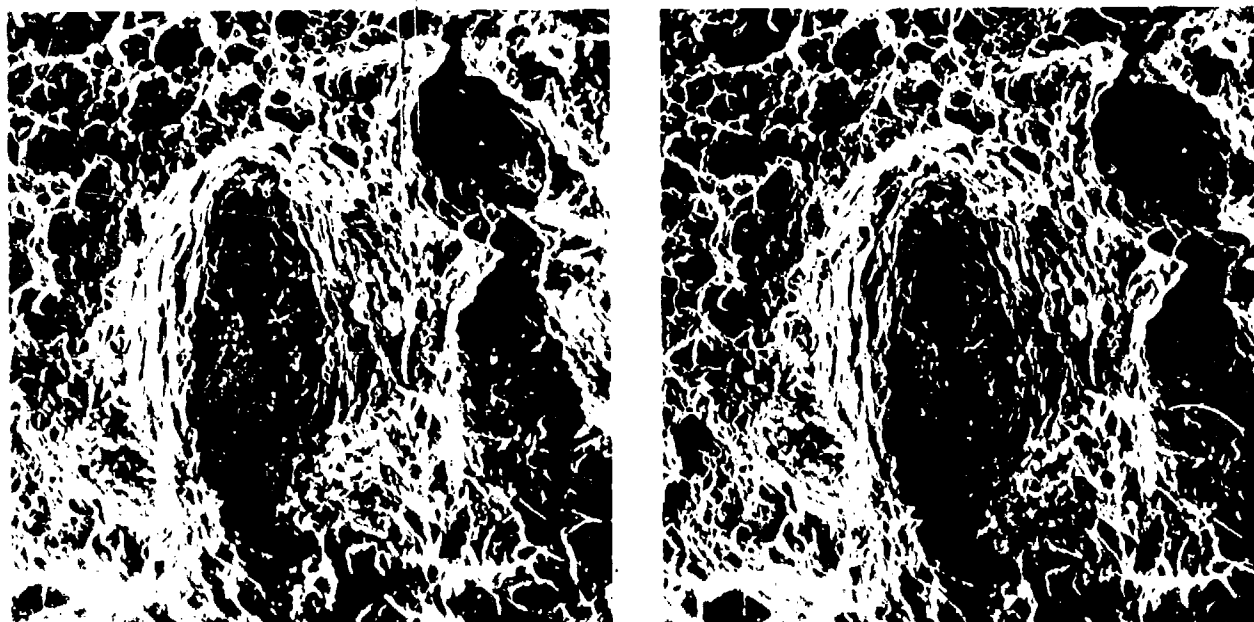
Figure 109. A stereomicrograph of the tensile overload region in a hydrogen-embrittled A-514 weld fatigue specimen, 1600x.

Material: AIRCO AX 110 Weld Metal

Process: GMA
Heat Treatment: Temper embrittled
Mode or Condition of Test: Fatigue
Test Temperature: Ambient
Test Environment: Air
Temper Embrittlement Heat Treatment:
   Temper 1 hour at $593^{\circ}C$
   Furnace cool to $538^{\circ}C$ and temper for 15 hours
   Furnace cool to $524^{\circ}C$ and temper for 24 hours
   Furnace cool to $496^{\circ}C$ and temper for 48 hours
   Furnace cool to $468^{\circ}C$ and temper for 72 hours
   Furnace cool to $315^{\circ}C$
   Air cool to room temperature

Test Results:

   Mechanical Properties:

         Maximum Stress
         100,000 psi (690 MPa)

         Minimum Stress
         15,000 psi (103.5 MPa)

         Test Frequency
         10 cycles/sec

         Cycles to Failure
               5110

   Fractographic Analysis:

      The fatigue region contained relatively few distinct fatigue pat-
   terns. The fatigue markings which were present consisted of small
   parallel striations. There was some evidence of lamellar tearing where
   the failure mode changed from fatigue to tensile overload. Failure in
   the central region was by dimple rupture and microvoid coalescence (Fig-
   ures 110 through 113). The fatigue regions were extremely flat while
   the tensile overload region was coarse and fibrous. Shear lips were not
   present in the central region.

137
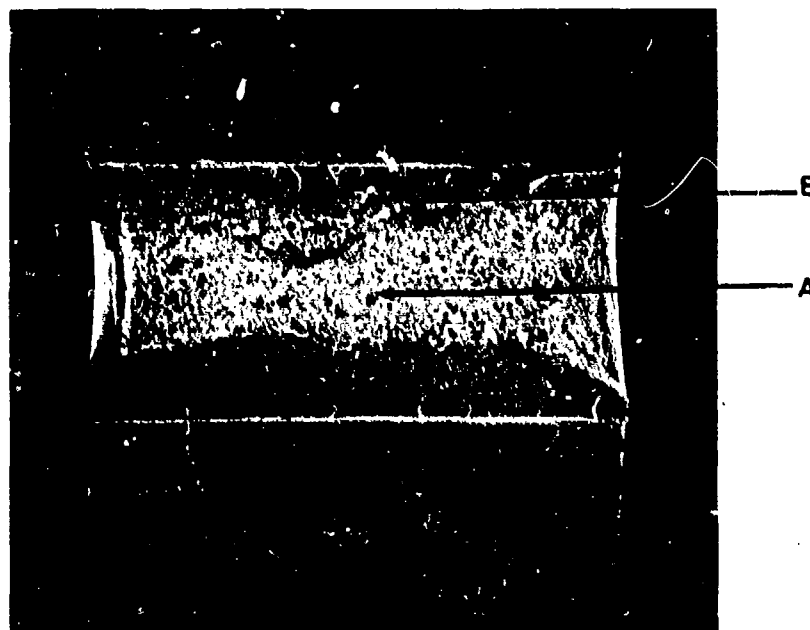
Figure 110. Fatigue fracture surface of a temper-embrittled A-514 weld specimen. 11x.
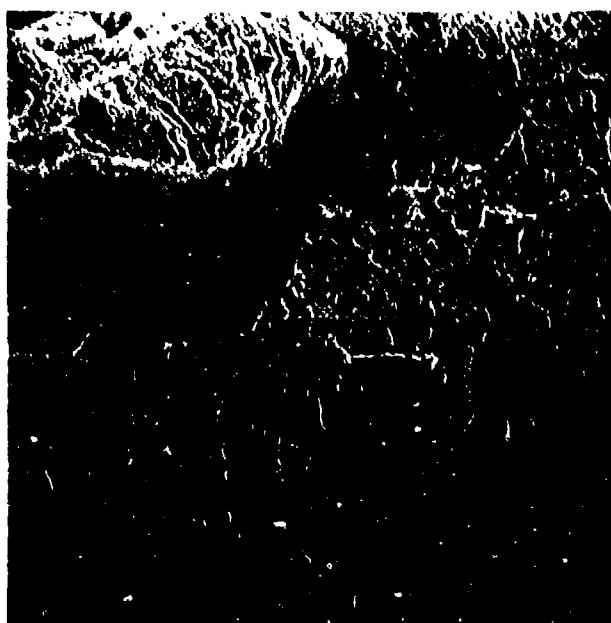
Figure 111. Lamellar tearing occurring in fatigue zone of a temper-embrittled A-514 weld specimen, 150x.

138
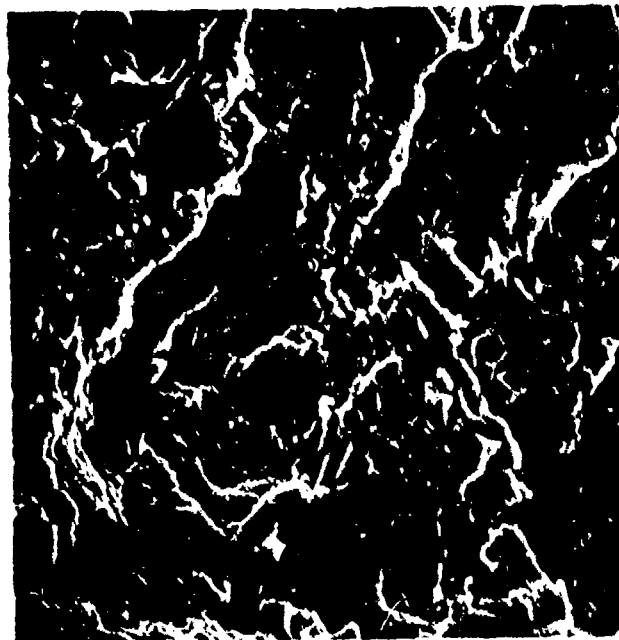
Figure 112. Fatigue markings on fracture surface of a temper-embrittled A-514 weld fatigue specimen, 1500x.
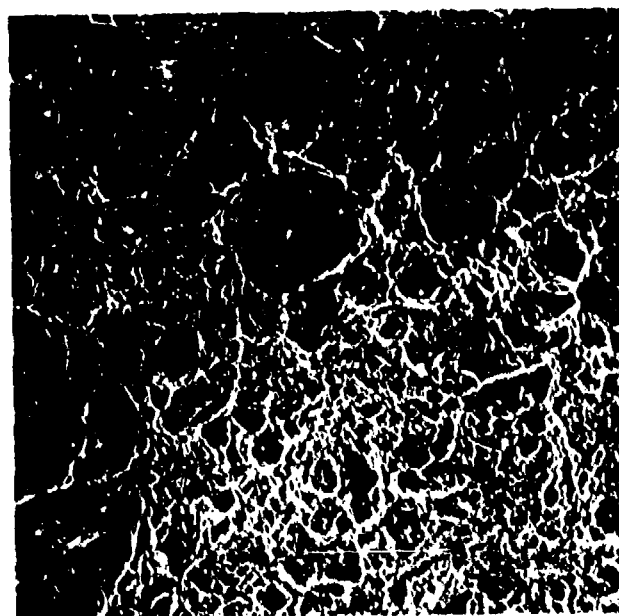
Figure 113. Tensile overload region in a temper-embrittled A-514 weld fatigue specimen, 750x.

Material: AIRCO AX 110 Weld Metal

Process: GMA
Heat Treatment: As welded
Mode or Condition of Test: Charpy impact
Test Temperature: -196°C
Test Environment: Air
Test Results:

Mechanical Properties:

Fracture Energy
18 ft-lb (24.5 joule)

Fractographic Analysis:

Failure occurred principally by cleavage, although small regions
which failed by microvoid coalescence were present (Figures 114 and
115). The fracture surface was completely flat. There were no shear
lips present.
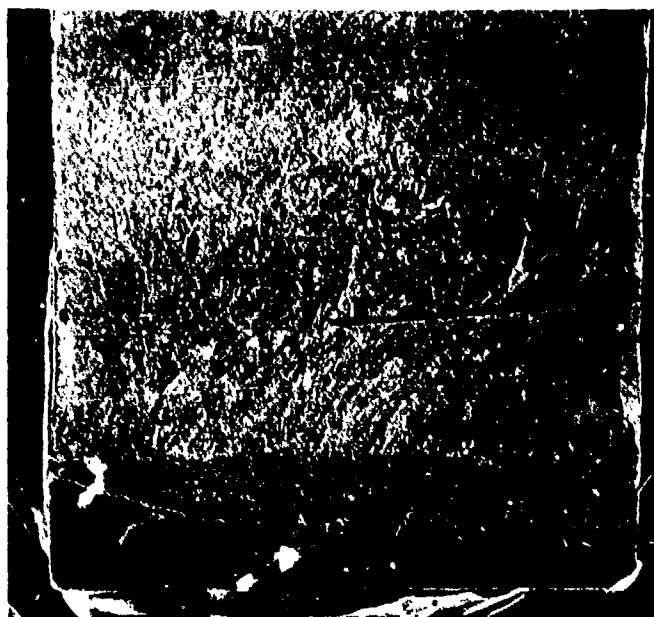
Figure 114. Fracture surface of an A-514 weld Charpy specimen tested at -196°C, 8x.

Figure 115. Failure of an A-514 weld Charpy specimen tested at -196°C by cleavage, 4000x.

Material: AIRCO AX 110 We'd Metal

Process: GMA
Heat Treatment: As welded
Mode or Condition of Test: Charpy impact
Test Temperature: -83°C
Test Environment: Air
Test Results:

Mechanical Properties:

Fracture Energy
46 ft-lb (62.6 Joule)

Fractographic Analysis:

The central region failed by cleavage while the outer areas failed
by dimple rupture (Figures 116 through 118). The central region was
fairly flat while the outside edges displayed prominent shear lips.

Figure 116. Fracture surface of an A-514 weld Charpy specimen
tested at -83°C, 8x.

142

Figure 117. Central region of an A-514 weld Charpy specimen tested at -83°C, 4000x.
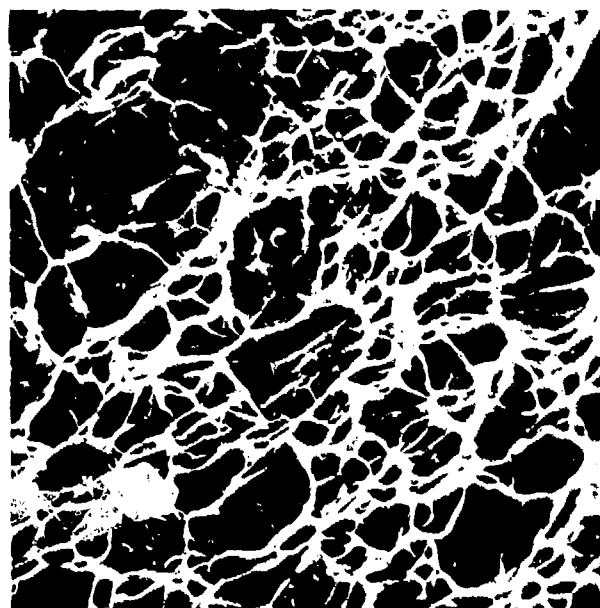
Figure 118. Edge region o   ı A-514 weld Charpy specimen tested at -83°C, 4000x.

143

Material: AIRCO AX 110 Weld Metal

Process: GMA
Heat Treatment: As welded
Mode or Condition of Test: Charpy impact
Test Temperature: -18°C
Test Environment: Air
Test Results:

Mechanical Properties:

Fracture Energy
77 ft-lb (104.7 joule)

Fractographic Analysis:

Failure was entirely by dimple rupture (Figures 119 and 120). Considerable plastic deformation was evident on the sides of the specimen where shear lips were present. The central region was irregular in contour and fibrous in appearance.
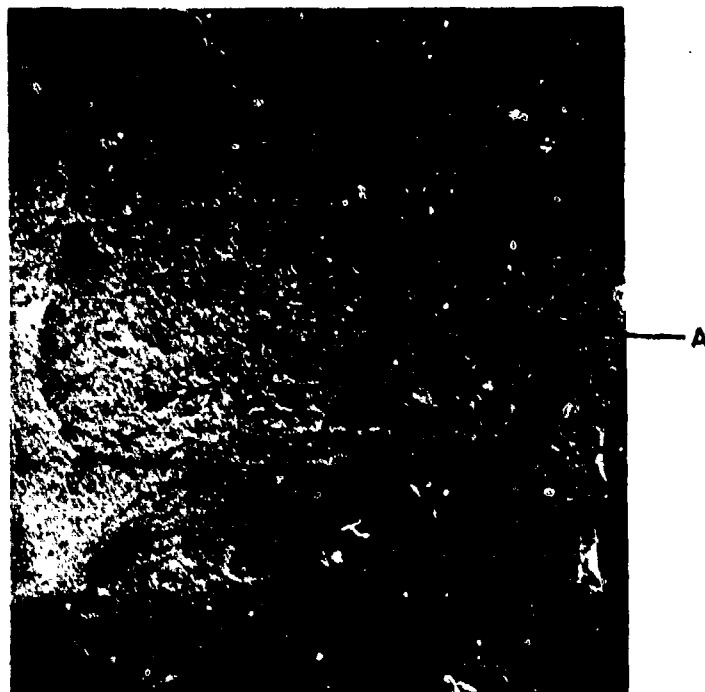
Figure 119. Fracture surface of an A-514 weld Charpy specimen tested at -18°C, 8x.
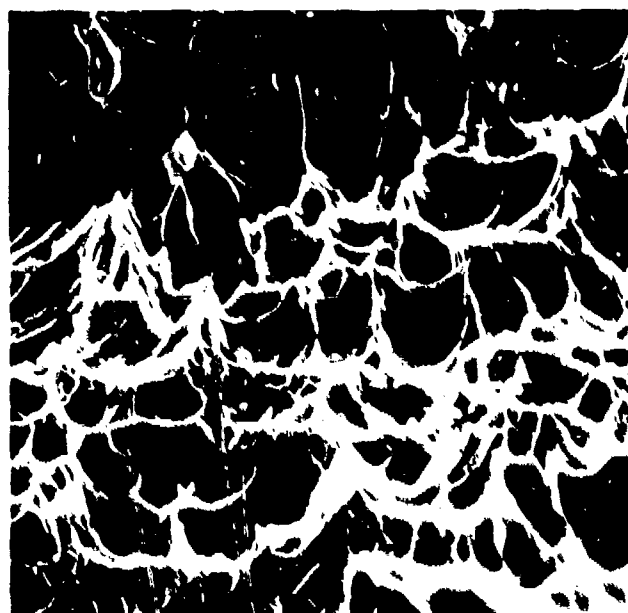
Figure 120. Fracture surface of an A-514 weld Charpy specimen tested at or above -18°C, 4250x.

Material: AIRCO AX 110 Weld Metal

Process: GMA
Heat Treatment: As welded
Mode or Condition of Test: Charpy impact
Test Temperature: Ambient
Test Environment: Air
Test Results:

Mechanical Properties:

Fracture Energy
86 ft-lb (117 joule)

Fractographic Analysis:

Failure was entirely by dimple rupture (Figures 121 and 122). The
central region was flat and fibrous in appearance while the outside
edges displayed massive shear lips.
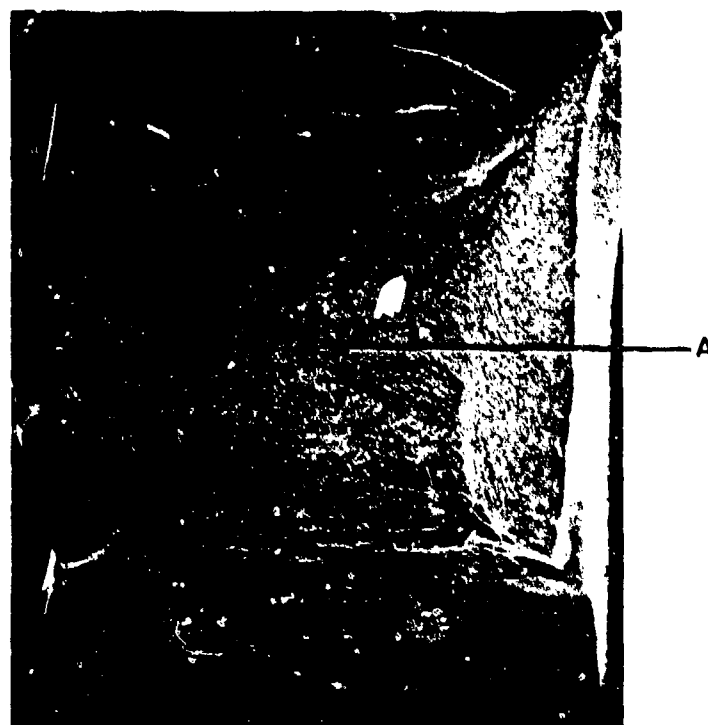
Figure 121. Fracture surface of an A-514 weld Charpy specimen tested at room temperature, 8x.
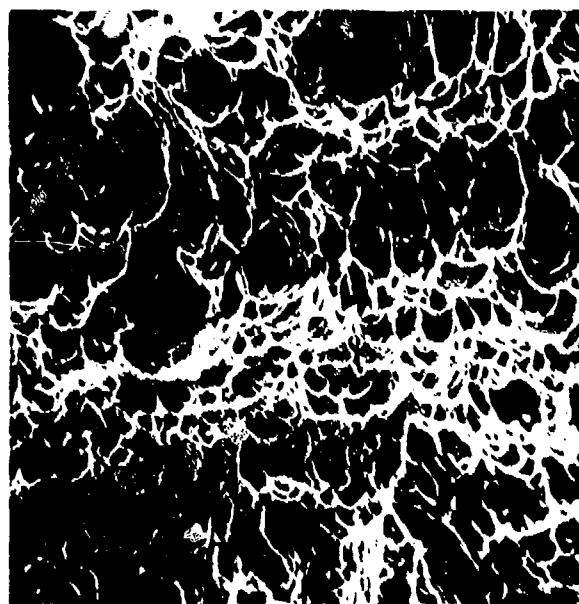
Figure 122. Edge region of A-514 weld Charpy specimen tested at room temperature, 1700x.

147

ASTM A-514 (AX 110) WITH DEFECT

Material: ASTM A-514, Grade F (USS T-1)

Weld Metal: AIRCO AX 110
Process: GMA
Type of Defect: Porosity
Heat Treatment: As welded
Test Direction: Transverse to weld
Mode or Condition of Test: Tensile
Test Temperature: Ambient
Test Environment: Air
Specimen Location and Configuration: (See Figure 123).

SPECIMEN LOCATION
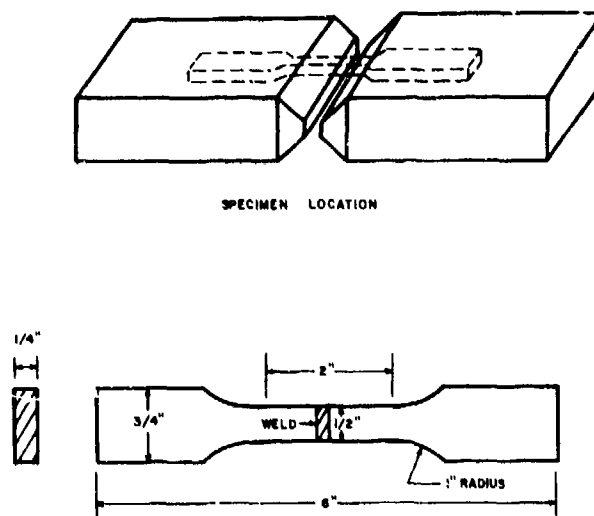
Figure 123. Specimen geometry for tensile, fatigue, and Charpy impact
tests of welded ASTM A-514 steel.

Test Results:

Mechanical Properties:

Ultimate Fracture Stress
68,800 psi (474.7 MPa)

Fractographic Analysis:

Failure occurred by dimple rupture. A structure resembling an oxide scale was evident in some areas within the porosity regions (Figures 124 through 126). A large number of very deep, jagged, dark blue porosity bubbles were revealed during the examination of the fracture surface under an optical microscope. Regions not containing porosity exhibited a dull, fibrous fracture appearance. Small striations were present on the surfaces of the pores. A high magnification of the striations revealed that they were actively dendrites.
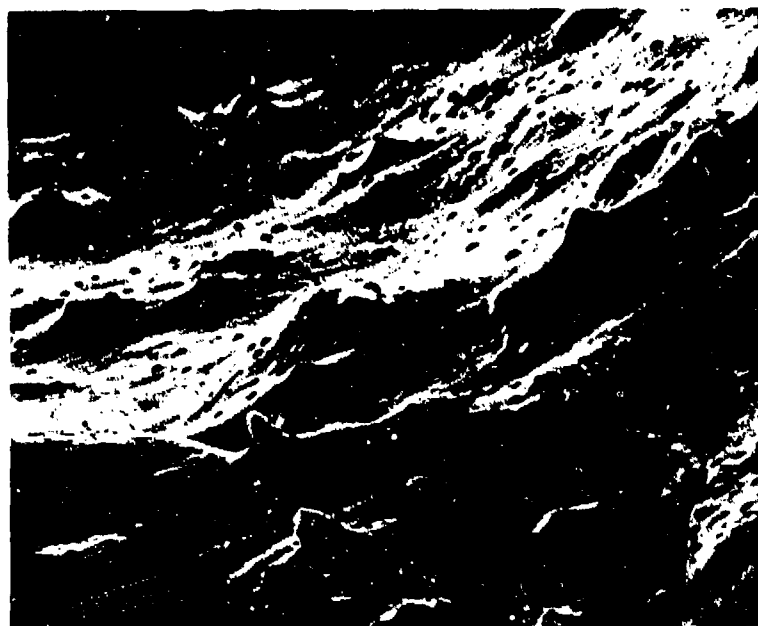
Figure 124.   Interior surface of a pore, 2500x.
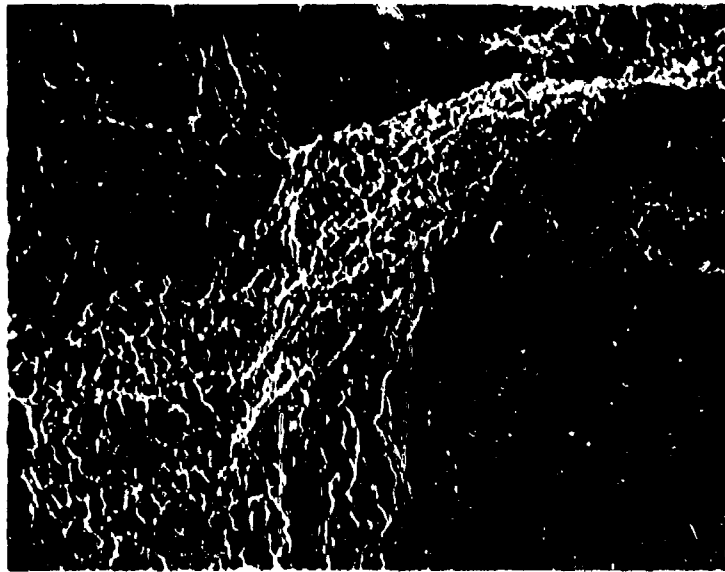
Figure 125. Fracture surface of a porosity defect, 650x.
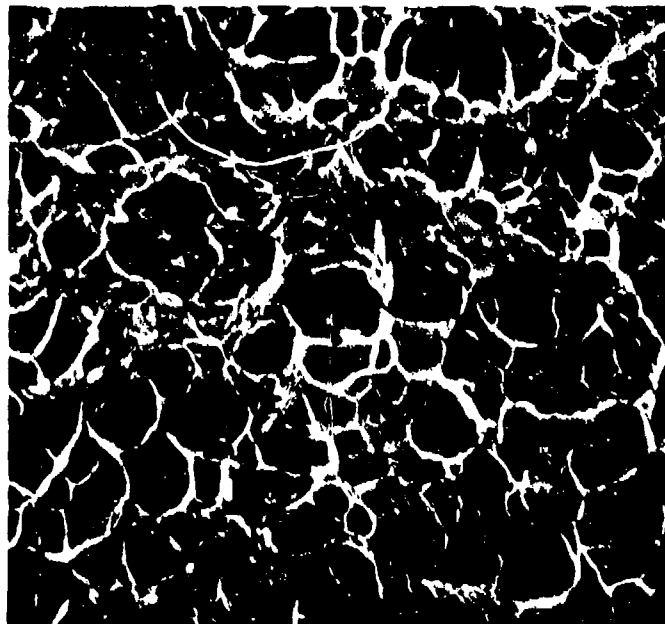
Figure 126. Fracture surface away from the porosity defects, 3500x.

Material: ASTM A-514, Grade F

Weld Metal: AIRCO AX 110
Process: GMA
Type of Defect: Lack of penetration
Heat Treatment: As welded
Test Direction: Transverse to weld
Mode or Condition of Test: Tensile
Test Temperature: Ambient
Test Environment: Air
Specimen Location and Configuration: See Figure 123.
Test Results:

Mechanical Properties:

Ultimate Fracture Stress
109,000 psi

Fractographic Analysis:

The fracture initiated from the LOP region in the center of the
specimen. As the crack propagated to the surface of the specimen, the
fracture mode changed from normal rupture exhibiting equiaxed dimples,
to shear rupture exhibiting elongated dimples (Figures 127 through 130).
The central region exhibited a rather dark, porous failure while the re-
mainder of the fracture surface consisted of a dull, fibrous fracture.
The LOP region is located in the center of the specimen where vertical
machine markings are clearly evident. A shear wall was on one of the
specimen's outside edges.
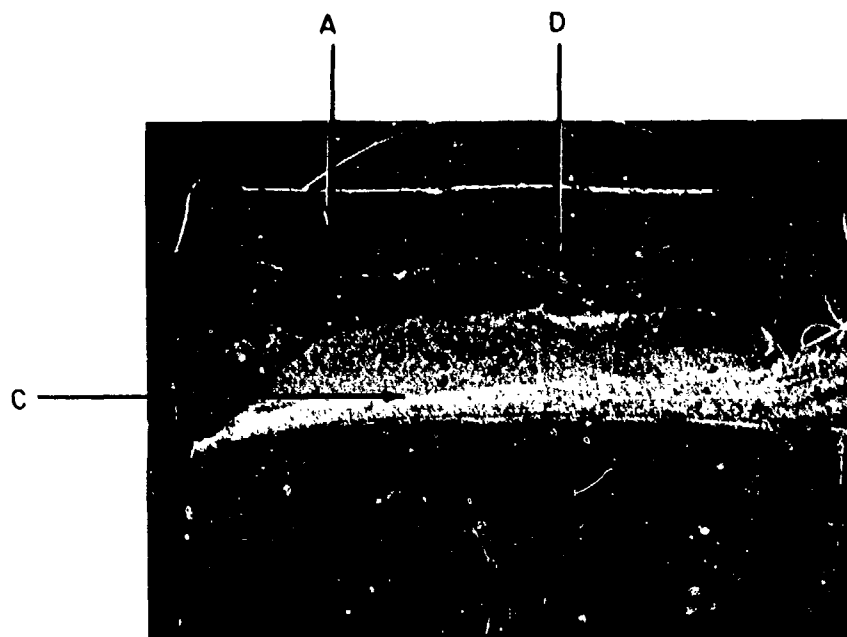
Figure 127. Tensile fracture surface of an A-514 weldment containing LOP, 8x.
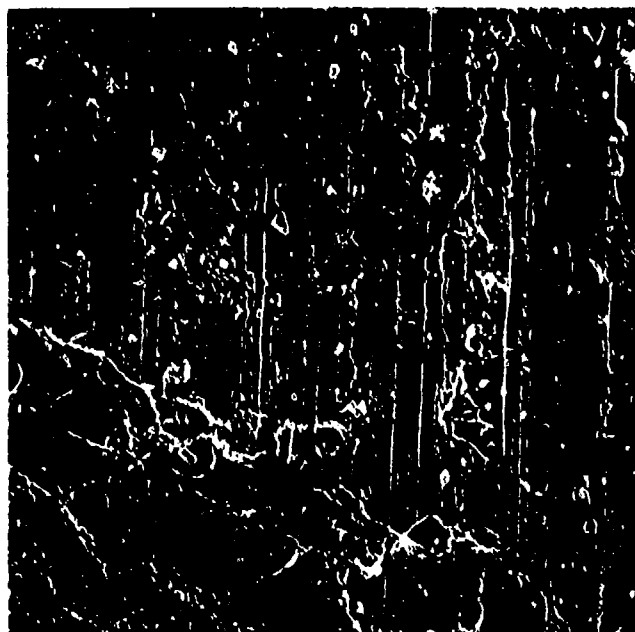
Figure 128. LOP region on tensile fracture surface of an A-514 weldment, 250x.
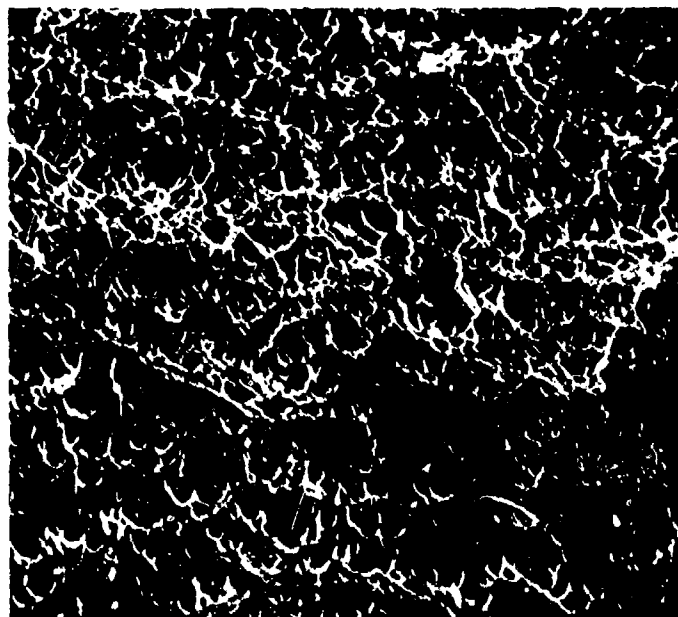
Figure 129. Transition region on tensile fracture surface of an A-514 weldment, 1800x.
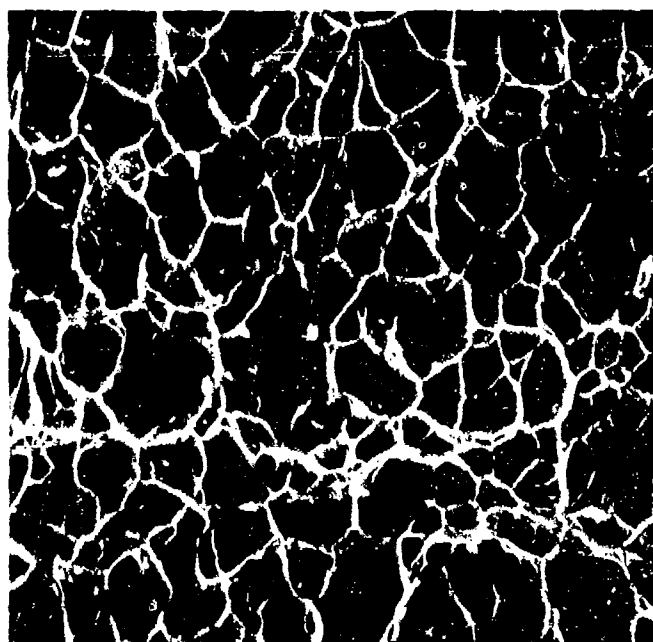
Figure 130. Transition region on tensile fracture surface of an A-514 weldment, 3750x.

Material: ASTM A-514, Grade F

Weld Metal: AIRCO AX 110
Process: GMA
Type of Defect: Porosity
Heat Treatment: As welded
Test Direction: Transverse to weld
Mode of Test: Fatigue
Test Temperature: Ambient
Test Environment: Air
Specimen Location and Configuration: See Figure 123.
Test Results:

> Mechanical Properties:

> > Maximum Stress
> > 36,000 psi (248.4 MPa)

> > Minimum Stress
> > 7200 psi (49.7 MPa)

> > Test Frequency
> > 10 cycles/second

> > Cycles to Failure
> > 34,250

> Fractographic Analysis:

The fatigue regions initiated at the pores. The fracture mode changed from fatigue to dimple rupture as the crack propagated through the specimen (Figures 131 through 136). The fracture was very rough and porous. The areas of porosity had a smooth, shiny texture, with small striations of dendrites across them, while the remainder of the fracture surface exhibited a dull, fibrous appearance.

154

Figure 131. Fatigue fracture surface of an A-514 weldment containing porosity, 8x.
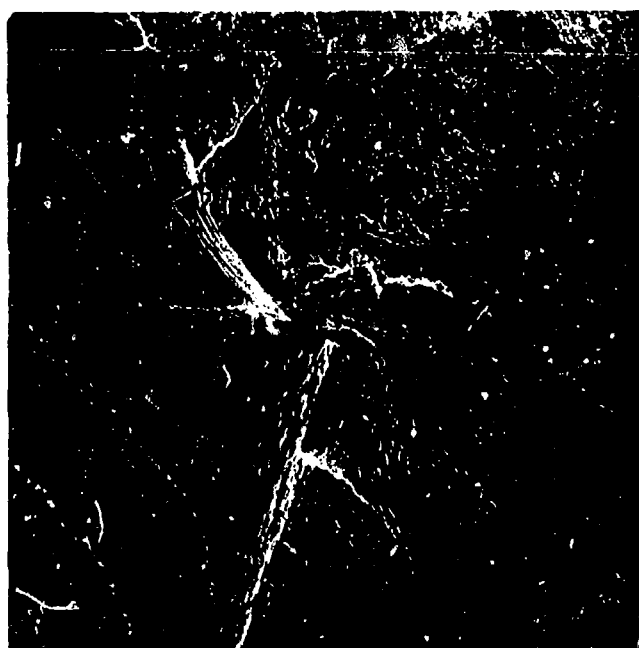
Figure 132. Fatigue initiation site on the fracture surface of an A-514 weldment containing porosity, 50x.

155
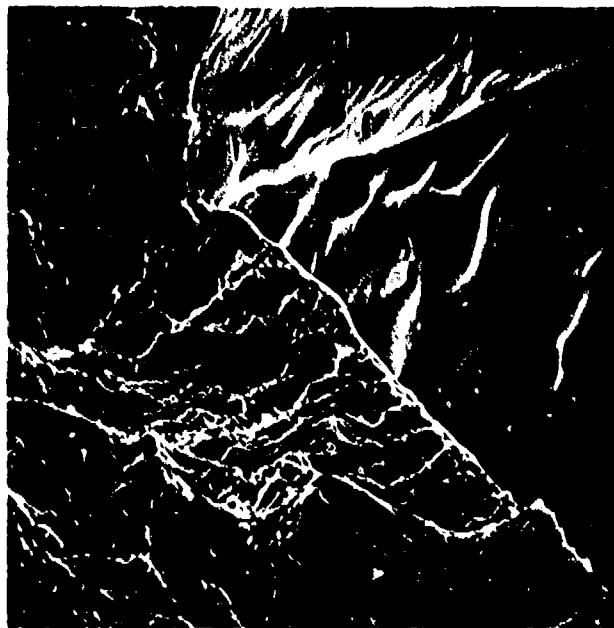
Figure 133. Fatigue initiation site on the fracture surface of an A-514
weldment containing porosity, 1380x.
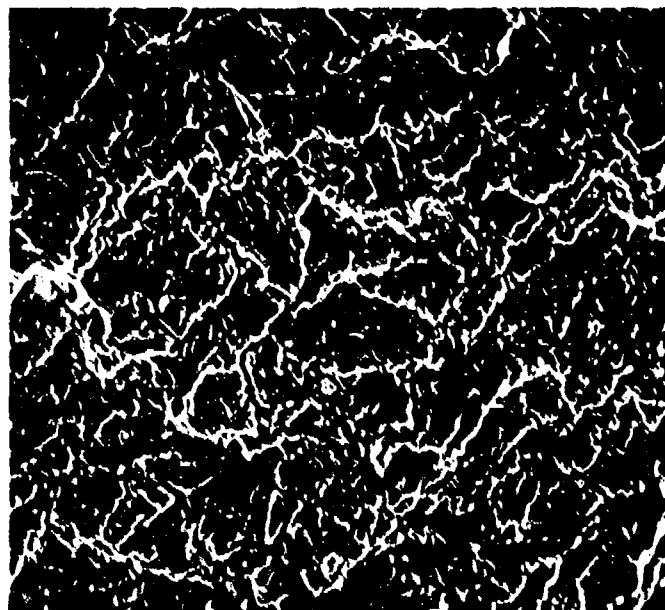
Figure 134. Fatigue region of fracture surface of an A-514 weldment
containing porosity, 1380x.
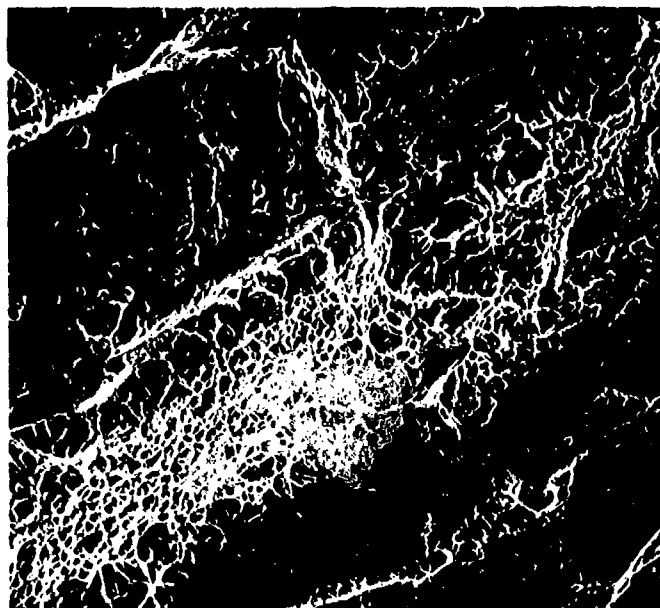
Figure 135. Tensile overload region of the fracture surface of A-514 weldment, 675x.
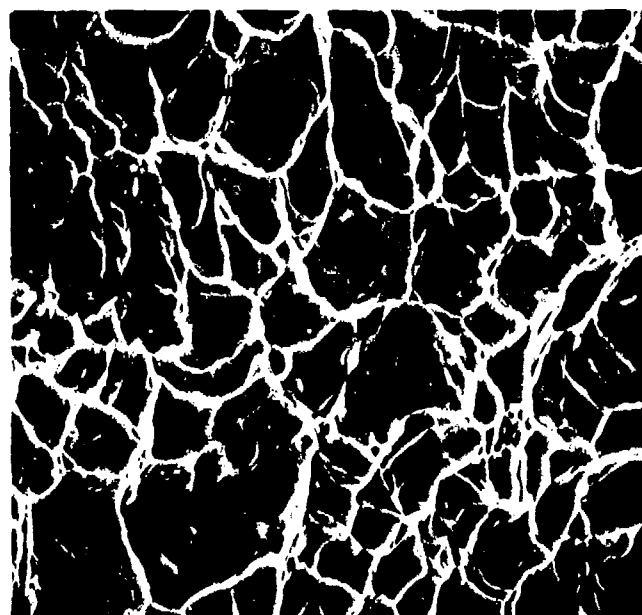
Figure 136. Tensile overload region of the fracture surface of A-514 weldment containing porosity, 3500x.

157

Material: ASTM A-514, Grade F

Weld Metal: AIRCO AX 110
Process: GMA
Type of Defect: Lack of penetration
Heat Treatment: As welded
Test Direction: Transverse to weld
Mode of Test: Fatigue
Test Temperature: Ambient
Test Environment: Air
Specimen Location and Configuration: See Figure 123.
Test Results:

Mechanical Properties:

Maximum Stress
56,000 psi

Minimum Stress
7850 psi

Test Frequency
10 cycles/second

Cycles to Failure
4150

Fractographic Analysis:

Fatigue striations originating from the defect were fairly well developed and easy to recognize. A fairly large crack running down the length of the defect was observed. Rapid fracture in the shear areas was by dimple rupture (Figures 137 through 141). Failure initiated from the porous LOP region in the center of the specimen. The fatigue regions emanating from the defect encompassed most of the fracture surface. The remainder of the fracture was shear. The LOP regions are characterized by vertical machine markings.
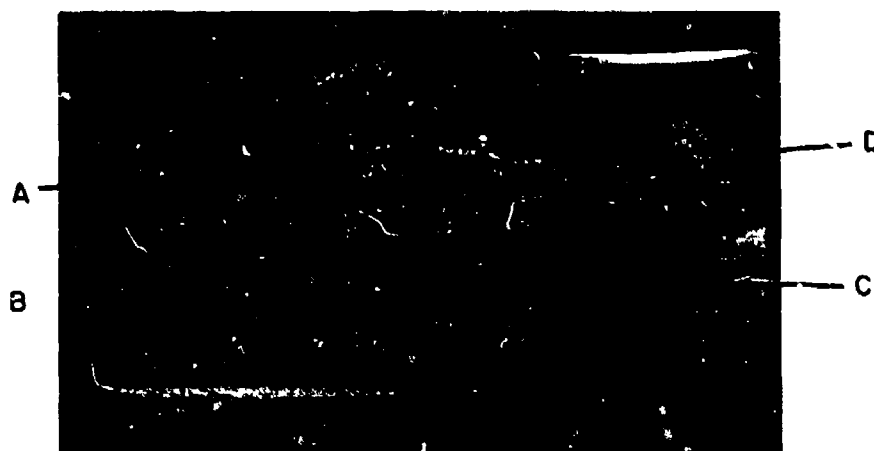
Figure 137. Fatigue fracture surface of an A-514 weldment containing LOP, 8x.
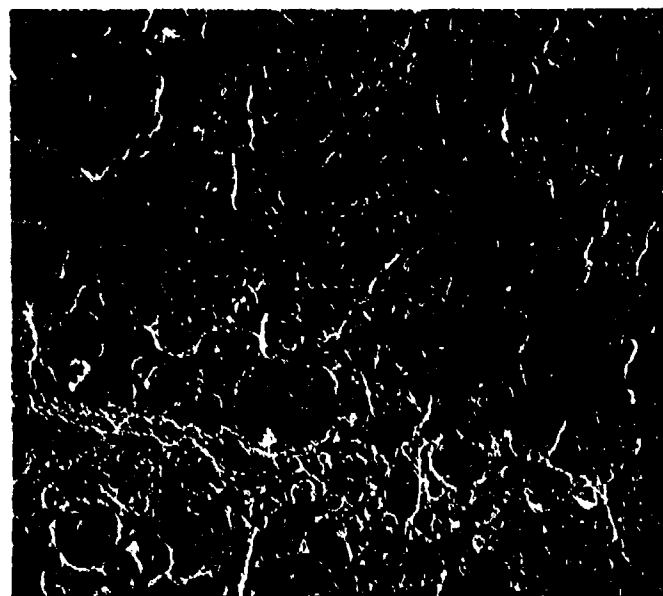
Figure 138. Fatigue fracture surface of A-514 weldment containing LOP, 650x.
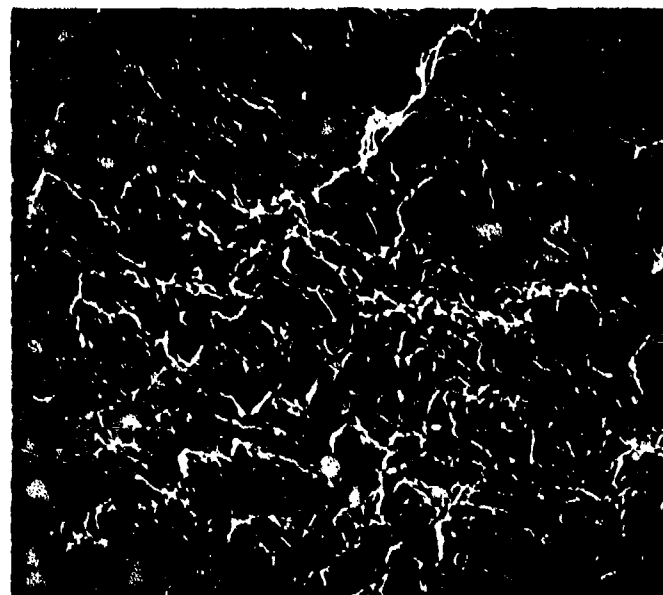
Figure 139. Fatigue region of fracture surface of an A-514 weldment containing LOP, 1700x.
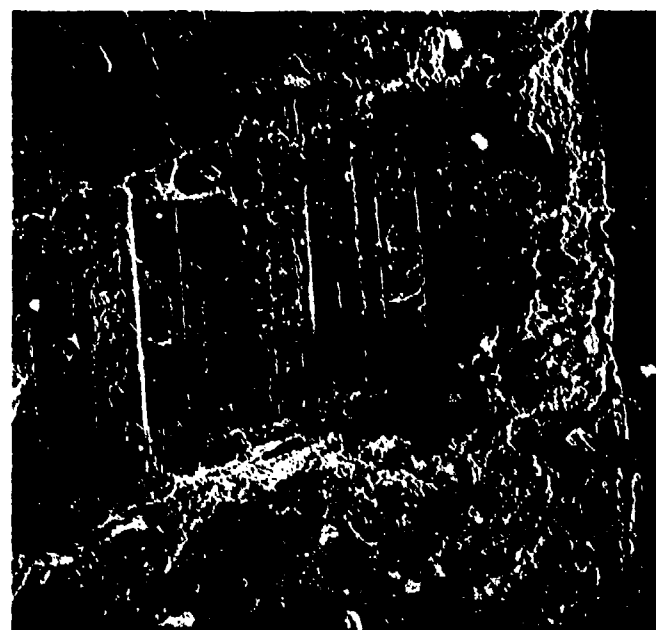
Figure 140. Fatigue fracture surface of A-514 weldment containing LOP, 130x.
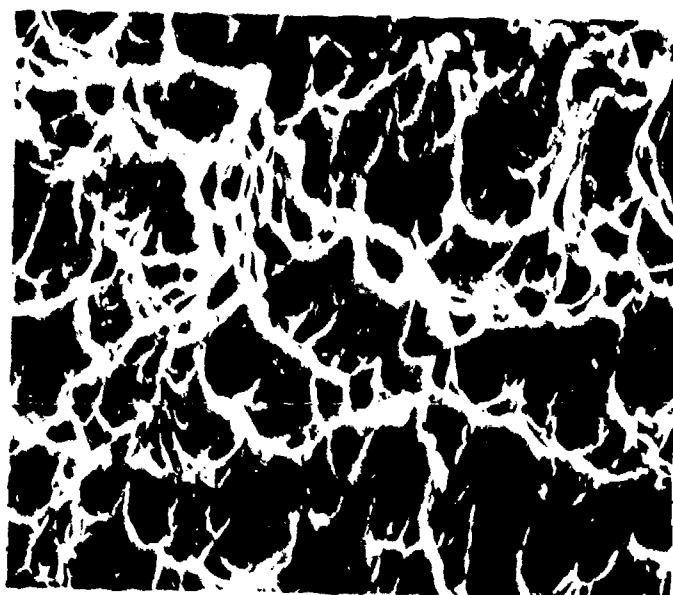
Figure 141. Tensile overload region of a fatigue fracture surface of
an A-514 weldment containing LOP, 3250x.

Material: ASTM A-514, Grade F

Weld Metal: AIRCO AX 110
Process: GMA
Type of Defect: Porosity
Heat Treatment: As welded
Test Direction: Transverse to weld
Mode or Condition of Test: Hydrogen-embrittled fatigue
Test Temperature: Ambient
Test Environment: Air
Hydrogen Charging Conditions:

  Current Density: 6 mA/in.^{2} (0.93 mA/cm^2)

  Charge Time: 12 hours

  Electrolyte: 0.3 wt% As_2O_3

            10.0 wt% H_2SO_4

Specimen Location and Configuration: See Figure 123.

Test Results:

  ### Mechanical Properties:

        Maximum Stress
        48,000 psi (331.2 MPa)

        Minimum Stress
        4800 psi (33.1 MPa)

        Test Frequency
        10 cycles/second

        Cycles to Failure
            3850 psi

  ### Fractographic Analysis:

  Fracture initiated at an outside corner of the specimen. As the
fatigue crack advanced through the specimen, craters began to form in
the fatigue region. The subsequent fibrous failure consisted of dimple
rupture (Figures 142 through 148). The fracture surface consisted of
flat fatigue region extending midway through the specimen followed by a
rough, jagged, fibrous failure. Large porosity bubbles were present in
both regions.* A shear lip was present at one end of the specimen.

---

*The surfaces of the porosity bubbles contained small, parallel stria-
tions of dendrites across them. There also seemed to be grain bound-
aries present inside the pore.
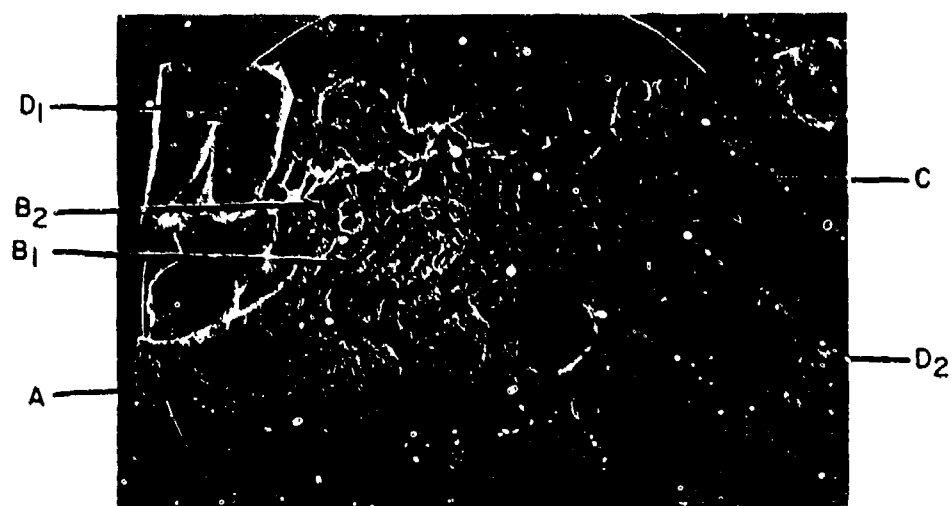
Figure 142. Fatigue fracture surface of a hydrogen-embrittled A-514 weldment containing porosity, 8x.
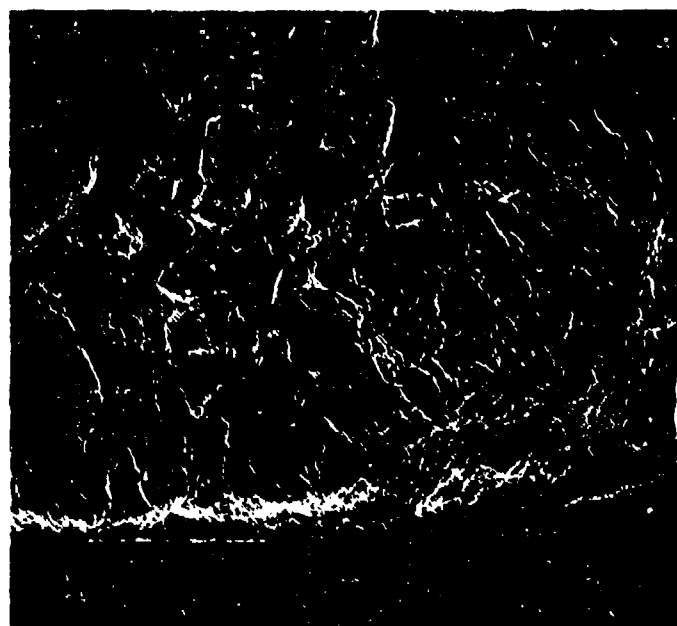
Figure 143. Origin of fatigue failure in a hydrogen-embrittled A-514 weldment containing porosity, 120x.
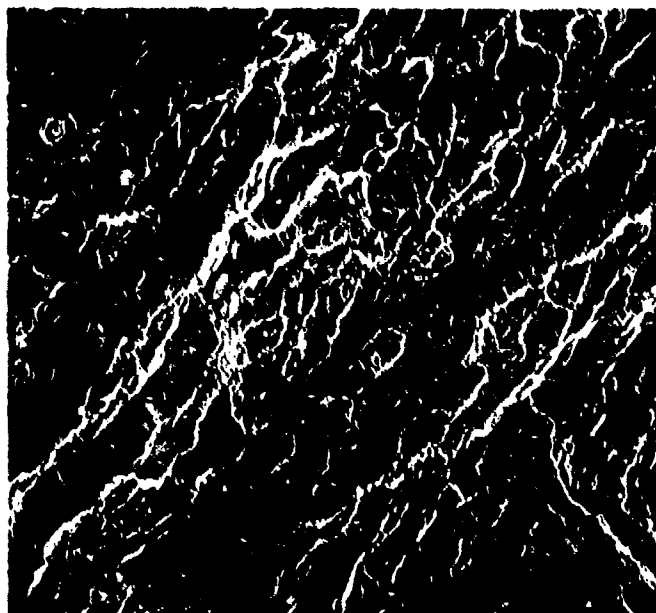
Figure 144. Micrograph of the fatigue region of the hydrogen-embrittled A-514 weldment containing porosity. 100x.
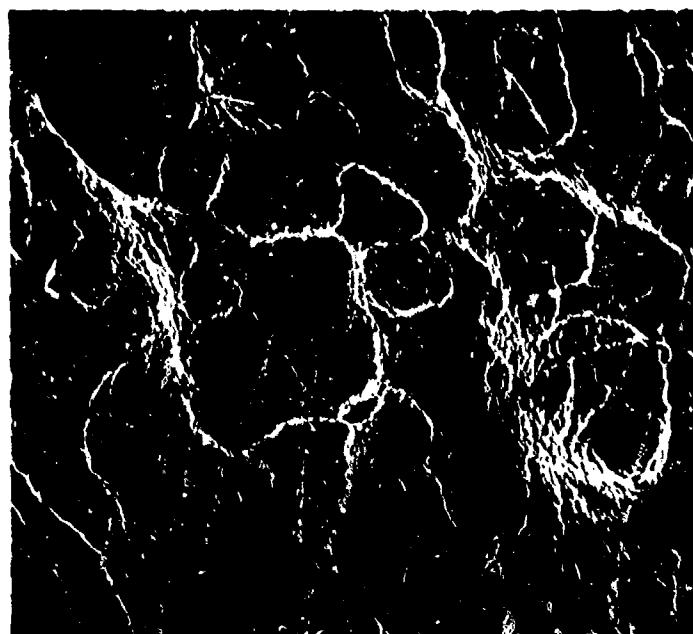
Figure 145. Micrograph of the fatigue region of the hydrogen-embrittled A-514 weldment containing porosity. 100x.
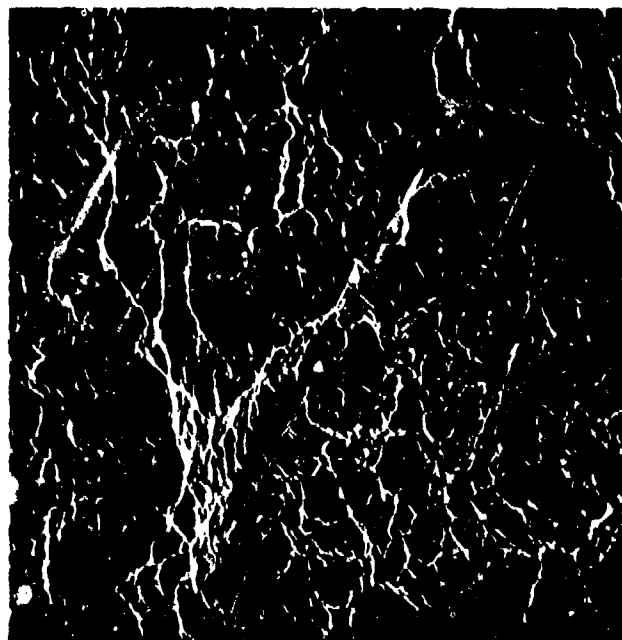
Figure 146. Tensile overload region in a hydrogen-embrittled A-514 weldment containing porosity, 1000x.
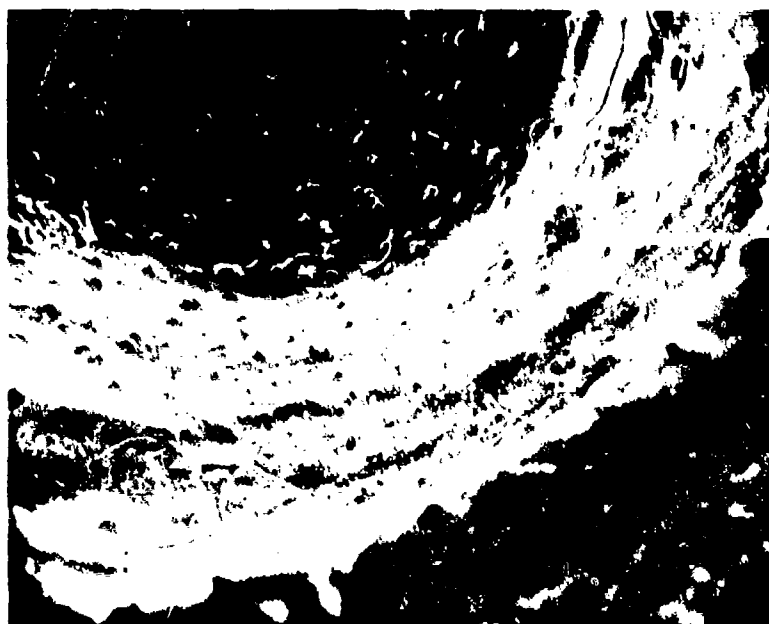
Figure 147. Micrograph of the porosity bubble in hydrogen-embrittled A-514 weldment, 500x.
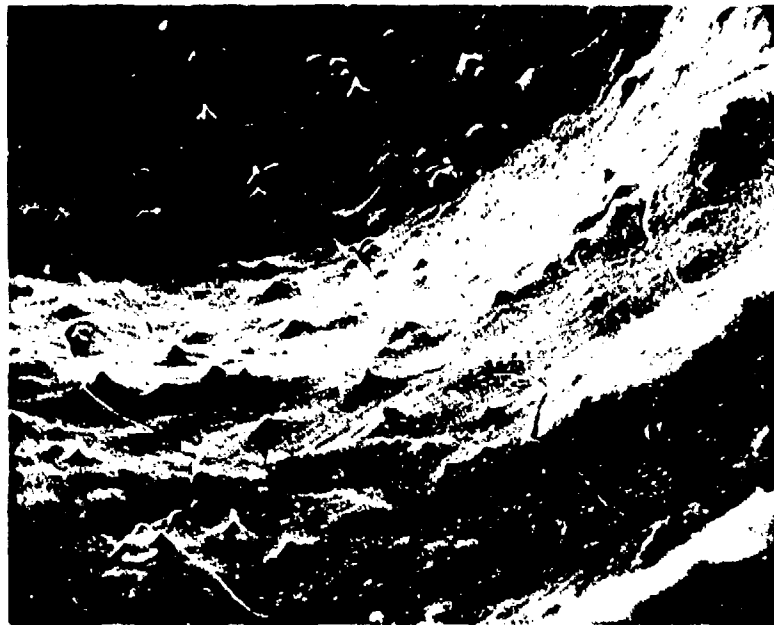
Figure 148. Porosity bubble in the hydrogen-embrittled A-514 weldment containing LOP, 1000x.

Material: ASTM A-514, Grade F

Weld Metal: AIRCO AX 110
Process: GMA
Type of Defect: Lack of penetration
Heat Treatment: Temper embrittled (1 hour at 950°F and furnace cool)
Test Direction: Transverse to weld
Mode or Condition of Test: Fatigue
Test Temperature: Ambient
Test Environment: Air
Specimen Location and Configuration: See Figure 123.
Test Results:

Mechanical Properties:

Maximum Stress
50,000 psi (345 MPa)

Minimum Stress
5000 psi (34.5 MPa)

Test Frequency
10 cycles/sec

Cycles to Failure
35,040

Fractographic Analysis:

Fatigue regions initiated from the central defect and the outside edge of the specimen. The peripheral shear lip exhibited typical elongated dimples (Figures 149 through 155). The fracture surface was fairly flat except for the rough LOP region located in the center of the specimen.* A small shear lip was present on the outside edge of the specimen.

* The longitudinal weld line in the center of the specimen was very shiny, while the remainder of the fracture surface was dull.
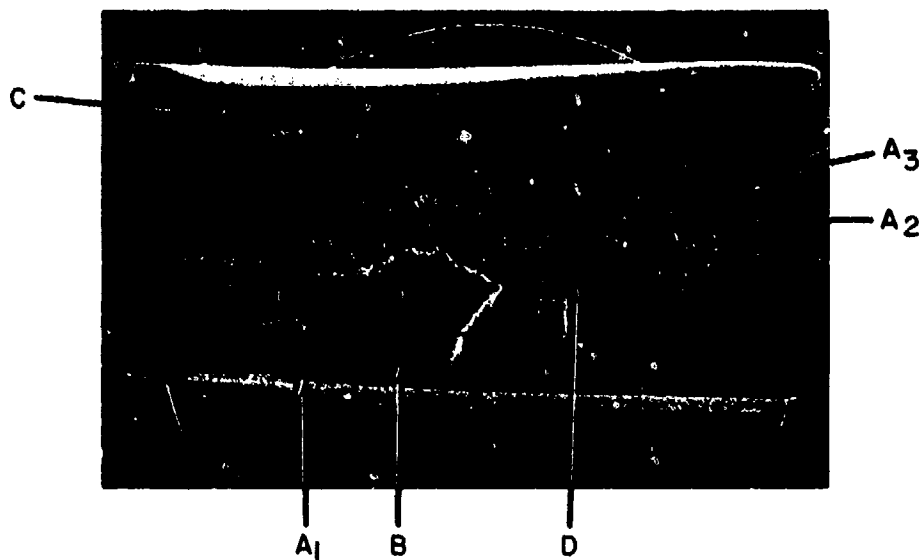
Figure 149. Fatigue fracture surface of a temper-embrittled A-514 weldment containing LOP, 8x.
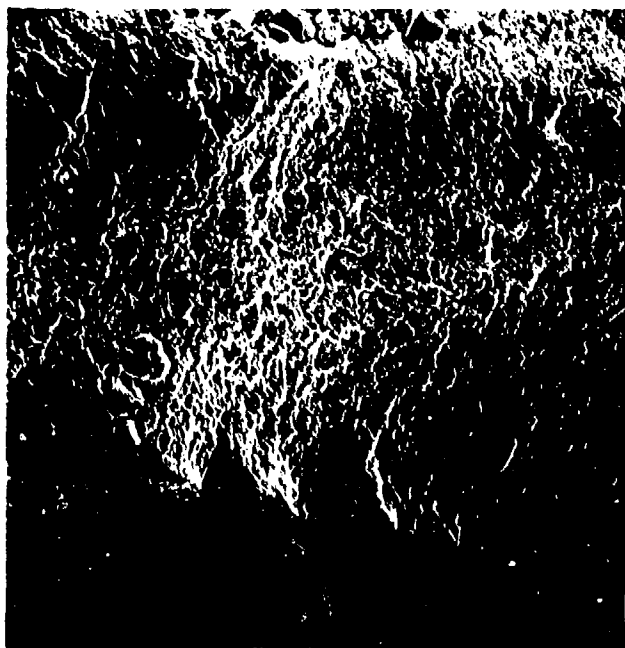
Figure 150. Secondary origin of fatigue failure of a temper-embrittled A-514 weldment 70x.
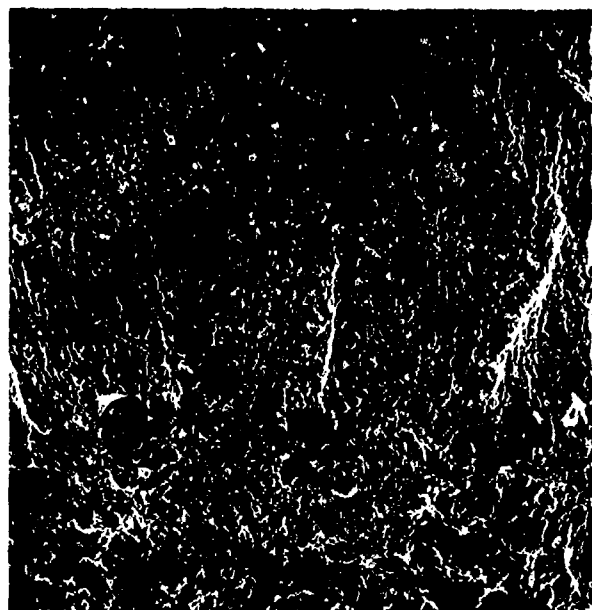
Figure 151.   Fatigue fracture surface of temper-embrittled A-514 weldment containing LOP, 70x.
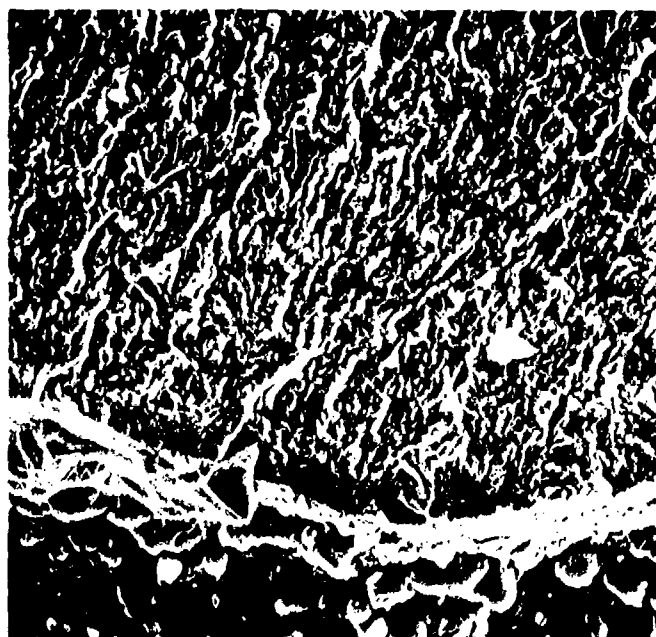
Figure 152.   Origin of failure of a temper-embrittled A-514 weldment containing LOP, 1400x.
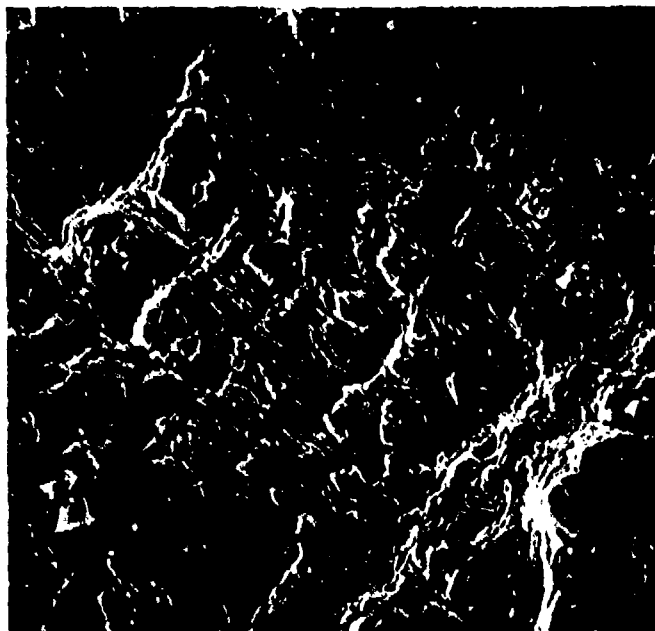
Figure 153. Fatigue striations on fracture surface of a temper-embrittled A-514 weldment containing LOP, 1400x.
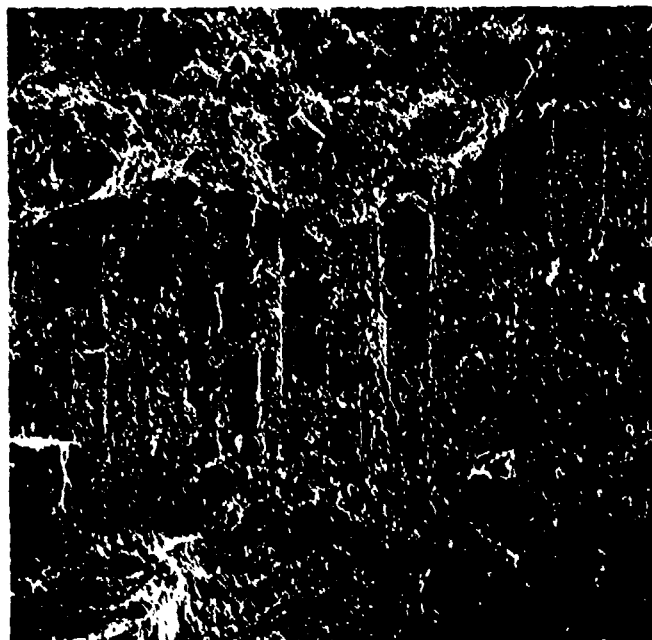
Figure 154. Fatigue fracture surface of the temper-embrittled A-514 weldment containing LOP, 140x.
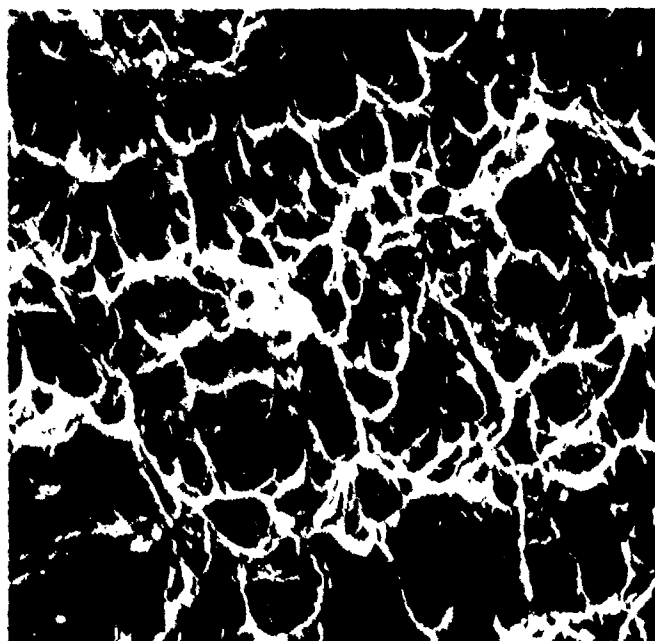
Figure 155. Elongated dimples on shear lip of fracture surface, 3500x.

ASTM A-588

Material: ASTM A-588

Specimen Orientation(s): Longitudinal
Heat Treatment(s): As rolled
Mode of Test: Tensile
Temperature(s) of Test: 23°C
Test Results:

Mechanical Properties:

Tensile Strength, ksi (MPa)
90.0 (621)

Yield Strength, ksi (MPa)
58.4 (403)

Fractographic Analysis:

The fracture surface of the A-588 unembrittled tensile sample is shown in Figure 156. Failure occurred by inclusion generated dimple rupture. Figue 157 shows various dimple sizes and several inclusions. Plastic deformation markings can be seen within the large concave dimples.
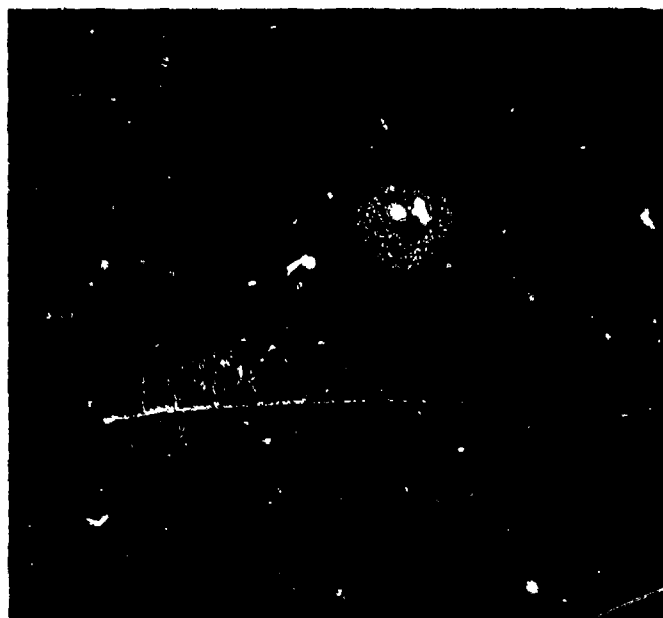
Figure 156. Tensile fracture surface of A-588 steel, 8x.
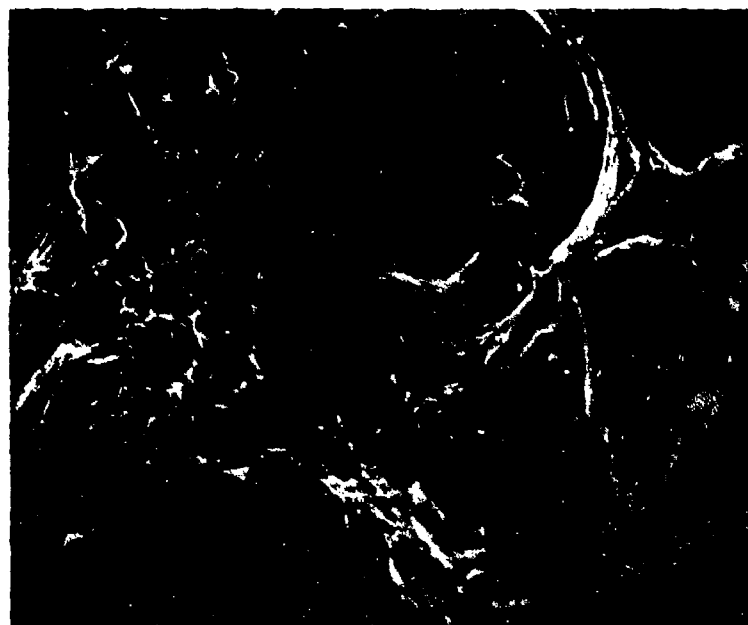
Figure 157. Dimple rupture in A-588 steel, 1500x.

173

Material: ASTM A-588

Specimen Orientation(s): Longitudinal
Heat Treatment(s): Slow cooled from austenitizing range
Mode of Test: Tensile
Temperature(s) of Test: 23°C
Test Results:

Mechanical Properties:

Tensile Strength, ksi (MPa)
83.2 (574.1)

Yield Strength, ksi (MPa)
57.6 (397.4)

Fractographic Analysis:

The fracture surface of the reaustenitized and slow cooled A-588
tensile specimen was very similar to that of the as-rolled sample (Fig-
ures 156 and 157). The mechanism of failure was inclusion-generated
dimple rupture.

Material: ASTM A-588

Specimen Orientation(s): Longitudinal
Heat Treatment(s): As rolled
Hydrogen Charging Conditions:

  Current density: 6 mA/in.^{2} (0.93 mA/cm^2)

  Charge time: 12 hours

  Electrolyte: 0.3 wt% As_2O_3, 10.0 wt% H_2SO_4

Mode of Test: Tensile
Temperature(s) of Test: 23°C
Test Results:

  Mechanical Properties:

      Tensile Strength, ksi (MPa)
           88.8 (612.7)

      Yield Strength,ksi (MPa)
           59.2 (408.5)

  Fractographic Analysis:

    The hydrogen-embrittled A-588 tensile specimen (Figure 158) shows
considerably less necking before failure than the unembrittled specimen
(Figure 156). The first indication of brittle failure is confirmed by a
higher magnification micrograph (Figure 159) which shows large cleavage
facets. The river patterns show the direction of crack propagation
within each facet.

175

Figure 158.   Tensile fracture surface of hydrogen-
            embrittled A-588 steel, 8x.

Figure 159.   Cleavage facets in hydrogen-embrittled
            A-588 steel, 1500x.

176

Material: ASTM A-588

Specimen Orientation(s): Longitudinal
Heat Treatment(s): As rolled
Mode of Test: Fatigue
Temperature(s) of Test: 23°C
Test Results:

Fractographic Analysis:

Fatigue and tensile overload regions can be easily identified on the fracture surfaces of the as-rolled (Figure 160) fatigue specimen. Failure in the tensile overload regions occurred by dimple rupture which initiated at inclusions (Figure 161). The fatigue regions consisted of parallel fatigue striations indicative of the stepwise, cyclic progression of the crack front across the fracture surfaces (Figure 162).

Figure 160. Fatigue fracture surface of A-588 steel, 8x.

177
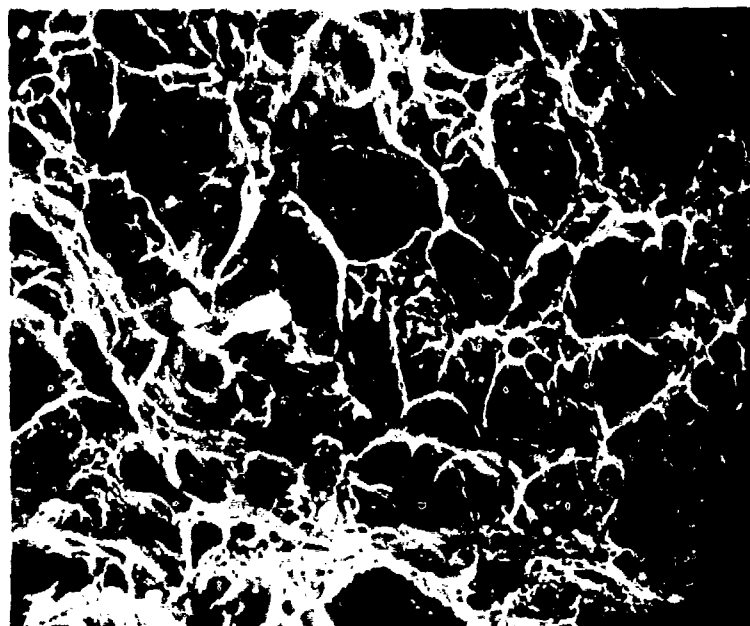
Figure 161. Dimple rupture in an A-588 fatigue specimen, 750x.

Figure 162. Fatigue striations in A-588 steel, 1500x.

Material ASTM A-588

Specimen Orientation(s): Longitudinal
Heat Treatment(s): Slow cooled from austenitizing range
Mode of Test: Fatigue
Temperature(s) of Test: 23°C
Test Results:

Fractographic Analysis:

The fracture surface of the reheat-treated fatigue specimen was very similar to the fracture surface of the as-rolled fatigue specimen. Failure in the tensile overload regions occurred by dimple rupture which initiated at inclusions. The fatigue regions consisted of parallel fatigue striations.

Material: ASTM A-588

Specimen Orientation(s): Longitudinal
Heat Treatment(s): As rolled
Hydrogen Charging Conditions:

Current density: 6 mA/in.^{2} (0.93 mA/cm^2)

Charge time: 12 hours

Electrolyte: 0.3 wt% As_2O_3, 10.0 wt% H_2SO_4

Mode of Test: Fatigue
Temperature(s) of Test: 23^{0}C
Test Results:

Fractographic Analysis:

The fracture surface of the hydrogen-embrittled fatigue specimen
(Figure 163) was quite complex since it contained various mixed modes of
fracture. Figure 164 shows areas of dimple rupture interspersed with
areas of fracture through pearlite colonies. The combination of fatigue
striations and intergranular fracture shown in Figure 165 is somewhat
uncommon. Intergranular fracture occurred in the regions that had a
preferred grain-boundary fracture path; in this case, as the result of
hydrogen accumulation in the grain boundaries.

Figure 163. Fatigue fracture surface of hydrogen-embrittled A-588 steel, 8x.
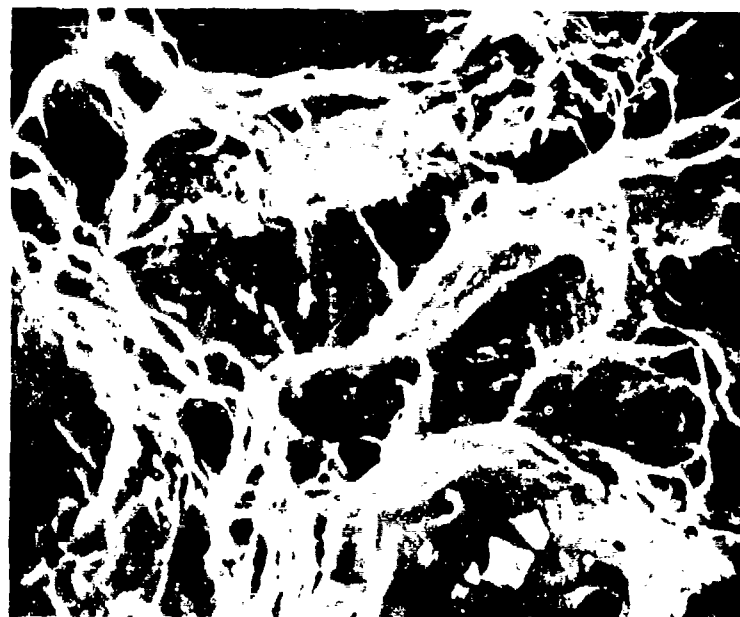
Figure 164. Dimple rupture and fractured pearlite colonies in a hydrogen-embrittled A-588 fatigue specimen, 1500x.
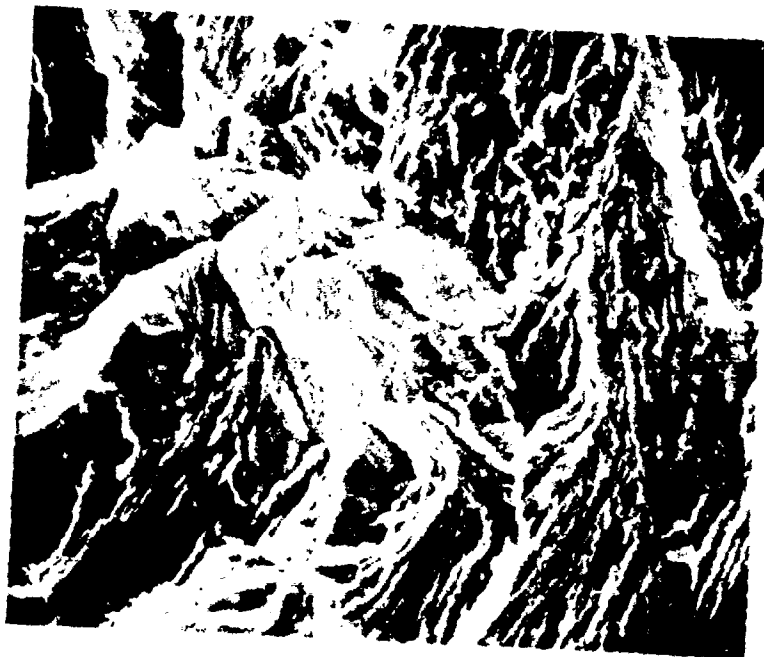
Figure 165. Intergranular and cleavage fracture in a hydrogen-embrittled A-588 fatigue specimen, 1500x.

Material: ASTM A-588

Specimen Orientation(s): Longitudinal
Heat Treatment(s): As rolled
Mode of Test: Impact
Temperature(s) of Test: -196°C, -103°C, -30°C, 23°C
Test Results:

Mechanical Properties:

Testing Temperature, °C	Absorbed Energy, ft-lb (joule)
-196	3.0 (4.1)
-103	5.0 (6.8)
- 30	13.0 (17.6)
23	24.5 (33.2)

Fractographic Analysis:

Figure 166 shows the fracture surface of an A-588 Charpy impact
specimen which was broken at -196°C. A higher magnification of the sur-
face (Figure 167) shows that failure occurred by cleavage. Numerous
river patterns are found on the facets. For the Charpy specimen tested
at -83°C, the fracture surface consisted primarily of cleavage facets
with some interspersed dimpled regions (Figure 168). When fracture oc-
curred at -18°C, the interior surface showed primarily cleavage facets.
At the edges, however, regions of mixed cleavage and dimples appeared.
At room temperature (23°C), one area in the interior of the surface
failed by cleavage, but most of the failure occurred by a combination of
cleavage and dimple rupture (Figure 169), which gave the surface a
fibrous texture (Figure 170).

Figure 166. Fracture surface of an A-588 Charpy specimen tested at -196°C, 8x.

Figure 167. Cleavage facets in an A-588 Charpy specimen tested at -196°C, 1000x.
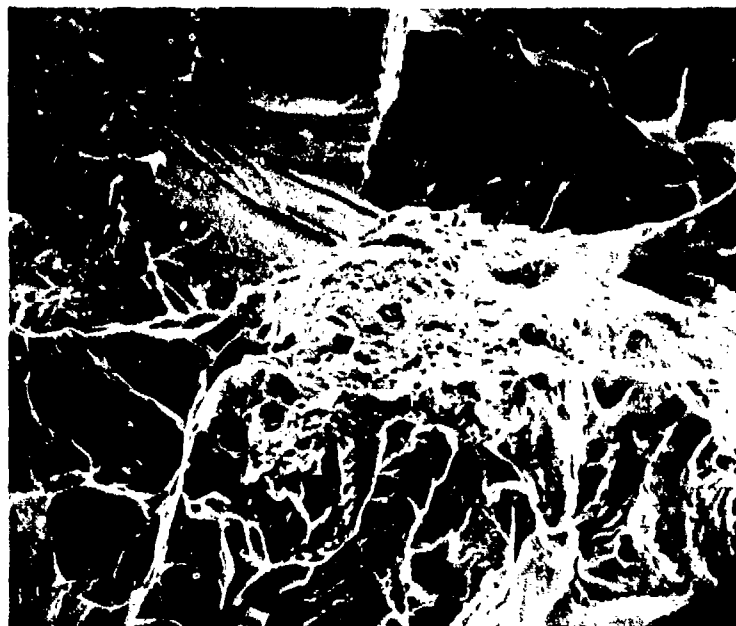
Figure 168. Cleavage fracture and dimple rupture in an
A-588 Charpy specimen tested at -103°C, 1000x.
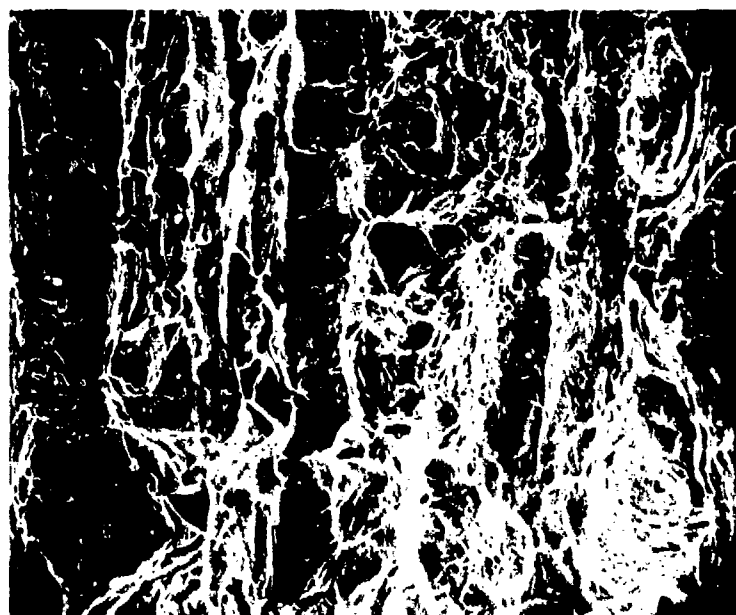
Figure 169. Cleavage fracture and dimple rupture in an A-588
Charpy specimen tested at 23°C, 250x.
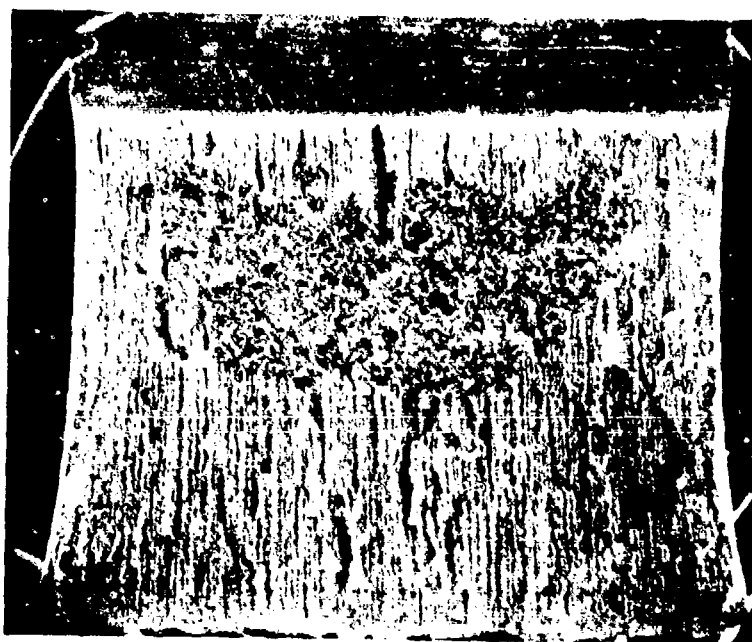
Figure 170. Fracture surface of A-588 Charpy
specimen tested at 23°C, 8x.

ASTM A-242

Material: ASTM A-242

Specimen Orientation(s): Longitudinal and transverse
Heat treatment(s): As rolled
Mode of Test: Tensile
Temperature(s) of Test: $23^{\circ}C$
Test Results:

Mechanical Properties:

Specimen	Tensile Strength ksi (MPa)	Yield Strength ksi (MPa)
A-242, as-rolled, longitudinal	76.0 (524.4)	48 (331.2)
A-242, as-rolled, transverse	75.2 (518.9)	48 (331.2)

Fractographic Analysis:

The fracture surface of the A-242 tensile specimen machined with its long axis longitudinal to the rolling direction of the steel is shown in Figure 171. Failure occurred by inclusion-generated dimple rupture; extensive secondary cracking and some necking also occurred. The fracture surface of the A-242 tensile specimen machined with its long axis transverse to the rolling direction is shown in Figure 172. Some necking occurred before failure. A higher magnification micrograph (Figure 173) shows that inclusion-generated dimple rupture was the failure mechanism. Since the plane of fracture is parallel to the rolling direction, flattened out inclusions can be easily seen on the fracture surfaces.
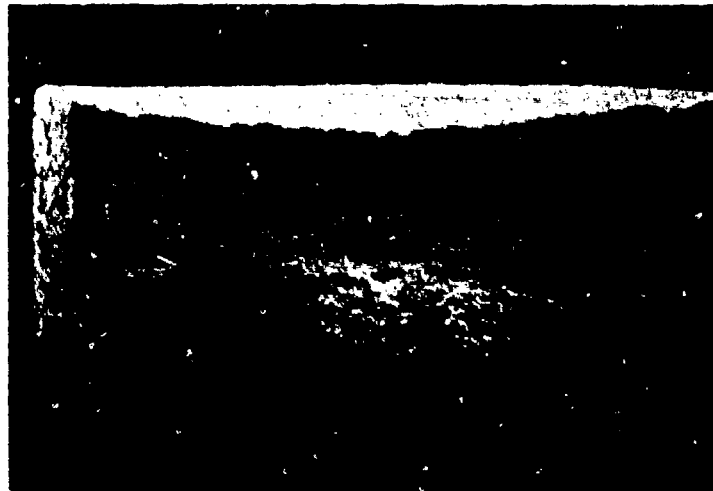
Figure 171. Tensile fracture surface of an A-242 longitudinal specimen, 12x.
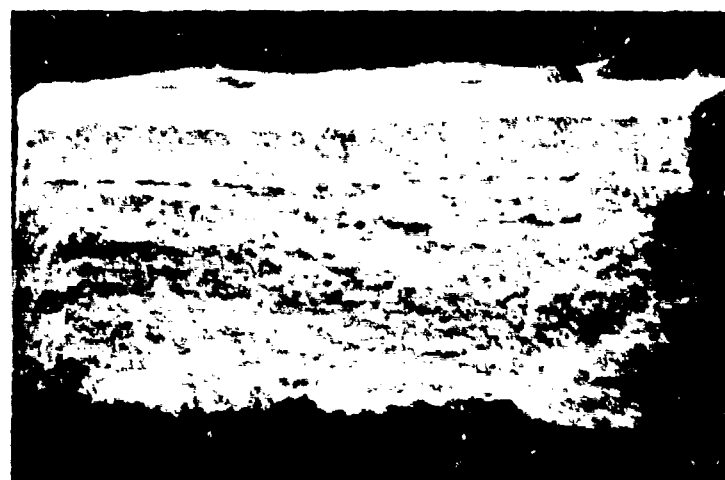
Figure 172. Tensile fracture surface of an A-242 transverse specimen, 12x.
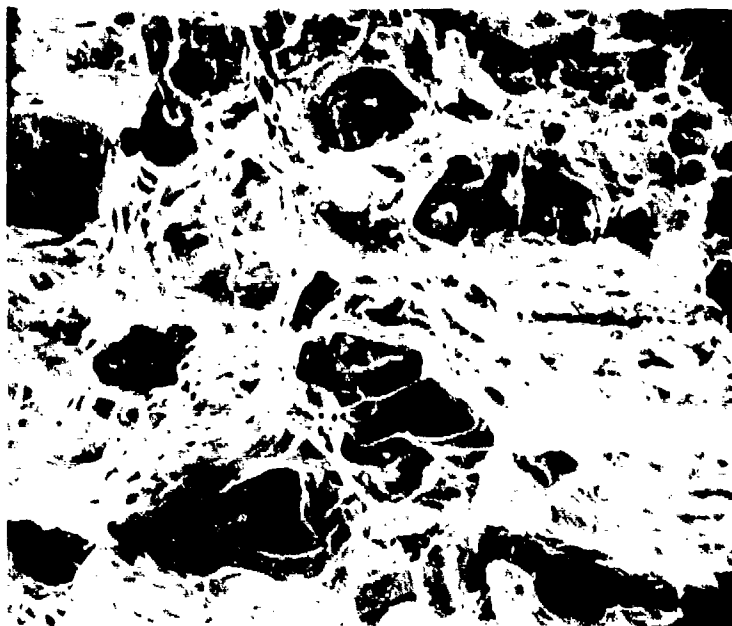
Figure 173.   Inclusion-generated dimple rupture in an
A-242 transverse specimen, 500x.

Material: ASTM A-242

Specimen Orientation(s): Longitudinal and transverse
Heat Treatment(s): Slow cooled through austenitizing range
Temperature(s) of Test: 23°C
Test Results:

Mechanical Properties:

Specimen	Tensile Strength ksi (MPa)	Yield Strength ksi (MPa)
A-242, reheat-treated, longitudinal	73.6 (507.8)	48.8 (336.7)
A-242, reheat-treated, transverse	68.0 (496.2)	42.4 (292.6)

Fractographic Analysis:

The reheat-treated specimens' fracture surfaces were similar to the
fracture surfaces of the as-rolled specimens. Failure in both the lon-
gitudinal and transverse specimens occurred by inclusion-generated
dimple rupture.

Material: ASTM A-242

Specimen Orientation(s): Longitudinal and transverse
Heat Treatment(s): As rolled
Hydrogen Charging Conditions:

  Current density: 6 mA/in.^{2} (0.93 mA/cm^2)

  Charge time: 12 hours

  Electrolyte: 0.3 wt% As_2O_3, 10.0 wt% H_2SO_4

Mode of Test: Tensile
Temperature(s) of Test: 23°C
Test Results:

Mechanical Properties:

Specimen	Tensile Strength ksi (MPa)	Yield Strength ksi (MPa)
A-242, hydrogen-embrittled, longitudinal	76.0 (524.4)	49.6 (342.2)
A-242, hydrogen-embrittled, transverse	72.8 (502.3)	47.2 (325.7)

Fractographic Analysis:

The fracture surface of the hydrogen-charged longitudinal A-242 tensile specimen was slanted towards a shear lip on one side (Figure 174). The mechanisms of failure were dimple rupture (Figure 175) and some cleavage. The transverse hydrogen-charged tensile sample (Figure 176) showed elongated inclusions (Figure 177). Failure occurred by a combination of dimple rupture and cleavage (Figure 178).

191

Figure 174. Fracture surface of a hydrogen-charged
            A-242 longitudinal tensile specimen, 10x.
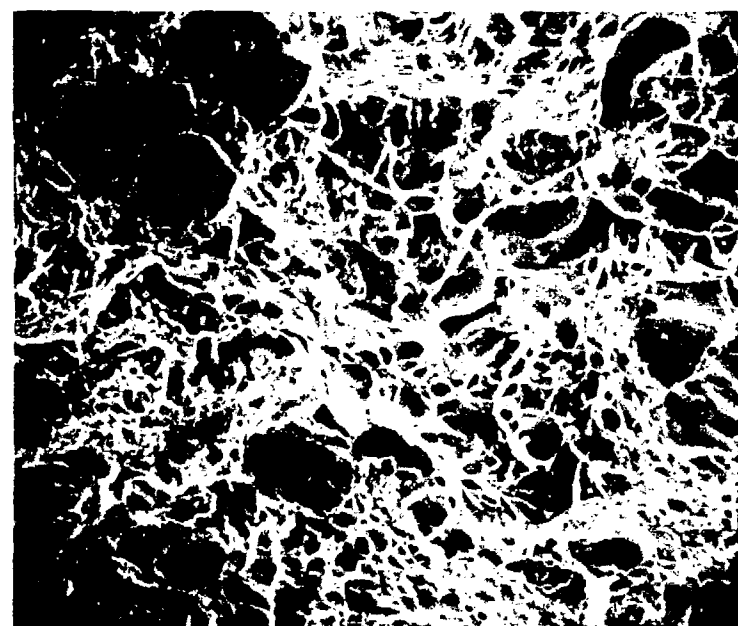
Figure 175. Dimple rupture in a hydrogen-charged A-242
            longitudinal tensile specimen, 600x.

192
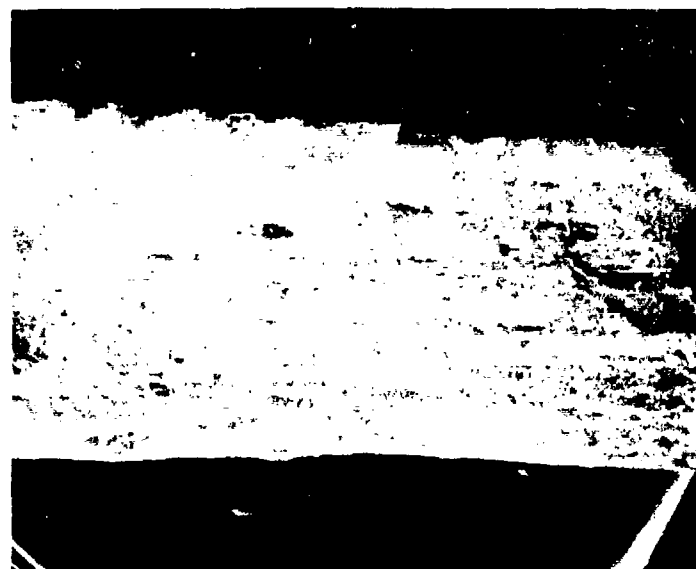
Figure 176. Fracture surface of a hydrogen-charged A-242
transverse tensile specimen, 10x.
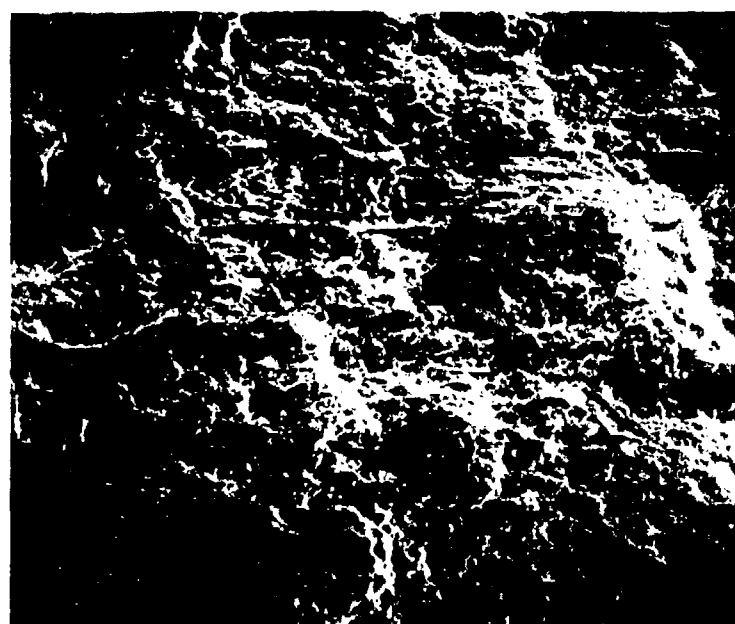
Figure 177. Elongated inclusion in a hydrogen-charged A-242
transverse tensile specimen, 55x.
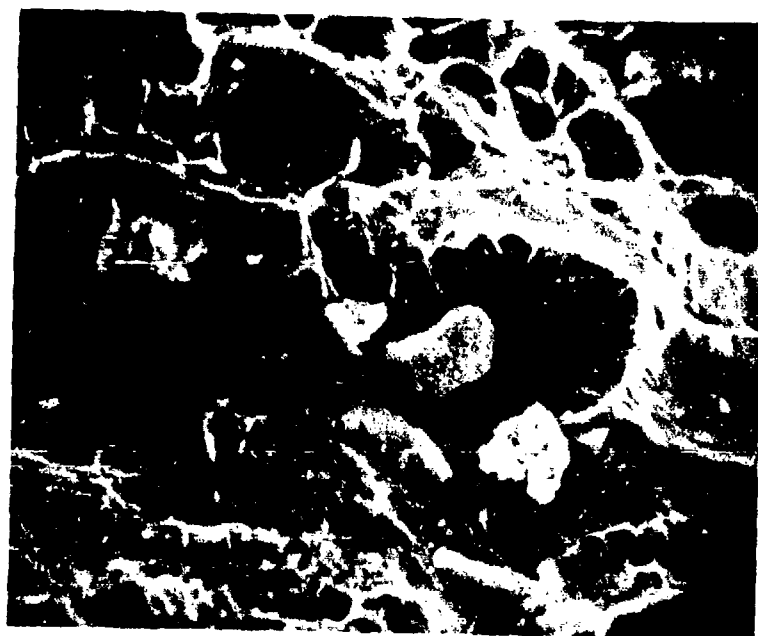
Figure 178.   Cleavage fracture and dimple rupture in a
hydrogen-charged A-242 transverse tensile
specimen, 1400x.

Material: ASTM A-242

Specimen Orientation(s): Longitudinal and transverse
Heat Treatment(s): As rolled
Mode of Test: Fatigue
Temperature(s) of Test: $23^{\circ}C$
Test Results:

Fractographic Analysis:

The as-rolled A-242 fatigue specimens failed by a combination of cleavage and dimple rupture (Figure 179) in the tensile overload region and by cleavage (Figure 180) in the fatigue region.
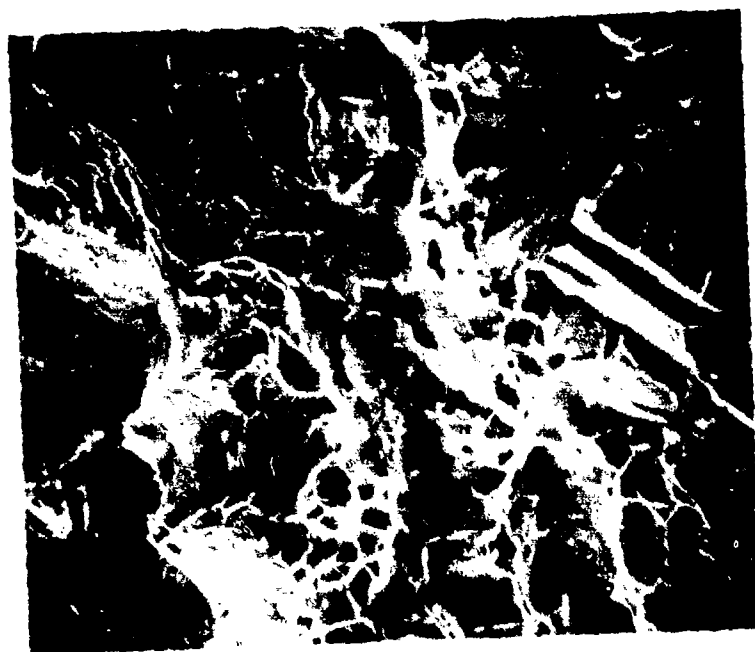
Figure 179. Cleavage fracture and dimple rupture in an
A-242 longitudinal fatigue specimen, 600x.

Figure 180. Cleavage fracture in an A-242 transverse fatigue specimen, 700x.

Material: ASTM A-242

Specimen Orientation(s): Longitudinal and transverse
Heat Treatment(s): Slow cooled through austenitizing range
Mode of Test: Fatigue
Temperature(s) of Test: 23°C
Test Results:

Fractographic Analysis:

The fracture surfaces of the reheat-treated fatigue specimens
closely resembled those of the as-rolled fatigue specimens. Failure oc-
curred by a combination of dimple rupture and cleavage in the tensile
overload region and by cleavage in the fatigue region.

Material: ASTM A-242

Specimen Orientation(s): Longitudinal and transverse
Heat Treatment(s): As rolled
Hydrogen Charging Conditions:

  Current density: 6 mA/in.^{2} (0.93 mA/cm^2)

  Charge time: 12 hours

  Electrolyte: 0.3 wt% As_2O_3, 10.0 wt% H_2SO_4

Mode of Test: Fatigue
Temperature(s) of Test: 23^{0}C
Test Results:

  Fractographic Analysis:

    The hydrogen-embrittled longitudinal and transverse fatigue speci-
mens produced similar fracture surfaces. The transverse specimen in
Figure 181 shows the long cracks formed as a result of elongated inclu-
sions. Failure occurred in both specimens by a combination of dimple
rupture and cleavage (Figure 182).
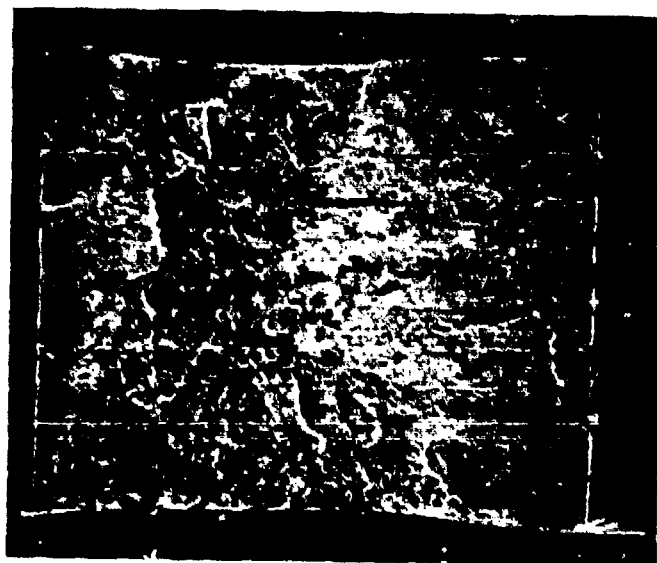
Figure 181.   Fracture surface of a hydrogen-charged
A-242 transverse fatigue specimen, 14x.
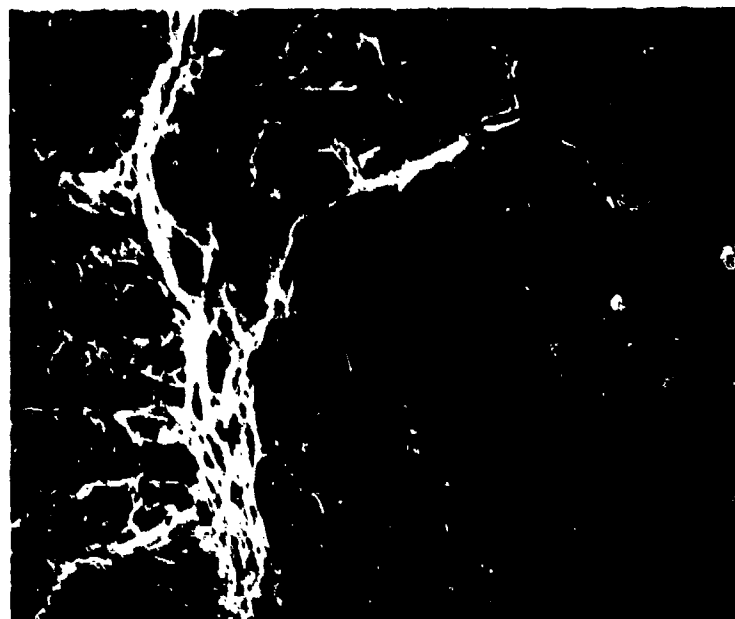
Figure 182. Dimple rupture and cleavage fracture in a hydrogen-charged A-242 transverse fatigue specimen, 250x.

Material: ASTM A-242

Specimen Orientation(s): Longitudinal and transverse
Heat Treatment(s): As rolled
Mode of Test: Impact
Temperature(s) of Test: -196°C, 0°C, 23°C, 121°C
Test Results:

Mechanical Properties:

Specimen	Testing Temperature, °C	Absorbed-Energy, ft-lb (joule)
A-242, longitudinal	-196	0.5 (.7)
A-242, longitudinal	0	4.0 (5.4)
A-242, longitudinal	23	8.0 (10.8)
A-242, longitudinal	121	74.0 (100.3)
A-242, transverse	-196	0.0 (0.0)
A-242, transverse	0	2.0 (2.7)
A-242, transverse	23	6.5 (8.8)
A-242, transverse	121	17.5 (23.7)

Fractographic Analysis:

The fracture surfaces of the A-242 Charpy specimens were shiny and faceted, indicating brittle fracture. The liquid nitrogen specimens were quite flat, and showed no lateral contraction (Figure 183). Both the longitudinal and transverse specimens failed by cleavage (Figure 184); in some places the fracture propagated along grain boundaries and the fracture surface revealed the presence of some type of precipitate (Figure 185). The amount of lateral contraction on the fracture surface increased as the testing temperature increased from 32°F (0°C) (Figure 186), to room temperature (Figure 187), to 250°F (121°C) (Figure 188). Failure occurred at all temperatures by cleavage (Figure 189) in the center of the specimens, and by a combination of cleavage and dimple rupture in the shear lips (Figure 190). In all cases the Charpy impact energy was much lower than normal. Even at room temperature the energy value was only 8.0 ft-lb (10.8 J)

Figure 183. Fracture surface of an A-242 transverse Charpy
specimen tested at -196°C, 10x.
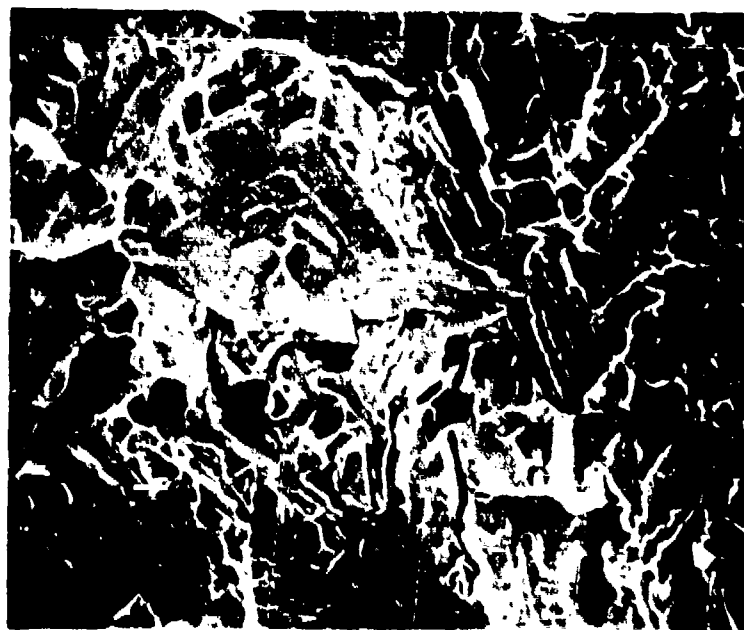
Figure 184. Cleavage fracture in an A-242 longitudinal Charpy
specimen tested at -196°C, 500x.

203
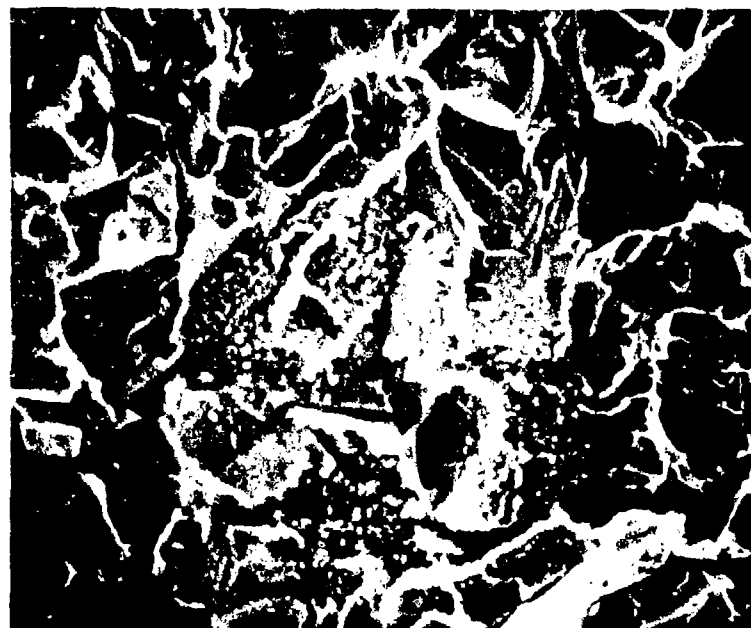
Figure 185. Grain boundary precipitation in A-242 Charpy
specimen tested at -196°C, 1000x.
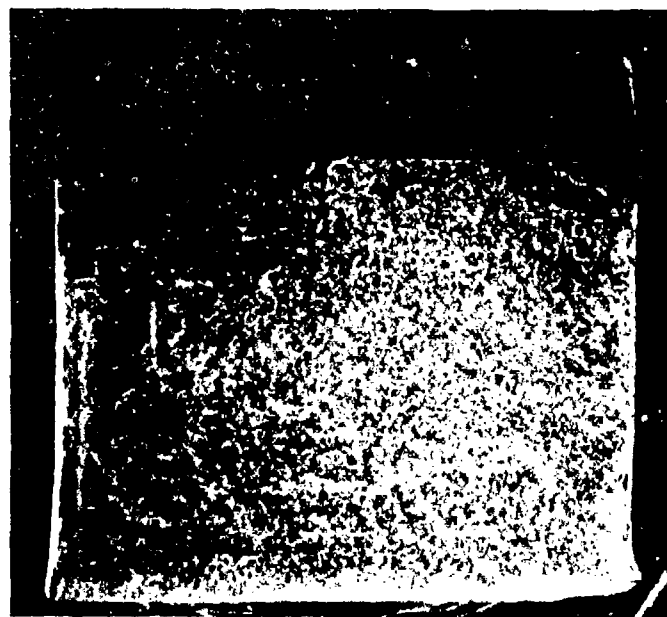
Figure 186. Fracture surface of A-242 transverse Charpy
specimen tested at 0°C, 10x.
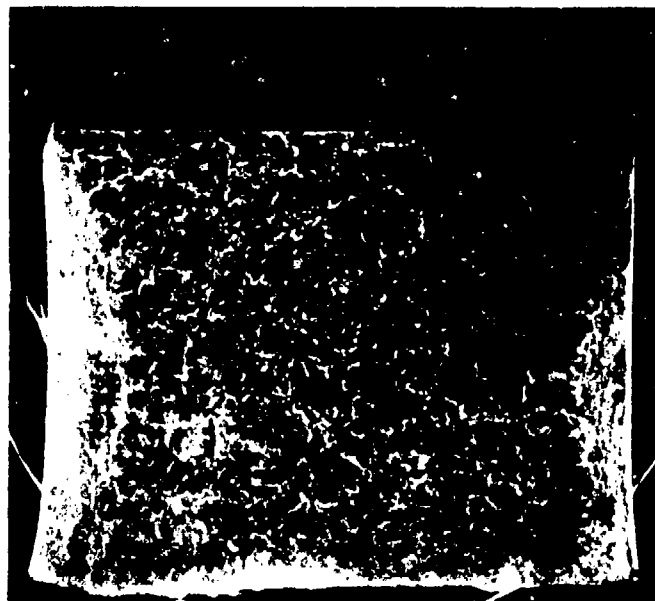
Figure 187.   Fracture surface of an A-242 transverse Charpy
specimen tested at 23^OC, 10x.
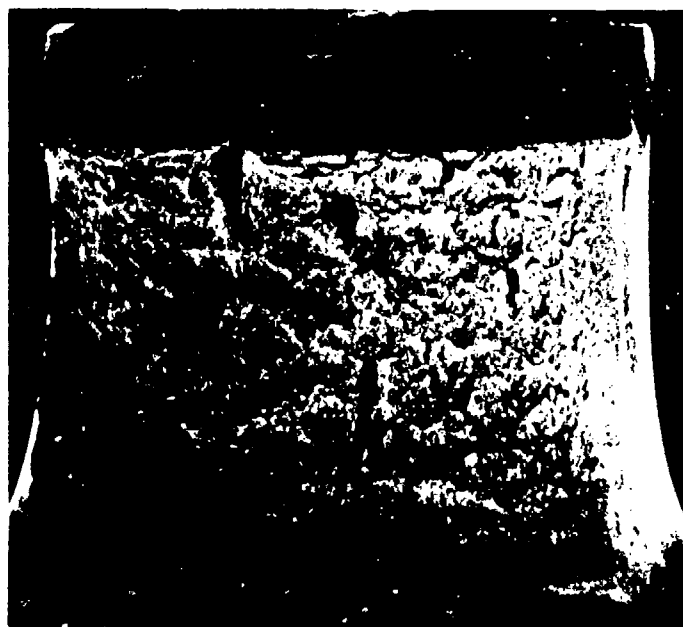
Figure 188.   Fracture surface of an A-242 longitudinal
Charpy specimen tested at 121^OC, 10x.

205
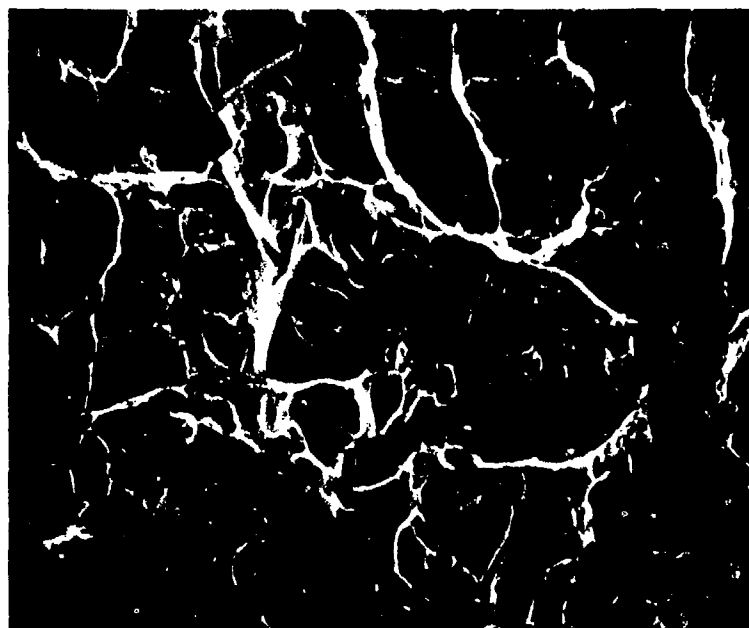
Figure 189. Cleavage fracture in an A-242 longitudinal
Charpy specimen tested at 23°C, 500x.
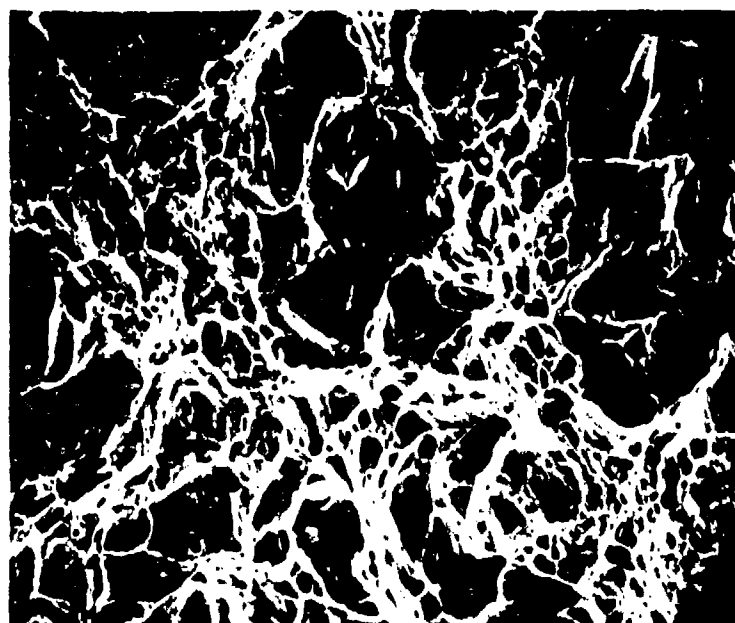
Figure 190. Dimple rupture and cleavage fracture in an
A-242 transverse Charpy specimen, 500x.

ASTM A-516

Material: ASTM A-516

Specimen Orientation(s): Longitudinal
Heat Treatment(s): As rolled
Mode of Test: Tensile
Temperature(s) of Test: 23°C
Test Results:

Mechanical Properties:

Tensile Strength, ksi (MPa)
77 (531)

Yield Strength, ksi (MPa)
40.8 (281)

Fractographic Analysis:

The fracture surface of the ASTM A-516 steel tensile specimen is
shown in Figure 191. Failure occurred as a result of inclusion gener-
ated dimple rupture. Figure 191 shows various dimple sizes and a large
inclusion.
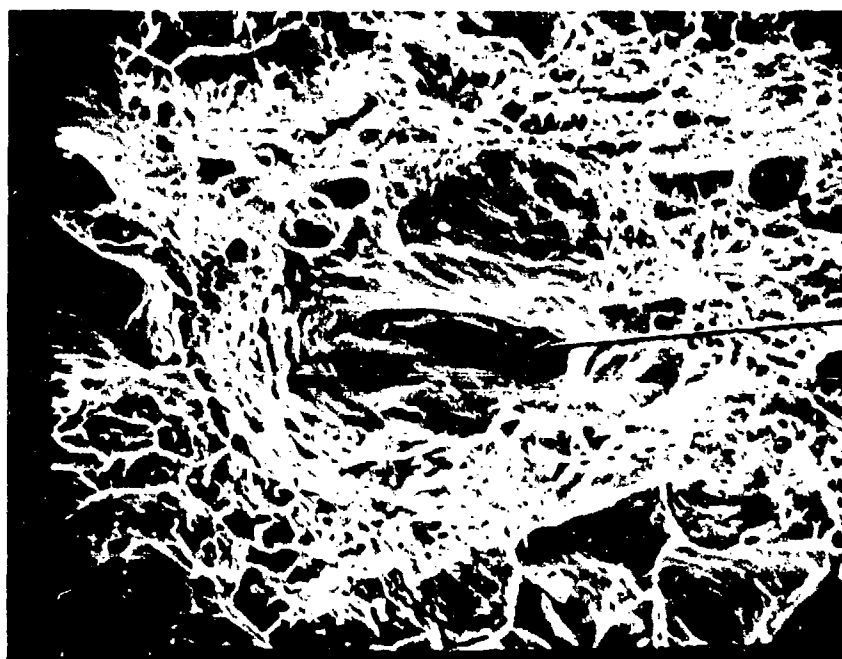
INCLUSION

Figure 191. Dimple rupture in A-516 steel, 1200x.

Material: ASTM A-516

Specimen Orientation: Longitudinal
Heat Treatment: As rolled
Mode of Test: Fatigue
Temperature of Test: $23^{\circ}C$

Fractographic Analysis:

Regions of fatigue and tensile overload can be identified on the fracture/surface of the ASTM A-516 fatigue specimen (Figure 192). Failure in the tensile overload regions occurred by dimple rupture which initiated at inclusions (Figure 193). Failure in the fatigue regions consisted primarily of transgranular fracture (Figure 194).

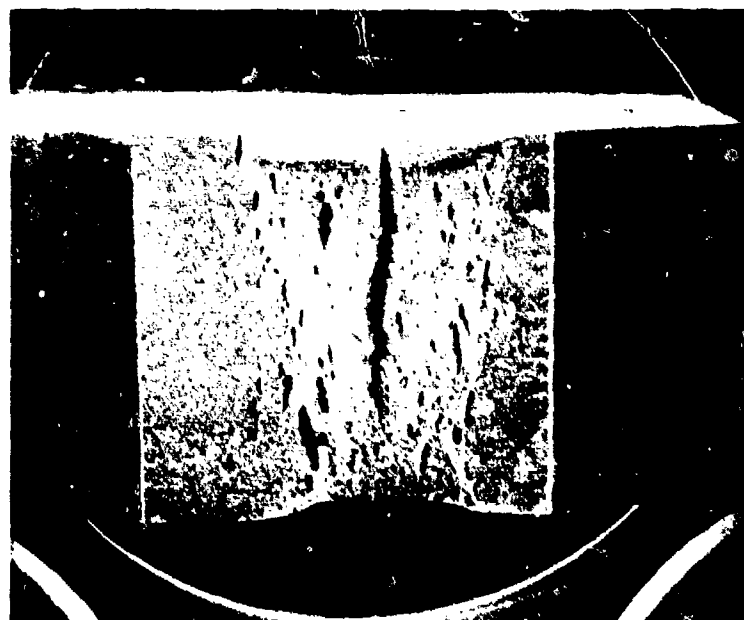Figure 192. Fatigue fracture surface of A-516 steel, 8x.

209
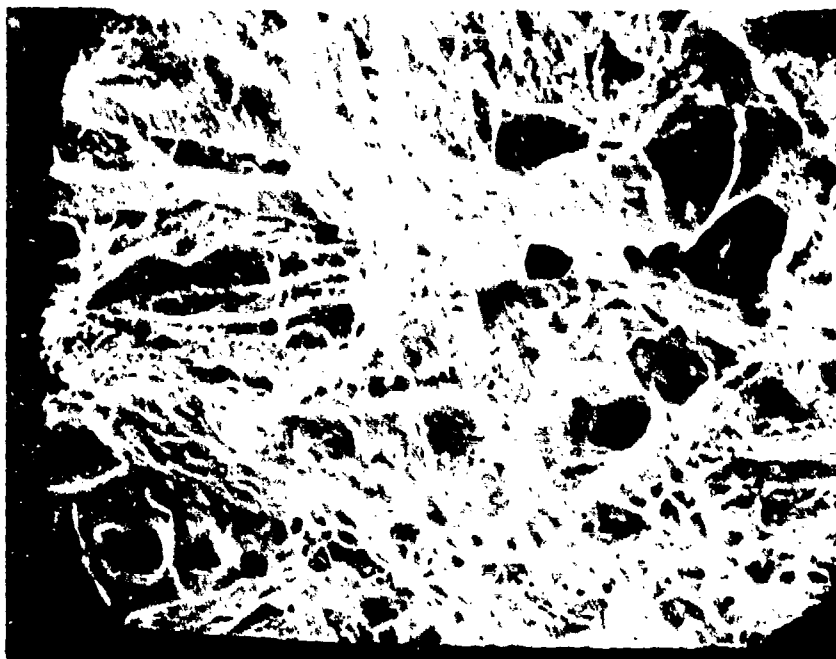
Figure 193. Dimple rupture in an A-516 fatigue specimen, 1000x.
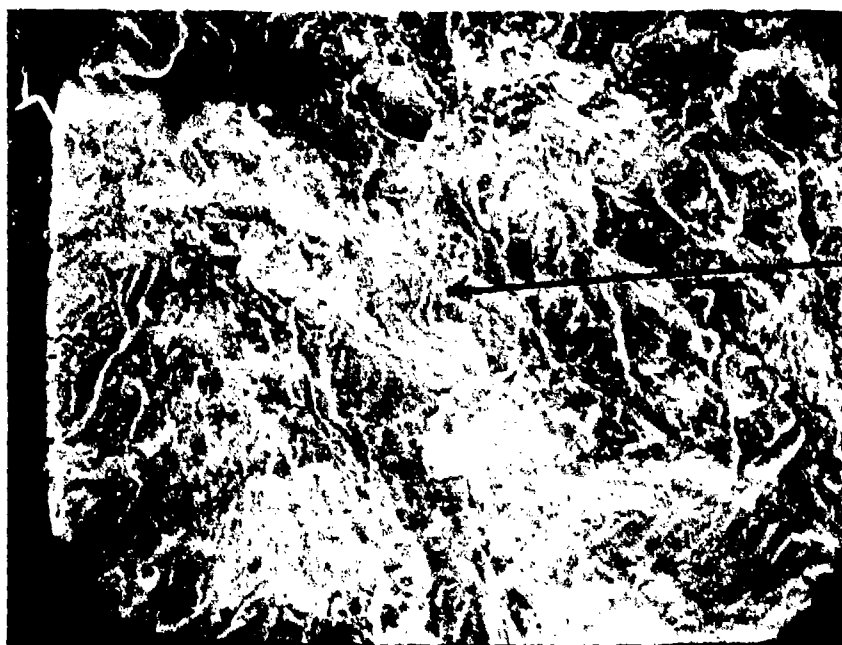
FATIGUE
STRIAE

Figure 194. Transgranular fracture in an A-516 fatigue specimen, 650x.

Material: ASTM A-516

Specimen Orientation: Longitudinal
Heat Treatment: As rolled
Hydrogen Charging Conditions

Current density: 6 mA/in.^{2} (0.93 mA/cm^2)

Charge time: 12 hours

Electrolyte: 0.3 wt% As_2O_3, 10.0 wt% H_2SO_4

Mode of Test: Tensile
Temperature(s) of Test: 23°C
Test Results:

    Mechanical Properties:

        Tensile Strength, ksi (MPa)
            78 (538)

        Yield Strength, ksi (MPa)
            42 (289)

Fractographic Analysis:

The fracture surface of the hydrogen-embrittled A-516 tensile and fatigue specimens are shown in Figures 195 and 196, respectively. The fracture surfaces were very similar to the unembrittled tensile and fatigue specimens. A fractured pearlite colony can also be identified on the fracture surface.

Regions of tensile overload and fatigue were found on the hydrogen-embrittled fatigue specimen surface. Failure occurred by dimple rupture in the tensile overload region and by transgranular fracture in the fatigue region. Some areas of fatigue striae were found in the fatigue region (Figure 197 and Figure 198).

211
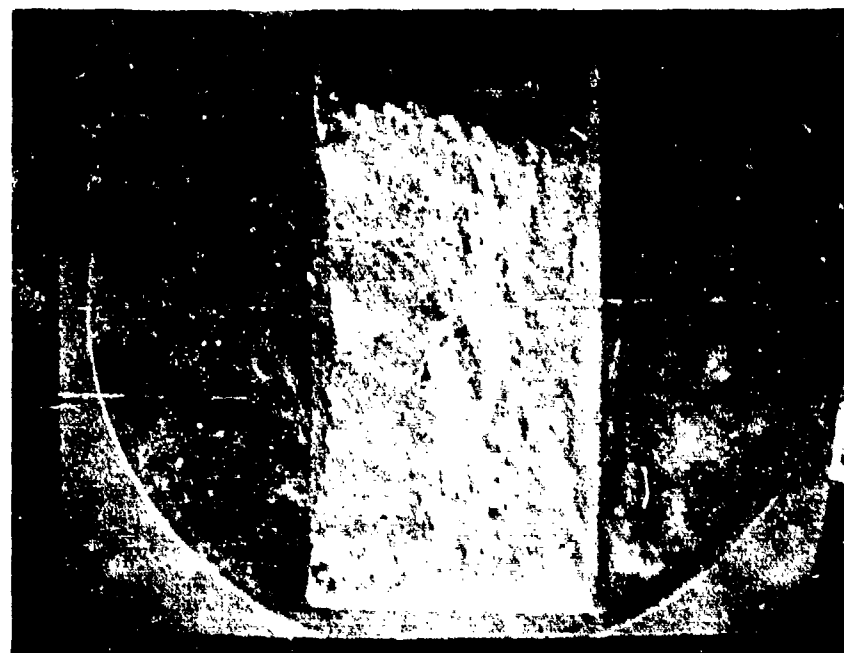
Figure 195. Tensile fracture surface of hydrogen-embrittled A-516 steel, 11x.

TENSILE
OVERLOAD
REGION
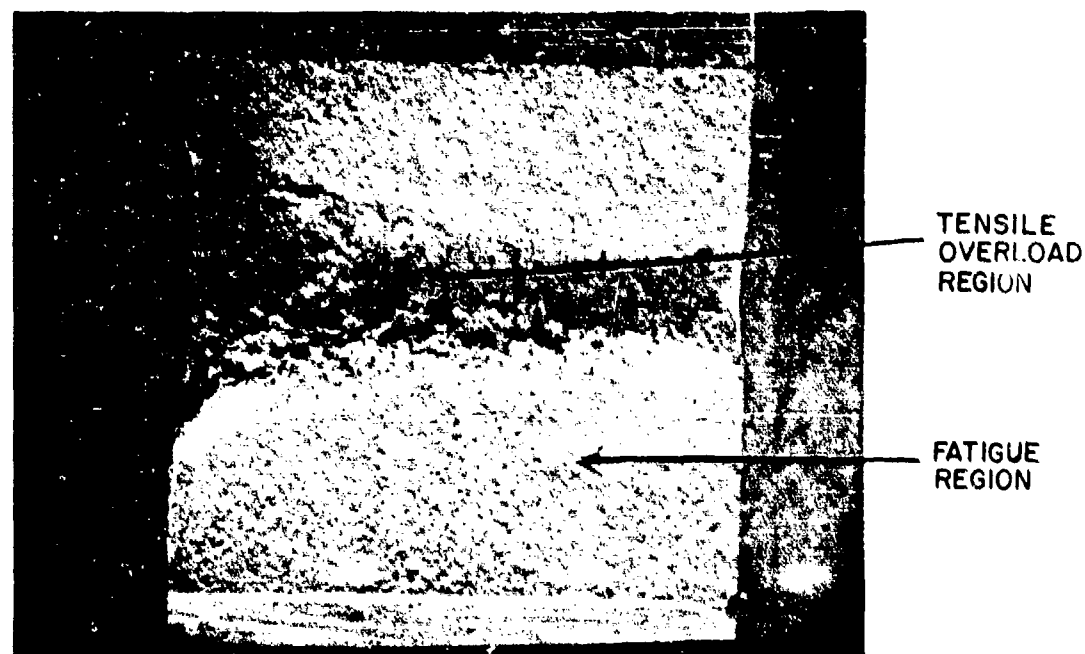
FATIGUE
REGION

Figure 196. Fatigue fracture surface of hydrogen-embrittled A-516 steel, 12x.
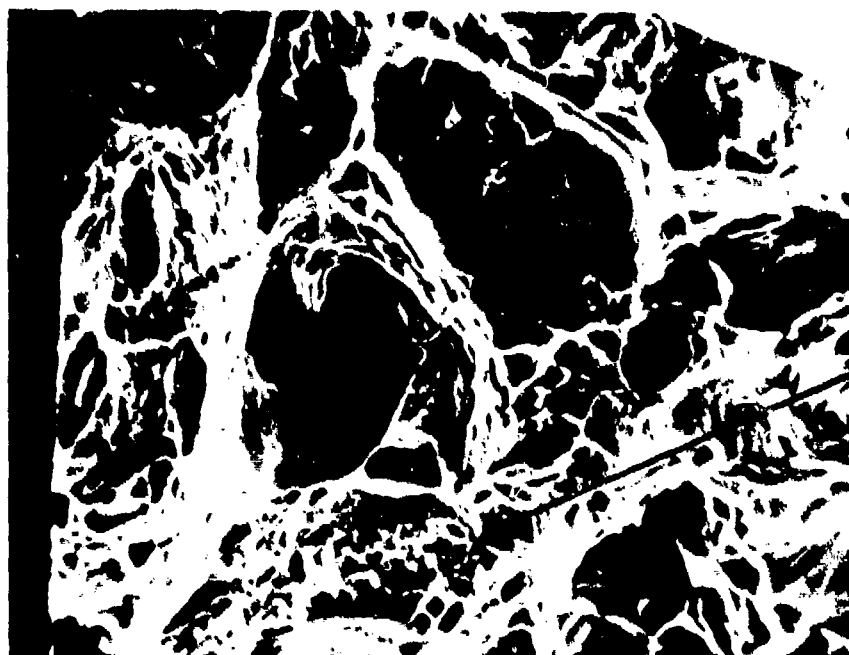
FRACTURED
PEARLITE
COLONIES

Figure 197.   Dimple rupture in a hydrogen-embrittled A-516
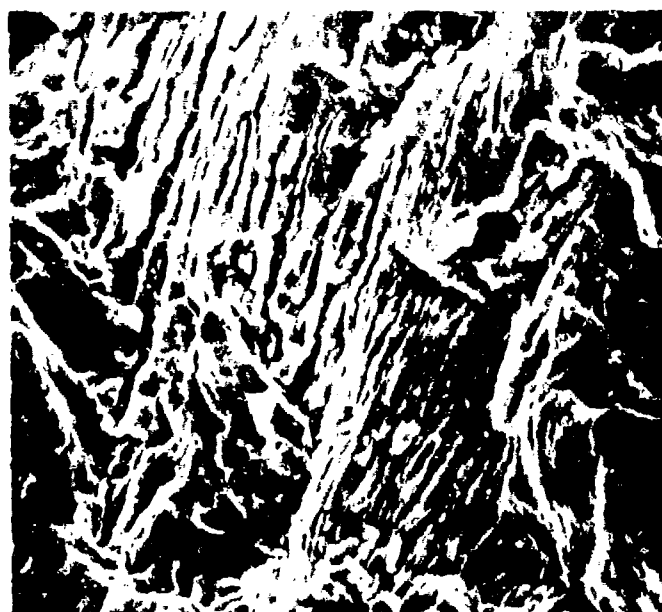steel, 800x.
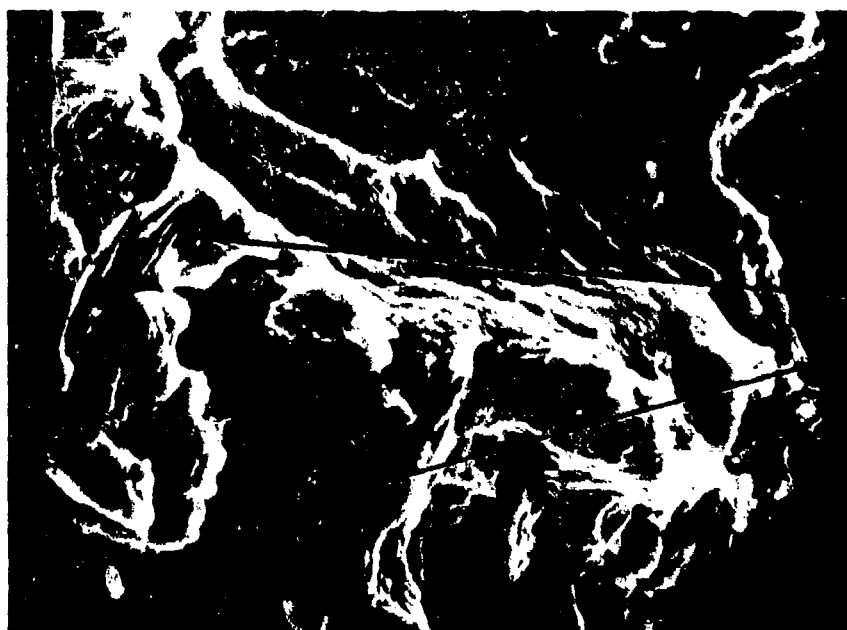
FATIGUE
STRIATIONS

Figure 198.   Fatigue striations in A-516 steel, 1800x.

Material: ASTM A-516

Specimen Orientation(s): Longitudinal
Heat Treatment: As rolled
Mode of Test: Impact
Temperature(s) of Test: -196°C, 0°C, 23°C, 121°C
Test Results:

Mechanical Properties:

	Test Temperature $^{\circ}$C	Absorbed-Energy, ft-lb(joule)
ASTM A-516	-196	2 (2.72)
	0	189 (257)
	23	178 (242)
	121	172 (234)

Fractographic Analysis:

Figure 199 shows the fracture surface of the as-received ASTM A-516 impact specimen tested to failure at -196°C. A higher magnification of the surface (Figure 200) shows that failure occurred by cleavage.

Numerous "river patterns" which represent steps between different local cleavage facets of the same general cleavage plane can be identified on the fracture surface. The impact specimens tested at 0, 25, and 100°C (Figures 201, 202, and 203) exhibited lamellar tearing caused by the presence of "stringers" (elongated inclusions) in the steel oriented perpendicular to the crack plane. As a result of these inclusions, the specimens were extremely tough and did not break completely. Photographs rather than SEM photomicrographs, are provided for these specimens.

214
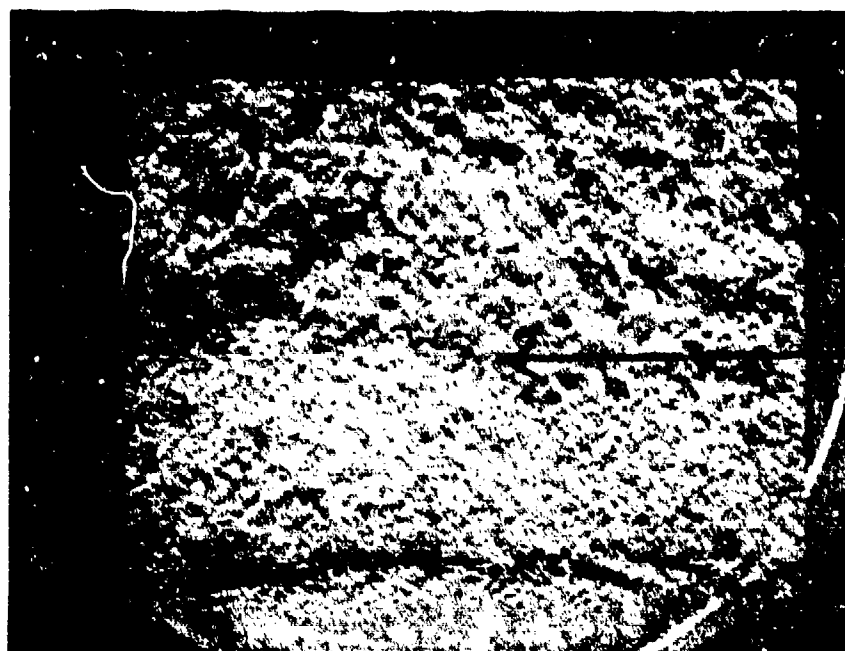
Figure 199. Fracture surface of an A-516 Charpy specimen
tested at -196°C, 1ix.
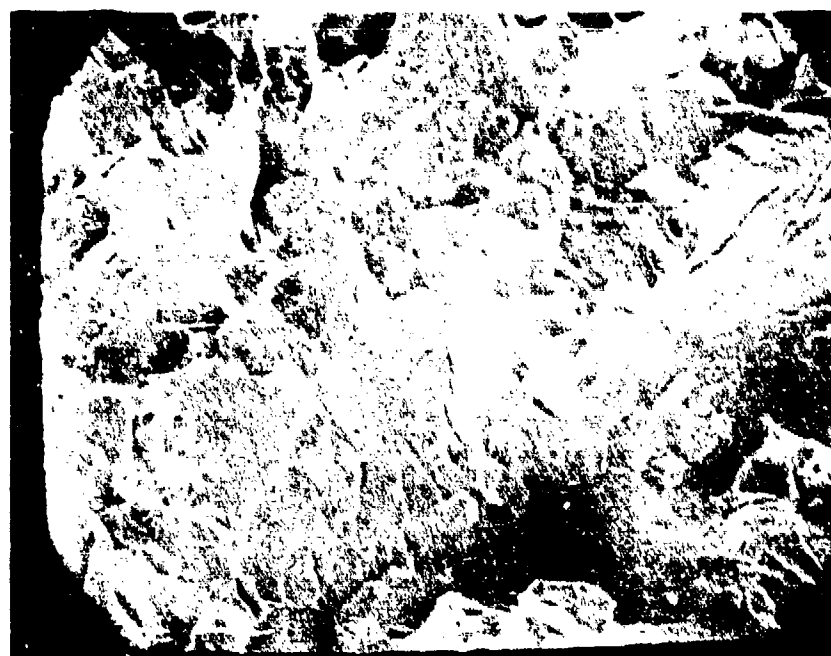
Figure 200. Cleavage facets in an A-516 Charpy specimen
tested at -196°C, 550x.

Figure 201. A-516 steel Charpy impact specimen tested at 0°C, 11x.

Figure 202. A-516 steel Charpy impact specimen tested at 25°C, 11x.
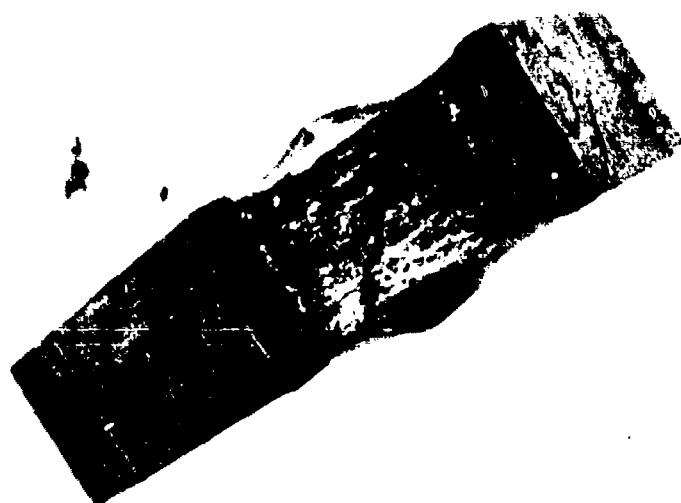
Figure 203. A-516 steel Charpy impact specimen tested at 100°C, 11x.

Material ASTM A-607

Specimen Orientation: Longitudinal
Heat Treatment: As-received pipe
Mode of Test: Tensile
Temperature of Test: 23°C
Test Results:

Mechanical Properties:

Tensile Strength, ksi (MPa)
856 (590.6)

Yield Strength, ksi (MPa)
71.2 (491.3)

Fractographic Analysis:

The fracture surface of the as-received ASTM A-607 tensile specimen in Figure 204 indicates a ductile fracture. Failure occurred by inclusion-generated dimple rupture. Figure 205 shows a higher magnification of a typical region of dimple rupture.

Figure 204.   Tensile fracture surface of A-607 steel, 11x.
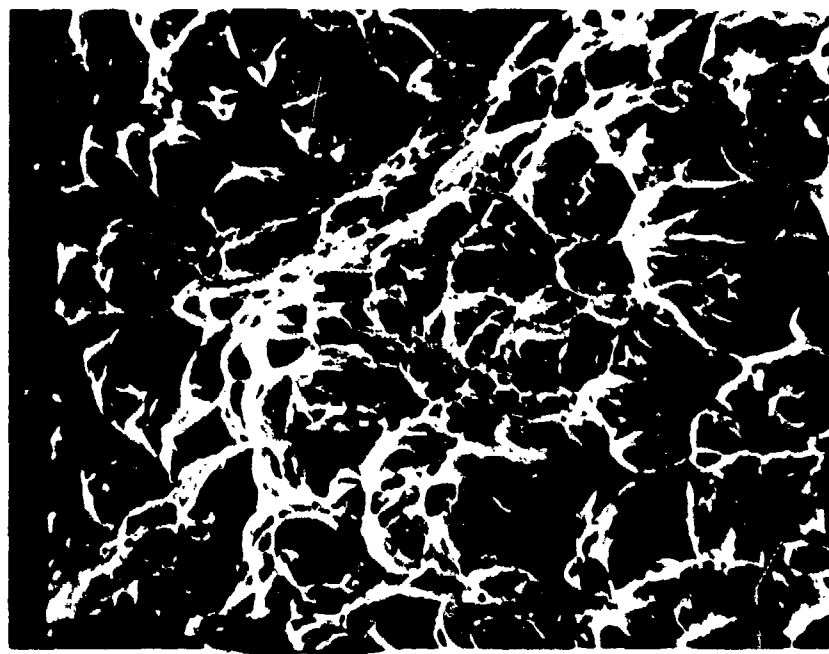
Figure 205.   Dimple rupture in A-607 steel, 800x.

Material: ASTM A-607

Specimen Orientation: Longitudinal
Heat Treatment: As-received pipe
Mode of Test: Fatigue
Temperature: 23°C
Test Results:

Fractographic Analysis:

The fracture surface of the as-received ASTM A-607 fatigue specimen shows a large fatigue region on one side, and a very small tensile over-load region and a small fatigue region on the other side (Figure 206). There is evidence of two inclusions on the side with the large fatigue region, indicating that rapid initiation of fatigue was caused by trans-granular fracture in regions where fatigue striae could be identified (Figure 207).
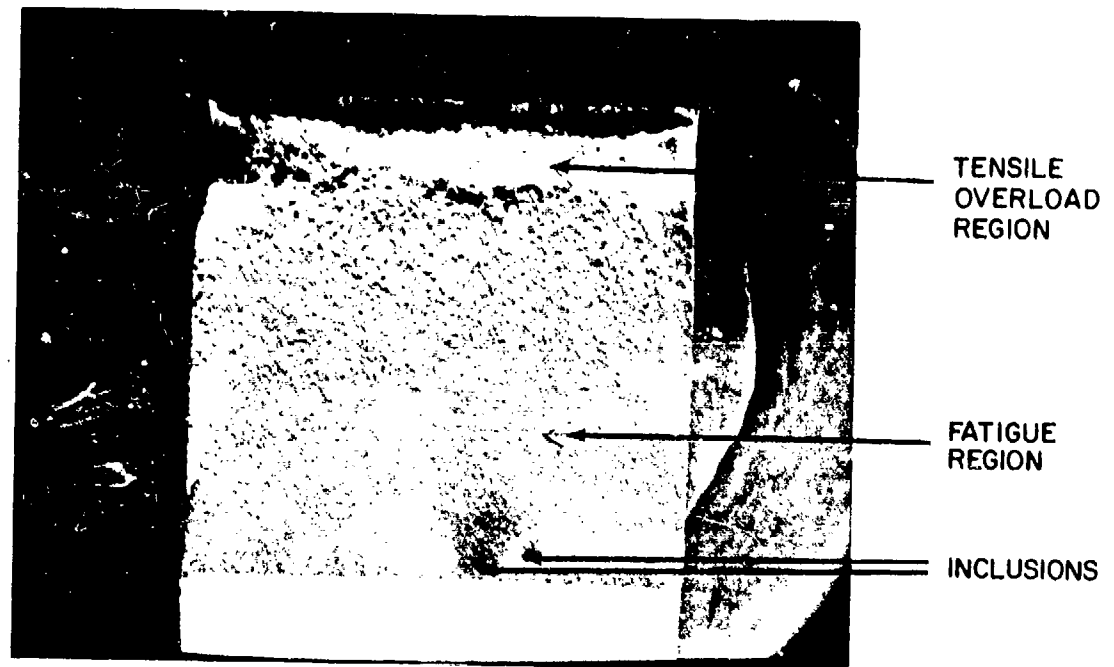
Figure 206. Fatigue fracture surface of A-607 steel, 12x.
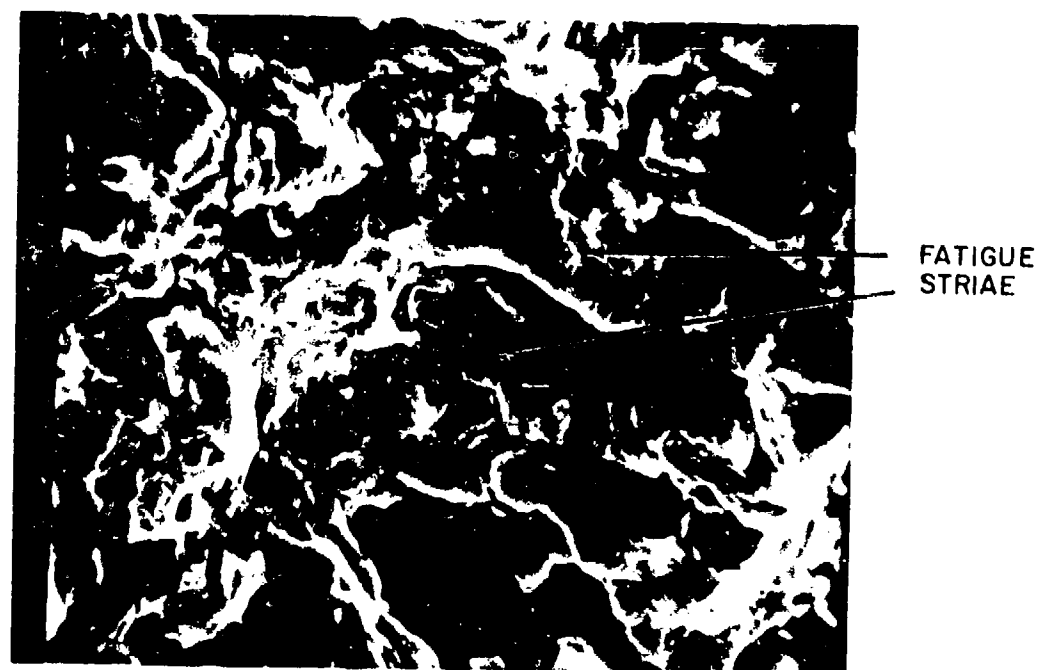
Figure 207. Fatigue striations in A-607 steel, 1000x.

Material: ASTM A-607

Specimen Orientation: Longitudinal
Heat Treatment: As-received
Hydrogen Charging Conditions:

Current density: 6 mA/in.^{2} (0.93 mA/cm^2)

Charge time: 12 hours

Electrolyte: 0.3 wt% As_2O_3, 10.0 wt% H_2SO_4

Mode of Test: Tensile and Fatigue
Temperature of Test: 23^{0}C
Test Results:

Fractographic Analysis:

The hydrogen-embrittled ASTM A-607 tensile specimen (Figure 208) demonstrated less plastic deformation than the unembrittled tensile specimen. The dimples were somewhat flatter than in the unembrittled sample. The hydrogen-embrittled fatigue specimen (Figure 209) showed a large region of fatigue on one side, indicative of an inclusion initiating rapid fatigue. More distinct fatigue striae are seen in the hydrogen-embrittled sample (Figure 210) than in the unembrittled sample.

Figure 208. Hydrogen-embrittled tensile A-607 steel specimen, 11x.

TENSILE
OVERLOAD
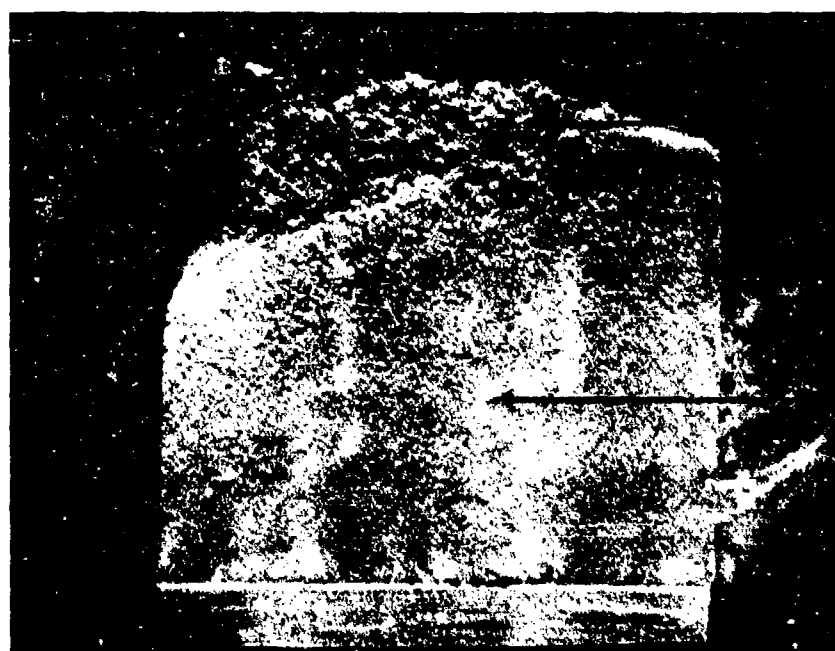
FATIGUE
REGION,

Figure 209. Hydrogen-embrittled fatigue A-607 steel specimen, 12x.
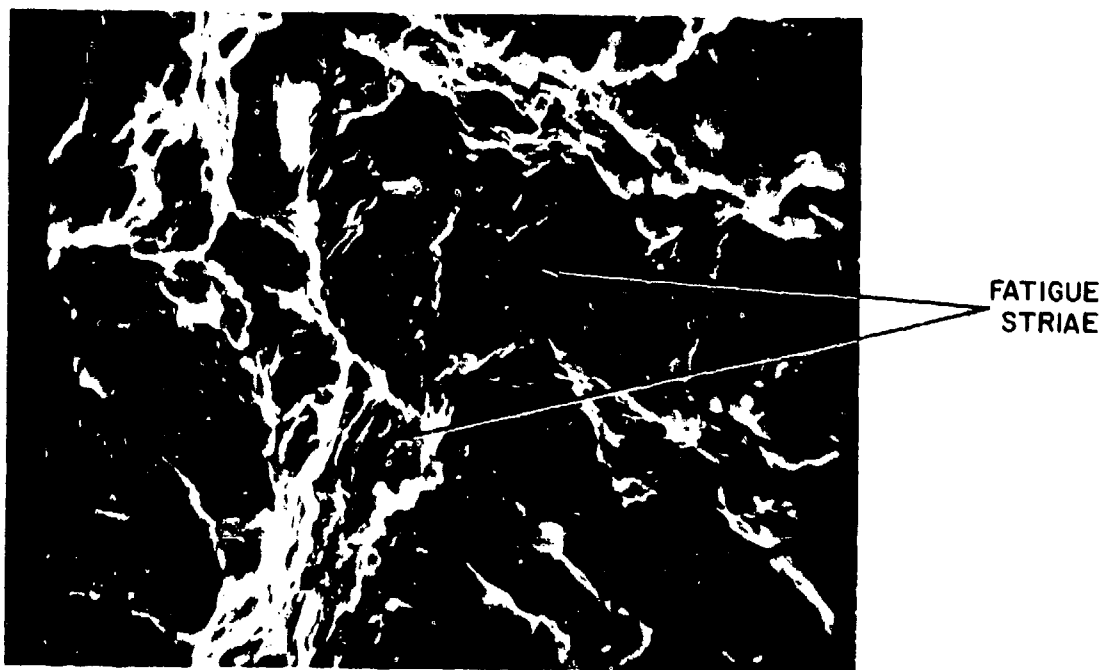
FATIGUE
STRIAE

Figure 210. Fatigue striae in a hydrogen-embrittled A-607
steel specimen, 1000x.

Material: ASTM A-607

Specimen Orientation: Longitudinal
Heat Treatment: As-received
Mode of Test: Impact
Temperature of Test: $-196^{\circ}C$, $0^{\circ}C$, $23^{\circ}C$, $121^{\circ}C$
Test Results:

Mechanical Properties:

	Testing Temperature, $0^{\circ}C$	Absorbed Energy, ft-lb (joule)
ASTM A-607	-196	2 (2.72)
	0	189 (257.04)
	25	178 (242.08)
	121	172 (233.92)

Fractographic Analysis:

The fracture surface of the as-received ASTM A-607 charpy impact specimen showed increasing plastic deformation with increasing testing temperature. Failure occurred by cleavage in the $-196^{\circ}C$ specimen (Figures 211 and 212) and by dimple rupture in the higher-temperature specimens (Figures 213 through 218).

The dimple rupture and the increase in shear lip size with increasing test temperature are evident of the increasing plastic deformation and increased ductility.
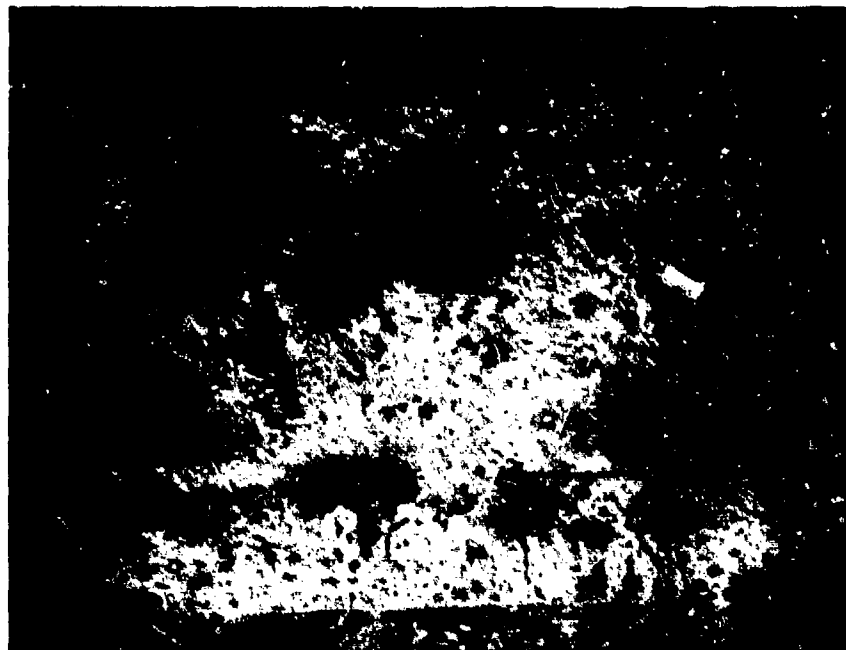
Figure 211. A-607 Charpy impact specimen tested at -196°C, 11x.
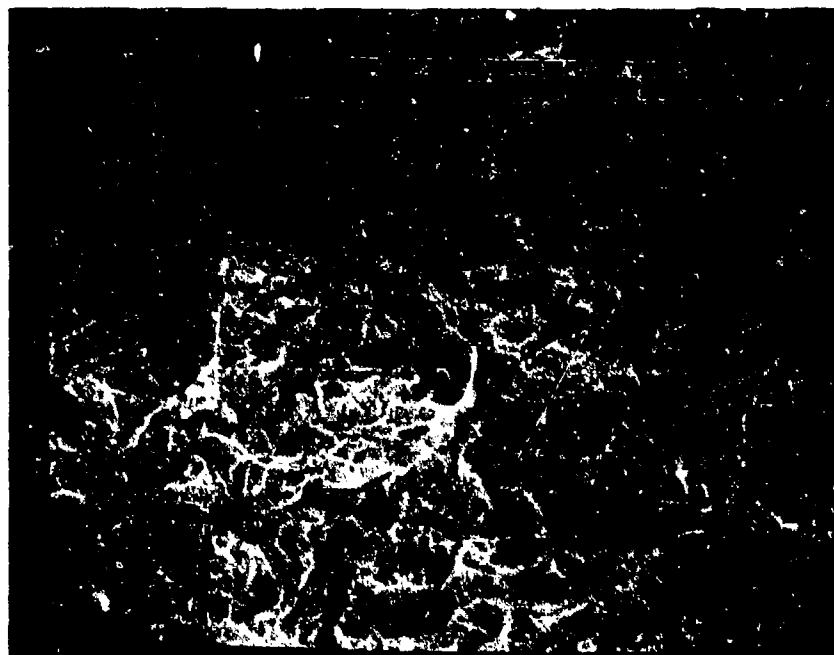
Figure 212. Cleavage facets in an A-607 Charpy impact specimen tested at -196°C, 550x.

INCLUSIONS

Figure 213.   A-607 Charpy impact specimen tested at 0°C, 9x.
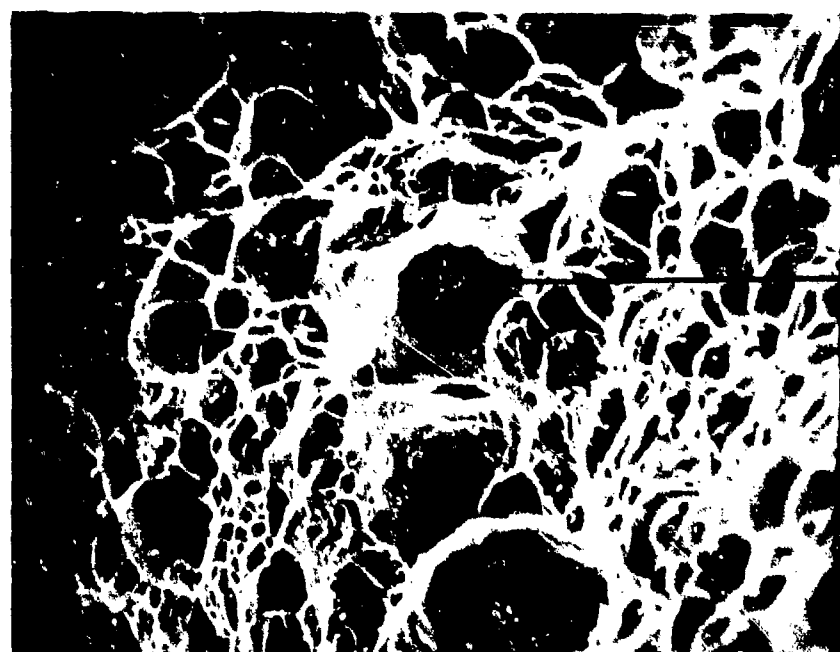
INCLUSION

Figure 214.   Dimple rupture in an A-607 Charpy impact specimen
tested at 0°C, 300x.
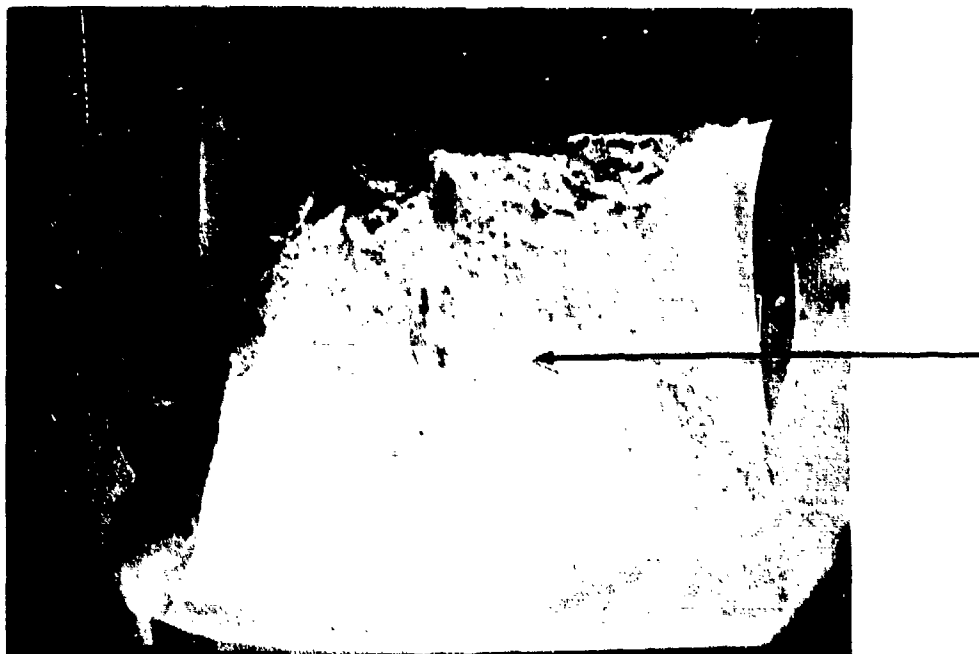
Figure 215. A-607 Charpy impact specimen tested at 25°C, 10x.
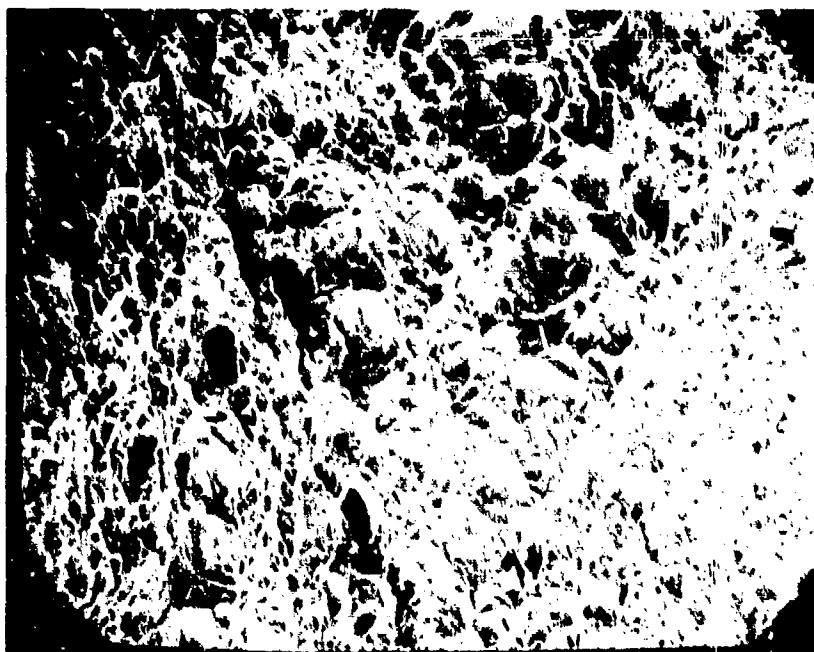
Figure 216. Dimple rupture in an A-607 Charpy impact specimen tested at 25°C, 250x.

228
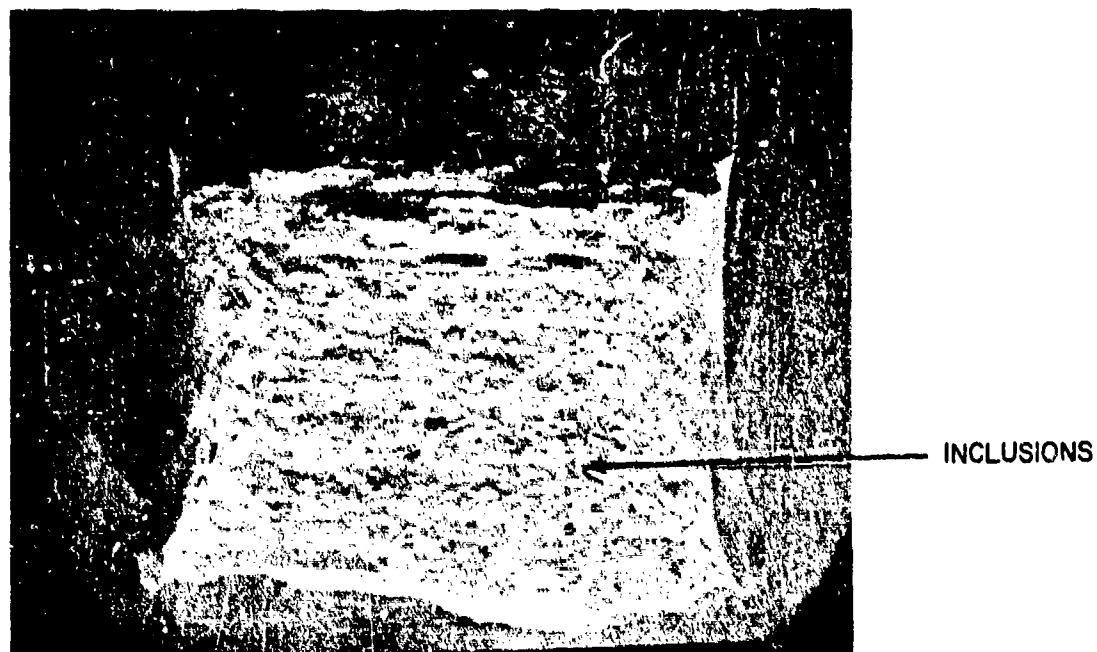
Figure 217. A-607 Charpy impact specimen tested at 100°C, 10x.

Figure 218. Dimple rupture and a large inclusion in an A-607 Charpy impact specimen tested at 100°C, 500x.

229

AISI 416

Material: AISI 416

Specimen Orientation(s): Longitudinal
Heat Treatment(s): As-quenched
Mode of Test: Tensile
Temperature(s) of Test: 23°C
Test Results:

Mechanical Properties:

Tensile Strength, ksi (MPa)
212.0 (1462.8)

Yield Strength, ksi (MPa)
168 (1159.2)

Fractographic Analysis:

The as-quenched 416 tensile specimen is shown in Figure 219. The fracture surface slanted towards a larger shear lip on one side, and some necking occurred prior to failure. The mechanisms of failure were dimple rupture and microvoid coalescence; some secondary cracking occurred (Figure 220).
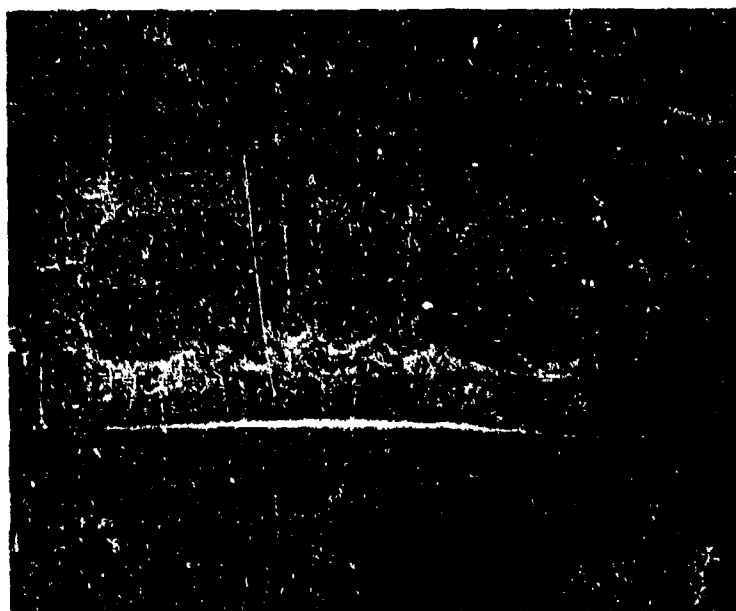
Figure 219. Fracture surface of AISI 416 specimen
tested at 121°C, 10x.

230
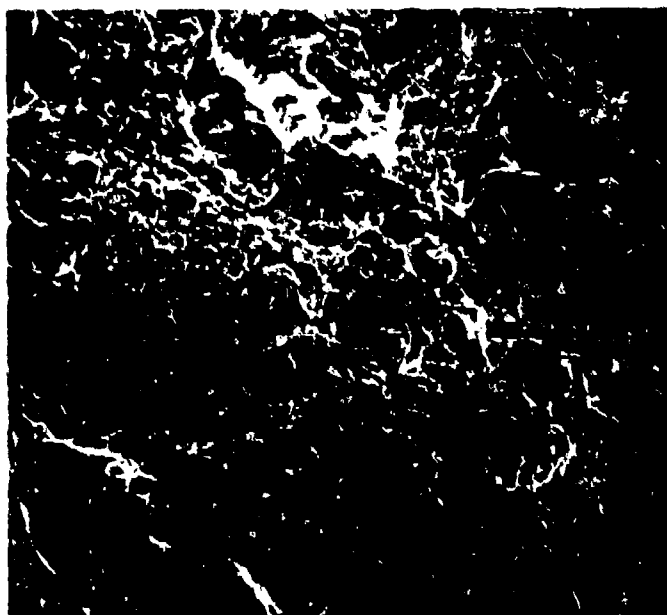
Figure 220. Dimple rupture and microvoid coalescence in a quenched 416 tensile specimen.

Material: AISI 416

Specimen Orientation(s): Longitudinal
Heat Treatment(s):

The 416 stainless steel specimens were placed in a preheated 538°C furnace, heated to 954°C, held for 30 minutes, then oil quenched. This treatment produces a microstructure consisting entirely of untempered martensite. Four groups of specimens were then tempered according to the following schedules:

1. Place in preheated 593°C furnace, temper for 1 hour, oil quench.

2. Place in preheated 316°C furnace, temper for 1 hour, oil quench.

3. Place in preheated 954°C furnace, hold for 1 hour, slow cool.

4. Place in preheated 483°C furnace, temper for 1 hour, slow cool.

Schedules 1 and 2 are normal tempering conditions; schedules 3 and 4 simulate possible embrittling conditions.

Mode of Test: Tensile
Temperatures(s) of Test: 23°C
Test Results:

Mechanical Properties:

Specimen	Tensile Strength,ksi(MPa)	Yield Strength,ksi(MPa)
416, tempered at 593°C	110.4 (761.8)	92 (634.8)
416, tempered at 316°C	193.6 (1335.8)	147.0 (1915.7)
416, tempered at 954°C	192.8 (1339.3)	120 (828.0)
416, tempered at 483°C	186.4 (1286.2)	144 (993.6)

Fractographic Analysis:

The fracture surfaces of the tempered tensile specimens were very similar to that of the as-quenched specimen. More extensive secondary cracking occurred in the specimen tempered at 593°C (Figure 221); very little secondary cracking occurred in the 316°C and 483°C specimens. The mechanisms of failure, i.e., dimple rupture and microvoid coalescence, were the same for all the tensile specimens.
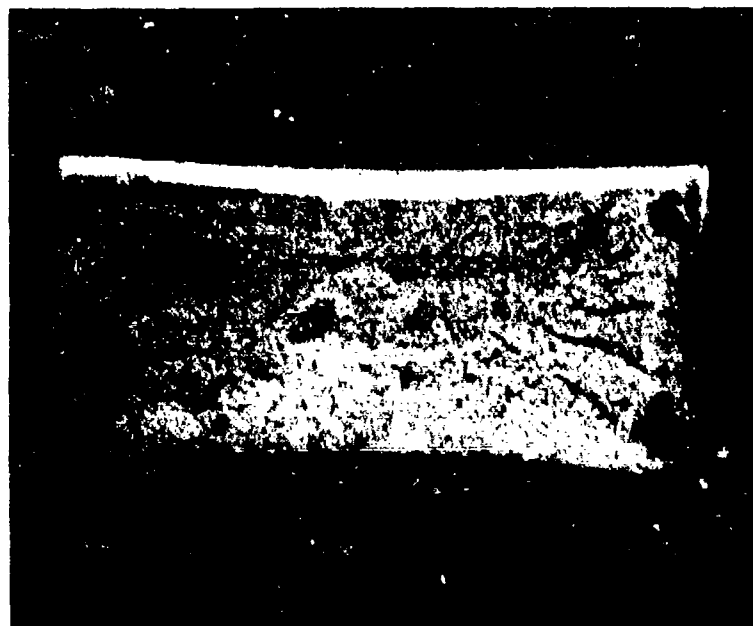
Figure 221. Fracture surface at a 416 tensile specimen tempered at 593°C, 11x.

Material: AISI 416

Specimen Orientation(s): Longitudinal
Heat Treatment(s): As-quenched
Hydrogen Charging Conditions:

  Current density: 6 mA/in.^{2} (0.93 mA/cm^2)

  Charge time: 12 hours

  Electrolyte: 0.3 wt% As_2O_3, 10.0 wt% H_2SO_4

Mode of Test: Tensile
Temperature(s) of Test: 23°C
Test Results:

  <u>Mechanical Properties:</u>

    <u>Tensile Strength, ksi (MPa)</u>
    214.0 (1479.4)

    <u>Yield Strength, ksi (MPa)</u>
    134.4 (927.4)

  <u>Fractographic Analysis:</u>

  The fracture surface of the hydrogen-charged tensile specimen was
very similar to that of the as-quenched specimen. The mechanisms of
failure were microvoid coalescence and dimple rupture.

Material: AISI 416

Specimen Orientation(s): Longitudinal
Heat Treatment(s): As-quenched
Temperature(s) of Test: 23°C
Test Results:

Fractographic Analysis:

The fracture surface of the as-quenched 416 fatigue specimen is shown in Figure 222. The very flat fracture surface was caused by quasi-cleavage (Figure 223).

Figure 222. Fracture surface of an as-quenched 416 fatigue specimen, 10x.
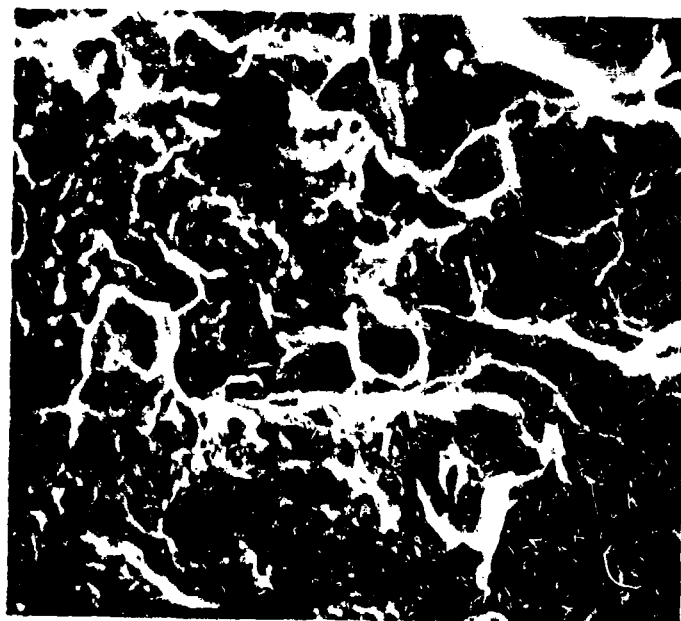
Figure 223.   Quasi-cleavage fracture in an as-quenched 416
fatigue specimen. 1400x.

Material: AISI 416

Specimen Orientation(s): Longitudinal
Heat Treatment(s): Tempered at 593°C, 316°C, 954°C, and 483°C
Test: Bending fatigue
Temperature(s) of Test: 23°C
Test Results:

Fractographic Analysis:

The fracture surfaces of all the tempered specimens closely resembled those of the as-quenched specimens. The failure in all the specimens was by quasi-cleavage. Dark areas on the low magnification micrographs of the 483°C tempered specimen were found to be very flat regions where fast fracture had evidently occurred through brittle inclusions.

Material: ASIS 416

Specimen Orientation(s): Longitudinal
Heat Treatment(s): As-quenched
Hydrogen Charging Conditions:

Current density: 6 mA/in.^{2} (0.93 mA/cm^2)

Charge time: 12 hours

Electrolyte: 0.3 wt% As_2O_3, 10.0 wt% H_2SO_4

Mode of Test: Bending Fatigue
Temperature(s) of Test: 23°C
Test Results:

Fractographic Analysis:

The fracture surfaces of the hydrogen-charged specimens closely resembled those of the as-quenched specimens. Failure in all the specimens was by quasi-cleavage. Dark areas on the low magnifications micrographs of the hydrogen-charged specimen were found to be very flat regions where fast fracture had evidently occurred through brittle inclusions.

Material: AISI 416

Specimen Orientation(s): Longitudinal
Heat Treatment(s): As-quenched
Mode of Test: Impact
Temperature(s) of Test: $-196^{\circ}C$, $23^{\circ}C$
Test Results:

Mechanical Properties:

Specimen	Testing Temperature, $^{\circ}C$	Absorbed Energy, ft-lb(joule)
416, quenched	-196	0.0 (0.0)
416, quenched	23	3.0 (4.1)

Fractographic Analysis:

The 416 as-quenched Charpy specimens were fairly brittle. At room temperature, only a very small amount of shear failure was present (Figure 224). Failure occurred from a combination of cleavage and dimple rupture (Figure 225).
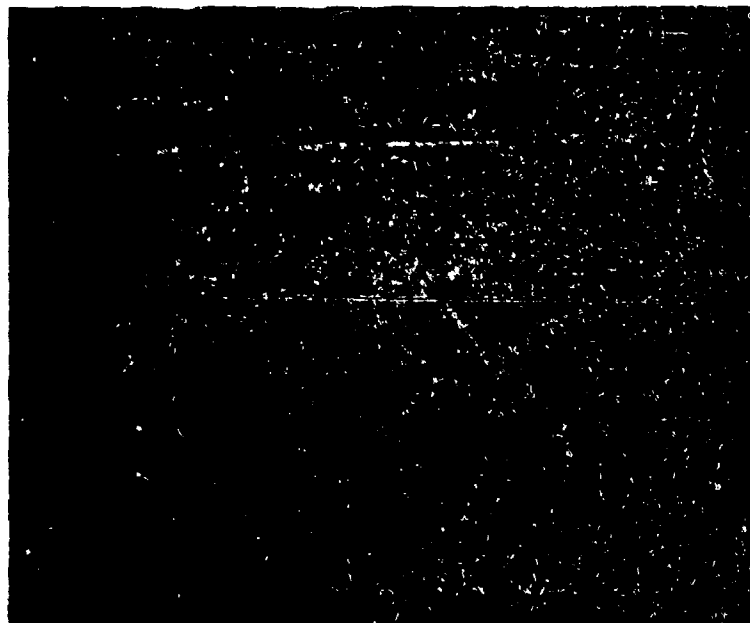
Figure 224. Fracture surface of as-quenched 416 Charpy
specimen tested at 23ºC, 10x.

240

Figure 225. Dimple rupture and cleavage fracture in an as-
quenched 416 Charpy specimen tested at 23°C, 500x.

Material: AISI 416

Specimen Orientation(s): Longitudinal
Heat Treatment(s): Tempered at 593°, 316°C, 954°C, 493°C
Mode of Test: Impact
Temperature(s) of Test: -196°C, 0°C, 23°C, 121°C
Test Results:

Mechanical Properties:

Specimen	Testing Temperature, °C	Absorbed Energy, ft-lb(joule)
416, tempered at 593°C	-196	1.5 (2.0)
416, tempered at 593°C	0	20.5 (27.8)
416, tempered at 593°C	23	18.0 (24.4)
416, tempered at 593°C	121	19.0 (25.8)
416, tempered at 316°C	-196	0.5 (.7)
416, tempered at 316°C	0	4.0 (5.4)
416, tempered at 316°C	23	3.5 (4.75)
416, tempered at 316°C	121	10.0 (13.6)
416, tempered at 954°C	23	12.5 (17.0)
416, tempered at 483°C	23	3.0 (4.1)

Fractographic Analysis:

The 416 Charpy specimens which had been tempered at 483°C and 316°C had fracture surfaces which were very similar to those of the as-quenched specimen. Failure occurred by cleavage at the lower testing temperatures and by a combination of cleavage and dimple rupture at room temperature and/or 121°C. The specimens slow cooled from 954°C or tempered at 593°C were more ductile than the other 416 Charpy specimens. Extensive secondary cracking occurred on the 954°C specimen (Figure 226), and failure occurred by dimple rupture (Figure 227). The fracture surface of the Charpy specimen tempered at 593°C and tested at liquid nitrogen temperature had a very fibrous appearance. The mode of fracture was quite complex; most of the surface failed by a combination of cleavage and dimple rupture (Figure 228), but areas of intergranular fracture were also observed (Figure 229). The specimens tested at higher temperatures failed by dimple rupture.
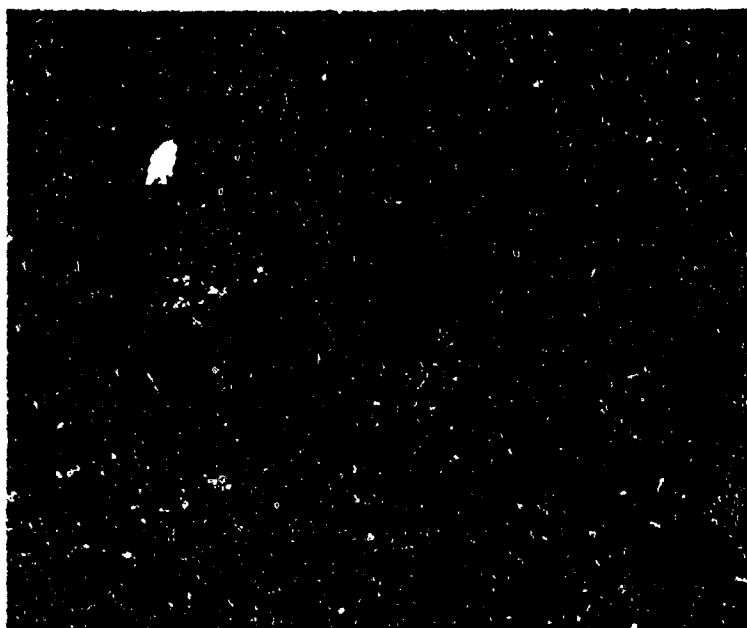
Figure 226.   Fracture surface of a 416 Charpy specimen
tempered at 954°C and tested at 23°C, 10x.
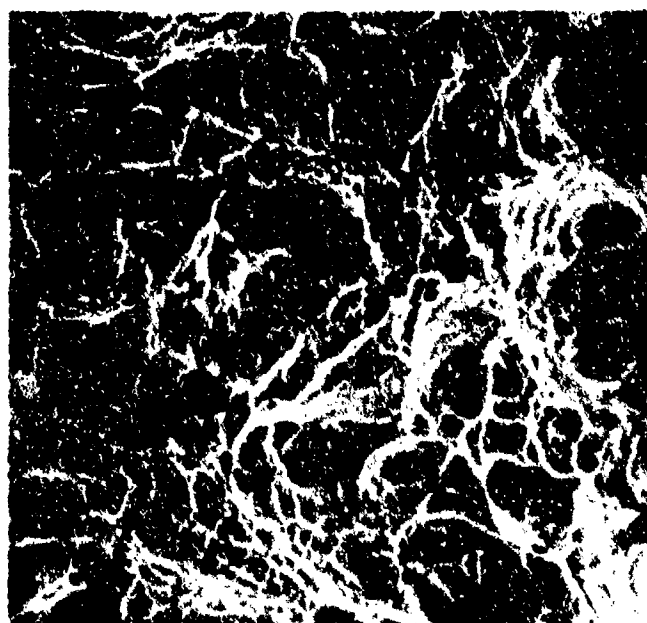
Figure 227.   Dimple rupture in a 416 Charpy specimen tempered
at 954°C and tested at 23°C, 1000x.

243
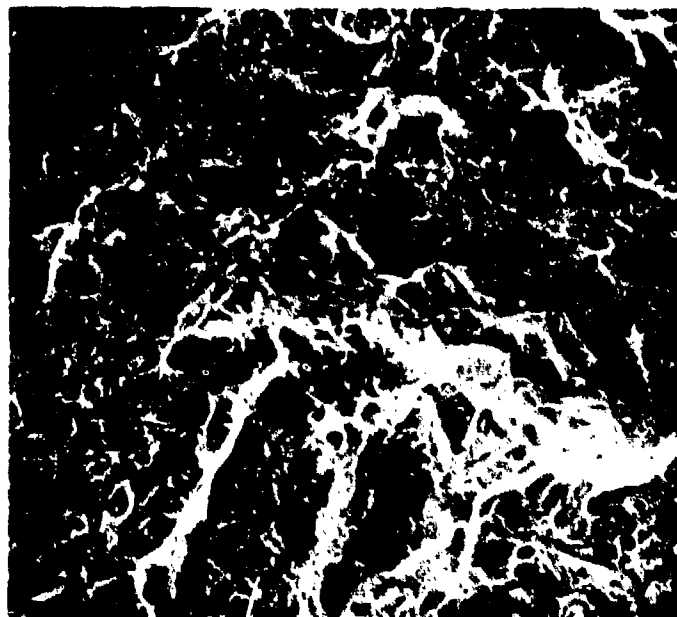
Figure 228. Dimple rupture and cleavage fracture in a 416
Charpy specimen tempered at 593°C and tested
at -196°C, 500x.
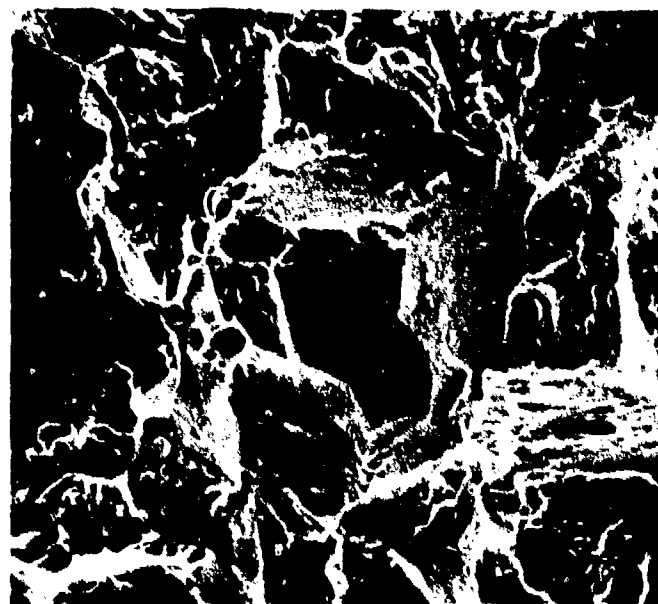
Figure 229. Intergranular fracture in a 416 Charpy specimen
tempered at 593°C and tested at -196°C, 1000x.

244

17-4PH

Material: 17-4PH

Specimen Orientation(s): Longitudinal
Heat Treatment(s): Solution heat-treated
Mode of Test: Tensile
Temperature(s) of Test: 23°C
Test Results:

Mechanical Properties:

Tensile Strength, ksi (MPa)
152 (1048.8)

Yield Strength, ksi (MPa)
97.6 (673.5)

Fractographic Analysis:

The fracture surface of the 17-4PH solution heat-treated tensile specimen is shown in Figure 230. Failure occurred as the result of dimple rupture and microvoid coalescence (Figure 231). A small amount of necking occurred before failure.

Figure 230. Fracture surface of a solution heat-treated 17-4PII
tensile specimen, 12x.
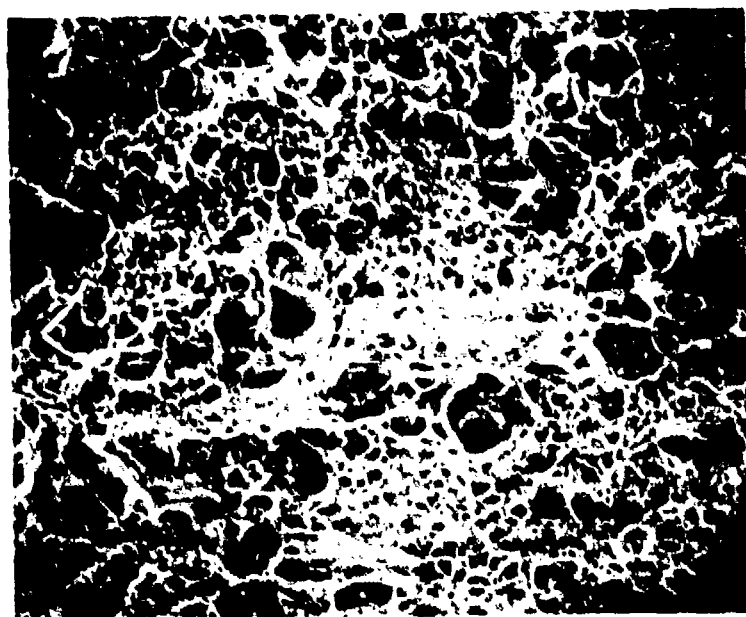
Figure 231. Dimple rupture in a solution heat-treated 17-4PH tensile specimen, 700x.

Material: 17-4PH

Specimen Orientation(s): Longitudinal
Heat Treatment(s): Solution heat-treated
Hydrogen Charging Conditions:

Current density: 6 mA/in.^{2} (0.93 mA/cm^2)

Charge time: 12 hours

Electrolyte: 0.3 wt% As_2O_3, 10.0 wt% H_2SO_4

Mode of Test: Bending fatigue
Temperature(s) of Test: 23°C
Test Results:

Fractographic Analysis:

The fracture surface of the 17-4PH hydrogen-charged fatigue specimen was quite flat. Failure occurred by quasi-cleavage.

Material: 17-4PH

Specimen Orientation(s): Longitudinal
Heat Treatment(s):

The 17-4PH specimens were solution heat-treated by a $538^{\circ}C$ preheat
followed by being heated to $1038^{\circ}C$, held for 30 minutes, then oil
quenched. Three groups of specimens were age hardened using the follow-
ing heat treatments.

1. Place in $482^{\circ}C$ preheated furnace for 1 hour, air cool.
2. Place in $538^{\circ}C$ preheated furnace for 1 hour, slow cool.
3. Place in $454^{\circ}C$ preheated furnace for 1 hour, slow cool.

Schedule 1 is a normal age hardening treatment; schedules 2 and 3
are embrittling treatments.

Mode of Test: Tensile
Temperature(s) of Test: $23^{\circ}C$
Test Results:

Mechanical Properties:

Specimen	Tensile Strength, ksi (MPa)	Yield Strength, ksi (MPa)
17-4PH, tempered at $482^{\circ}C$	164.8 (1137.1)	150.4 (1037.8)
17-4PH, tempered at $538^{\circ}C$	164.0 (1131.6)	153.6 (1059.8)
17-4PH, tempered at $454^{\circ}C$	184.8 (1275.1)	156.0 (1076.4)

Fractographic Analysis:

The fracture surfaces of the tensile specimens which were quenched
and subsequently age hardened at either $482^{\circ}C$ or $538^{\circ}C$ were very simi-
lar. Some necking occurred before failure and there were shear lips on
one or both sides (Figure 232). Extensive secondary cracking occurred
around large inclusions (Figure 233). The mechanisms of failure were
dimple rupture and microvoid coalescence (Figure 234).

Figure 232. Fracture surface of 17-4PH tensile specimen aged at 482°C, 12x.
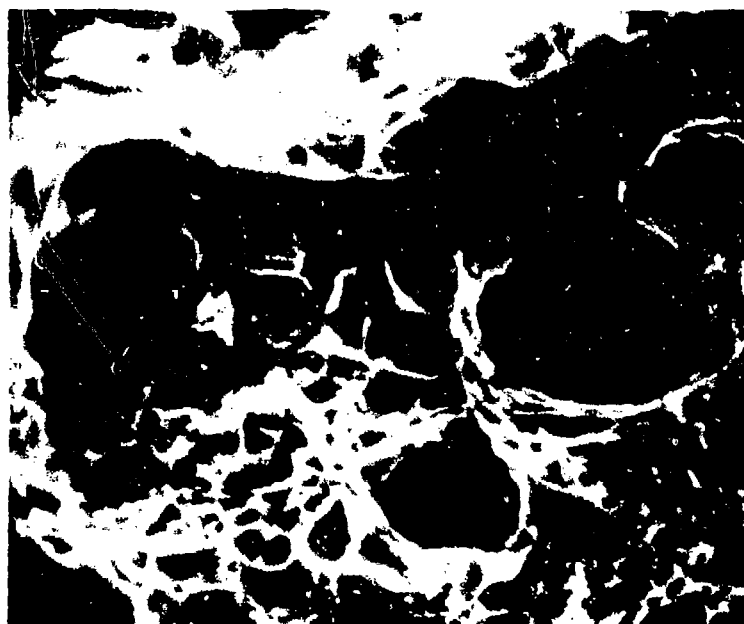
Figure 233. Inclusions in a 17-4PH tensile specimen aged at 538°C, 3500x.

250
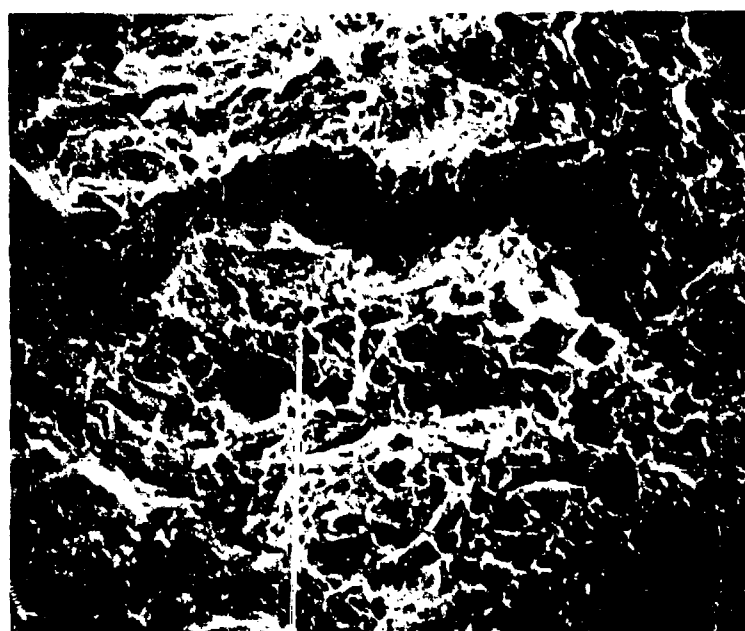
Figure 234. Dimple rupture and microvoid coalescence in a 17-4PH
tensile specimen aged at 454°C, 700x.

Material: 17-4PH

Specimen Orientaiton(s): Longitudinal
Heat Treatment(s): Solution heat-treated
Hydrogen Charging Conditions:

Current density: 6 mA/in.^{2} (0.93 mA/cm^2)

Charge time: 12 hours

Electrolyte: 0.3 wt% As_2O_3, 10.0 wt% H_2SO_4

Mode of Test: Tensile
Temperature(s) of Test: 23°C
Test Results:

Mechanical Properties:

Tensile Strength, ksi (MPa)
152.8 (1054.3)

Yield Strength, ksi (MPa)
104.0 (717.6)

Fractographic Analysis:

The hydrogen-charged 17-4PH tensile specimen is shown in Figure
235. The fracture surface slants towards a prominent shear lip on one
side. The mechanism of failure was dimple rupture (Figure 236).
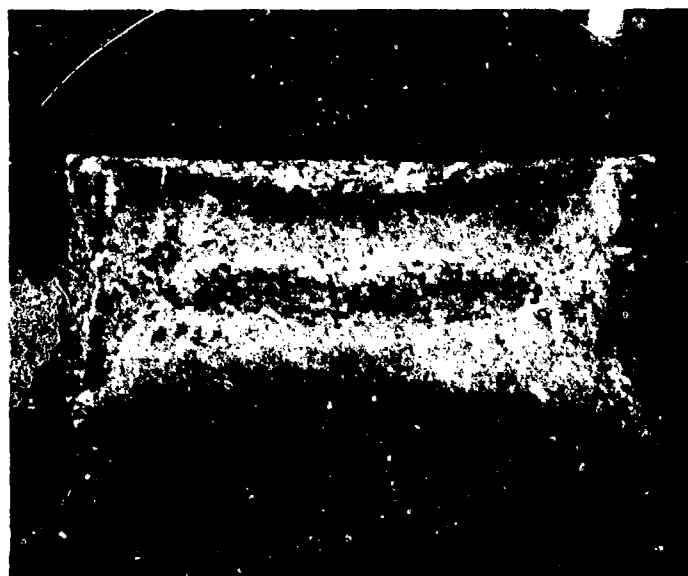
Figure 235. Fracture surface of a 17-4PH hydrogen-charged tensile specimen, 10x.
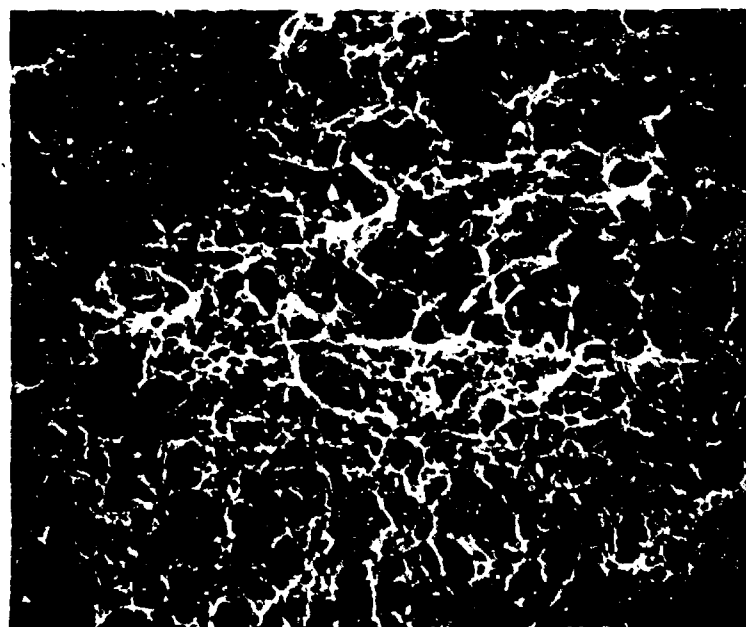
Figure 236. Dimple rupture in a 17-4PH hydrogen-charged tensile specimen, 1000x.

253

Material: 17-4PH

Specimen Orientation(s): Longitudinal
Heat Treatment(s): Solution heat-treated
Mode of Test: Bending fatigue
Temperature(s) of Test: 23°C
Test Results:

Fractographic Analysis:

The fracture surface of the quenched 17-4PH fatigue specimen was very flat (Figure 237). Failure occurred by quasi-cleavage (Figure 238).

Figure 237. Fracture surface of a solution heat-treated
17-4PH fatigue specimen, 9x.
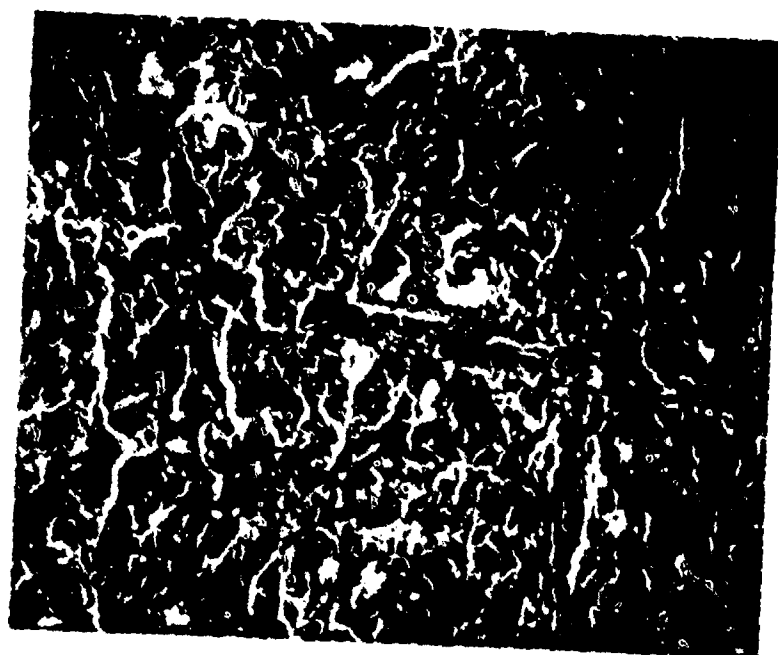
Figure 238. Quasi-cleavage fracture in a solution heat-treated 17-4PH fatigue specimen, 700x.

Material: 17-4PH

Specimen Orientation(s): Longitudinal
Heat Treatment(s): Solution heat-treated, then aged at $482^{\circ}C$, $454^{\circ}C$, or $538^{\circ}C$
Mode of Test: Bending fatigue
Temperature(s) of Test: $23^{\circ}C$
Test Results:

Fractographic Analysis:

The fracture surfaces of the 17-4PH fatigue specimens tempered at $482^{\circ}C$ (Figure 239), or $538^{\circ}C$ are all quite flat. Failure occurred by quasi-cleavage (Figure 240) in all three specimens. The $482^{\circ}C$ and $538^{\circ}C$ specimens had dark areas on the low magnification micrographs which at higher magnification was shown to be unusually flat regions (Figure 241). The appearance of this area indicated that a very low energy fracture occurred through a very brittle material or interface, probably some kind of inclusion.

257

Figure 239. Fracture surface of a 17-4PH fatigue specimen aged at 482°C, 10x.
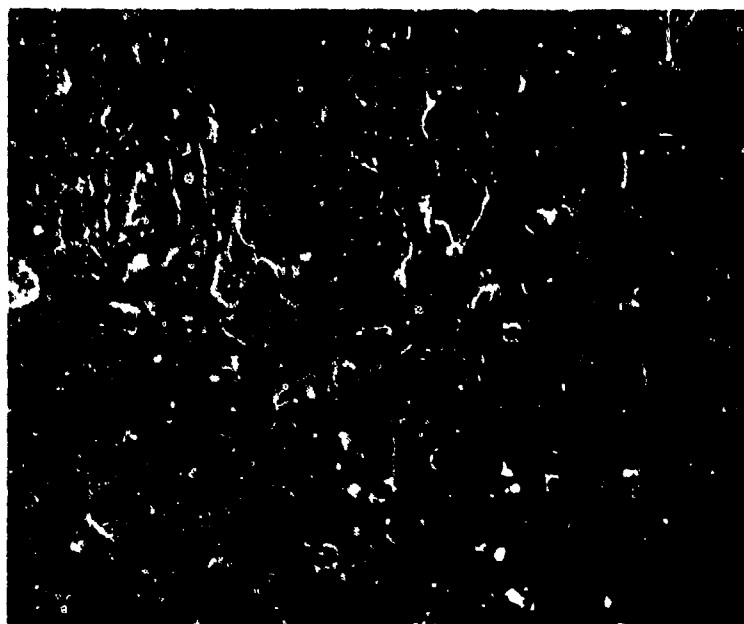
Figure 240. Quasi-cleavage fracture in a 17-4PH fatigue specimen aged at 482°C, 1000x.
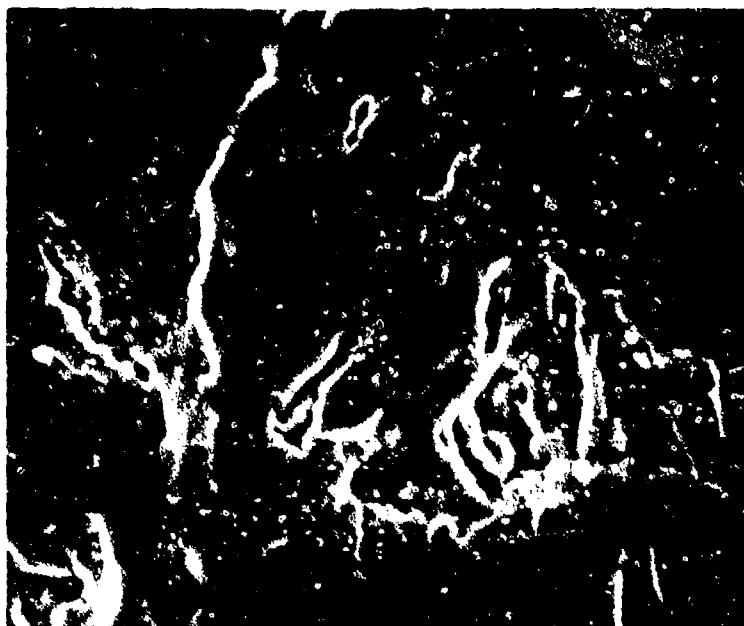
Figure 241. Brittle inclusion in a 17-4PH fatigue specimen aged at 538°C, 2500x.

Material: 17-4PH

Specimen Orientation(s): Longitudinal
Heat Treatment(s): Solution heat-treated
Mode of Test: Impact
Temperature(s) of Test: $-196^{\circ}C$, $0^{\circ}C$, $23^{\circ}C$, $121^{\circ}C$
Test Results:

Mechanical Properties:

Specimen	Testing Temperature,C	Absorbed-Energy, ft-lb (joule)
17-4PH, quenched	-196	33.0 (44.7)
17-4PH, quenched	0	66.5 (90.2)
17-4PH, quenched	23	73.5 (99.7)
17-4PH, quenched	121	82.0 (111.2)

Fractographic Analysis:

The fracture surfaces of the as-quenched 17-4PH Charpy specimens tested at liquid nitrogen, $32^{\circ}F$ ($0^{\circ}C$), room temperature, and $250^{\circ}F$ ($121^{\circ}C$) were very similar. The amount of lateral contraction and the size of the shear lips increased as the testing temperature increased and the material became more ductile (Figures 242 and 243). The liquid nitrogen specimen failed by a combination of dimple rupture and cleavage in the center and by dimple rupture in the shear lip regions. The remaining specimens failed entirely by dimple rupture.
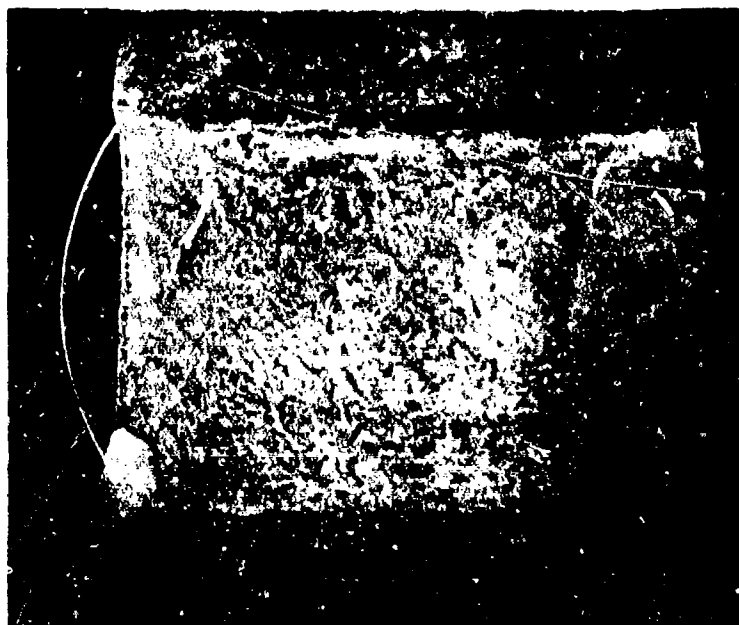
Figure 242. Fracture surface of 17-4PH solution heat-treated Charpy specimen tested at -196°C, 10x.
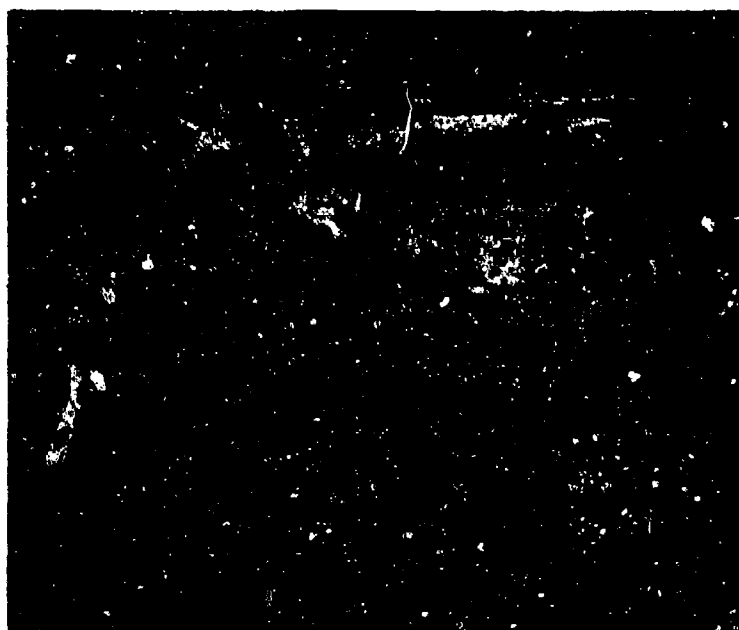
Figure 243. Fract re surface of 17-4PH solution heat-treated Charpy specimen tested at 121°C, 10x.

Material: 17-4PH

Specimen Orientation(s): Longitudinal
Heat Treatment(s): Solution heat-treated, then aged at 482°C, 538°C,
                    or 454°C
Mode of Test: Impact
Temperature(s) of Test: -196°C, 0°C, 23°C, 121°C
Test Results:

Mechanical Properties:

Specimen	Testing Temperature, ^{O}C	Absorbed Energy, ft-lb (joule)
17-4PH tempered at 482°C	-196	0.0 (0.0)
17-4PH tempered at 482°C	0	9.0 (12.2)
17-4PH tempered at 482°C	23	31.0 (42.0)
17-4PH tempered at 482°C	121	62.0 (84.1)
17-4PH tempered at 538°C	-196	2.0 (2.7)
17-4PH tempered at 538°C	23	23.0 (31.2)
17-4PH tempered at 538°C	121	62.0 (84.1)
17-4PH tempered at 454°C	-196	0.0 (0.0)
17-4PH tempered at 454°C	23	5.0 (6.8)
17-4PH tempered at 454°C	121	18.0 (24.4)

Fractographic Analysis:

The solution heat-treated and age-hardened 17-4PH Charpy specimens
were considerably more brittle than the solution heat-treated Charpy
specimens. The liquid nitrogen specimens were very flat; no lateral
contraction occurred, and failure mode was by cleavage. The ductility
and impact energy of the specimens increased with increasing test tem-
perature. The fracture surfaces of the specimens aged at 538°C and
482°C were comparable at each temperature. The fracture surfaces of the
specimens aged at 454° were less ductile than the 482°C and 583°C speci-
mens.

5 CONCLUSIONS

The fracture surfaces of steels can be characterized by scanning electron microscope. A permanent record of fracture surfaces can be obtained. The characteristic features of a fracture surface indicate the probable mode of loading which caused failure. Ductile fractures in all the steels studied were characterized by dimple rupture and microvoid coalescence. Low-temperature impact fractures were characterized by brittle fracture showing cleavage. Fatigue striations and spacing could be easily distinguished on fracture surfaces of steel specimens broken under fatigue.

GLOSSARY

crystal: A solid composed of atoms, ions, or molecules arranged in a pattern which is repetitive in three dimensions.

crystallographic plane: A plane which is formed by the atoms, ions, or molecules in a crystal.

grain: An individual crystal in a polycrystalline metal or alloy.

slip: Plastic deformation by the irreversible shear displacement (translation) of one part of a crystal relative to another in a definite crystallographic direction and usually on a specific crystallographic plane. Sometimes called "glide."

slip plane: The crystallographic plane in which slip occurs in a crystal.

slip system: A specific plane and direction in which slip occurs. Generally the slip plane is the plane of greatest atomic density, and the lip direction is the closest-packed direction within the slip plane.

REFERENCES

Aleszka, J., and Y. Kim, Fracture Characteristics of Structural Steels and Weldments, Technical Report M-170/ADA019930 (Construction Engineering Research Laboratory [CERL], November 1975).

Ault, R. T., R. B. Holtmann, and J. R. Meyers, Heat Treatment of a Martensitic Stainless Steel for Optimum Combination of Strength, Toughness, and Stress Corrosion Resistance, Technical Report AFML-TR-68-7 (Air Force Materials Laboratory, April 1968).

Beck, W., Electrochemical Technology, Vol 2 (1964), pp 74-78.

Beck, W., E. J. Jankowski, and P. Fisher, Hydrogen Stress Cracking of High-Strength Steels, NADC-MA-7140 (Naval Air Development Center, 1971).

Bernstein, I. M., "The Role of Hydrogen in the Embrittlement of Iron and Steel," Materials Science and Engineering, Vol 6, No. 1 (1970), pp 1-19.

Cotterill, P., "The Hydrogen Embrittlement of Metals," Progressive Materials Science, Vol 9, No. 4 (1961).

Forsyth, P. J. E., "Fatigue Damage and Crack Growth in Aluminum Alloys," ACTA Metallurgica, Vol 2, (1963), p 703.

"Fractography and Atlas of Fractographs," ASM Metals Handbook, Vol 9, 8th Edition (American Society for Metals [ASM], 1974).

Harrison, J. D., and G. C. Smith, British Welding Journal, Vol 14 (1967), pp 493-502.

"Heat Treating, Cleaning, and Finishing," ASM Metals Handbook, Vol 2, 8th Edition (1964), p 245.

Hydrogen Embrittlement Testing, ASTM STP543 (American Society for Testing and Materials [ASTM], 1974).

Joshi, A., and D. F. Stein, Temper Embrittlement of Alloy Steels, ASTM STP499 (ASTM, 1972), pp 59-89.

Kim, Y. G., and J. Aleszka, Fatigue Failure of Hydrogen-Embrittled High-Strength Steels, Technical Report M-143/ADA013380 (CERL, July 1975).

Laird, C., and G. C. Smith, "Crack Propagation in High Stress Fatigue" *Philosophical Magazine*, Vol 2 (1962), p 847.

Low, J. R., Jr., *Fracture of Engineering Materials* (ASM, 1964), p 127.

Low, J. R., Jr., D. F. Stein, A. M. Turkalo, and R. P. Lafarci, *Transactions of AIME*, MT6TB, Vol 242 (1968), pp 14-24.

Marcus, H. L., Jr., and P. W. Palmberg, "Effect of Solute Elements on Temper Embrittlement of Low Alloy Steels," *Temper Embrittlement of Steels*, ASTM STP499 (ASTM, 1971), pp 90-103.

McMahon, C. J., Jr., *Temper Embrittlement in Steel*, ASTM STP407 (ASTM, 1968), p 127.

Ohtani, H., H. C. Feng, and C. J. McMahon, Jr., "New Information on the Mechanism of Temper Embrittlement of Alloy Steels," *Metallurgical Transactions*, Vol 5 (1974), pp 516-518.

Petch, N. J., "The Ductile Fracture of Polycrystalline-Iron," *Philosophical Magazine*, Vol 1 (1956), pp 186-191.

Phillips, A., ed., *The Welding Handbook*, Vol 1 (American Welding Society, 1968).

Schwen, G., G. Sachs, and K. Tonk, *ASTM Proceedings*, Vol 57 (1957), pp 682-697.

Sptizig, W. A., P. M. Talda, and R. P. Wei, "Fatigue-Crack Propagation and Fractographic Analysis of 18 Ni (250) Maraging Steel Tested in Argon and Hydrogen Environments," *Engineering Fracture Mechanics*, Vol 1 (1968), pp 155-165.

Tetelman, A. S., and A. J. McEvily, Jr., *Fracture of Structural Materials* (John Wiley, 1967).

Troiano, A., "The Role of Hydrogen and Other Interstitials in the Mechanical Behavior of Metals," *Transactions of the American Society for Metals (ASM)*, Vol 52 (1960), p 52.

Warren, D. and R. D. Stout, *Welding Journal*, Vol 3, No. 8, Research Support 381-5 (1952).

Zaffe, C. A., *Journal of Iron and Steel Institutes*, Vol 154, No. 123 (1946).

APPENDIX:

FAILURE ANALYSIS CASE HISTORIES

This appendix summarizes fracture analysis studies conducted at CERL in which the SEM was an analytical tool. The experimental approach and techniques used to determine the mechanism(s) responsible for metallic fractures are outlined for four failures: (1) the exciter shaft of a diesel generator, (2) bolts in a cable assembly, (3) welded rail joints, and (4) structural support springs. The SEM was used in conjunction with optical microscopy and nondestructive and destructive mechanical tests.

1 FAILURE ANALYSIS: NORAD EXCITER SHAFT

Construction Design of Original Structure

The basic power plant at the NORAD Cheyenne Mountain Complex (NCMC) in Colorado Springs, Colorado, consists of six 950-kW, resiliently mounted diesel generator (D/G) sets. These sets are the prime source of power to the complex. The D/G units are manufactured by the Nordberg Manufacturing Company. The normal power load at NCMC is provided by three D/G units operating at 600 to 700 kW. If a breakdown of a single unit occurs, the load is switched to the remaining two operating units until unit one of the standby units becomes operational. Each unit is shut down for an oil change after 700 service hours.

Nordberg engines usually have exciters mounted on a concrete pad on the floor beside the main generator. However, because of the shock isolation needs at the NCMC, the exciters are mounted above the main generator on the same base. The operating speed of the generator is 450 rpm, while that of the exciter is 1750 rpm. A previous vibration survey conducted by the Navy Ship R&D Center (NAVSHIPRANDCEN)[21] pointed out that one-half-order and fourth-order amplitude components of the main generator dominate the spectral content of the subbase vertical vibration. This results in resonant sympathetic vibration of the exciter unit mounted on the subbase of the D/G unit. Furthermore, the D/G subbase is mounted on springs which do not attenuate vibrations as much as normal concrete pads.

Incidence of Failure

There have been five shaft failures since NCMC opened in 1965.

Specimen Received for Analysis

A shaft which broke at the fillet on 14 March 1973 was sent to CERL for analysis. The records show that the shaft had experienced a problem with the pulley turning on that shaft. NCMC had the shaft polished, the pulley bored out, and a bushing installed.

The shaft was ground on a belt and the old keyway was filled with weld metal. Gas-metallic-arc (GMA) welding was used with Linde 65 wire. The shielding gas consisted of a mixture of 75 percent argon and 25 percent carbon dioxide. The shaft was remachined. No pre- or post-heat treatment was applied, and no nondestructive inspection was performed.

---

[21] W. R. Fontaine, *Preliminary Vibration Survey of NORAD Resiliently Mounted Diesel Generator Set* (NAVSHIPRANDCEN, 1971).

Material Specifications

Engine: Manufacturer = Nordberg Manufacturing Company
           BHP = 1344 at 450 rpm (1.00 MW)
           Bore = 13 in. (0.33 m)
           Stroke = 16-1/2 in. (0.42 m)

Generator: Number of poles = 8
             Rated output = 905 kW

Exciter: Manufacturer - Ideal Electric & Manufacturing Company,
            Mansfield, Ohio

Type "D" Shunt Wound

Top Mounted

kW 15, Volts 125, Amps 120, 1750 rpm

Frame D - 364, Temperature rise - 104°F (40°C)

Laboratory Inspection Procedure

The entire exciter shaft assembly was visually inspected for evidence of corrosion, fatigue, unusual wear, nicks, or other abnormal conditions.

The broken end of the exciter shaft was inspected by dye penetrant for evidence of cracks, porosity, and other surface defects.

The fracture surface was visually inspected to determine the origin and nature of the failure. The surface was fractographically examined under a low-power bifocal microscope.

A portion of the shaft near the fracture surface was cut and etched with Nital to observe microscopic features and weld defects.

A section of the shaft near the fracture surface was cut and mounted in plastic. This piece was polished and etched and prepared for metallographic observation. The microstructure of the shaft and weld metals was determined.

The entire fracture surface of the shaft was observed under a SEM. The magnification was varied from 350x to 4,000x to resolve the details on the fracture surface.

A section of the shaft was cut near the fracture surface and hardness was measured with a Rockwell Hardness Tester.

A section of the shaft was cut and sent to Materials Research Laboratory, Glenwood, IL, for spectrochemical analysis.

Laboratory Test Results

Visual Inspection of Entire Shaft

The entire shaft assembly after shipment to CERL is shown in Figure A1. The failure appeared typical of rotating bending fatigue fractures. In the general area of the failure there were no nicks, tool marks, etc., which would indicate abuse. There was no evidence of corrosion. The fracture surface consisted of a dull "off center" ductile fracture surrounded by high cycle fatigue markings. The shaft broke at the fillet, which is vulnerable to fatigue crack failure because the stress concentration is high. The keyway stops 1-1/2 in. (3.81 cm) before the fillet, which is a good design practice, otherwise the keyway would cause even more stress concentration.

Dye Penetrant Inspection

The shaft was cleaned and dye penetrant inspected (Figure A2). This examination revealed an abundance of weld porosity and a shallow crack on the surface, although no deep cracks were found. The largest pore was about 1/16 in. (1.59 mm) in diameter, and the surface crack was about 3/4 in. (1.91 cm) in length.

Visual Inspection of the Fracture Surface

The fracture initiated at a fillet where the diameter was reduced from 2.1 in. to 1.9 in. (5.33 cm to 4.83 cm). The fracture surface showed an "off center" ductile fracture area surrounded by fatigue-marked zones. The fracture markings were typical of high cycle-low stress bending fatigue. The fracture surface, as shown in Figure A3, can be divided into three zones based on appearance. Zone 1 shows the weld metal on the surface. The thickness of the weld metal is not uniform and varies from 0 to 1/16 in. (1.59 mm). A crack can be observed in the surface layer that propagated inwards. When the load-carrying cross section of the exciter shaft was reduced below a critical size, the shaft failed by ductile fracture as shown in Zone 3.

Macroetch Observation

A section of the shaft near the fracture surface was cut, etched lightly with Nital and observed under a low-power microscope for weld defects. The results are shown in Figure A4a. The base metal, the weld metal on the surface, the weld metal in the keyway, and the heat-affected zone can be easily distinguished. The thickness of the weld metal is not uniform and varies from 0 to 1/16 in. (1.59 mm). The circumferential depth of the heat-affected zone is about 3/8 in. (9.53 mm). The weld metal in the original keyway shows a lack of fusion in one of

271

the corners. For comparison, the other end of the shaft was cut and etched with Nital (Figure A4b). The macrostructure is uniform throughout the cross section. A piece was removed from the failed end of the shaft, mounted in plastic, and polished. The polished piece was etched with Nital and observed in a low-power microscope for defects in the weld metal (Figure A5). The weld metal contained many defects: the original rebuilt keyway had weld porosity as well as lack of fusion. It is significant that the weld metal had macrocracks just below the surface. Obviously, such cracks will not be detected by dye penetrant inspection since they do not reach the surface.

Metallographic Examination

A portion of the shaft was cut off, polished, and etched for metallographic observation. The microstructure is shown in Figure A6. The microstructure of the base metal (Figure A6a) consists of ferrite with pearlite within the grains. The grain size as determined by standard ASTM grain size number is 3, which is a larger grain size than normally found in items of this nature. The microstructure of the weld metal is shown in Figure A6b. The microstructure shows most pearlite with a very small amount of ferrite at the grain boundaries, which is typical of the weld metal.

Scanning Electron Microscope Examination

The fracture surface was cleaned and observed with an AMR 900 SEM for characteristic features. The weld metal on the surface had a granular appearance as shown in Figure A7. Hot cracks, which are significant in that they can reduce the fatigue life considerably, were observed. The hot cracks were pronounced and appeared deep when observed under a stereoscope. The SEM micrographs were taken in Zone 1 of Figure A3. The fatigue striations were observed in weld metal and in base metal as shown in Figure A8a. The fatigue striations in the weld metal were wavy and appeared to follow colonies of pearlite (Figure A8). The fatigue striations in the base metal were rather long and straight. (Figure A8b).

Hardness Traverse

The average hardness of the shaft metal is Rockwell B (RB) 88. The hardness of the weld metal approached RB 94 in the keyway. A section of the shaft was removed from the back end of the shaft and its hardness was uniform and averaged about RB 88. Thus, the hardness of the weld metal was RB 94 as compared to RB 88 for the base metal.

Spectrochemical Analysis

The material was found to meet the chemistry requirements for AISI 4130 steel.

Discussion of Results

Figure A3 shows that the shaft failed at a fillet in rotating bending. Fillets and changes in diameter create a stress concentration.

As observed in Figure A5 and the SEM micrographs in Figure A7, the rebuilding of the shaft by welding introduced hot cracks, macrocracks, and porosity. These surface defects are extremely harmful because they reduce the fatigue life by providing sharp cracks which can propagate. Thus, the rebuilt shaft weld metal provided a reservoir of defects which reduced the fatigue life considerably.

The welding operation introduces residual stresses that are alternately compressive and tensile in nature. The presence of a tensile stress immediately beneath the surface weld metal layer increases the propagation rate of the cracks in the surface weld metal. Furthermore, the heat-affected zone was rather large, as shown in Figure A3. The sudden heating and cooling of welding affects the mechanical properties of the base metal. The large-grained ferrite and pearlite microstructures signify that a higher austenitizing temperature was used. Reheating this structure followed by a sudden cooling of the heat-affected zone could cause deterioration in the fracture toughness and fatigue resistance. Since the desired microstructure is a tempered martensite, the failure can also be attributed to improper heat treatment.

Since three other shafts which were not rebuilt also failed on Unit No. 1, which this shaft failed on, it appears that Unit No. 1 was a significant factor in the failures. Unit No. 1 probably has an excessive vibration problem and/or a misalignment. The vibration analysis conducted by Navy Ship R&D Center showed that the one-half-order and the fourth-order harmonics of the D/G unit whose speed is 450 rpm are rather large.

Since the exciter speed is 1750 rpm, it has a tendency for sympathetic resonance vibration. The vibration problem is rather extensive on all the units as bolts connecting the exciter base plate and the support plate have often fractured. The vibration could be reduced if a gusset was attached as shown in Figure A9.

Another cause of bending could be misalignment of the exciter shaft with respect to the generator shaft. At present, the alignment procedure consists of using a straightedge to line up the exciter pulley with the generator pulley. The same straightedge has two marks distance 'D' apart which are used to set the distance of the bolts on the exciter mounting plate and the support plate (Figure A9). It is recommended that the alignment procedure be modified. The straightedge should be made as wide as the exciter pulley. The parallelism of the pulley faces should be checked by slowly rotating the exciter pulley and noting the clearance between the exciter pulley and the straightedge held against the generator pulley. The present alignment

272

procedure does not check the eccentricity between the pulleys and the shafts of the generator or exciter. A special tool, which will circumvent the obstructions, should be fabricated to check the parallelism of the exciter shaft with the generator shaft. A misalignment between the two shafts could give rise to bending stresses resulting in the type of fatigue failure observed in rotating bending.

Conclusions

The mode of failure of the exciter shaft was determined to be rotational bending fatigue.

The presence of macrocracks in the surface weld metal reduced the fatigue life of the rebuilt exciter shaft considerably.

The alignment procedures are not sufficient to assure the parallelism between the exciter shaft and the generator shaft.

Recommendations

1. A rebuilt exciter shaft should not be used.

2. A log of the service life of each shaft should be kept so that a suspect unit with a misalignment and/or vibration problem can be identified definitely.

3. A gusset should be attached between the exciter shaft mount and the D/G subbase. The gusset could be a 2-in. (5.08-cm) diameter pipe welded or riveted at the ends to the structures. The gusset will reduce the rotation of the exciter mount assembly around the D/G subbase. This will also reduce bolt breakage on the exciter plate because of reduced vibrations.

4. The straightedge used to line up the exciter pulley with the generator pulley should be made as wide as the exciter pulley. A light source should be used to check the clearance between the aligning straightedge and the exciter pulley.

5. It is recommended that one end of the straightedge be held against the generator pulley and the exciter pulley slowly rotated at the other end to obtain a uniform contact.

6. The alignment procedure should include checking the parallelism of the generator shaft and the exciter shaft. A special tool should be made which contacts the generator shaft at the lower end and the exciter shaft at the upper end.
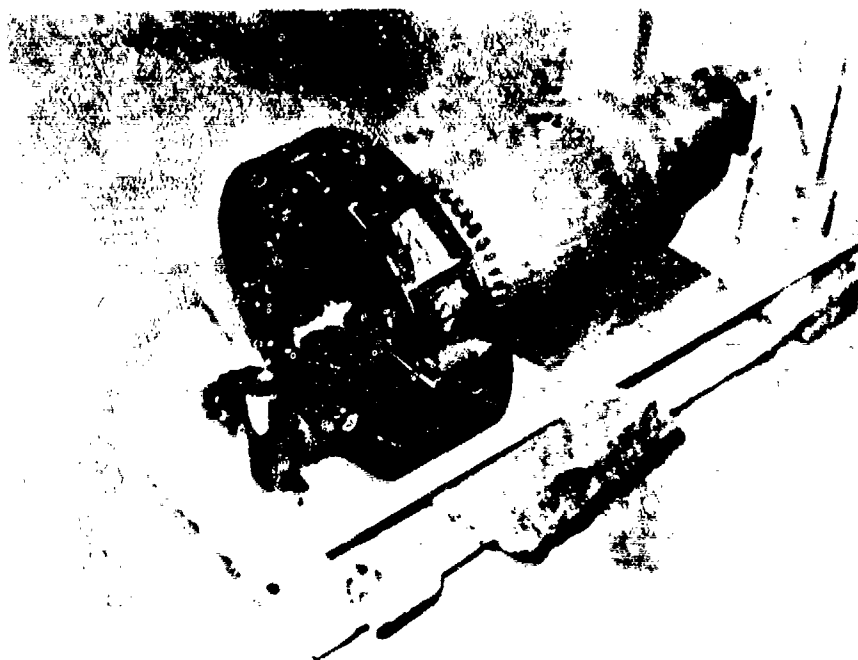
Figure A1. Failed exciter shaft as received by CERL.
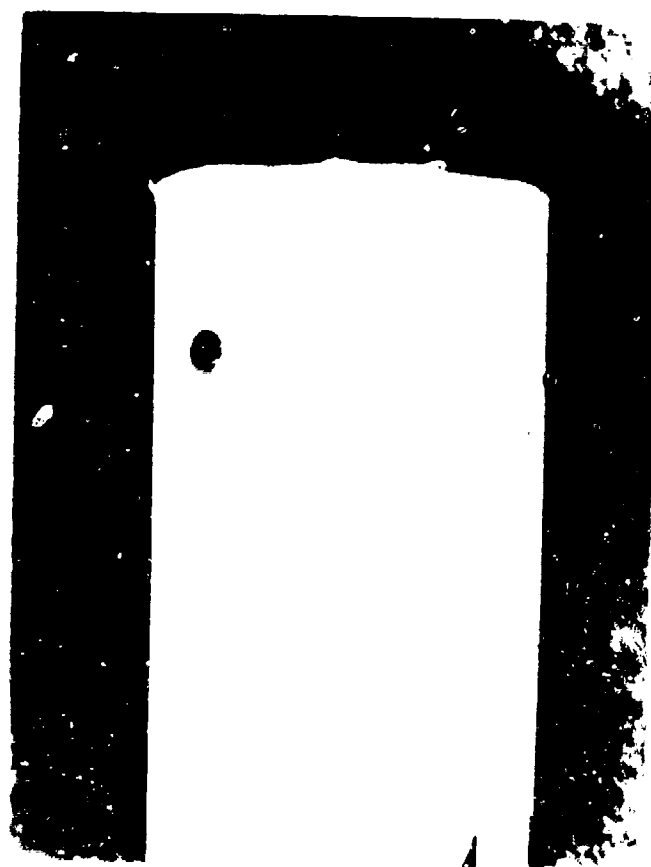
Figure A2. Dye penetrant inspection of the broken end of the exciter shaft.
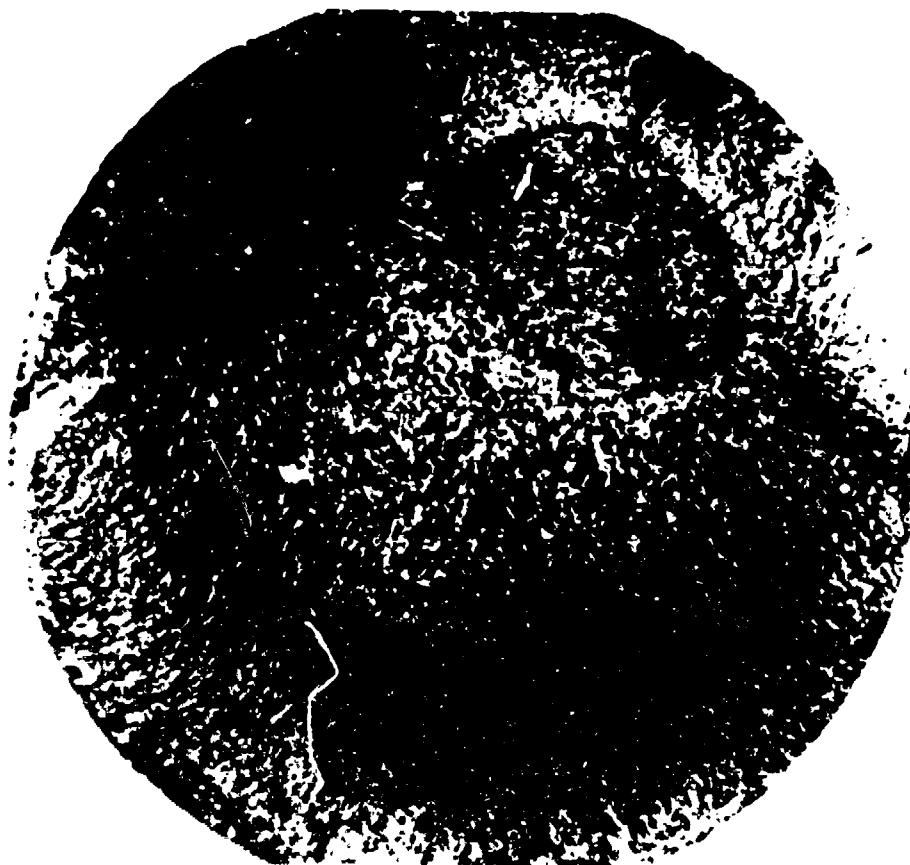
Figure A3. Fracture surface of the exciter shaft
failed in rotating bending.

Figure A4. Macroetch photo of the exciter shaft.
(a) The front pulley end. Note the
weld metal and large heat-affected
zone.   (2x)
(b) The back pulley end. Note the
uniform structure.

277
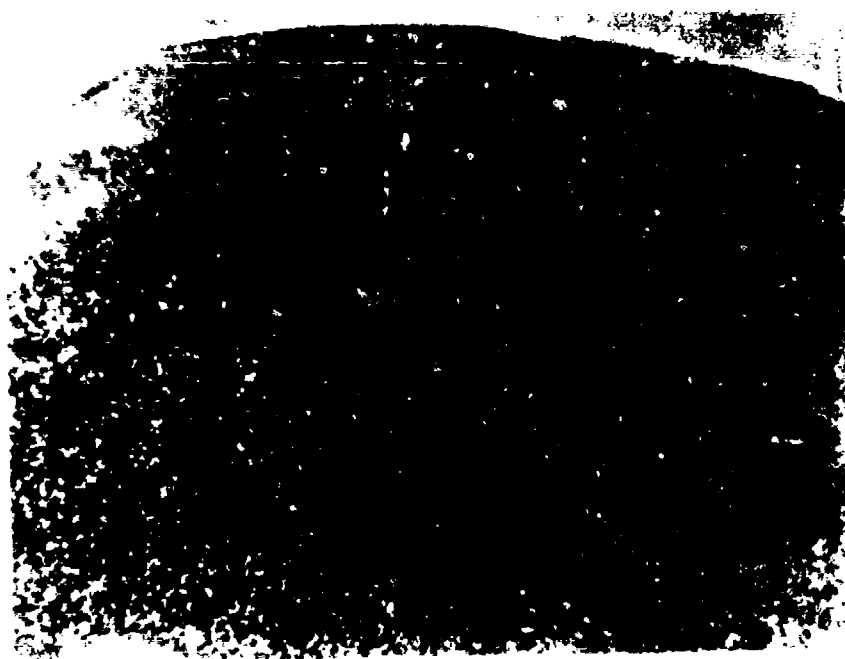
Figure A5. Macroetch photo of a section
of the exciter shaft (8x).
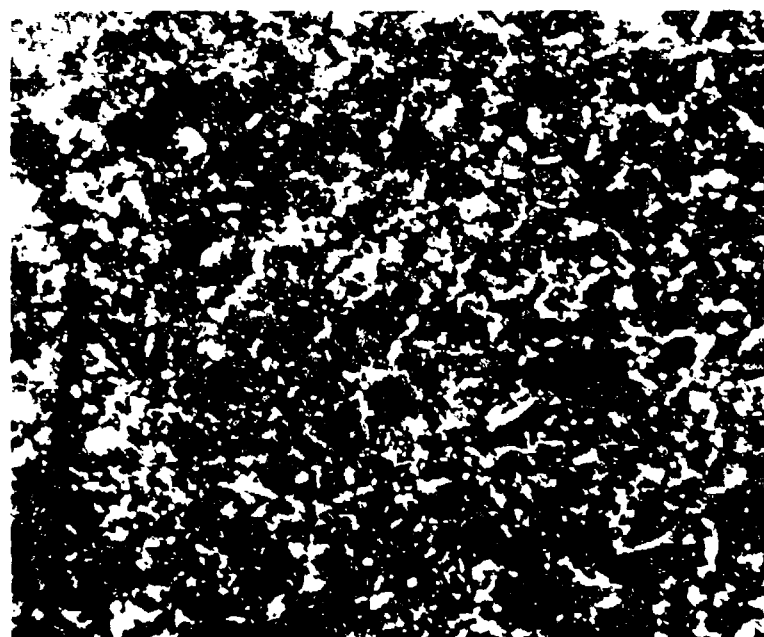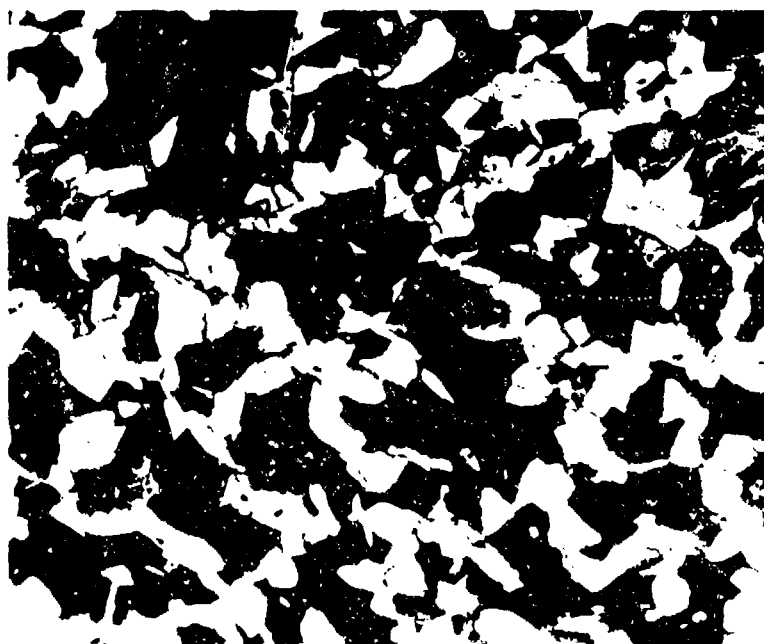
Figure A6. Microstructure of the exciter shaft.
(a) Near the center of the shaft (100x)
ASTM standard grain size number 3.
(b) Near the surface in the weld metal (100x).
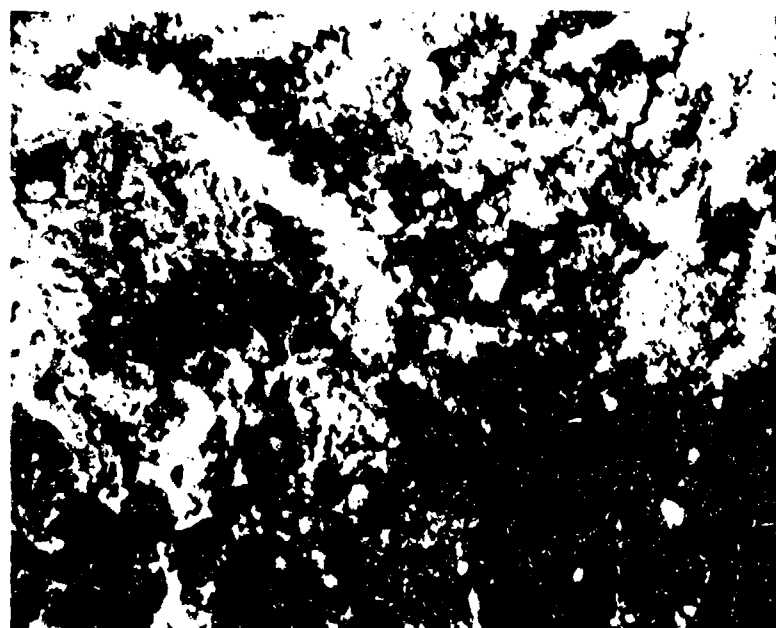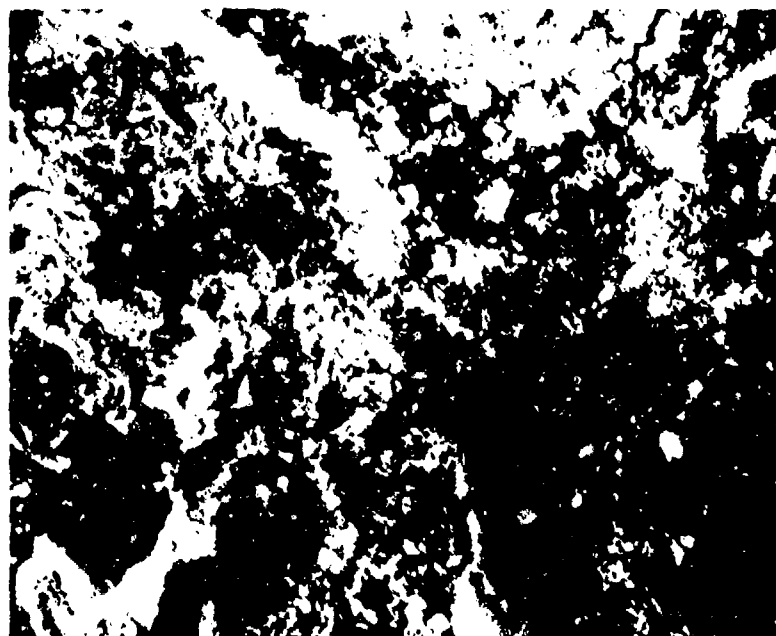
Figure A7. SEM photo of the surface weld metal.
Stereo pair (1750x).
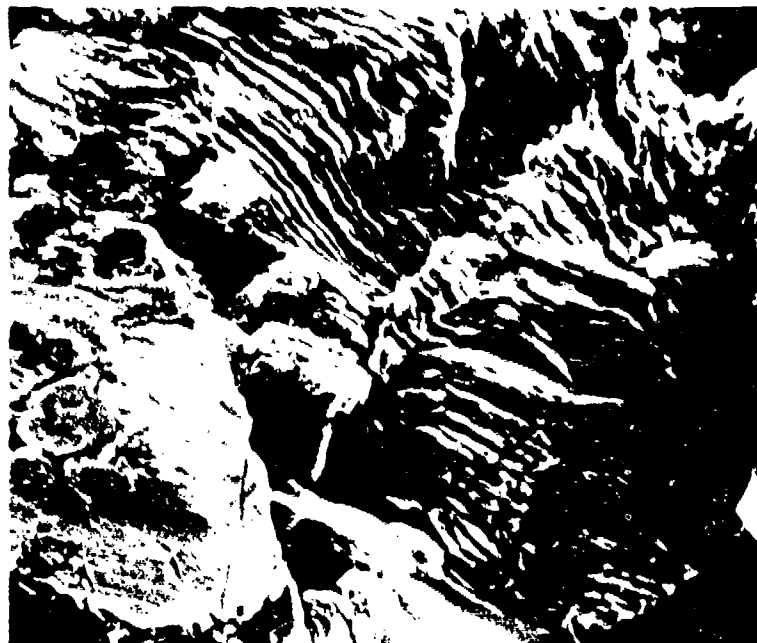
Figure A8.   Fatigue striations.

(a)   Weld metal in the surface (1600x).

(b)   Bulk metal in the shaft (650x).
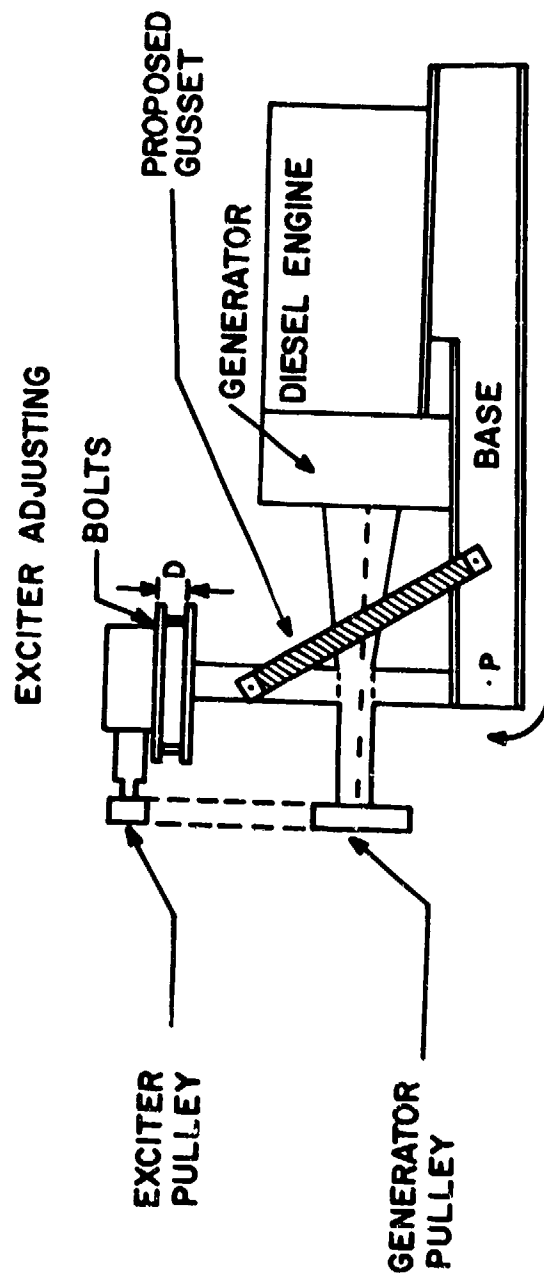
Figure A9. Schematic arrangement of generator and exciter base and mountings.

2 FAILURE ANALYSIS: NORAD SPRINGS

Construction Design of Original Structure

The NORAD Cheyenne Mountain Complex (NCMC) in Colorado Springs, Colorado, consists of a three-story welded steel structure supported entirely on 880 springs. The environment in which these springs stand is reported to have approximately 75 percent humidity. There is extensive seepage from the roof and the walls of the underground excavation. Some of this underground water trickles down the sides of the steel structure and drips down to the spring bottom. Some of the springs supporting Building No. 8 have been standing in 8 in. (0.2 m) of water for 2 to 3 years.

Incidence of Failure

Three spring failures have occurred.

Specimens Received for Analysis

Five springs were received at CERL; one had broken in service, the other four were rejected during an Aerospace Defense Command (ADC) inspection as described below.

ADC Inspection

A two-phase program was initiated by ADC after three springs had broken. Based on the results of Phase I, which consisted of removal and inspection of 34 springs, the number of springs to be removed in Phase II was determined. Initially, 20 springs which showed the most severe corrosion damage were pulled. The springs were cleaned and inspected by wet magnetic particle analysis by a qualified operator. Six springs were rejected based on a conservative criterion. Five of the rejected springs appeared to have microcracks associated with corrosion pits in corroded areas which were about 0.5 to 0.75 in. (1.27 cm to 1.91 cm) wide. These pits were in the active coils with depths up to 0.060 in. (1.52 mm). One of the springs had a radial indication which appeared to be a shallow crack in an active coil which was not corroded. Most of the springs have large areas which have been ground away. The inside circumference of some of the springs showed continuous grind marks for two to three coils.

An additional 14 springs were removed and inspected by wet magnetic particle analysis. Of these 14 springs, five were corroded springs, and nine were chosen from a batch of 600 apparently uncorroded springs. Three springs (including one of the 600) from this batch of 14 springs were rejected. Two of the springs had shallow

283

linear indications in the middle of the ground areas, and the third had a large mill scale pit containing corrosion. Thus, a total of nine springs out of 39 inspected in Phase I were rejected.

Four of the nine rejected springs were sent to CERL for metallurgical analysis along with a spring which was discovered broken during an inspection in July 1972. The CERL investigation was to determine the extent of the corrosion damage on these rejected springs and then to formulate a criterion for removal and inspection of springs in Phase II.

Material Specifications

The specifications for NORAD springs are summarized in Table A1.

Laboratory Inspection Procedure

All NCMC springs have serial numbers stamped on them as well as being identified by their position numbers. The five springs which form the basis of this analysis are identified in Table A2 which also summarizes the inspection results.

The broken spring identified as spring No. 21 was uncrated and inspected visually. The thickness and the adhesion of the paint film in areas where it was intact were measured. The spring was soaked in xylene and wirebrushed. The fracture surface was cleaned in boiling NaOH and zinc dust. The fracture surface was photographed under normal light and under black light with wet magnetic particles sprayed on the surface to enhance the ridges. Both the corrosion pits and the entire fracture surface were observed in a SEM at magnifications from 14x to 1600x.

A section of the spring 1/2 in. (1.27 cm) from the fracture surface was cut off. The surface was polished, macroetched, and observed under a microscope. The hardness of the section was also measured.

When the four springs rejected in the field inspection were uncrated at CERL, the turnbuckles and the end plates were removed. Spring No. 1 was soaked in xylene to remove the tar coat. The remaining three springs were cut by a flame torch, 1-1/2 coils away from the end of the corroded region. The cut-off segments were soaked in xylene to remove the tar from the spring surface. All four springs were inspected visually and by wet magnetic particle analysis. The largest and the deepest pits were cut both longitudinally and transversely. More than 20 pit cross sections were prepared from springs No. 10 and No. 16. These samples were polished, etched in picral, and observed on a metallograph.

A deep corrosion pit in spring No. 10 was split open for observation. A small area containing the pit was cut off and saw cuts were

then made below the bottom of the pit. The pit was broken open and observed in the SEM.

Spring No. 1 had a shallow linear radial indication 1/2 in. (1.27 cm) long in the field inspection, which disappeared after wirebrushing. Hence, this spring was not sectioned.

A section across the longitudinal defect in spring No. 79 was cut off, polished, and observed on a metallograph to establish the depth of the defect which was 1/2 in. (1.27 cm) long.

Laboratory Test Results

Fractured Spring No. 21

Spring No. 21, which was discovered broken, showed large areas where the paint had flaked off. The thickness of the paint film in areas where it was intact was of the order of 2-1/2 to 4 mils (0.64 m to 1.02 m). A peel test showed that the film did not have proper adhesion. Areas where the paint film had flaked off showed numerous pits in a con- tinuously corroded band 1-1/2 in. (3.81 cm) wide (Figure A10). Pit depths were up to 0.060 in. (1.52 cm). This band was located on the bottom of the lowest active coil close to the bearing plate, which is a favorable area for moisture to collect. Wet magnetic particle in- spection showed no cracks in any of the pits near the fracture surface of the spring.

Figure A11 is the SEM photograph of the corrosion pits which ini- tiated the fracture. Extensive microcracking in corrosion products within the pits can be observed. Similar microcracks were observed in adjacent pits. The largest microcrack connecting two adjacent pits was less than 0.005 in. (0.13 mm) long.

Figures A12 and A13 are photographs of the fracture surface under normal and black light, respectively. Three regions can be identified in the fracture region (Figure A14). The first region is about 1-1/2 in. (3.81 cm) wide and 0.025 in. (0.64 mm) deep and is bounded on the outside by many corrosion pits adjacent to each other. The pits them- selves consist of many pores joined together to form jagged boundaries. The deepest pits are in the middle of this region and are 0.050 to 0.060 in. (1.27 mm to 1.52 mm) deep. Two adjacent pits 0.2 in. (5.08 mm) in diameter and 0.060 in. (1.52 mm) deep formed the origin of fracture. All the pits in this region show corrosion tunnels to a distance of 0.025 in. (0.64 mm) from the pit bottom. This region, strewn with cor- rosion tunnels, is referred to as the corrosion sponge region. A more detailed view of a corrosion sponge region in a section 1/2 in. (1.27 cm) away from the fracture surface is shown in Figure A15.

The second region started with the formation of a crack 1-1/2 in. (3.81 cm) long and 0.025 in (0.64 mm) deep from the corrosion tunnels,

which was then propagated by stress corrosion. The presence of water containing dissolved oxygen and ions led to the formation of atomic and molecular hydrogen, which diffuses quickly to the crack tips. This hydrogen reduces the stress corrosion growth resistance of martensitic steels drastically, and the crack grows rapidly to a critical size. Once the critical size is reached, catastrophic fracture occurs (region 3). The boundary between regions 2 and 3 cannot be clearly defined because these regions tend to merge. The rapid fracture in region 3 leaves numerous river lines. The critical crack size is characterized by a length, $2c$, and depth, a. In spring No. 21, $2c$ was equal to 1.5 in. (3.81 cm) and was equal to 0.5 in. (1.27 cm). Spring No. 18, which was analyzed by Alco Spring Industries, was reported to have a crack length $2c$ equal to 2 in. (5.08 cm) and crack depth a equal to a 0.3 in. (7.62 mm).

Figure A16 shows a hardness traverse 1/2 in. (1.27 cm) from the fracture surface. The traverse showed that the spring material hardness was within specifications. Macroetching did not reveal any abnormal concentration of inclusions or any pipes. There were no indications of a seam or lap in the fracture area of spring No. 21. The depth and size of the corrosion pit which initiated fracture was of the same order as other pits in surrounding regions of spring No. 21 and in other springs removed from the same building.

Rejected Springs No. 10, No. 16, No. 1, No. 79

Springs No. 10 and No. 16 were rejected because of field indications believed to be cracks. Both of these springs had corrosion bands which were 3/4 in. (1.91 cm) wide in the active coil region. These bands contained many corrosion pits with depths to 0.060 in. (1.52 mm). Figure A17 shows the corroded area of spring No. 10 under normal and black light. The perimeters of corrosion pits are enhanced by the presence of fluorescent magnetic particles. This enhancement was due both to microcracks or tunnels at the perimeter as well as steep ridges. Figure A18 is the SEM photograph of microcracks associated with corrosion pits in spring No. 10. The ridges of the corrosion pit reduce the crack detention sensitivity of wet magnetic particle inspection considerably; no cracks were detected in spring No. 10 and spring No. 16.

A large number of pits were cut longitudinally as well as transversely and observed on a metallograph and in the SEM. Most of the pits contain corrosion tunnels and corrosion sponge extending 0.025 in. (0.64 mm) beyond the pit perimeters. The deepest pits are 0.06 in. (1.52 mm) deep. The fracture surface of a freshly opened corrosion pit in spring No. 10 did not show any evidence of stress corrosion cracking (Figure A19).

Discussion of Results

The 4160M steel alloy used in the springs was quenched from 1750°F (954°C) and tempered at 750°F (399°C). This leads to a tempered

martensitic structure with a tensile yield strength of 180 ksi (1.24 GPa) and an ultimate tensile strength of 210 ksi (1.45 GPa). The tempered martensitic structure, although strong, is extremely susceptible to stress corrosion cracking and hydrogen embrittlement. The paint film on NORAD springs failed either because it was too thin, or because it had insufficient surface adhesion. The ruptured area in the paint film exposed the spring steel to underground water containing dissolved oxygen and chloride. The oxidation of iron to iron oxide resulted in a large increase in volume which lifted the paint film away from the surface. Although the pH of the water at the surface is around 7 or 8, it has been observed that the pH of the water within the corrosion pits can be as low as 3 or 4. This acidic solution within the pits forms tunnels by anodic dissolution below the pit perimeter. The rate of pit formation is further increased because of a large ratio of cathodic area to anodic area. A network of corrosion tunnels forms paths around grain boundaries and into the grains. As the corrosion tunnel progresses, the sides are passivated by corrosion products, and the corrosion tunnel front continues to grow by anodic dissolution. When the tunnels become too numerous, the metal turns into a corrosion sponge. The corrosion pit grows by connecting the pores in the corrosion sponge. The jagged boundaries of pits are obvious in Figure A20.

The corrosion pits in springs No. 10 and No. 16 were of the same size and depth as those in spring No. 21. All of these springs contained tunnels in pits. The only major difference found in spring No. 21, which failed, was that corrosion tunnels in the sponge were larger and had begun to join to form microcracks (Figure A15). This was also accompanied by a much greater width of the corrosion area, which was 1-1/2 in. (3.81 cm) wide in spring No. 21, as compared to only 3/4 in. (1.91 cm) wide in springs No. 10 and No. 16. Based on these observations, and taking into account a safety factor of 2, a new inspection criterion can be proposed. In this criterion, springs containing corroded areas of dimensions greater than 3/4 in. (1.91 cm) should be rejected in future inspections.

This criterion is proposed to be used in conjunction with magnetic particle inspection and to be applied only to springs which have indications of heavy corrosion damage. Because it has not been shown that any defect other than a corrosion pit has led to spring fracture (except for an isolated case of a manufacturing defect found in 1968), it does not appear necessary to remove and inspect springs which show no evidence of corrosion damage. It is extremely important, however, to maintain a diligent, regularly scheduled, visual inspection program to determine immediately when springs have suffered corrosion attack.

Use of wet magnetic particle inspection as the sole inspection criterion is severely hampered by its high sensitivity and the rough surface of the in-service springs. Pits, ridges, corrosion tunnels, and oxide cracks in the springs can result in so much extraneous information that more significant defects are masked. It is suggested that a new standard which is more representative of the crack size that is

significant for stress corrosion failure be prepared and used in future inspections. The proposed standard should be an electro-discharge machine (EDM) slot 0.025 in. (0.64 mm) long by 0.025 in. (0.64 mm) deep by 0.005 in. (0.13 mm) wide.

The only reliable way to stop the springs from corroding is to paint them properly and inspect them regularly. Measures should be taken to keep the water away from the springs. The importance of surface preparation by proper sandblasting and application of the proper thickness of paint, as specified, cannot be overemphasized. After installation, springs should be inspected and holidays found on the paint should be retouched.

Conclusions

The fracture of spring No. 21 was caused by stress corrosion cracking. Fracture originated from corrosion pits 0.060 in. (1.52 mm) deep in the middle of a corroded band which was 1-1/2 in. (3.81 cm) wide, in an area close to the end of the bottom most active coil. The estimated time for the formation of this corroded band is 1 to 2 years after paint failure.

The composition and the heat treatment of 4160 steel results in a steel extremely susceptible to stress corrosion cracking and hydrogen embrittlement. The critical depth of the crack in spring No. 21 which led to catastrophic fracture was 0.5 in. (1.27 cm). The estimated time for the stress corrosion crack to grow to the critical depth is 10 to 100 hours.

Springs No. 10 and No. 16 had corroded areas to 3/4 in. (1.91 cm) wide that contained pits 0.060 in. (1.52 mm) deep. However, no cracks were found by wet magnetic particle analysis or metallurgical analysis. The presence of a corrosion sponge containing numerous tunnels was confirmed by metallographic observation. The depth of the corrosion sponge was 0.025 in. (0.64 mm) beyond the pit boundaries.

The manufacturing defect in spring No. 79 was shallow and less than 0.005 in. (0.13 mm) deep. The indication on spring No. 1 was a crack in the mill scale which disappeared on wirebrushing. These defects do not harm the performance of springs.

Recommendations

All springs should be inspected visually and with a paint thickness gage by a team of paint and corrosion experts. Only those springs which show paint film damage beyond on-site repair and heavy corrosion damage should be removed for inspection.

Springs that have developed corrosion pits should be removed, cleaned, and inspected visually and by wet magnetic particle analysis using the following criteria:

1. Springs having corroded areas of widths greater than 0.75 in. (1.91 cm) in active coil regions shall be rejected.

2. Springs having corrosion pit depths less than 0.030 in. (7.62 mm) and corroded areas less than 0.75 in. (1.91 cm) wide should not be ground. These springs should be sandblasted and repainted.

3. Springs having corrosion pit depths less than 0.060 in. (1.52 mm) and a corrosion band less than 0.75 in. (1.91 cm) wide should be ground off with a flat, medium-hard g.inder. The ground areas of springs should be stress relieved, reinspected for grinding cracks, sandblasted, and repainted.

4. Springs having cracks greater than 0.025 in. (0.64 mm) long, 0.025 in. (0.13 mm) deep, and 0.005 in. (0.13 mm) wide should be rejected.

5. Contract specifications for surface preparation and repainting procedures for acceptable springs should be followed strictly.

6. The rate of pit formation is not affected by shotpeening since stress corrosion crack growth occurs at depths at which shotpeening has no effect. Therefore, acceptable springs need not be shotpeened.

7. A program for regular inspection of paint and corrosion damage to springs should be aggressively pursued.

ORIGIN OF THE FRACTURE
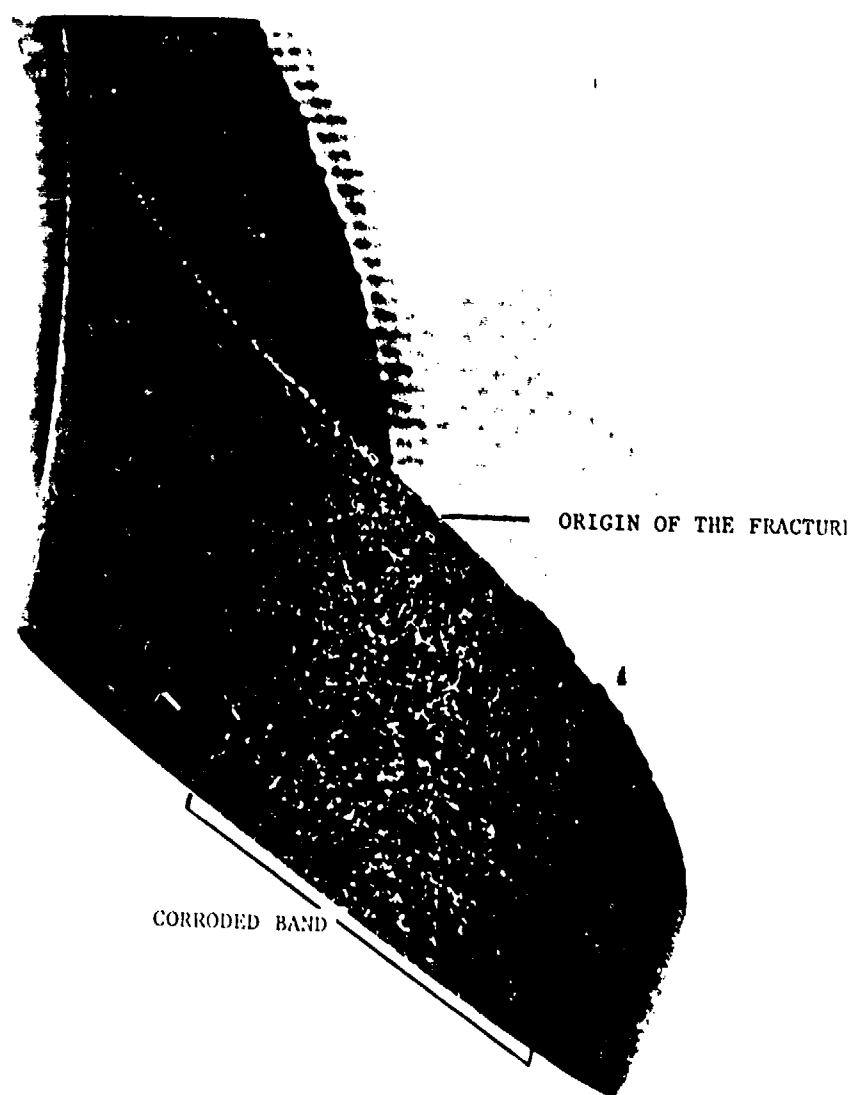
CORRODED BAND

Figure A10. The bottom of spring No. 21, which shows a corroded area.
Fracture initiated at the middle of this corroded band
which is 1 1/2 in. (3.8 cm) wide.
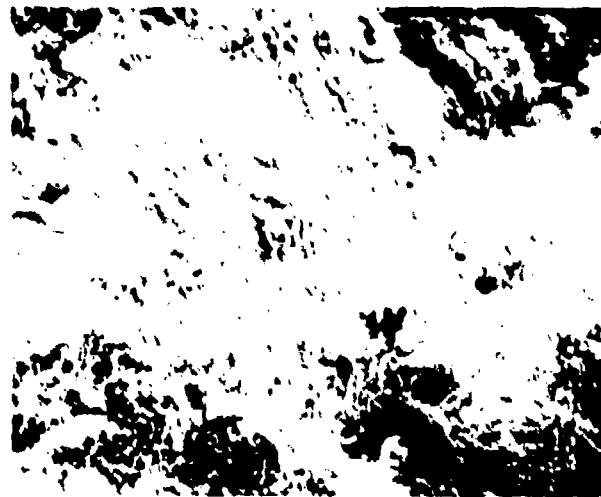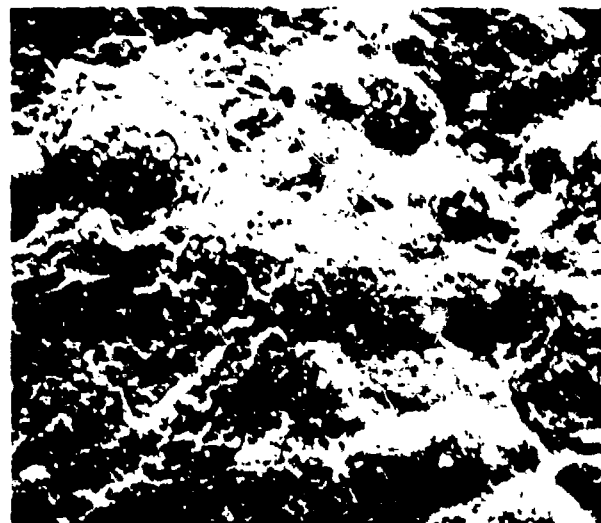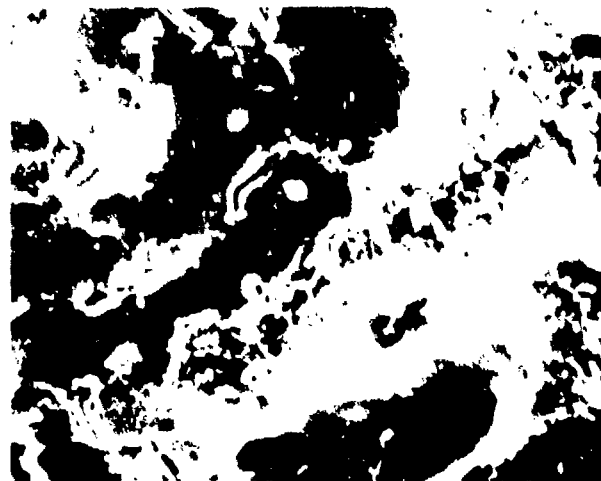
1375 A   X375 B   X750 C

Figure A11.   SEM photograph of the corrosion pits near the fracture surface. Microcracking associated with corrosion pit perimeter can be observed in (a) while microcracks connecting two pits are shown in (b). Stress corrosion cracking on the fracture surface near the origin is obvious in (c).

291
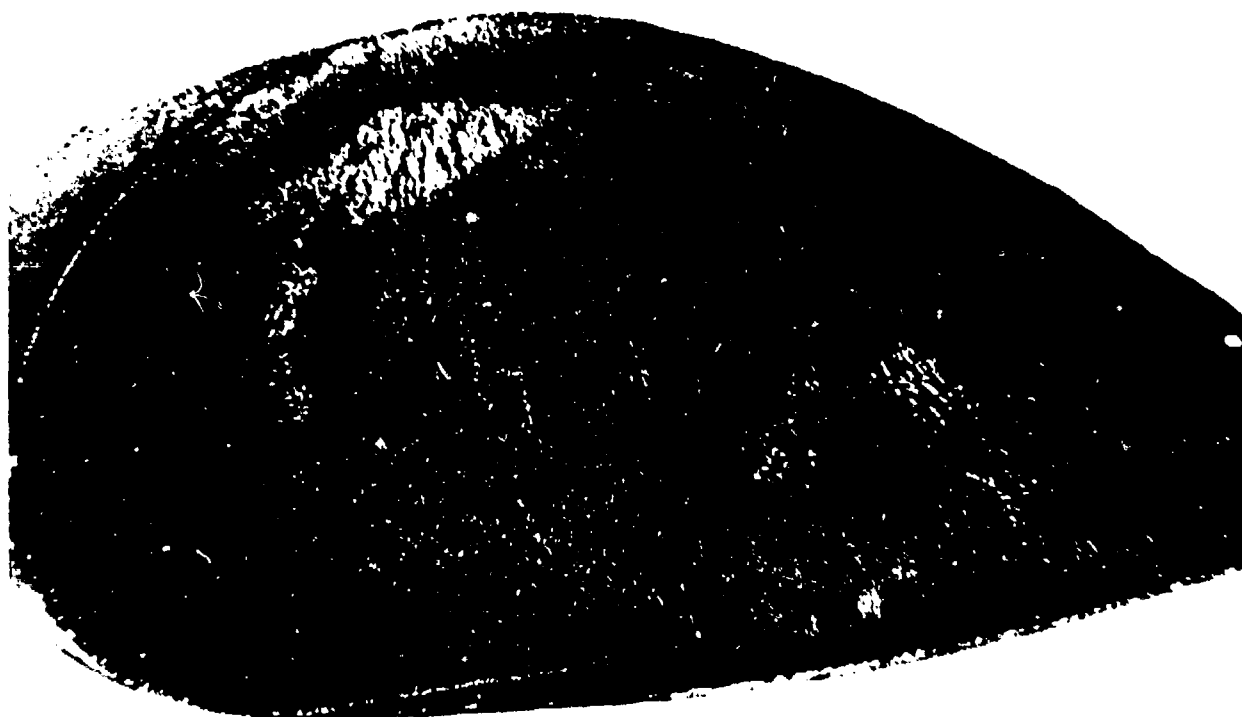
Figure A12. Fracture surface of spring No. 21. The shiny area appears to be formed by a chemical compound adhering to the surface after the fracture. Photographs under fluorescent light with magnetic particles do not show this feature.
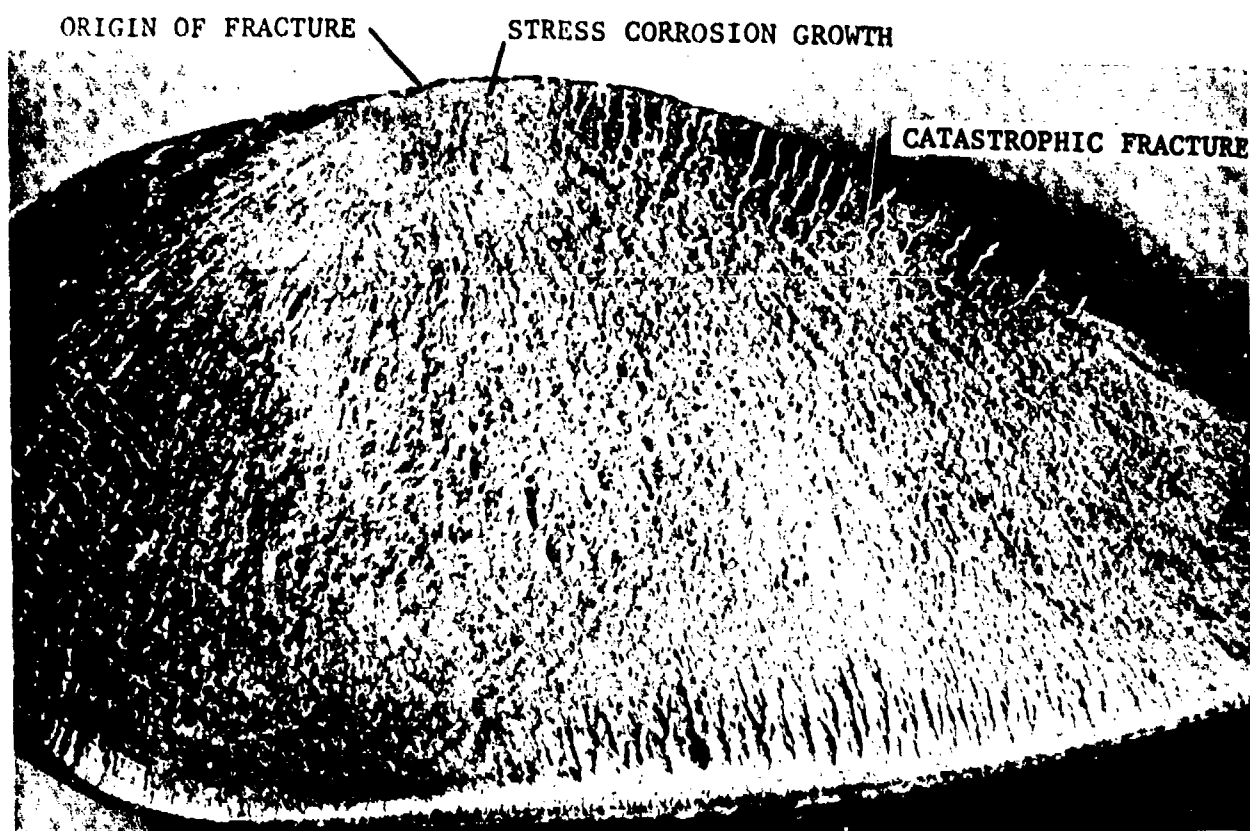
Figure A13. Fracture surface of spring No. 21 as photographed under fluorescent light, with wet magnetic particles sprayed on the surface to enhance ridges.

293
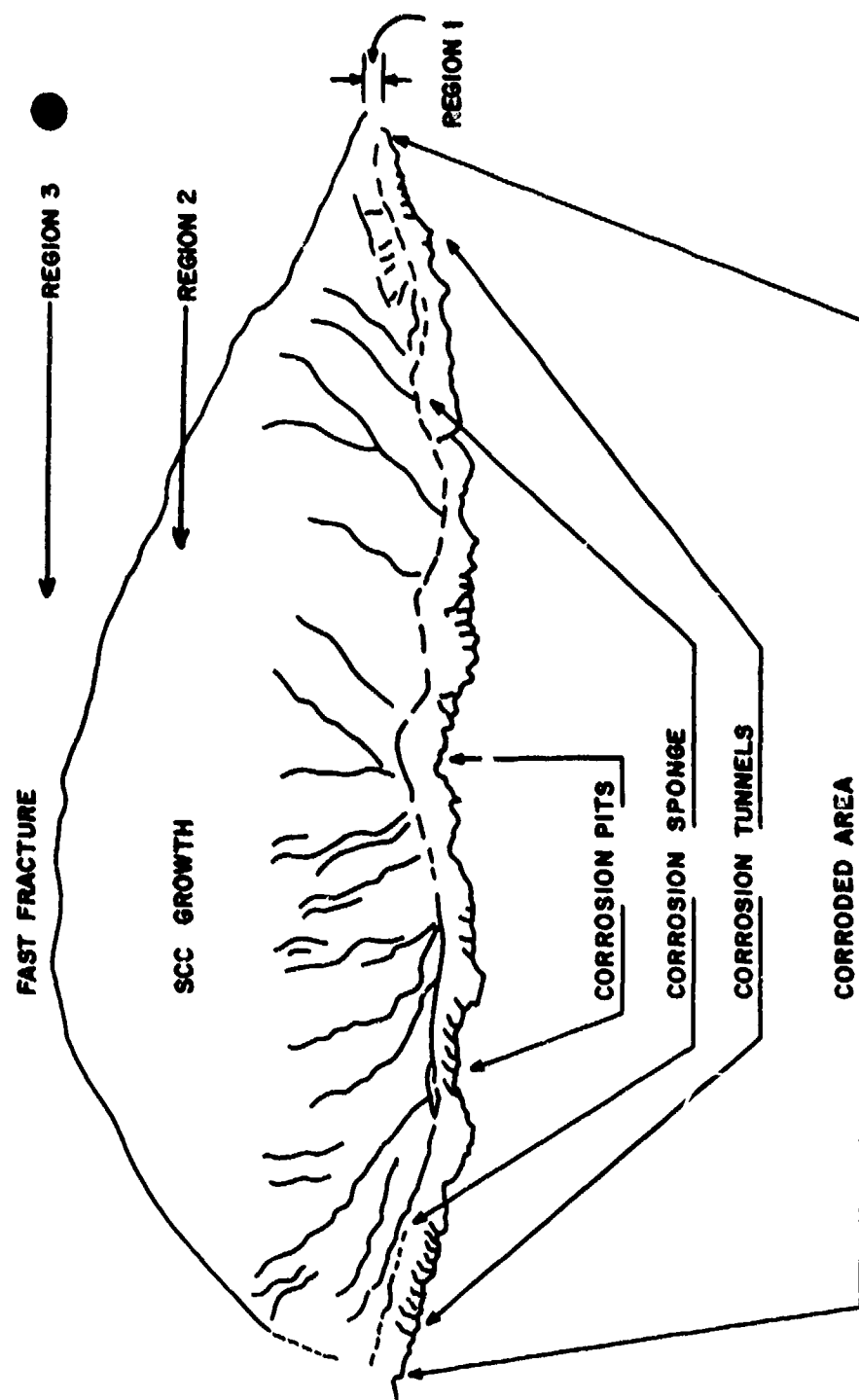
Figure A14. The fracture surface of spring No. 21 showing three regions. Microcracks formed in Region 1 grow by stress corrosion to Region 2 and reach a critical depth for catastrophic failure in Region 3.

SPRING #21 TRANSVERSE CROSS SECTION X50

Figure A15. Photomicrograph of corrosion pit cross section, showing the depth of corrosion damage.

CORRODED AREA
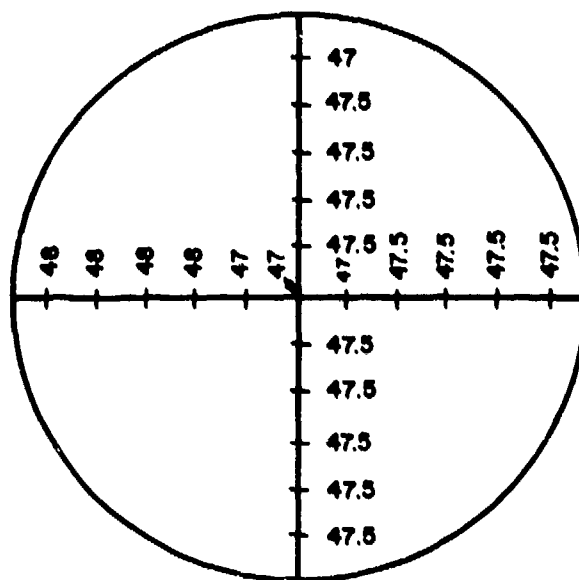
THE NUMBERS SHOW ROCKWELL C HARDNESS.

Figure A16. The hardness traverse of the spring No. 21, 1/2 in. (1.27 cm) from the fracture surface.
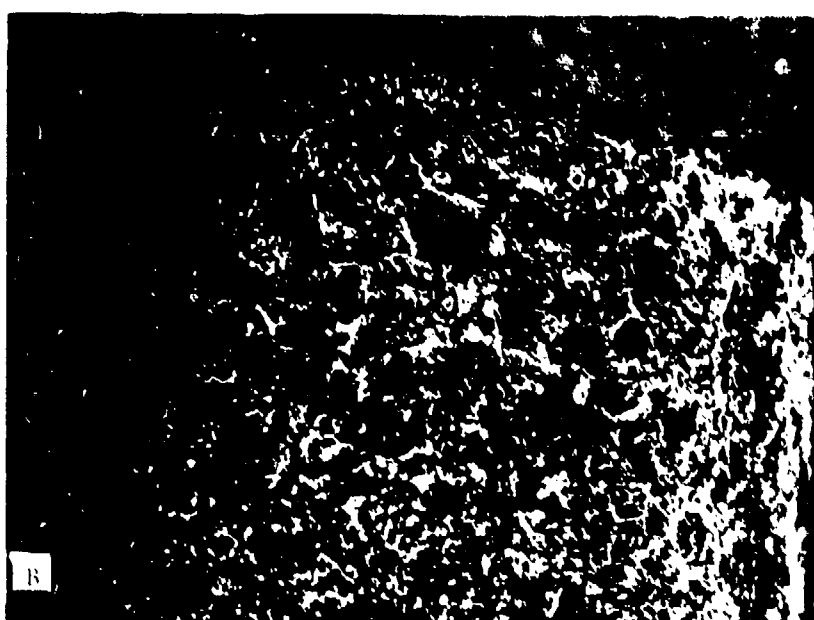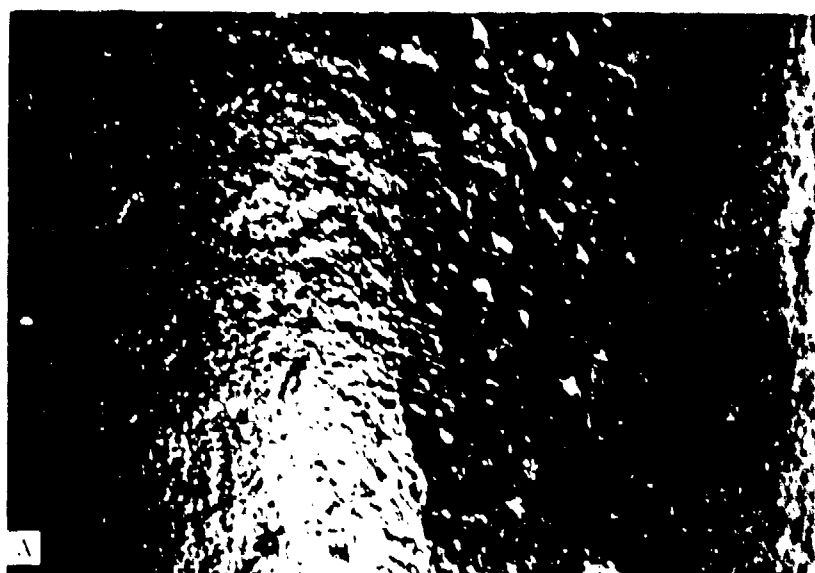
Figure A17. Corroded area on spring No. 10.

(a) Photograph showing the width of the
     corroded area under normal light.
(b) Photograph under fluorescent light.

Figure A18. SEM photographs of a corrosion pit bottom in spring No. 10 at various magnifications. Microcracking at the perimeter of the pit can be observed.

Figure A19. Photomicrograph of the manufacturing defect
in spring No 79. No microcracking beyond
the shallow defect was observed.
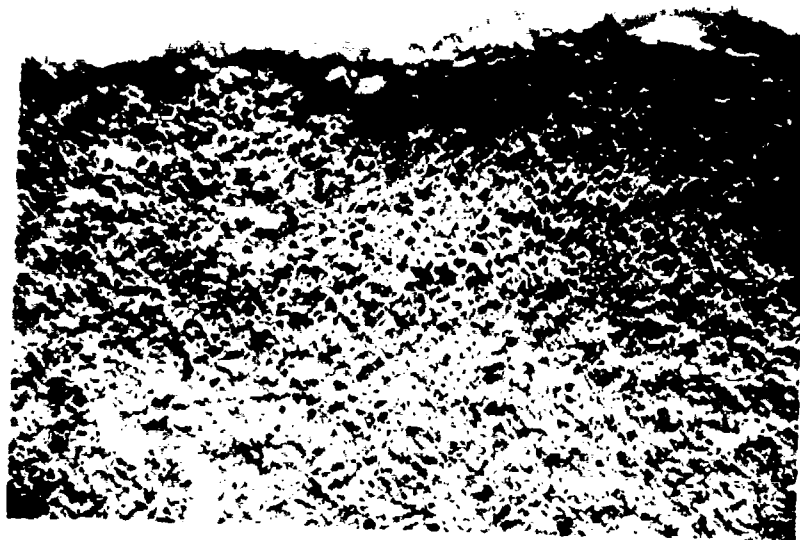
X400
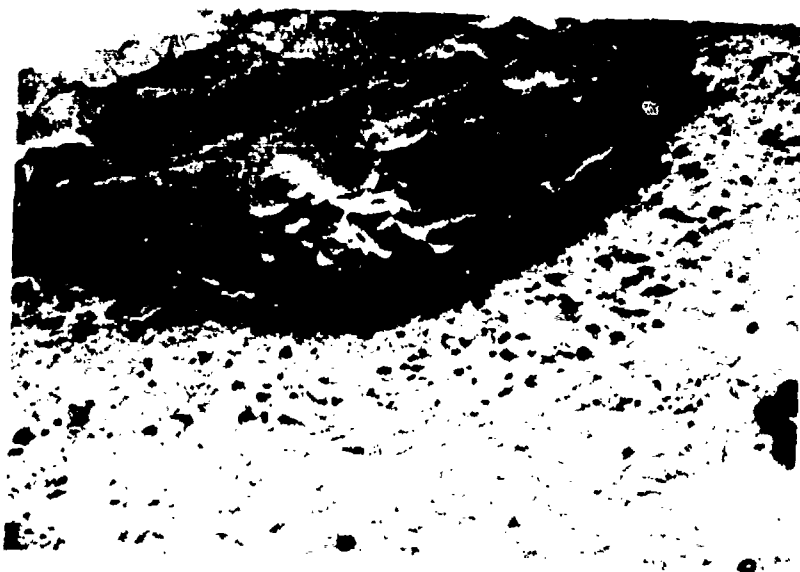
X700

Figure A20. SEM photograph of corrosion pit cross sections which have been polished and etched in picral. Corrosion tunnels beyond the pit perimeters can be observed in spring No. 10.

300

3 FAILURE ANALYSIS: TAINTER GATE CABLE-ADJUSTING BOLTS

Construction Design of Original Structure

The Uniontown Locks and Dam, located on the Ohio River near Union-town, KY, consists of ten tainter gates and two miter gates. The tainter gates are raised and lowered using a cable-and-winch system, as illustrated in Figure A21. Thirteen cables are attached to each side of the tainter gates by a bolt assembly, as shown in Figure A22. The cables are tensioned until each pair of stainless steel bolts securing them is subjected to a load of about 25,000 lb (11.35 Mg). The bolt assembly on each side of the gate consists of two rows of 13 bolts, which are 2 ft 4-1/2 in. (0.7 m) long and 1-7/8 in. (4.8 cm) in diameter. Under normal maximum load conditions, each pair of bolts could exper-ience a 33,000 lb (14.98 Mg) tensile load. It has been calculated that if a gate should jam, each cable would be loaded to 2.8 times 33,000 lb (14.98 Mg) or 92,500 lb (42.0 Mg).

Incidence of failure

Eight of 208 bolts have broken in 2 years.

Specimens Received for Analysis

Four bolts were received: two broken in the threads, one broken in the shaft, and one broken underneath the head.

Material Specifications

AISI 416 stainless steel, ASTM A-193-68 Grade B, coated with vinyl paint.

Laboratory Inspection Procedure

The sides of the bolts were wire-brushed to remove the rust and oxide scale.

The bolts were nondestructively inspected using a dye penetrant as specified by Mil Spec 1-6866 and a magnetic-particle analysis accord-ing to Mil Spec 1-6868C.

The fracture surfaces were removed from the bolts and cleaned to remove rust by immersing them in a 6N solution of HCl containing 2 g/L of hexamethylene tetramine as an inhibitor.

The rust-free fracture surfaces were examined with an AMR 900 SEM.

A small wafer was cut from the bolt, polished, and etched with picral to reveal the microstructure.

On-Site Inspection Procedure

The lock and dam system was visually examined and photographed.

Laboratory Test Results

Two of the broken bolts received by CERL are shown in Figure A23. Inspection of these bolts, along with their corresponding nuts, revealed that they had not been completely painted.

Figure A24 shows the appearance of the bolts after being brushed and then sprayed with dye penetrant. Circumferential cracks in the shaft and pits and longitudinal cracks in the threads are clearly evident. The other bolts also revealed extensive pitting and cracking when inspected with dye penetrant.

Examination of the cleaned fracture surfaces in the SEM revealed extensive corrosion; Figure A25 shows the crack on the outside edge of one of the bolts which initiated the failure. Figure A26, a higher magnification of Figure A25, clearly reveals the intergranular cracking pattern. The total fracture was not intergranular, however; Figure A27 shows that the tensile overload region consists of a mixed mode of transgranular cleavage and microvoid coalescence.

The fracture surface of the bolt which broke just below the head had alternating dark and light semicircular striations across it. Examination of this surface in the SEM revealed a grain-boundary separation failure over the entire surface. No fatigue striations were observed.

An optical microscopy study of a thin wafer of the bolt sectioned just below the fracture surface revealed two large radial cracks (shown in Figure A28), one of which was about 1/4 in. (6.4 mm) long. These were the cracks discovered during dye-penetrant inspection. A higher magnification of this area, reproduced in Figure A29, showed that the cracks in the martensitic matrix seemed to follow the prior austenite grain boundaries.

Discussion of Results

Laboratory Tests

The cable-adjusting bolts have been failing at stress levels calculated to be far below the material's yield strength. The most effective strength-reducing mechanism in high strength steels is the formation of

a crack (or cracks). Dye-penetrant inspection (Figures A26 and A28) showed there were indeed cracks in the bolts. These cracks were believed to result from a tempering embrittlement. This embrittlement in stainless steel is attributed to the precipitation of a brittle high-chromium sigma phase along the prior austenite grain boundaries. The formation of the chromium-rich area not only decreases the ductility of the metal but also depletes the adjacent regions of chromium and lowers their corrosion resistance. Thus, when the material is exposed to a corrosive environment, preferential attack, usually in the form of stress corrosion cracking, occurs at these chromium-depleted regions. The stress corrosion crack initially propagates as a result of inter-granular fracture, as shown in Figure A26.

As a result of the embrittlement, the bolts had a reduced corrosion resistance. Pits formed after an abnormally short time, creating stress concentration sites and the formation of cracks. Cracking propagation progressed by relatively slow electrochemical processes until the crack was sufficiently large to initiate mechanical fracture. The corrosion rate may also have been aggravated by joining the stainless steel bolt to the cables (dissimilar metals), which increased the electrochemical attack.

If type 416 stainless steel is properly heat treated, it will meet all specifications and should perform well in service. The corrosion resistance of the bolts can be optimized if the following heat treatment steps are performed:

    Preheating to 1200°F-1400°F (649°C-760°C) for 1 hour
    Austenitizing at 1700°F-1850°F (927°C-1010°C) for 1 hour
    Oil quenching
    Tempering at 1100°F-1200°F (593°C-649°C) for 1 hour
    Oil quenching

Inspection of Uniontown Locks and Dam

During a tour of the Uniontown Dam, it was noted that the drum around which the cable is wrapped during the lifting of the tainter gate was not taking up the cables evenly, as a result of uneven cable wrapping. To insure a uniform load on the bolts, and maximum life, the cables should be equally tensioned at all times. This should be accomplished by checking the cable tension, cycling the gate several times, and then rechecking the tension. The procedure should be repeated until all cables are equally tensioned.

It was also noted that a vortex of turbulent, high-velocity water occurs at both ends of the gate and, when the gates are raised to a certain height, impinges on the cable-adjusting bolt assembly. It is believed that the considerable amount of pitting observed on the bolts was caused by cavitation erosion from this high-velocity water. It is possible that cavitation erosion can become important as a failure mechanism in the future.

A significant amount of vibration occurs when the gates are kept partially open to modulate the flow of water. The vibration causes cyclic loading of the bolts which, if the loads are great enough, can result in fatigue failure. This factor is especially important because the small fillet radius between the shaft and head of the bolt constitutes a stress concentration area. The radius under the head should not be less than one-tenth of the bolt diameter for 3/4-in. (1.9 cm) diameter bolts and larger. Thus, in this instance, the fillet radius should be about 1/4 in. (6.4 mm).

Conclusions and Recommendations

1. The failure mode of the cable-adjusting bolts was determined to be stress corrosion cracking which occurred as a result of a tempering embrittlement during heat treatment. The embrittlement reduced the bolt's corrosion and crack propagation resistance.

2. The embrittled bolts can be restored to their proper condition by heat treating.

3. Type 416 stainless steel is a suitable bolt material for this service environment. If increased corrosion protection and/or toughness is desired, type 431 stainless steel can be used.

4. It is recommended that the type 416 bolt material meet the following specifications:

Tensile Strength: 110 ksi - 140 ksi (7.58×10^8Pa - 9.65×10^8Pa)

Hardness: R_B95-R_C26

(BHN 209-BHN 259)

Tempering Temperature: 1100°F to 1200°F (593°C - 649°C).

5. The fillet radius between the bolt head and shaft should be increased to reduce the stress concentration.

6. The cables should be adjusted by repeated cycling until a uniform tension is achieved.

7. It was also recommended that Carpenter 450, a precipitation hardened steel, be used instead of the AISI 416. The quality control requirements for heat treatment are not required, as is the case for AISI 416.

Figure A21. Tainter gates at Uniontown Locks and Dam.
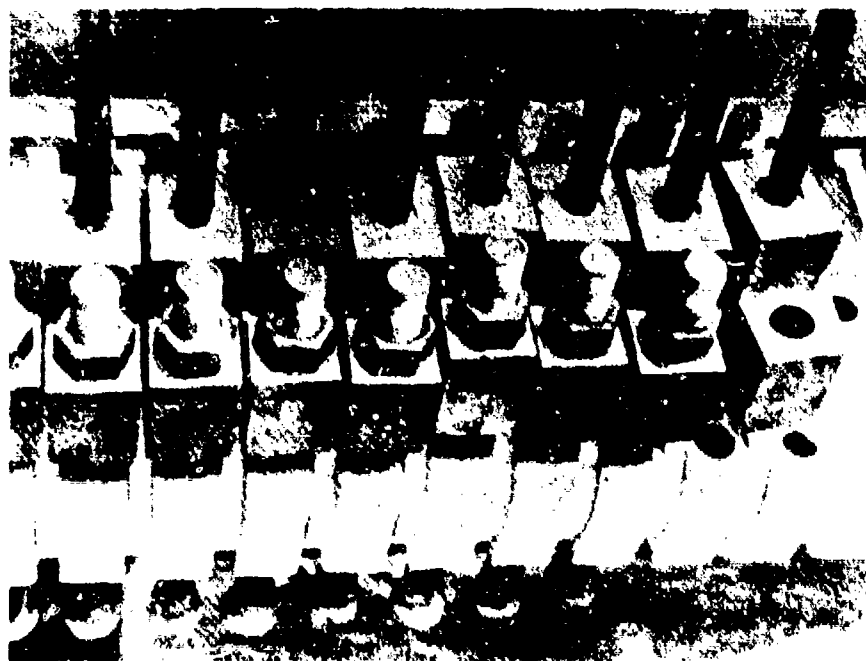
Figure A22. Bolt assembly securing lifting cables.
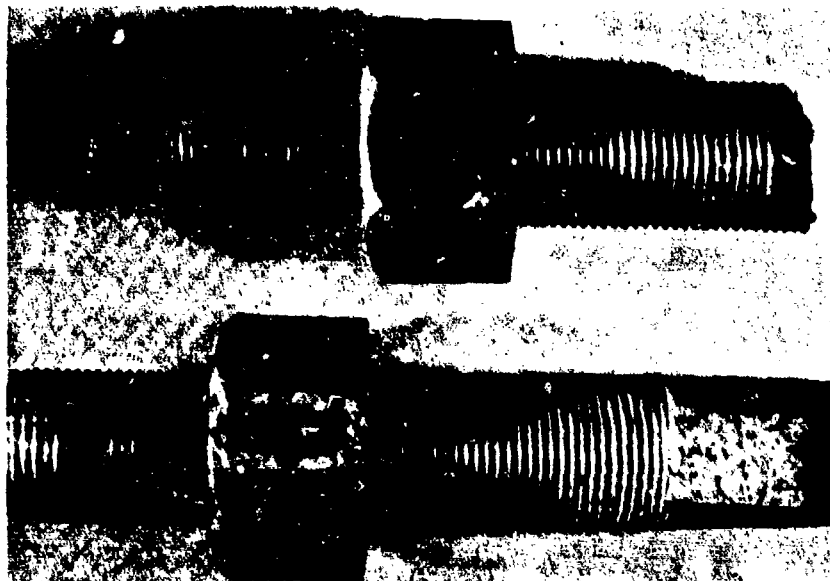
Figure A23. Fractured bolts as received by CERL.
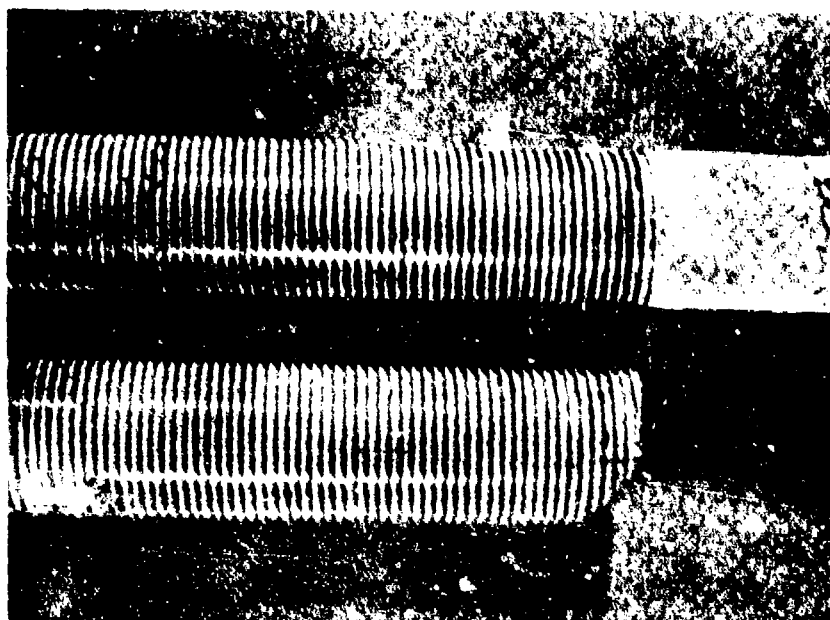
Figure A24. Radial and circumferential flaws
revealed by dye-penetrant inspection.

Figure A25.   Circumferential crack on outside
edge of bolt (10x magnification).
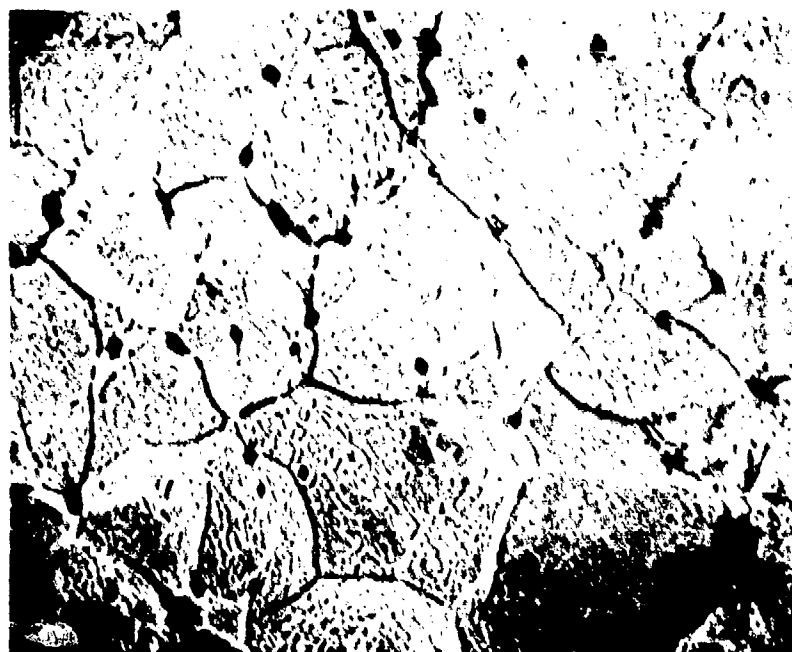
Figure A26.   Intergranular cracks resulting from
a grain-boundary separation failure
mode (1100x magnification).
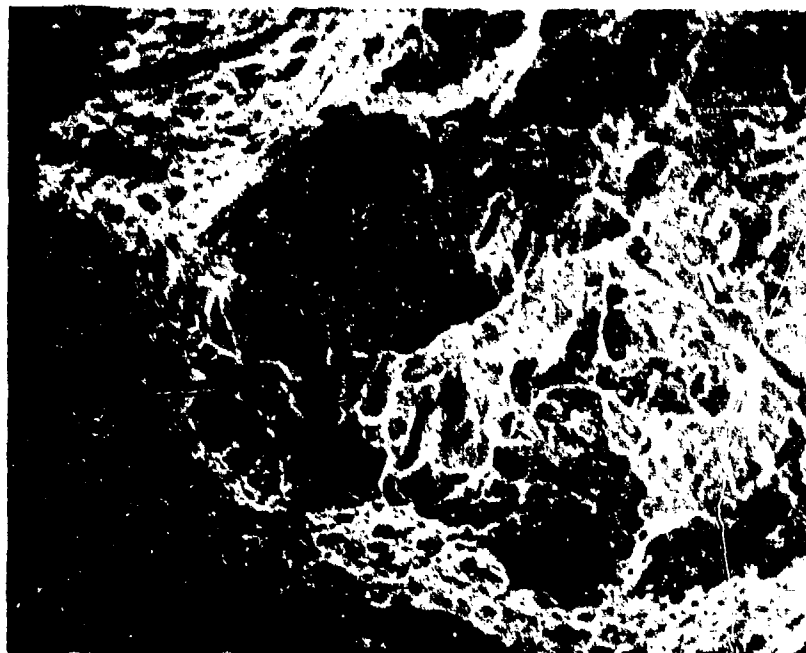
Figure A27. Mixed failure mode consisting of transgranular cleavage and micro-void coalescence (750x magnification).
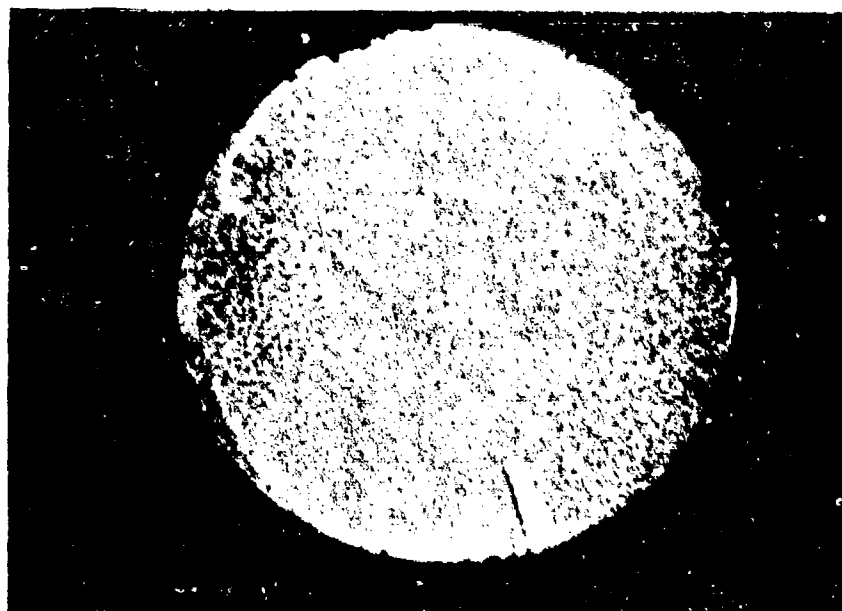
Figure A28. Radial cracks in bolt revealed by dye-penetrant inspection (1.45x magnification).

Figure A29. Radial crack in bolt material (336x magnification).

4 FAILURE ANALYSIS: HOLLOMAN ROCKET TEST TRACK

Construction Design of Original Structure

The high velocity test track at the Holloman Air Force Base, Ala-
mogordo, NM, consists of three parallel 171-lb (77.63-kg) Bethlehem
crane rails. The test track has been extended 15,000 ft (4.58 km). For
the purpose of this extension, the Government has furnished some of the
rails to the contractor. The rail ends were prepared and welded by the
"Oxweld" process according to specifications provided by the U.S. Army
Engineer District, Fort Worth, Texas. A welding temperature range of
2250°F to 2300°F (1232°C to 1260°C) and an upsetting force of 31,000 to
33,000 lb. (14.07 Mg - 14.98 Mg) was specified. Welding was completed
when the distance between the thrusting clamps was reduced by 7/8 in.
(2.22 cm). Heating was accomplished by an oxyacetylene heating head con-
taining four units arranged at the top, bottom, and sides of the rail.
The amplitude of oscillation was required to be 1-7/8 in. (4.76 cm)
centered over the joint and the frequency of oscillation was 40 cycles
per minute. After welding, the upset bulge was flame cut off, and the
rail joints were normalized at 1500°F (843°C). Heating for the normal-
izing operation was accomplished by oscillating the heating heads 3 in.
(6.62 cm) on each side of the joint. After checking for alignment, the
rail was ground to a surface roughness of 100 m in. (0.25 mm). The rail
was tested by magnetic particle and ultrasonic inspection according to
Mil Spec I-6868 and ASTM E 164-65, respectively. Any joint showing
flaws or cracks was to be sawed out according to specification.

As each successive 78-ft (23.77-m) length of rail was welded, the
entire section previously joined was moved out longitudinally over the
track girder on ball bearing rollers spaced at intervals of less than
50 ft (15.24 cm). Two 7500-ft (2.29-km)-long welded sections were re-
quired for each track girder. After positioning, the 1500-ft (2.29-km)-
long section was stressed by means of jacks to obtain elongations of
each rail equivalent to the elongation of an unstressed rail subjected
to a temperature of 120°F (49°C). The coefficient of expansion to be
used was 6.7 x 10-6 per degree Fahrenheit. Prior to tensioning, the
rails were required to be proof-loaded with 200,000 lb (60.96 Mg) and
maintained at this load for 4 hours. After 4 hours, the elongation was
reduced to the amount required by the ambient temperature. The rail
was then anchored. The rail clips with wedge plates were installed and
all nuts turned to a finger-tight condition.

Incidence of Failure

Eight failures have occurred in weld joints as a result of thermal
contraction.

310

Specimen Received for Analysis

A section of rail containing a welded and normalized joint was received for analysis.

Laboratory Inspection Procedure

The entire rail joint was inspected visually for cracks or abnormal conditions.

The rail joint was inspected by magnetic particle analysis according to Mil Spec I-6868C.

The rail joint was inspected by ultrasonic testing using an angle beam according to ASTM Specification 164 as well as a longitudinal beam.

A section of the rail containing the weld zone was macroetched with Nital as well as with ammonium persulfate to reveal the heat-affected zone (HAZ).

A section of the rail was polished and etched to reveal the microstructure in the HAZ and in the parent rail metal.

The fracture stress of the parent rail was determined.

Five tensile specimens were machined out of the rail joint, which contained the weld zone in the middle of the gage section. The diameter of the tensile specimens in the gage section was 0.500 in. (1.27 cm). The specimens were machined according to Mil Std 418-C. The specimens were pulled to failure in tension and a load vs deformation curve obtained. The fracture surface was observed in an optical microscope as well as in a SEM. The tensile specimens for the parent rail were 0.250 in. (6.35 mm) diameter in the gage section.

On-Site Inspection Procedure

The fracture surfaces of two rails were examined and photographed.

Laboratory Test Results

1. The visual inspection revealed no surface cracks. The grinding procedures covered the weld zone with a thin layer of flowed metal which may have obscured surface defects in magnetic particle inspection.

2. The surface of the weld zone was cleaned and the magnetic particle inspection revealed no surface defects.

3. The ultrasonic inspection showed no defects.

311

4. The macroetch revealed that the HAZ was 2 in. (5.08 cm) on both sides of the weld zone. The weld line as well as the flow lines were distinguishable.

5. The microstructures of the parent metal of the rail and of the HAZ are shown in Figures A30a and b, respectively. The weld zone can be seen in Figure A30b. The microstructure in Figures A30a and b shows a ferrite and pearlite mixture. The microstructure in Figure A30b does not show any unusually large grain growth, which could cause brittleness in the HAZ.

6. A close examination of the fracture surfaces of the specimen from the weld joint showed that the fracture occurred in the weld zone. The initiation point appeared as a flat spot as shown in Figure A31. There was a small fibrous zone around the flat spot, and the rest of the fracture surface was extremely smooth, indicating a low toughness weld zone. Figures A32 and A33 show the results of the SEM examination of the fracture surface. The flat spot with the surrounding fibrous fracture area is shown in Figure A32a. The flat spot area shows a low energy microvoid coalescence type of fracture at a higher magnification (Figure A32b). Many nonmetallic particles are associated with the fracture in this area. The fracture surface away from the flat spot is shown in Figure A33a, and the fracture surface of the parent rail metal is shown in Figure A33b for comparison. The parent rail metal shows a transgranular cleavage fracture and the weld zone fracture in Figure A33a shows a mixture of both cleavage and microvoid coalescence.

On-Site Inspection

The fracture surfaces of the rail joints which were inspected on-site are shown in Figures A34 and A35. Figure A34 shows that the fracture of the west rail initiated at a rusted area. The corroded area confirms that the weld defect was open to the atmosphere and should have been detected by magnetic particle inspection. It is also observed that the failure is mixed in appearance and is believed to have occurred partly in the HAZ and partly in the weld. The rusted area, which indicated incomplete bonding, introduced a stress concentration in the weld area. As the temperature decreased, the failure was governed by fracture mechanics criteria rather than by yield criteria.

The fracture of the central rail (Figure A35) appears to have occurred predominantly in the weld and partly in the HAZ. The point of initiation of the fracture was not established. The fracture surface topography is extremely smooth, indicating a rather brittle fracture.

Discussion of Results

Laboratory Tests

The fracture surfaces of the tensile specimens from the welded joint showed a small (1/8 in. diameter [3.18 mm]) flat spot as the point

of initiation of fracture. This flat spot was surrounded by a small fibrous area. The rest of the fracture surface was extremely smooth, indicating a low ductility weld zone as shown in Figures A36 and A31. The results of the SEM analysis in Figure A32 show the structure of the flat spot as well as the fibrous zone around it. For comparison, the fracture surface of the parent rail metal is shown in Figure A33. The exact cause of flat spots and the conditions leading to low ductility smooth fracture surface cannot be established without additional testing.

It appears that the most probable cause of the failure was an extremely low toughness at the weld zone, coupled with the presence of weld defects. Decreasing the temperature further reduced the toughness of the weld zone.

Since the use of NDT techniques such as the two-transducer angle beam ultrasonic technique is limited to the detection of large gaps, many poor welds may go undetected by ultrasonic testing because of the nature of weld defects in the "Oxweld" process. One way to test the integrity of the welds would be to proof-test the rail at a low temperature to at least the maximum stress anticipated by thermal contraction.

On-Site Inspection

The failure of the welds shown in Figures A34 and A35 occurred at low stress levels, which indicates poor weld quality. The failure in Figure A34 was caused by an unbonded area in the rail weld. This weld defect should have been detected by magnetic particle inspection. The unbonded area created a stress concentration in the web of the rail and the stress intensity at the tip reached the critical stress intensity necessary to cause failure. The point of initiation of fracture was easily determined to be the rusted area. The other failure in Figure A35 shows that the fracture took place mostly in the weld zone. The initiation point of failure was not determined. The extremely smooth surface of the fracture signifies a low ductility weld zone.

Conclusions and Recommendations

1. The failure of the Rocket Test Track welds at 25°F (-4°C) occurred at a calculated average stress of 19.1 ksi (613 GPa). The tensile strength of the parent rail is 130 ksi (0.89 GPa). This extremely low joint fracture stress is indicative of poor welds in high strength-low toughness steels.

2. One of the investigated failures in the western rail resulted from the stress concentration in the weld area. The stress concentration was a corroded weld defect which should have been detected by nondestructive tests.

313

3. Another investigated failure in the central rail occurred in the weld zone. The smooth fracture surfaces indicate an extremely low toughness metal in the weld zone.

4. The weld joints tested in the laboratory showed room temperature tensile strengths of 110 to 120 ksi (0.76 GPa to 0.83 GPa) as compared to 130 ksi (0.90 GPa) for the parent rail. The fracture of the tensile specimens obtained from the weld joint occurred in the weld zone showing a smooth surface typical of low fracture toughness.

5. Angle beam ultrasonic testing using two transducers sometimes detects only a few extremely poor welds with large unbonded areas. Welds which pass ultrasonic inspection may still fail in service.

Table A1

Specifications for NORAD Springs

Material	Electric Furnace 4160 M Steel Alloy, Aircraft Quality
Hardness	45.7 - 49.6 Rc
Tensile Yield (at 0.2% offset) Strength	180,000 psi (1.24 GPa)
Ultimate Tensile Strength	215,000 psi (1.48 GPa)
Corps of Engineers Drawing	No. AW 60-02-02
Outside Diameter	21.80 in. (0.55 m)
Inside Diameter	15.80 in. (0.40 m)
Bar Diameter	3 in. (7.62 cm)
Free Height	47.40 in. (1.20 m)
Solid Height	22.40 in. (0.57 m)
Total Defection	25 in. (0.64 m)
Load Rate	2600 lbs (1.18 Mg)
Solid Stress - Corrected	150,000 psi (1.03 GPa)
Solid Stress - Uncorrected	112,000 psi (0.77 GPa)
Installed Height (12.7 in. Defl)	34.70 in. (0.88 m)
Installed Load	33,000 lbs (14.98 Mg)
Installed Load Stress - Corrected	76,000 psi (0.52 GPa)
Installed Load Stress - Uncorrected	57,000 psi (0.52 GPa)
Total Turns	8.2 (6.7 Active)
Shotpeening Requirements	0.010 - 0.012 C Intensity, 98% min. Coverage

Magnetic Particle Inspection Required per Mil-I-6868 (No Defects)

Paint Finish:
     Primer - One Coat Zinc Chromate Primer (MIL-STD-35613)
     Finish Coat - One Coat White Laquer (MIL-L-7178)

Service:
     Essentially static loading, no cyclic
     Axial loading with no evident laterally applied loading.

Temperature:
     Estimated 65°F year round (18°C)

Relative Humidity:
     Reported 75%

Table A2

Results of Field Inspection of Springs Sent to CERL

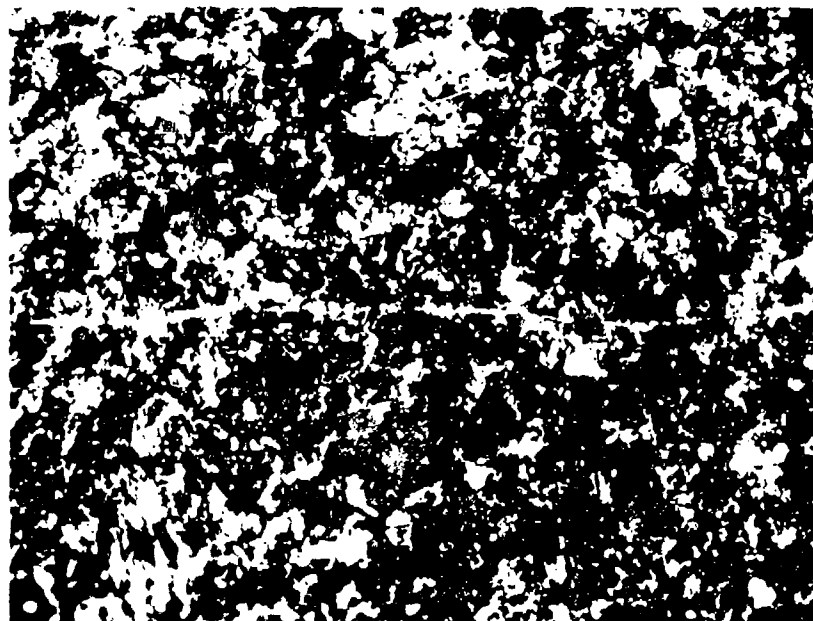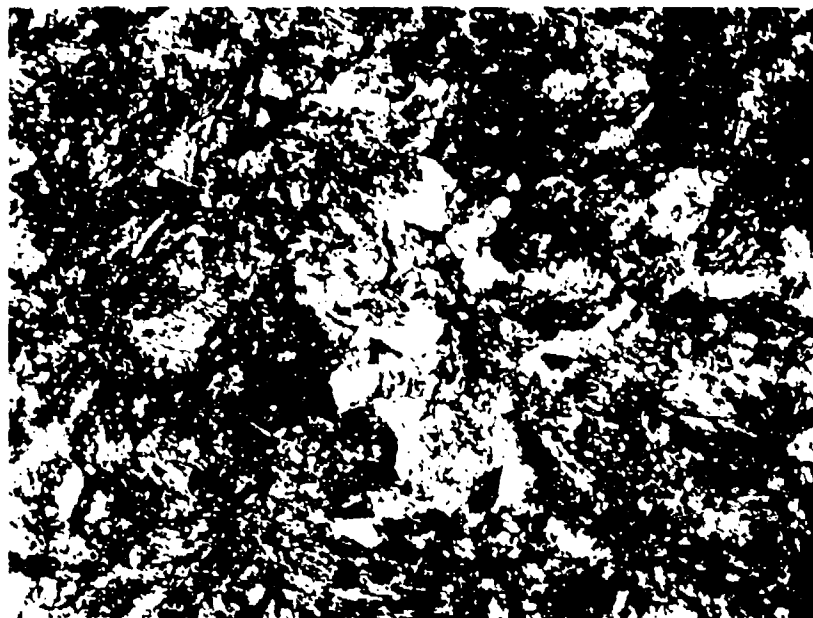| Position Number	Serial Number	Inspection Results
21	UP 585	Broken
10	UR 102	Cracks associated with pits in active coils.
16	UP 518	Cracks associated with pits in active coils.
1	UR 87	Shallow radial crack 0.5 in. (1.27 cm) long
79	UA 1003	Shallow longitudinal crack 0.5 in. (1.27 cm) long

Figure A30. Microstructure of parent rail metal (a) and heat-affected
zone (b) containing the weld zone. The microstructure in
a and b consists of ferrite and pearlite, which is normal
for this alloy.

317

Figure A31. Fracture surface of the specimen No. 4 machined from the weld joint and pulled to failure. The specimen failed in the weld zone. The initiation zone of the fracture was a flat spot surrounded by fibrous fracture. The rest of the specimen showed smooth surface.
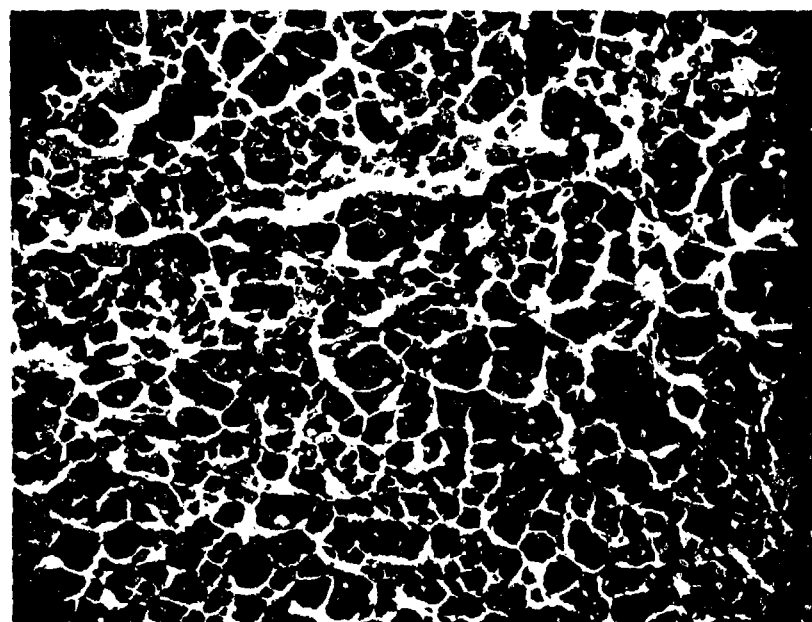
Figure A32. SEM photograph of the fracture surface of tensile specimen No. 4. The "flat spot" in the weld zone where the fracture initiated is shown. The fibrous fracture around the spot can be observed. The gold wire was used as a marker (a). The structure of the "flat spot" is shown under higher magnification (b).
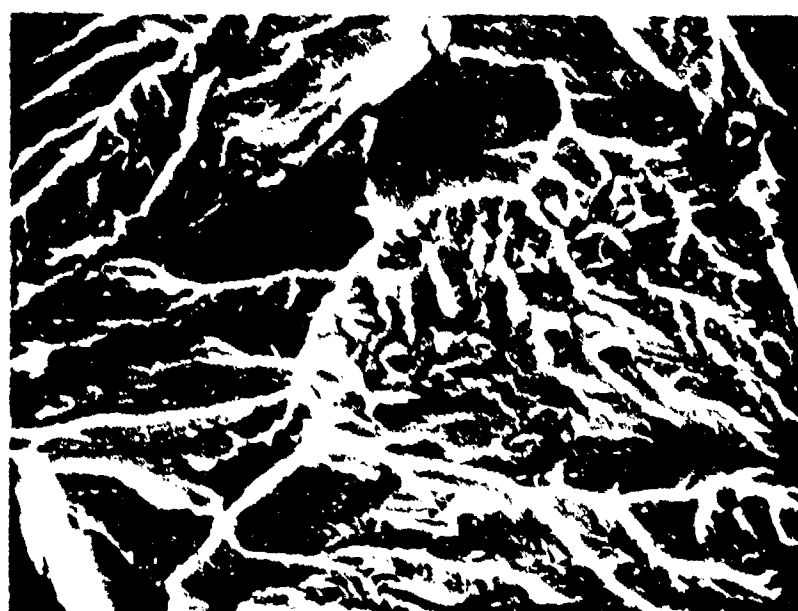
319
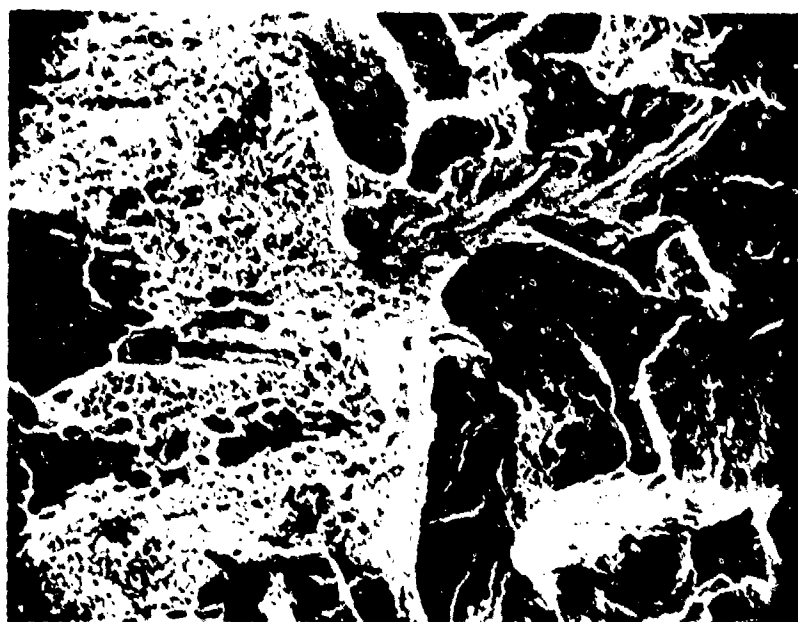
Figure A33. SEM photograph of the fracture surface of tensile specimen
No. 4 (a) which failed in the weld zone. The area shown
has features typical of the fracture surface away from
the "flat spot" parent rail metal (b) pulled to fracture
in tension.

Figure A34. Cross section of the fractured west rail.

Figure A35. Fracture surface of tensile specimen No. 3 (a). Specimens machined from the welded joint failed in the weld zone showing a smooth fracture surface with a flat spot. Specimens machined from the parent rail metal (b) show fibrous fracture surface.

CERL DISTRIBUTION

Director of Facilities Engineering
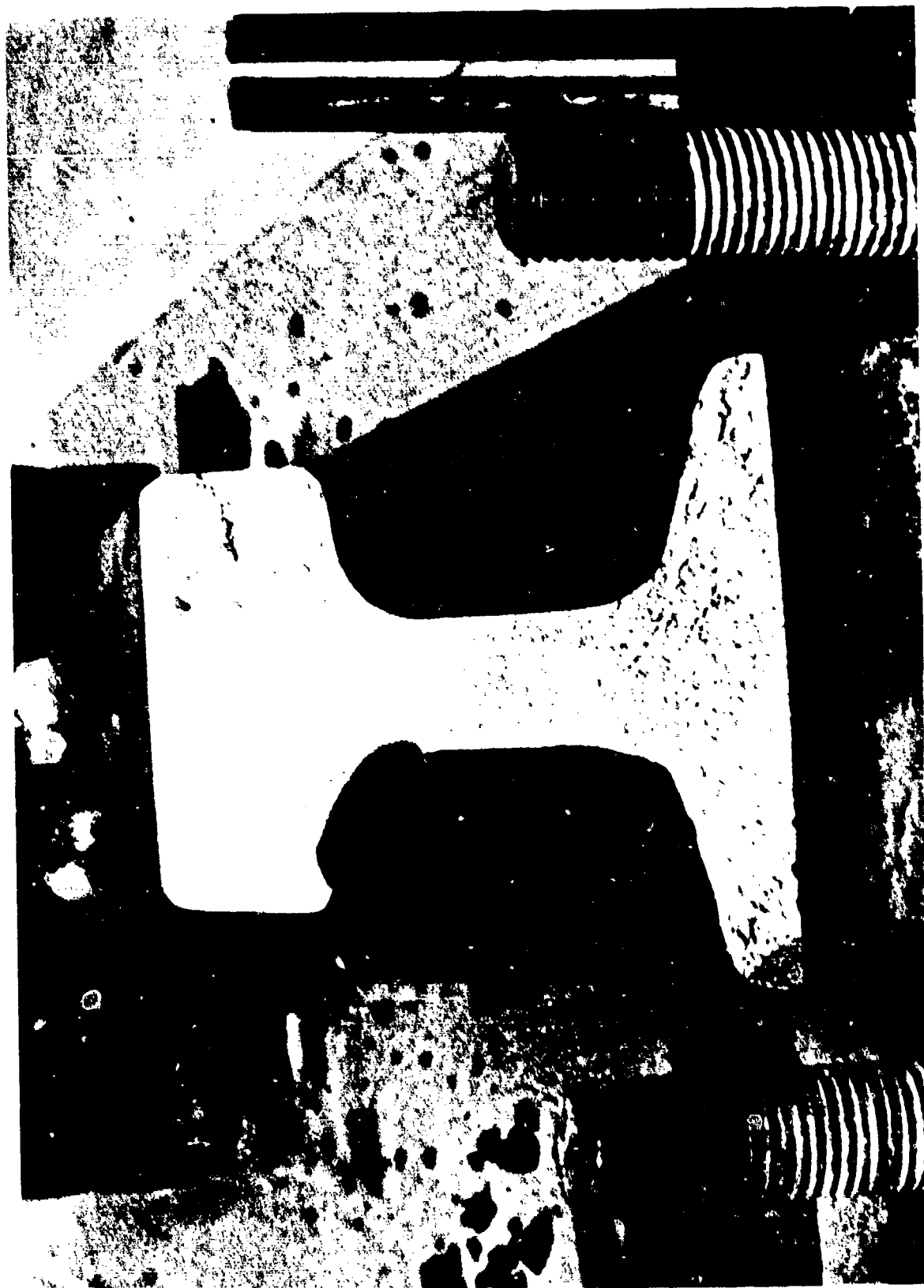APO NY 09827

DARCOM STIT-EUR
APO New York 09710

West Point, NY 10996
ATTN: Dept of Mechanics
ATTN: Library

Chief of Engineers
ATTN: DAEN-ASI-L (2)
ATTN: DAEN-MPO-U
ATTN: DAEN-MPZ-A
ATTN: DAEN-MPR
ATTN: DAEN-RDL
ATTN: DAEN-PMS (6)
  for forwarding to
  National Defense Headquarters
  Director General of Construction
  Ottawa, Ontario K1A0K2
  Canada

  Canadian Forces Liaison Officer (4)
  U.S. Army Mobility Equipment
    Research and Development Command
  Ft Belvoir, VA 22060

  Airports and Const. Services Dir.
  Technical Information Reference
    Centre
  KAOL, Transport Canada Building
  Place de Ville, Ottawa, Ontario
  Canada, K1A0N8

Ft Belvoir, VA 22060
ATTN: Kingman Bldg, Library

Ft Monroe, VA 23651
ATTN: ATEN

Ft McPherson, GA 30330
ATTN: AFEN-FED

USA-WES
ATTN: Concrete Laboratory
ATTN: Library

6th USA
ATTN: AFKC-LG-E

US Army Science & Technology Center
 - Far East Office

US Army Engineer District
  Buffalo
    ATTN: Library
  Pittsburgh
    ATTN: Library
  Philadelphia
    ATTN: Library
    ATTN: Chief, NAPEN-D
  Baltimore
    ATTN: Chief, Engr Div
  Norfolk
    ATTN: Chief, NAOEN-D
  Wilmington
    ATTN: Chief, SAWEN-D
  Charleston
    ATTN: Chief, Engr Div
  Savannah
    ATTN: Library
    ATTN: Chief, SASAS-L
  Jacksonville
    ATTN: Library
    ATTN: Const. Div
  Mobile
    ATTN: Chief, SAMEN-C
    ATTN: Chief, SAMEN-D
  Nashville
    ATTN: Library
  Memphis
    ATTN: Chief, LMMED-DM
  Vicksburg
    ATTN: Chief, Engr Div
  Louisville
    ATTN: Chief, Engr Div
  St Paul
    ATTN: Chief, ED-D
  St Louis
    ATTN: Library
  Kansas City
    ATTN: Library (2)
  Omaha
    ATTN: Chief, Engr Div

US Army Engineer District
  New Orleans
    ATTN: Library
    ATTN: Chief, LMNED-DG
  Little Rock
    ATTN: Chief, Engr Div
  Tulsa
    ATTN: Library
  Albuquerque
    ATTN: Library
  San Francisco
    ATTN: Chief, Engr Div
  Sacramento
    ATTN: Chief, SPKED-D
  Japan
    ATTN: Library
  Portland
    ATTN: Chief, DB-6
  Seattle
    ATTN: Chief, NPSCO
  Walla Walla
    ATTN: Library
    ATTN: Chief, Engr Div
  Alaska
    ATTN: Library
    ATTN: NPADE-R

US Army Engineer Division
  Europe
    ATTN: Technical Library
  New England
    ATTN: Library
    ATTN: Chief, NEDED-T
  North Atlantic
    ATTN: Chief, NADEN-T
  South Atlantic
    ATTN: Chief, SADEN-TS
    ATTN: Library
  Huntsville
    ATTN: Library (2)
    ATTN: Chief, HNDED-CS
    ATTN: Chief, HNDED-SR
  Lower Mississippi Valley
    ATTN: Library
  Ohio River
    ATTN: Library
    ATTN: Chief, Engr Div
  North Central
    ATTN: Library
  Missouri River
    ATTN: Library (2)
  Southwestern
    ATTN: Library
    ATTN: Chief, SWDED-TM
  Pacific Ocean
    ATTN: Chief, Engr Div
  North Pacific
    ATTN: Chief, Engr Div

Facilities Engineers
  Ft Campbell, KY 42223
  USAECOM
    Ft Monmouth, NY 07703
  OFAE, USAIC
    Ft Benning, GA 31905
  TRADOC
    Ft Knox, KY 40121
    Ft Sill, OK 73503
    Ft Bliss, TX 79916
  HQ, 1st Inf Div & Ft Riley
  HQ, 5th Inf Div & Ft Polk
  HQ, 7th Inf Div & Ft Ord

AFESC/XRL
Tyndall AFB, FL 32403

Naval Air Systems Command
ATTN: Library
WASH DC 20360

Naval Facilities Engr Command
ATTN: Code 04
Alexandria, VA 22332

Port Hueneme, CA 93043
ATTN: Library (Code L08A)

Washington, DC
ATTN: Transportation Research Board
ATTN: Library of Congress (2)
ATTN: Dept of Transportation Library

Defense Documentation Center (12)

Engineering Societies Library
New York, NY 10017

American Society of Metals
Metals Park, OH 44073